Analysis of variable VHE gamma-ray emission from the hard spectrum blazar 1ES 1218+304

by

Asif Imran

A dissertation submitted to the graduate faculty
in partial fulfillment of the requirements for the degree of
DOCTOR OF PHILOSOPHY

Major: Astrophysics

Program of Study Committee:
Frank Krennrich, Major Professor
David Carter-Lewis
Jim Cochran
Charles Kerton
Andrew Miner

Iowa State University
Ames, Iowa
2010

To *Ammu* and *Abbu*

TABLE OF CONTENTS

LIST OF TABLES

LIST OF FIGURES

ACKNOWLEDGMENTS

It has been a long journey writing and finishing this chapter of my life. Along the way, I am truly humbled to have been mentored by a number of great teachers and friends. Both my personal and academic endeavors have been enriched as a result of their collective wisdom, experience and help. To all of them, I am forever indebted.

I would like to especially acknowledge the contribution of my supervisor, Frank Krennrich. His deep insights and appreciation for scientific rigor have been a true source of inspiration for me. It is no small feat to emulate Frank's tenacity and enthusiasm for science! I tried my best and I have grown as a scientist along the way.

I also would like to thank David Carter-Lewis at ISU and Charie Duke at Grinnell College. It was always a pleasure talking to David over a cup of coffee. I truly appreciate his guidance and support over the years. While I was still an undergraduate student, Charlie provided me with an excellent research opportunity through the summer mentoring program at Grinnell College. It was my introduction to the wonderful world of gamma-ray astronomy and for that I am grateful to Charlie. I also acquired most of my programming knowledge from Charlie, who never ceases to amaze me with his ROOT skills!

I am particularly indebted to our former postdoc and my dear friend, Tomo Nagai. I will forever be thankful to him for holding my hands and guiding me at the beginning of my research career. It was a stroke of luck that Tomo took up office next to my desk. He always made himself available to answer my questions. I can not thank him enough for his remarkable patience, which was certainly tested by my incessant questioning at all times of the day. Thanks, Tomo-san, for your friendship and I look forward to our business empire someday.

Many thanks to Martin Schroedter for putting up with my often hard-to-decipher code and throwing wonderful *soirees* at his house. Thanks to the wonderful ladies at the main office– without whom I'd be hopelessly lost over the years: Linda Shuck, Lori Hockett, Diane Smith, and Gloria Oberender. Thanks to my friends from graduate school who made the experience a little bit more enjoyable and helped maintain my sanity: Bagmeet, Ada, Supriyo, Sehwook, Qian, Mun and Kang. I am also indebted to the various members of the VERITAS collaboration with whom I have come in contact. This thesis would not have been possible without the hard work of all the dedicated members and staff at the basecamp- so, a big thank you to each and every one of them!

Finally, I would like to thank my family for their unwavering support and prayers throughout my life. My dear parents, Shahana Begum and MAK Talukder have made immense sacrifices in raising their three sons over the years. I can never repay you for your encouragement and unyielding love. A very special thank you to *Ammu* and *Abbu*! Thanks to my wonderful brothers Saquib and Rafi. I am forever grateful to Sajib bhai, Swapon bhai, and Nadim kaka, my old *gang* back in Dhaka– I can not describe what your friendship has meant to me over the years.

At the end of this journey, I would like to thank my beloved wife, Courtney– for her constant love and enduring support. I would never have got this far without her patience and encouragement throughout the writing of this thesis (not to mention the never ending supply of sandwiches and cookies!). I am truly lucky to have you in my life. Thank you!

ABSTRACT

This thesis is a study of the very high energy gamma-ray emission from the hard spectrum blazar 1ES 1218+304. The data were collected during the 2008/09 observing season by the VERITAS observatory, an array of four atmospheric Cherenkov telescopes in Southern Arizona. This work describes the development of a set of analysis tools suitable for the extraction of the energy spectra of astrophysical objects. Initially, the tools are applied to the Crab nebula data to optimize and calibrate the analysis. Afterwards, the analysis is applied to the high energy observations of the blazar 1ES 1218+304. We report an intense, day-scale flare observed on January 30, 2009. This marks the first detection of variability in gamma-ray emission from 1ES 1218+304. I also investigate the possibility of detecting a spectral feature in the observed energy spectra of blazar due to extragalactic background light. I demonstrate the presence of a spectral cut-off in the simulated multi-TeV energy spectra of blazars at around 1 TeV. This novel technique has a strong potential to discover the first observable signature of absorption of very high-energy photons due to the extragalactic background light.

List of Acronyms and Abbreviations

1ES	First Einstein Survey
2MASS	Two Micron All Sky Survey
3EG	Third Egret
AGN	Active Galactic Nuclei
asl	Above sea level
BATSE	Burst and Transient Source Experiment
BL Lac	BL Lacertae
CANGAROO	Collaboration of Australia and Nippon for a Gamma-Ray Observatory in the Outback
CFD	Constant Fraction Discriminator
CGRO	Compton Gamma-Ray Observatory
CMB	Cosmic Microwave Background
COBE	COsmic Background Explorer
dc	Digital Counts
DIRBE	Diffuse Infrared Background Experiment
EAS	Extended Air Shower
EBL	Extragalactic Background Light
EC	External Compton
EGRET	Energetic Gamma-Ray Experiment Telescope
eV	Electron Volt
FADC	Flash Analog to Digital Converter
Fermi	Fermi Gamaa-Ray Space Telescope
FIR	Far Infrared
FIRAS	Far Infrared Absolute Spectrometer
FOV	Field of View
FSRQ	Flat Spectrum Radio Quasar
GeV	Giga Electron Volt
GRB	Gamma-Ray Burst
GrIsep	Grinnell ISU Energy Package
HBL	High frequency-peaked BL Lac object.
HE	High Energy

HESS	High Energy Stereo System
HST	Hubble Space Telescope
HV	High Voltage
IACT	Imaging Air Cherenkov Telescope
IBL	Intermediate frequency-peaked BL Lac object
IC	Inverse Compton
IPD	Interplanetary dust
IR	Infrared
ISU	Iowa State University
L1/2/3	Level 1/2/3
LBL	Low frequency-peaked BL Lac object
MAGIC	Major Atmospheric Gamma-ray Imaging Cherenkov
MC	Monte Carlo
MeV	Mega Electron Volt
MHD	Magneto HydroDynamaics
MIR	Medium Infrared
Mkn	Markarian
MJD	Modified Julian Date
MRSL/W	Mean-Reduced Scaled Length/Width
NIR	Near Infrared
NIRBE	Near Infrared Background Excess
ns	Nano-second
nm	Nano-meter
NSB	Night Sky Background
pc	Parsec
pe	Photoelectron
PMT	Photomultiplier Tube
PSF	Point Spread Function
PST	Pattern Selection Trigger
PWN	Pulsar Wind Nebula
QE	Quantum Efficiency
RMS	Root Mean Squared
RXTE	Rossi X-ray Timing Explorer
SED	Spectral Energy Destribution (or Density)
SMBH	Super Massive Black Hole
SNR	Supernova Remnant
SPB	Synchrotron Proton Blazar
SSC	Synchrotron Self Compton

TeV	Terra Electron Volt
ToO	Target of Opportunity
UV	Ultraviolet
VBF	Veritas Bank Format
VERITAS	Very Energetic Radiation Imaging Telescope Array System
VHE	Very High Energy
VLA	Very Large Array
VLBI	Very Long Baseline Interferometry

CHAPTER 1. INTRODUCTION

1.1 Astrophysical Source of VHE Gamma-Rays

In a universe that is teeming with countless bright objects, the 19th-century German astronomer Heinrich Olbers grappled with the darkness of the night sky in sheer wonderment and curiosity– how can an infinite universe full of stars not be aglow with light in every direction? Modern observations have revealed a much vaster realm that is blazing with light in wavelengths not visible to the naked eyes. Moreover, a new generation of space- and ground-based instruments have opened a window to a universe that is surprisingly rich and complex at the highest gamma-ray energies. The evolving field of gamma-ray astronomy probes astronomical objects at photon energies above 10 MeV, photons 10^7 times more powerful than optical photons. In this energy band, the universe is dominated by non-thermal emission from some of the most violent astrophysical environments in the universe. This energy regime is further divided into two broad bands roughly based on different interaction phenomena and methods used in their detection (Weekes, 2003): the high energy (HE) band from 30 MeV to 100 GeV and the Very High Energy (VHE) band from 100 GeV to 100 TeV. Efforts to detect HE gamma-rays began with the Explorer XI satellite instrument in 1965 followed by SAS-2 and Cos-B orbital experiments.

One of the earliest credible detections of HE gamma-ray sources arrived with the launch of the Energetic Gamma-ray Experiment (EGRET) on board the Compton Gamma Ray Observatory (CGRO) in 1990. During its highly successful career, EGRET, a pair conversion telescope, provided unprecedented energy coverage between 20 MeV and 10 GeV. EGRET observations opened up an exciting new window to the universe in gamma-ray energy (Schönfelder, 2001). It confirmed that the galaxy is a strong emitter of gamma-rays due to the interaction of cosmic rays with the interstellar medium and identified pulsars as a source of gamma-rays. Most importantly, it established blazars as the largest class of extragalactic gamma-ray sources. The total of 271 sources discovered by EGRET at energy > 100 MeV (Hartman et al., 1999) proved to be one of the most important sources of information on gamma-ray emission from blazars in the sub-GeV range. Of these sources, 170 have yet to be identified with objects at other wavelengths. In the Third Catalog of EGRET observations, a total of 70 active galactic nuclei (AGN) were identified as gamma-ray emitters.

As with earlier satellite-borne gamma-ray experiments, EGRET was limited by large sta-

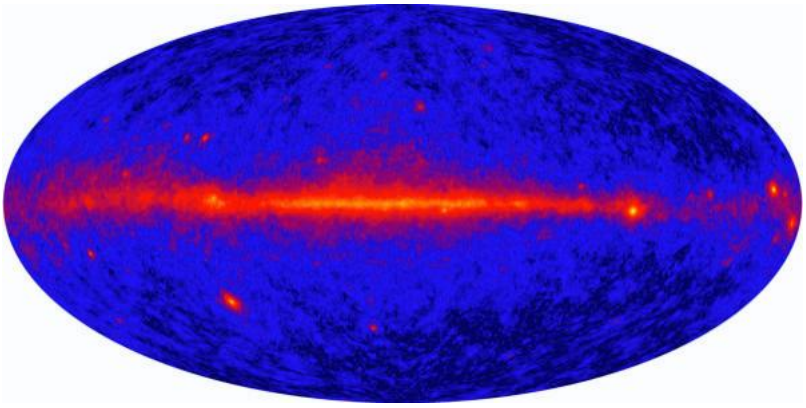

Figure 1.1 Fermi all sky map showing the gamma-ray intensity for energies above $>$ 300 MeV. [*Credit:* NASA/DOE/International LAT team.]

tistical uncertainties. More importantly, the sensitivity of satellite instruments to objects at higher wavelength decreases due to the steeply falling gamma-ray energy spectra. Consequently, gamma-ray flux becomes extremely sparse beyond 10 GeV, requiring prohibitively large collection areas for space-based instruments. Fortunately, the development of ground-based Atmospheric Imaging Cherenkov Telescopes (IACT) with large detection areas are beginning to close the gap for detection at higher energies. The Whipple Observatory in Southern Arizona, a premiere Cherenkov instrument, pioneered the detection of astrophysical sources of VHE gamma-rays above $\gtrapprox$ 350 GeV with the detection of the Crab Nebula. In addition to the first successful detection of the TeV gamma-rays from an extragalactic source Mkn 421 (Punch et al., 1992), Whipple established Crab nebula as a steady emitter VHE gamma-rays. More recently, the advent of the latest generation of IACTs such as H.E.S.S.(Aharonian et al., 2006a), MAGIC, and VERITAS (Holder et al., 2006) has dramatically increased the number of VHE gamma-ray sources. These instruments employ stereoscopic observations using multiple IACTs to significantly reduce the energy threshold, thus enabling detection of VHE sources down to 50 GeV.

The *Fermi Gamma-ray Space Telescope* (*Fermi*), successor to the highly successful CGRO instrument was launched in 2008. With greatly improved sensitivity, angular resolution, and energy range ($30 <$ MeV < 300GeV), the first ~ 5 months of *Fermi* observations has already yielded a deeper and better resolved map of the gamma-ray sky than any previous space mission (Abdo et al., 2009a). Figure 1.1 shows the all-sky map produced by *Fermi* in the first 3 months of observations (Abdo et al., 2009b). The sky survey detected GeV emission from 21 TeV-detected AGNs, and from 17 AGN's previously detected by TeV experiments. For the first time, the complementary energy coverage between spaced-based *Fermi* and current ground-based IACTs will allow detailed and *in-depth* multiwavelength observations of VHE

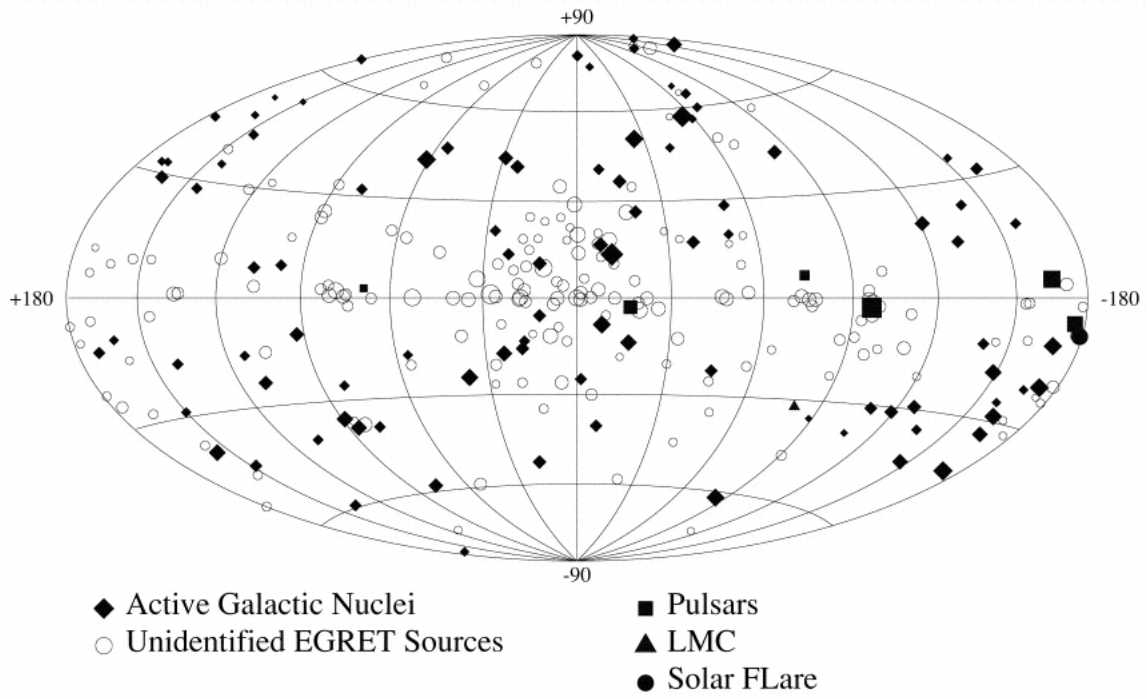

Figure 1.2 Sky map of the abundance of both galactic and extragalactic sources in the third EGRET catalog (Hartman et al., 1999)

gamma-ray sources in the near future. In the following section, we briefly discuss the two main categories of VHE sources, namely galactic sources and extragalactic source. In addition, we also discuss possible detection of VHE gamma-ray emission from unidentified sources.

1.1.1 Galactic Sources of VHE gamma-rays

A large number of the potential galactic sources of VHE gamma-ray emission are associated with massive star formation and therefore are predominantly found along the Galactic plane. Figure 1.2 shows the EGRET sky map indicating the abundance of sources for non-thermal radiation in our own galaxy. These strong galactic sources are briefly described below:

Supernova remnants

The final fate of massive stars depends upon a delicate balance between the quantum degeneracy pressure against the contracting force of gravity. For a sufficiently large star, pressure from gravity can cause the star to collapse as it runs out of fuels necessary to counteract the gravity. This eventual collapse of the star is an explosive process followed by the ejection of the outer shells of the stellar material. During this violent explosion or **supernova**, the core becomes a compact object, a neutron star or a black hole depending on the mass of the original star. The ejected material shrouding the remaining compact object subsequently

form a supernova remnant (SNR). It has been long suspected that Galactic SNR could be the acceleration sites for the production of cosmic ray with energies up to $\sim 10^{15}$ eV. The primary mechanism for the production of high energy emission in SNR is the diffusive (first order Fermi) shock acceleration of charged particles as the resulting blast-wave sweeps up ambient matter in the expanding remnant (for reviews see e.g., Begelman et al., 1984; Malkov & Drury, 2001). Furthermore, Galactic supernovae and the subsequent SNRs are the only known potential sources which can produce the necessary energy observed in the cosmic ray spectrum. Accelerated charged particles on the shock fronts, primarily protons, produce VHE gamma-ray emission through intermediate pion production and decay $p+p \rightarrow \pi^0 \rightarrow 2\gamma$ (Drury et al., 1994). In addition, electrons accelerated in the shock also generate non-thermal emission through bremsstrahlung, inverse-Compton upscattering of cosmic microwave background and through synchrotron emission in the magnetic field of the SNR. The observed radio and X-ray emission from shell type SNR are considered to be produced by the radiation from electrons. Observed synchrotron emission in the X-ray wavelengths point to strong evidence for the existence of $\sim$ 100 TeV electron in shell-type SNRs (Koyama et al., 1995). Shell-type SNRs have also been established as confirmed sources of TeV gamma-rays by different TeV groups including VERITAS collaboration (Acciari et al., 2009d, 2010b). TeV emission from SNR has provided direct proof of particle acceleration in the SNR shock fronts. However, these observations have thus far failed to provide direct proof of hadron acceleration in the SNR since effects from the Galactic magnetic field makes it difficult to accurately determine the true origin of protons and electrons. Furthermore, the pion-decay model to explain the TeV observations of SNR RX J1713.7–3496 by the CANGAROO collaboration has proven to be inadequate for explaining the GeV data in multi-band spectrum of SNRs (Reimer & Pohl, 2002).

Pulsars and Plerions

Pulsars are rapidly spinning neutron stars left over in the aftermath of a collapse of the iron core in a massive star supernova. These objects have long been considered as a possible source of VHE gamma-rays (e.g., Harding, 1996). Pulsars usually have intense magnetic fields ($\approx 10^{12}$ G) with very short rotational periods (as low as milliseconds) which induces a very large electric field at the surface. These objects are thought to be powered by the slowing of the spinning neutron star. The production of pulsed VHE emission has been described by to two models: the "polar cap" model and the "outer gap" model. In the first model, fast rotation rips away electrons or ions from the polar region of the neutron star. The imbalance of electric charges around the pole results in a charged plasma. Subsequently, the plasma particles are accelerated to relativistic speed by the induced electric field. As the electrons follow the curved magnetic field lines, VHE gamma rays are emitted in the form of curvature radiation. The accelerated particles also inverse-Compton upscatter thermal X-ray photon

from the surface producing VHE gamma rays (Ruderman & Sutherland, 1975). The presence of a large magnetic field in the accelerating region allows photon pair production ($\gamma \rightarrow e^{\pm}$) which give rise to a sharp cutoff in the observed gamma-ray spectrum around several GeVs. In the "outer gap" model, acceleration of charged particles takes place much further from the surface of the neutron star. Accelerated particles in the highly magnetized environment similarly radiates away gamma rays in the form of curvature radiation or inverse-Compton scattering (Cheng & Ruderman, 1986).

A plerion is a SNR with a pulsar at the center. The plerion emission is dominated by a central core nebula, with strong non-thermal optical and X-ray emission along with a radio spectrum. The X-ray and radio emission from plerions are produced by the relativistic electrons surrounding the central pulsar. VHE gamma-ray emission (up to TeV energies) from plerion occurs through the inverse-Compton upscattering of the synchrotron photons by the high energy electrons. In addition, plerions can produce MeV photons through shock-acceleration of electrons in the nebula. Such objects are expected to exhibit a pulsed radiation component-from the pulsar together with a steady component from the shock region and beyond. The steady emission of VHE gamma rays from the Crab Nebula is one of the prime examples of a plerion. Crab was first discovered in the TeV energies by the Whipple Collaboration in 1989 (Weekes et al., 1989). Since then it has been routinely observed by many high-energy experiments and currently regarded as the standard candle for VHE gamma-ray astronomy in the Northern hemisphere.

X-ray binaries

X-ray binary systems consist of a compact object such as pulsar with, a large companion star orbiting the central object. The intense, close gravitational field from the compact object are responsible for stripping matter away from the large star, creating an accretion disk around the compact object. Several X-ray binaries are also known as *microquasars* since radio observations have revealed relativistic jets similar to Active Galactic Nuclei. Traditionally, X-ray binaries have been considered a thermal source where gravitational energy is converted into X-ray energies but the evidence for relativistic outflow points toward non-thermal high energy processes. VHE gamma ray from X-ray binaries are attributed to inverse-Compton upscattering of stellar photons by relativistic electrons. Emission models of X-ray binaries with jets predict hard non-thermal radio and X-rays produced by synchrotron emission of ultra-relativistic electrons. The H.E.S.S collaboration made the first discovery of VHE gamma-ray emission from the X-ray binary LS 5039 (Aharonian et al., 2005c). This was followed by the detection of a second X-ray binary LS I+61 303 by the MAGIC collaboration (Albert et al., 2006d). Both these objects exhibited periodic modulation of the observed VHE emission due to the orbital motion.

O-B association

HEGRA Collaboration discovered VHE emission from a serendipitous source TeV J2032+4130 without any obvious counterpart (Aharonian et al., 2005e). However, the source location was found to be in proximity to a region of numerous OB-stars. Sites containing massive O- and B- stars are marked by high rates of star formation such that OB associations are remarkable for extremely high density of pulsars and SNR. The presence of rapidly evolving stars generate dense molecular clouds filled with strong interstellar winds together with possible SNR shock fronts and pulsar winds. Such an environment around the O-B association region serve as a plausible location for the production of VHE gamma-ray (Torres et al., 2004).

1.1.2 Extragalactic Sources of VHE gamma-rays

Active Galactic Nuclei

In a small fraction of about 1% of the observable galaxies in the universe, the central core greatly out-shines the rest of the host galaxy. These unusually bright galaxies are known as Active Galactic Nuclei (AGN). The extreme amounts of radiation together with sometimes powerful jets emanating from the central region of these galaxies cannot be attributed to nuclear processes typically associated with stellar emission. Furthermore, the non-thermal emission from AGN generally comprise of powerful continuum emission at UV to soft X-ray energies in contrast to the less energetic UV-infrared radiation from stars present in the galaxy. As a result, emission from the central bright core of AGN greatly dominates the combined stellar emission of the rest of the galaxy.

AGNs are thought to be powered by accretion of material onto a central super-massive black hole (SMBH) forming a disk of hot plasma. The SMBH with a mass of $\sim 10^6 - 10^{10}$ $M_\odot$[1] is typically constrained in a region the size of our solar system with a Schwarzschild radius of $\sim 10^{-5}$ pc[2]. As matter whirls into the black-hole, friction and turbulent processes convert gravitational energy into thermal radiation within the accretion disk. The resulting thermal emission, peaking at UV wavelengths, in turn ionizes surrounding fast-moving gas clouds (extends up to ~ 30 pc). Thus producing Doppler-broadened emission lines (broad-line region). A dusty torus-shaped structure envelops the broad-line region. Further out from the core and the torus, slower molecular-clouds generate narrow emission lines (narrow-line region).

AGNs are often characterized by the formation of either one or two ultrarelativistic outflow (jets) of charged particles or plasma perpendicular to the plane of the accretion disk. In certain AGNs, two opposite and, highly collimated jets have been observed emanating from the central region. While the mechanism responsible for forming the jet is not well understood, Section 1.2.1 discusses some of the viable theoretical model for explaining the jet. Radio

[1] where M$\odot$ corresponds to 1 solar mass.
[2] 1pc $\approx 3 \times 10^1$8 cm

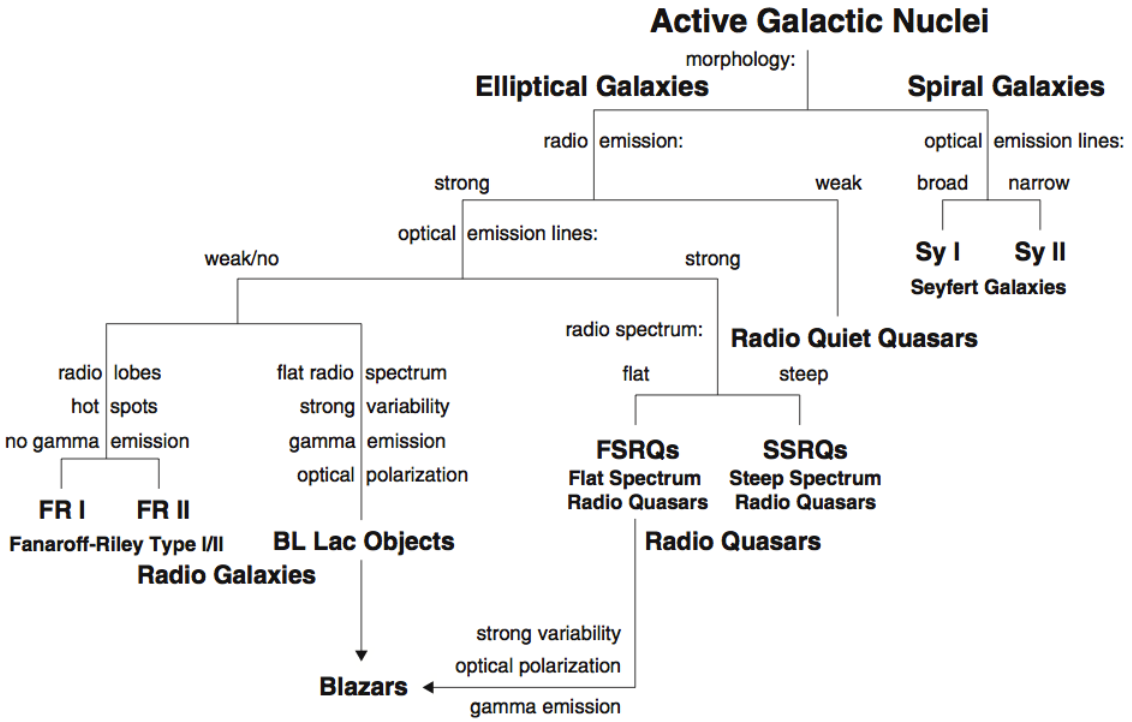

Figure 1.3 Empirical paradigm of AGN based largely on observational properties of the different classes of AGNs. [Taken from Wagner (2006)]

imaging of these jet-structures have revealed inhomogeneous regions of increased density or knots flowing along the length of the jet. The highly relativistic velocity of the knots are usually given by the bulk Lorentz factor $\gamma = 1/\sqrt{(1-\beta^2)}$, where β is the velocity of the knot relative to the galaxy in units of the speed of light. Given the viewing angle of the jets, the knots can appear to travel at a velocity greater than the vacuum speed of light c. This forward-boosting of the jet is a purely relativistic phenomenon that is quantified by the Doppler factor,

$$\delta = \frac{1}{\gamma(1-\beta\,\cos\theta)} \tag{1.1}$$

where θ is the angle between the jet and the observer's line of sight. Hence, for certain values of the viewing angle the material within the jet appears superluminal.

One of the great surprises from the EGRET mission was the discovery of gamma-rays from a large number of extragalactic sources, most of them belonging to the AGN class of objects. Earlier, extragalactic sources were largely ruled out as viable targets for VHE observations due to significant absorption of gamma rays in the extragalactic space. Since the EGRET

mission, highly sensitive telescopes based on the evolving imaging Cherenkov technique have discovered numerous AGNs that emit electromagnetic radiation over a wide range of energies and over a large range of redshifts. The observed radiation from AGNs exhibit a rather large range of measurable properties. Not surprisingly, the taxonomy of AGN in the past followed categorization by their radio emission, the properties of their optical emission lines, morphological considerations, degree of polarizations, rapid variability and peak-emission wavelengths (Figure 1.3). These distinctions often reflect the historical context for the detection of AGNs and may not provide any insights into their underlying astrophysical properties. In the present AGN paradigm, various subclasses of AGNs are believed to be connected by the unified AGN scheme (Figure 1.4). In this scenario, the observed properties of the different types of AGN are determined by the observation angle. Hence, the orientation effect may explain the observation of an AGN when looking directly down the jet. The radiation consists of Doppler boosted radiation from the jet, continuum emission from the accretion disk together with both broad- and narrow-line emission from the neighboring molecular cloud. The above listed properties are distinctly characteristic of the blazar class of AGN, (discussed in more detail in Section 1.2). At larger viewing angles, radiated emission from AGN consists of narrow- and broad-lines from the unobscured central region while the jet is no longer visible. This may explain the observed properties of steep-spectrum radio quasars, some radio-loud radio galaxies, and radio-quiet Seyfert type I galaxies. For larger observation angles, the dusty torus shields the fast molecular cloud allowing only narrow-line emission to be observed from Seyfert type 2 galaxies and certain narrow-line radio-galaxies. Finally, viewing at right angles to the jet corresponds to the observations of radio galaxies where two opposite jet structures may be seen (M87, e,g., Acciari et al., 2009c).

Starburst galaxies

Observations show that a small fraction of the galaxies in the present-day universe are regions of prodigious star formation rate. Some starburst galaxies have been observed to form new stars at rates exceeding 100 stars per year, significantly more than 1 new star per year in our Milky Way galaxy. The importance of the starburst galaxies were initially overlooked by astronomers since optical- and UV-emission from stars are efficiently shielded by dust grains in the surrounding molecular clouds. However, the advent of space-based telescopes revealed the rich structures of the starburst galaxies in infrared wavelengths. These regions were associated with dense interstellar medium, hot stars, and a very high supernova rate. Considering the close connection between SNR and cosmic-ray acceleration, the importance of VHE observations of starburst galaxies was quickly realized. The high density of SNR is considered sufficiently high to fuel cosmic ray interaction with interstellar gas to generate detectable level of VHE gamma rays. In 2002, CANGAROO Collaboration reported tentative detection of diffuse emission from the starburst galaxy NGC 253 (Ito et al., 2002) but the result could not be

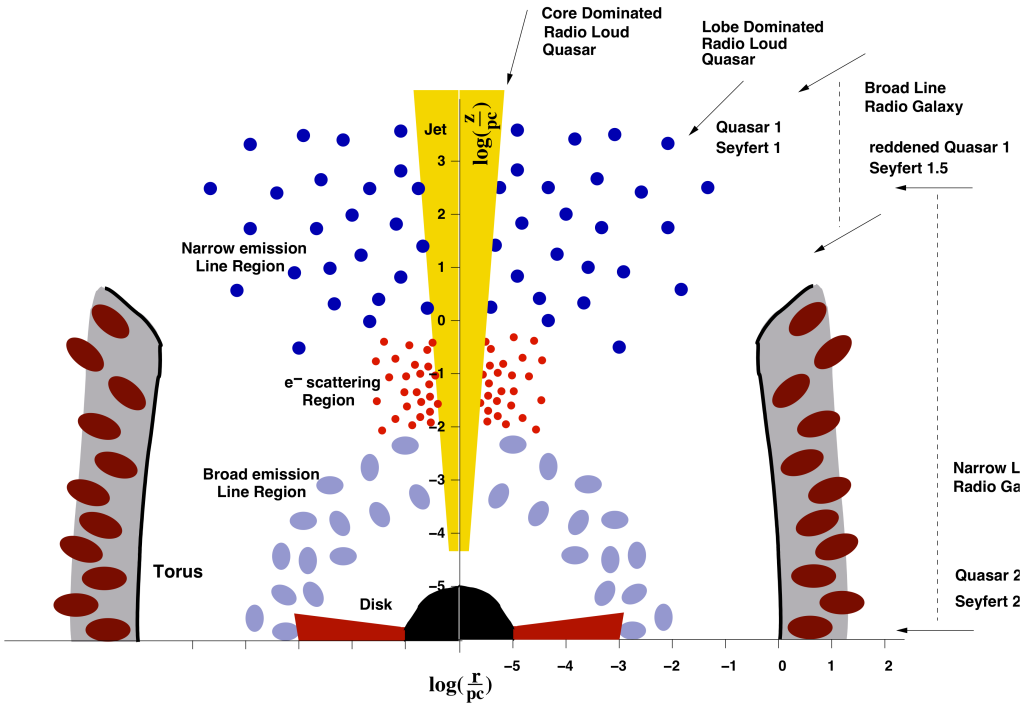

Figure 1.4 Model of an AGN in the unified AGN scheme by Biermann et al. (2003)

confirmed later by the H.E.S.S. Collaboration (Aharonian et al., 2005d). In 2009, VERITAS Collaboration reported excess gamma-ray event above > 700 GeV from small starburst galaxy M82, citing supernovae and massive-star winds as the primary mechanism for the acceleration of cosmic ray responsible for diffuse VHE gamma-ray emission (Acciari et al., 2009e). Shortly afterwards, HESS reported VHE gamma-ray emission from NGC 253 with high statistical confidence (Aharonian et al., 2009b).

Gamma-ray bursts

Classified as the most luminous emission in the universe at any wavelength (Weekes, 2003), the phenomenon of Gamma-ray Bursts (GRBs) over cosmological distances provide new experimental tools to probe objects at the edge of the observable universe (Weekes, 2003). GRBs were serendipitously discovered by the *Vela* series of surveillance satellites, originally tasked with ensuring nuclear non-proliferation during the cold war era. These bursts have been detected over milliseconds to thousands of seconds of duration, where almost all the radiation is emitted at energies above 50 keV with a smooth continuum spectra. VHE emission from GRBs

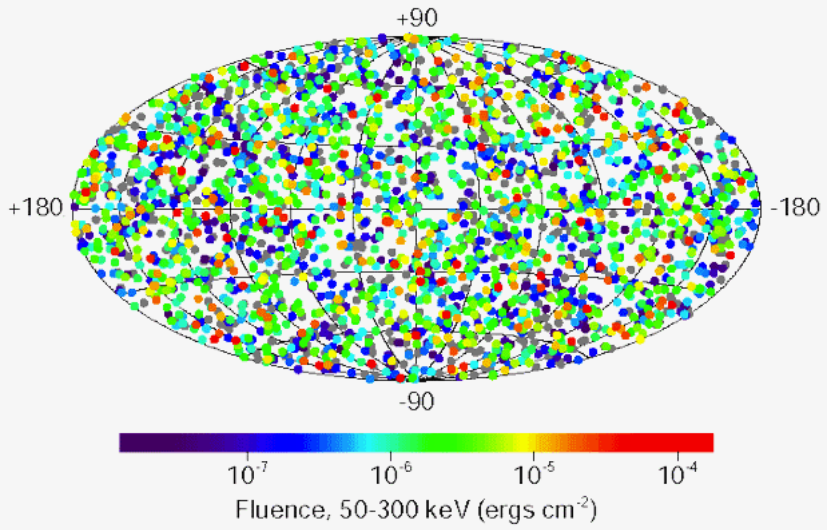

Figure 1.5 The isotropic distribution of 2704 gamma-ray bursts recorded by the BATSE detector on the CGRO. [Credits: Fishman, NASA, BATSE, CGRO.]

can be stronger than any other known gamma-ray sources, with 10^{52} erg being released in the span of a mere second. BATSE (Burst and Transient Source Experiment), a dedicated GRB monitor on board the CGRO satellite recorded a total of 2700 GRB events and the resulting sky map (Figure 1.5) showed an isotropic but inhomogeneous[3] distribution of GRBs in the sky (Briggs et al., 1996). The mean distance to the source of these bursts has been measured to be $z = 2.8$, with a small fraction 7% of the events originating even further away at $z > 5$ (Jakobson et al., 2006). One of the most widely accepted models to explain the HE emission from GRBs invokes the relativistic *fireball model*. In this model, shells of expanding plasma are ejected into the interstellar medium in a succession of explosive events of unknown origin. During the course of the expansion, shells collide to produce internal shocks which is thought to accelerate electrons to ultrarelativistic energies. Consequently, VHE emission from GRBs can be explained by the production of synchrotron and inverse-Compton radiation from the energetic population of electrons (For review, see e.g., Meszaros, 2002).

1.1.3 Unidentified EGRET sources

In addition to the point sources of galactic and extragalactic sources of VHE radiation, it became clear from the results of early satellite experiments such as COS-B and CGRO that the observed gamma-ray emission consists of a diffuse component. Moreover, out of a total of 271 detections, the 3rd EGRET (3EG) catalog identified only 101 sources with known

[3]A homogeneous distribution would correspond to same number density of GRBs regardless of distance or direction

counterparts (66 AGN with high confidence, 5 pulsars, the Large Magellanic Cloud, and solar flares). An additional 27 AGNs were detected with lower confidence but about two thirds of the EGRET gamma-ray sources (170) still remain unidentified. This has prompted intense multiwavelength campaigns with particular emphasis on time-correlated, deep observations at different wavelengths with a variety of scientific instruments. The sky map of EGRET-catalog sources clearly indicate that the distribution of unidentified sources primarily fall into two categories: a dominant Galactic component (Figure 1.2) and a smaller but more isotropic extragalactic contribution (Reimer, 2001). The most likely candidate objects for the galactic unidentified sources are plerions and supernovae based on confirmed gamma-ray emission from these objects. In addition, statistical analyses involving correlation with population studies shows that the unidentified 3EG source at mid-galactic latitude are almost coincident with the Gould Belt region in our galaxy (Gehrels, 2000). This is a local collection of star forming region where the presence of a large amount of molecular cloud and SNR is believed to be a source for diffuse gamma ray emission. Despite large uncertainties associated with individual source identifications, similar studies of the low-latitude sources have revealed 22 unidentified 3EG sources that have positional correlation with known OB associations (Romero et al., 1999). Additionally, high mass X-ray binaries, microquasars and massive O-type stars have been suggested as possible candidate objects for the unidentified 3EG sources of galactic origin (Grenier, 2002; Kaaret et al., 2000). For possible extragalactic gamma-ray source, AGNs (blazars in particular) are believed to make up a substantial fraction of the unidentified sources. Other possible source types include starburst galaxies, radio galaxies, and galaxy clusters. In the latter, on-going merger between galaxies with active-shocks are expected to be sites for VHE gamma-ray emission (Totani & Kitayama, 2000). In summary, unidentified EGRET objects present a rich list of sources with a potential for discovery of VHE gamma-ray from both existing and new classes of objects.

1.2 Blazar Class of AGN

One of the primary research objectives in this dissertation is the analysis of VHE emission from blazar with the VERITAS telescopes. In this section, an overview of the phenomenology of blazars is presented along with a summary of the status of VHE observations of blazars with space- and ground-based instruments. In addition, we give a summary of currently accepted theories of pure leptonic and hadronic models of gamma-ray emission from blazars.

1.2.1 Properties of blazars

Blazars belong to a particularly interesting family of AGN where high energy emission makes them ideal candidates for VHE observations. Blazars jointly comprise flat spectrum radio quasars (FSRQs) with broad, strong emission lines, and BL Lacertae ("BL Lac") ob-

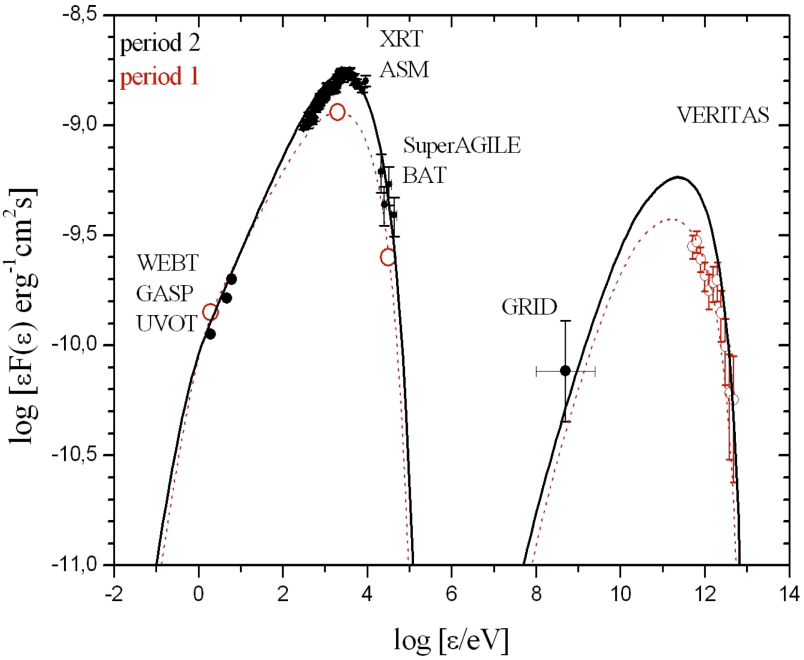

Figure 1.6 The broadband SEDs of Mrk 421 at two different periods of increased emission as observed by GASP-WBT, SWIFT/UVOT, RossiXTE/ASM, XRT, SuperAGILE, BAT, GRID, and VERITAS. The spectral fit corresponds to a specific model, namely one-zone SSC model. Of note is the typical double-humped SED observed in blazars.(Donnarumma et al., 2009)

jects, which show no evidence for emission lines[4] (Angle & Stockman, 1980; Urry & Padovani, 1995). As one of the most extreme classes of active galaxies, blazars are characterized by a relativistic plasma jet oriented at a small angle with respect to the observer's line of sight. They are broadband sources often accompanied by prominent emission of electromagnetic radiation throughout the entire electromagnetic spectrum, some 20 decades of energy from radio to VHE emission (Weekes, 2003). As a consequence of the jet orientation, the bulk of the observed radiation is dominated by non-thermal processes pointing to relativistic phenomenon at the core of these objects. Emission from blazars is marked by variability at all wavelength and time scales along with a high degree of optical polarization (up to 20%).

The question of gamma-ray emission from blazars can be broken down into the following: (i) Formation of jet and particle acceleration within the jet, and (ii) production of gamma-rays. The exact details of the various models for jet formation and particle acceleration are beyond the scope of this work, and hence a brief overview is presented. The prevailing picture of blazars consists of a central engine in the form of a SMBH accreting matter from a disk, with the formation of opposing jets of relativistic matter emitted perpendicular to the accretion

[4]BL Lac objects are believed to lack the molecular clouds responsible for emission lines.

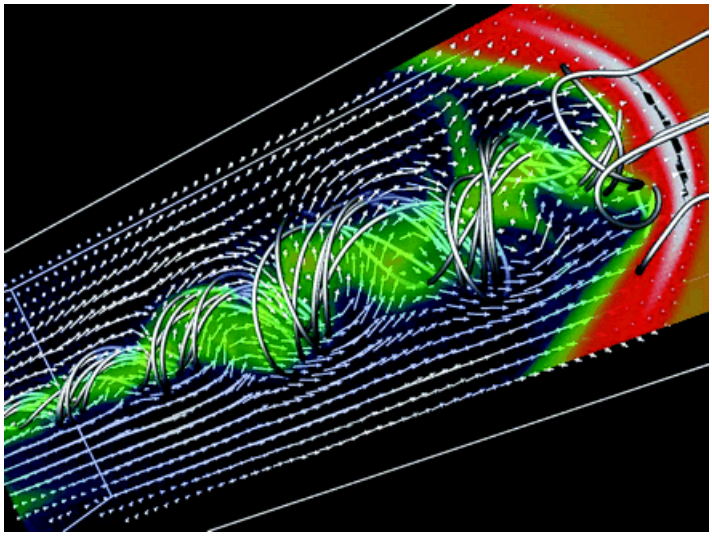

Figure 1.7 A 3D simulation of the development of a magnetized jet using a MHD models. The arrows show the flow velocity within the jet while the metal tubes represent magnetic force lines. The rotating jet has developed a helical-kink instability that distorts the initial axisymmetric jet. High energy particles accelerated in the vicinity of the rotating magnetic field will bend, producing synchrotron radiation.

disk (Marscher et al., 2002). Depending on the viewing angle of the jet with respect the observer, it is possible to identify the structure of the jets. Twin jet structures are visible for large angles with jets extending up to a few megaparsecs in the intergalactic space. For jets directly pointed at the observer, the approaching jet appears Doppler brightened, while the receding jets often appear too dim to be observed. Despite the ubiquitous presence of jets in the vicinity of blazars, the formation of these jets remains one of the most challenging and difficult to explain features of the gamma-ray emitting blazars. It is generally accepted that the jets are tightly collimated flows of plasma containing high energy particles, trapped in a magnetic field. Moreover, the relativistic jets carry away kinetic energy and internal angular momentum in the direction of the flow. Conventional Magnetohydrodynamic (MHD) models of the accretion disk by Meier et al. (2001) show that the jets are a natural consequence of a rotating disk in the presence of a magnetic field. In such models, the formation of jets begins with a magnetized and rotating inflow towards a compact object, which in turn winds the magnetic field lines into a rotating helical magnetic field structure. Subsequently, the magnetic field anchored to the plasma stream builds up magnetic pressure resulting in material being collimated into a jet outflow along the field lines. Figure 1.7 shows results from numerical simulations where a tightly collimated, relativistic outflow along the rotational axis is generated in the presence of differential rotation of a magnetic field. For a sufficiently high magnetic field, the ejected

material in the jets can be accelerated in excess of a Lorentz factor of $\gamma > 10$. Acceleration of a particle to ultrarelativistic velocity within the jet is attributed to Fermi processes, where energetic plasma is accelerated by repeatedly scattering off magnetic instabilities or turbulence (shocks). The Fermi process of diffusive shock acceleration is believed to produce the non-thermal power-law particle distributions observed in the SED of blazars.

1.2.2 Spectral classification of blazars

Recent advances in gamma-ray observations have revealed that blazars radiate most of their energies in the gamma-ray regime. The broadband continuum spectra of blazars are characterized by two distinct, broad components spanning from radio to TeV energies. Figure 1.6 shows an example of the spectral energy distribution of a blazar in a νF_ν representation. The double peaked SED consists of: A low-energy component spanning from radio through UV or X-rays, and a high-energy component spanning from X-rays to gamma-rays. While it is commonly accepted that the low energy peak is due to synchrotron radiation from relativistic electrons in magnetic fields, competing models primarily involving leptonic and hadronic scenarios exist to explain the high-energy peak. These models are discussed later in Section 1.2.3

Prior to the latest generation of ground-based IACTs (in particular VERITAS, H.E.S.S and MAGIC), there were only six confirmed detections of extragalactic VHE gamma-ray sources between 1991 and 2003. Since then, the total number of blazar detected in the GeV–TeV energies have swelled past 20. Furthermore, the addition of the *Fermi Gamma-ray Space Telescope* (*Fermi*) has provided complementary abilities to detect blazars at 0.1 GeV to hundreds of GeV. To date, all confirmed extragalactic VHE gamma-ray sources belong to the class of high-frequency-peaked BL Lac objects (HBLs) and the giant radio galaxy M87 [5]. In the case of HBLs, the lower energy peak typically lies at X-ray while the higher energy peak is in the TeV regime. Moreover, IACTs in recent years have successfully detected a number of objects with lower peak energies, namely low-frequency-peaked BL Lacs (LBLs; Albert et al., 2007b; Teshima et al., 2008) and intermediate-frequency-peaked BL Lacs (IBLs; Acciari et al., 2008a,b, 2009b; Ong et al., 2009a). These detections are particularly noteworthy since the gamma-ray luminosity of LBLs and IBLs are predicted to peak at sub-GeV to tens of GeV range, and therefore are more suitable targets for the*Fermi* instrument instead.

There is further observational evidence that suggests a trend in the properties of different flavors of blazars from FSRQs, LBLs, HBLs up to the so-called extreme BL Lac objects with their synchrotron peak in the X-ray regime of $E^{syn}_{peak} > 0.1\ keV$. Fossati et al. (1998) constructed a SED from archival flux measurements spanning radio to X-ray energies for 117 sources from a total sample of 126 radio and X-ray selected blazars. Figure 1.8 shows the average blazar SEDs binned according to radio luminosity and subsequently fit with analytical functions to guide the eyes. The plots shows two peaks present in each of the SEDs, with a strong correlation

[5] M87 has since been identified as a misaligned BL Lac object (Acciari et al., 2008c)

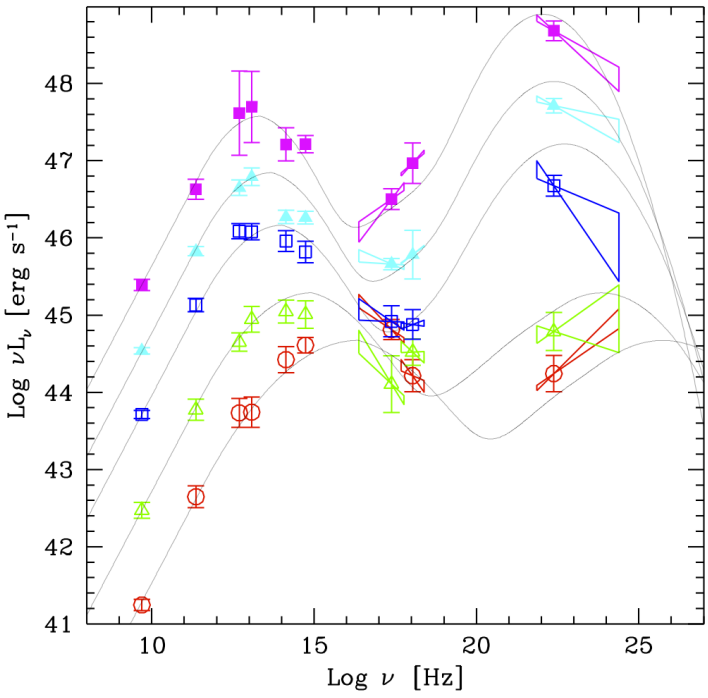

Figure 1.8 The sequence of blazar SEDs shows the progression of higher synchrotron and IC-peak with decreasing flux. (Donato et al., 2001)

between the position of the first and the second component. This study of the blazar population gave rise to the interesting notion of the so-called 'blazar sequence'. It was suggested that the subclass of blazars, from FSRQs to LBLs to HBLs form sequences when arranged along the location of their synchrotron peak frequencies and their relative νF_ν peak fluxes. Consequently, going from FSRQs to HBL marks an increase in the νF_ν frequency that is accompanied by a decreasing dominance of the gamma-ray flux over the low-frequency emission, and a decreasing bolometric luminosity (Böttcher, 2007). The anticorrelation between source luminosity and synchrotron peak frequency is thought to be governed by the balance of electron acceleration and the cooling process. Thus, higher energy density in the more luminous sources result in increased cooling efficiency and is responsible for a lower peak energy. However, recent work by Padovani (2007) using a large well defined sample with relatively high sensitivity has raised questions about the validity of the blazar sequence. The lack of evidence for correlation between bolometric luminosity and synchrotron peak energy in the new data set has been attributed to a selection effect from an undersampling of low-luminosity LBLs and high-luminosity HBLs in the previous data sample. While the blazar sequence is tested by observational data, an even

larger sample of blazars may be necessary to eliminate all selection effects and advance any possible blazar-ordering scheme.

1.2.3 Models of VHE emission in blazars

The high luminosity, rapid variability, and relativistic motion associated with gamma-ray emitting blazars clearly point to a non-thermal origin for this emission. Different models of gamma-ray emission attempt to reproduce the broad-band spectra of blazars and the observed variability. Here, a short review of the standard theoretical models for VHE gamma-ray emission in blazars is outlined. In particular, the leptonic versus the hadronic origin of the high-energy peak in the context of the double humped νF_ν SED of blazars is discussed.

Leptonic model

Initially, highly relativistic electrons moving in a homogeneous magnetic field take a helical trajectory along the field lines due to the Lorentz force $\overrightarrow{v} \times \overrightarrow{B}$. As a result, the charged particles are constantly accelerated and react with the emission of the characteristic synchrotron radiation. The rate of energy loss for the electron scales linearly with the energy density of the magnetic field U_B, and in quadrature with particle energy γ i.e.,

$$-\dot{E} \propto U_B \gamma^2 \tag{1.2}$$

For relativistic electrons with a Lorentz factor γ, the synchrotron emission is strongly boosted in the forward direction along a cone with a width $1/\gamma$. It is a commonly adopted view that this synchrotron emission gives rise to the first peak, ν^{syn}_{peak} at lower energy in the SED of blazars. This is further supported by observational evidence for the highly polarized and variable radio and optical emission of blazars.

In leptonic models, the non-thermal VHE gamma-ray emission can be produced via inverse Compton scattering of optical to X-ray photons on the same population of ultrarelativistic electrons (or positrons) producing the synchrotron emission at lower energies. In the case of an incoming photon with energy ϵ in the rest frame of the relativistic electron (with Lorentz factor γ), the scattered photon essentially has the same direction as the scattering electron with a final photon energy ϵ_s, where,

$$\epsilon_s \approx \begin{cases} \gamma^2 \epsilon & \epsilon \ll \gamma^{-1} \qquad \text{Thomson-regime} \\ \frac{1}{2}\gamma & \epsilon \gg \gamma^{-1} \qquad \text{Klein-Nishina-limit} \end{cases} \tag{1.3}$$

Thus the maximum energy exchange between the electron and the soft photon boosts up the latter energy by a factor of γ^2 for Thomson scattering in the low-energy regime.

However, the origin of the available soft target photons for the IC process remains a matter of debate. In Synchrotron-Self Compton (SSC) model (Marscher & Gear, 1985; Maraschi et

al., 1992; Bloom & Marscher, 1996), the target photon fields are the same synchrotron photons produced by the electrons within the jet. In the simplest "one component" model, it is assumed that both synchrotron and IC take place in a single homogeneous region such that the "seed" photons needed for IC radiation and photons produced in the synchrotron process are identical. As a result of upscattering of these photons to very high energies, the characteristic double humped structure in the broadband SED emerges. A turnover, or Klien-Nishina suppression is expected from the high energy in the IC peak due to the decrease in the cross-section from quantum-electrodynamic effects. SSC models that are more complex, requiring multiple emission zones, have also been introduced to fit the observational data. These multi-zone SSC models invoke secondary emission jets or regions of different magnetic field strength to explain certain flaring behavior from blazars (Krawczynski et al., 2000; Celotti et al., 2001). Finally, the connection between the first and second peaks in the SSC model is borne out by a considerable amount of experimental evidence from multiwavelength observations where a flux variability in VHE gamma-rays during large flares has been correlated with variable X-ray emission (Maraschi et al., 1999; Krawczynski et al., 2001; Takahashi et al., 2000). As a result, the SSC model has been widely accepted to describe the VHE gamma-ray emission of blazars.

Alternate models suggest external sources for the seed photons required for IC scattering (the so-called external Compton or EC process). Possible source of external seed photons are UV to soft X-ray emission from accretion-disks surrounding the SMBH directly entering the jet (Dermer & Schlickkeiser, 1993). Other EC models use reprocessed photons in the circumnuclear material such as the broad line regions around quasars to supply the photons for the IC process (Sikora et al., 1994; Dermer et al., 1997). In a variation on the EC model, Ghisellini & Madau (1996) suggested synchrotron radiation produced in the jet being reflected off clouds in the circumnuclear material as a possible source for the seed photons. In this scenario, a relativistic blob moving through the jet emits synchrotron photons at the surrounding broad-line clouds resulting in re-processed softer X-ray photons being reflected back into the jet. Additionally, this model offers to explain VHE gamma-ray flares from blazars as a consequence of the blob passing through the broad-line region. Finally, Błażejowski et al. (2000) considered infrared emission from a dust torus around the central engine of the blazar as a plausible source for external photons. In recent years, the lack of strong emission lines from BL Lac objects has been used to argue that the ambient photon fields are not as important as the synchrotron photons. Although the SSC models are more likely to explain observational data than the EC model, observed emission levels below the predicted SSC emission makes the EC contributions necessary.

Hadronic model

These models assume that the VHE gamma rays are produced by high energy proton initiated cascades within the jet. In addition to explaining the origin of VHE emission from

blazars, hadronic models offer an attractive solution to the puzzling nature of the extragalactic cosmic radiation with extreme energies of 10^{19} eV and above. Leptnoic modes are generally not able to account for the production of the highest energy cosmic rays. The production of VHE gamma rays from energetic hadron involves a dense cloud in the jet containing an electron-proton plasma. The shock accelerated protons in the jet can reach energies up to 10^{18} eV by sweeping up ambient matter (Pohl & Schlickkeiser, 2000). The acceleration of protons occur more efficiently than electrons because protons suffer less synchrotron losses compared to electrons. In fact, the low energy peak in the SED of blazars can be explained by the synchrotron radiation of co-accelerated electrons. The protons then collide with some target photons producing mesons or other nucleonic debris by photoproduction.

$$\begin{aligned} p + \gamma &\rightarrow \pi^0 + p \\ p + \gamma &\rightarrow \pi^{\pm} + p \end{aligned} \tag{1.4}$$

Subsequently, the pion decays into a gamma-ray pair where the latter undergoes further decay to generate an electromagnetic cascade (proton-induced cascade) (Mannheim & Biermann, 1992; Mannheim, 1993). Additional electromagnetic cascades can result from electrons via $\pi^{\pm} \rightarrow \mu^{\pm} \rightarrow e^{\pm}$ decay ("$\pi^{\pm}-$ cascade"), proton synchrotron photons ("p-synchrotron cascade"), and $\mu-, \pi-$ and $K-$ synchrotron photons ("$\mu^{\pm}-$synchrotron cascade"). For large enough jet Lorentz factor, a significant fraction of the jet kinetic energy can be transferred into the acceleration of relativistic protons. In this case, the $\pi^0 - decay$ gamma rays can appear in the TeV energy band if the energy of the parent neutral pion energy is high enough. The secondary electrons/positrons from the decay of charged pions in the cascade produce a synchrotron low-frequency component and also contribute to the gamma-ray emission by IC scattering.

Ultra high energy proton beams ($E > 10^{19}$ eV) can also directly generate synchrotron radiation in a highly magnetized field of at least several tens of Gauss within the jet (Aharonian, 2000; Mücke & Prothroe, 2000). Considering the proton cooling by synchrotron radiation is less efficient than that of electrons by a factor of $(m_e/m_p)^3$, VHE emission from protons in this model has been shown to provide good fits to the data for Mkn 421 and Mkn 501 flare data. Additionally, Mücke et al. (2003) used both synchrotron radiation of the primary protons and the radiation from the secondary muons and mesons in the proton-induced cascade to construct a self-consistent synchrotron proton blazar (SPB) model. In this scenario, the p-synchrotron photons and the $\mu^{\pm}-$synchrotron cascade have been shown to produce the characteristic double-humped spectrum of gamma-ray emitting blazars. The dominant target photon field in this case is produced by directly accelerated electrons. Furthermore, they show that direct synchrotron radiation from protons and $\mu^{\pm}$ in the presence of a high magnetic field can explain the high energy bump in blazars. At the same time, synchrotron radiation from the primary electrons combined with a contributions from secondary electrons is mainly responsible for the low-energy peak. The neutrinos produced in the decay chain of charged

pions also raise an interesting possibility of direct measurement of these particles. In fact, observing these neutrinos would be a direct clue to the hadronic origin of VHE emission in blazar jets.

In general, both leptonic and hadronic models have demonstrated the ability to successfully reproduce the simultaneous SEDs of several blazars. Leptonic interpretation of the blazar sequence described earlier points to an increasing external-Compton contribution to the gamma-ray spectrum. In particular, the SEDs of HBLs are shown to be consistent with pure SSC models (e.g., Krawczynski et al., 2002), whereas LBLs require an additional external-Compton component to explain the observed spectra (Böttcher et al., 2002). Hadronic models have difficulty explaining the observed correlation of X-ray and VHE gamma-ray during rapid flares because of the longer proton cooling time. Nevertheless, these models offer a reasonable physical interpretation of the observed properties of blazars. Mücke et al. (2003) showed that the low bolometric luminosity observed at the first peak of HBLs is well explained by the p-synchrotron dominated SPB models when the intrinsic primary synchrotron photon energy density is relatively small. For hadronic models, the increased synchrotron photon energy density observed in LBLs implies that protons suffer a larger $p \rightarrow \gamma$ pion production loss. The stronger radiation losses result in a lower maximum proton energy and a decreasing νF_ν peak frequency of the blazar SED.

However, it should be noted that both leptonic and hadronic acceleration may be present in blazar jets at the same time. In such a scenario, a purely hadronic acceleration or an admixture of the two might account for the baseline flux observed in typical blazars, whereas rapid variability in VHE gamma rays is produced as a consequence of additional electron acceleration within the jet.

1.2.4 Variable emission

One of the most distinguishing features of the VHE emission from blazars is time variability on all time scales. During these flaring episodes, the emission level of electromagnetic radiation can easily vary by more than one order of magnitude. One of the earliest detections of flaring activity in the VHE emission of blazar was recorded by the Whipple observatory in 1994 - a dramatic 10-fold increase was observed in the VHE gamma-ray emission from Mkn 421 with the highest flux reaching 150% of the Crab nebula flux (Punch et al., 1992). Since then several distinct episodes of VHE flares from Mkn 421 have revealed VHE emission of gamma ray energies doubling over time scales as short as $\sim$ 15 minutes (Gaidos et al., 1996). Generally, the broad-band emission from all AGN has been observed to be highly variable. However, blazar emissions are particularly noteworthy for their most extreme flux variability i.e., largest magnitude and shortest time scale. H.E.S.S observation of the PKS 2155-304 (a Southern HBL) in 2006 gave strong indications of rapid flux variability on time scales of $\sim$ 3 minutes, the fastest variation recorded from any blazar (Aharonian et al., 2007a). Moreover, gamma-ray

emission from the radio-galaxy M87 has been shown to vary over a range of time scales from yearly to just over days (Acciari et al., 2010c).

Flux variability in blazars plays an important role in understanding the non-thermal processes and the relativistic emission mechanisms in jets. Most of the flaring states detected in the VHE gamma-ray range are usually correlated with an increase in X-ray flux. Moreover, in the cases of Mrk 421 (Krennrich et al., 2002; Aharonian et al., 2002b), Mrk 501 (Djannati-Ataï et al., 1999; Aharonian et al., 2001) and 1ES 1959+650 (Aharonian et al., 2003), changes in the flux levels have been accompanied by variations in the spectral shapes. Rapid flux and spectral variability of blazars are also observed in the optical regime, often characterized by a spectral hardening during flaring periods. This work reports on the more recent observation of gamma-ray flux variability from the BL Lac object 1ES 1218+304 for the first time. The short variability time scale of ~ 1 day imply a very small emission region by invoking the causality argument. Consequently, we use the experimental evidence for a short variability time scale to rule out emission from extended jets as the sole reason for baseline flux observed in many hard spectrum blazars.

Generally, the models discussed in the previous section are able to describe the SED of blazars to a certain degree. However, constraints imposed by the observation of rapid, large scale flux variations are beginning to test the different models, as these models are sensitive to changing initial conditions such as source environment or injection parameters. Further complications arise from the limited sensitivity of instruments to provide sufficient resolution to probe flux variations down to the sub-hour time scales. Moreover, standard SSC models have been unable to explain the origin of rapid flares in some blazars, thus making it necessary to consider additional, complex external components. Krawczynski et al. (2002) carried out a study of selected SSC blazar models by considering the full time-dependent calculations in an effort to explain the variable X-ray and VHE gamma-ray emissions from blazars. Wagner (2006) summarized several of the mechanisms presently put forward to explain the origin of rapid flares:

- **Increased production rate of particles or high energy cut-off**: In this scenario, Mastichiadis & Kirk (2002) showed that variation in only one parameter in the SSC model, namely the high-energy cutoff of the injected electron distribution, γ_{max} can reproduce large variations in the X-ray and VHE gamma-ray energies. Furthermore, this model requires a Doppler factor of $\delta \gtrapprox 15$ to cause time variations of about one day, which is close to the usually assumed values of the Doppler factor for blazars. In this scenario, a reasonably good fit to the multiwavelength spectrum of Mkn 421 flare can be found by increasing the γ_{max} by a factor of 5. Detailed time-independent modeling of the 1997 Mkn 501 flare by Krawczynski et al. (2002) explored the time variability through varying rate of accelerated particles as well as γ_{max}. For a higher production rate in a two-component SSC model with a quasi-steady X-ray component, this model describes

both the X-ray and TeV flux for the flare data well. However, this model requires a high Doppler factor $\delta \approx 45$, which is considerably higher than indicated by the observations of superluminal motion (Vermeulen & Cohen, 1994; Marscher, 2006).

- **Changes to the ambient photon field for the IC process**: Bednarek & Prothroe (1997) proposed an alternative geometric model to explain the rapid variability using a small X-ray hot-spot orbiting with the accretion disk around the central black hole. For a TeV emission region extending out of the jet and not too far away from this hot spot, TeV gamma-rays are absorbed by photon-photon pair production with ambient X-ray seed photons from this blob. The observed absorption will strongly depend on the location of the TeV emission region relative to the hot-spot and the observer. Subsequently, the observed gamma-ray flux will be modulated by the orbital period of the hot-spot and may result in simultaneous quasi-periodic oscillations of X-ray and TeV gamma-ray emission. In addition to offering a physical interpretation of the flux variability, this model predicts a time delay of the peak TeV gamma-ray flux with respect to the X-ray emission which may be confirmed with dedicated multiwavelength observations of flaring objects.

- **Additional shocks inside the jet**: In another family of models, fast flaring behavior may be explained by assuming an unsteady jet which is intermittently injected with plasma. Recent radio imaging of the radio-galaxy M87 (Acciari et al., 2009c) has revealed the presence of bright knots in radio frequencies along with similar structures in optical and X-ray wavelengths (Figure 1.9). With the advent of Very Long Baseline Interferometry (VLBI), these knots are seen to be moving outward from the center of the galaxy. Moreover, a period of strong VHE gamma-ray flare from M87 was accompanied by a strong increase of the radio flux from its nucleus. A possible interpretation involves possible injection of plasma at the base of the jet observed at optical and X-ray energies with a delayed passage through the radio core (Acciari et al., 2009c). Other models invoke the passage of thin shock waves accelerating plasma shells with varying mass, energy, and velocity down the jet of the blazars (Spada et al., 2001). Subsequently, faster moving shells catches up with slow moving ones resulting in collisions shock to develop within the jets. Diffusive shock acceleration in this model successfully predicts correlations between flares at high energies and the injection of superluminal radio knots and possible radio flares.

- **Varying acceleration environment**: This scenario suggests that in addition to changes in the primary electron population or injection of external photons, there may also be changes to the acceleration environment. Mastichiadis & Kirk (1997) along with Coppi & Aharonian (1999) have discussed changes to the magnetic field density in the context of inverse-Compton processes. Hence, very fast flares imply small inhomogeneity developing within the acceleration region such as small scale enhancement of the magnetic

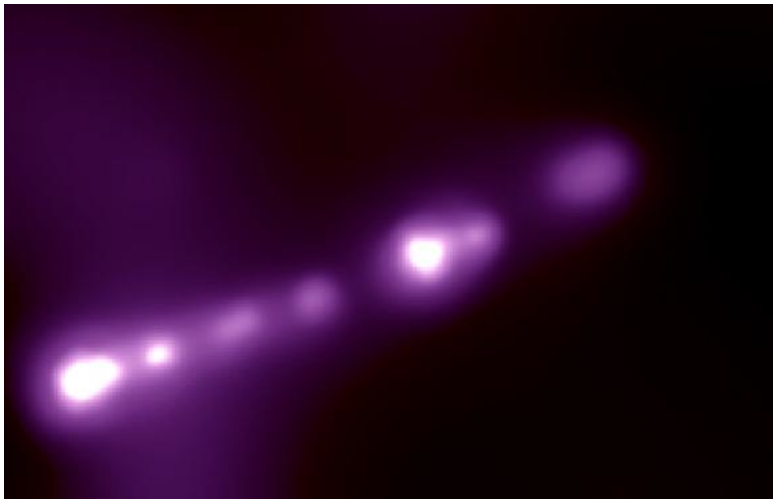

Figure 1.9 M87 in X-ray where knot-like structures are clearly visible. [Credit: NASA/Chandra X-ray Observatory Science Center/Massachusetts Institute of Technology]

field strength inside the jet.

In order to better understand rapidly variable VHE emission from blazars, more multi-wavelength observations of blazars are necessary. The observed flux variability offers a strong diagnostic tool to discriminate among theoretical models while constraining physical parameters of the source. A strong correlation between X-ray and the VHE gamma-ray flux would imply a SSC origin of the flare combined with sub-shocks in jets. In contrast, an absence of correlation would point to IC scattering of soft photons where modulation models are more viable for explaining variability.

1.2.5 Summary of blazar observations

The VHE gamma-ray sky has seen a recent explosion in the number of sources as a new generation of space- and ground-based instruments have revealed a universe that is rich and complex at the highest energies. The success of gamma-ray astronomy has been largely fueled by a vigorous rate of evolution in imaging atmospheric Cherenkov telescopes such as VERITAS, H.E.S.S and MAGIC. Since the first discovery of TeV gamma-rays from Mrk 421 ($z = 0.031$) and Mrk 501 ($z = 0.034$), these instruments have confirmed VHE gamma-ray emission from 32 AGNs including HBL, LBL, IBL, FSRQ, and Radio-galaxies (Figure 1.10). Most of these AGNs belong to the blazar subclass. Moreover, the VHE gamma-ray blazars are predominantly HBLs with a broad redshift-range of $z = 0.03 - 0.35$. VHE observations of blazars have revealed an equally impressive array of time variability ranging from days down to time scales of minutes along with strong correlations between TeV and X-ray emission. Although, energy

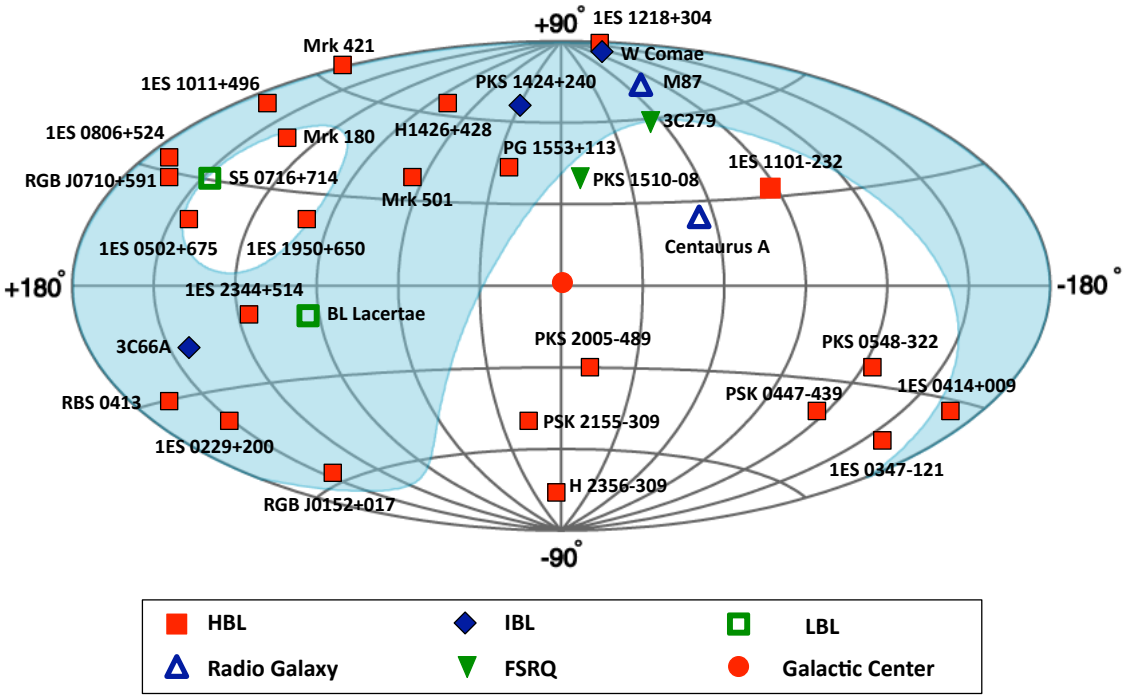

Figure 1.10 A glimpse of the sky in VHE gamma rays. The figure shows the distribution of different classes of AGNs detected by various IACT groups around the globe. Catalog compiled from the very helpful *tevcat* website : *www.tevcat.uchicago.edu*. The blue shaded region correspond to the part of the sky visible to the VERITAS array.

spectra with a photon indices of ~ 2 have been observed from Mrk 421 and Mrk 501, recent measurements have found numerous blazars with steep energy spectra. For relatively distant blazars with $z > 0.1$, the steepness is expected from the absorption of gamma-ray due to the intergalactic radiation field. However, it is also likely that the observed steepness of VHE spectra of blazars is partly intrinsic to the sources. There is an early indication for intrinsic spectral steepness in the observations of nearby blazars such as 1ES 2344+514 ($z = 0.044$), Mkn 180 ($z = 0.045$), 1ES 1959+650 ($z = 0.047$) and PKS 2005-498($z = 0.071$). Conversely, observations of distant blazars with hard spectra extending to relatively high energies have provided unique challenges to the existing models for VHE emission in blazars. A list of currently observed blazars along with their predicted intrinsic photon indices and redshifts can be found in Table 2.6.3. Furthermore, the detection of the FSRQ 3C279 at $z = 0.54$ also raises new questions about the opacity of the universe to gamma-rays. At present, the selection of targeted VHE blazars candidates are primarily derived from the list compiled by Costamante & Ghiselellini (2002). The authors predicted strong TeV emission from these "good" candidates

based on the observational evidence for high energy electrons and a sufficient population of seed photons for the required IC process. Thus, the selection procedure requires objects with both a strong X-ray flux and a Radio-through-optical flux, indicative of strong synchrotron emission from electrons and thermal emission from seed photons, respectively. Since the publication of the list of TeV candidates by Costamante & Ghiselellini in 2002, a total of 11 new AGNs have been discovered belonging to the original list. The recent launch of *Fermi* has provided yet another alternative for compiling prospective VHE gamma-ray sources. In this scheme, the SEDs of *Fermi*-detected sources are extrapolated to GeV-TeV energies where only sources with measurable flux intensity by ground-based Cherenkov telescopes are selected.

An important issue that is critical to the study of VHE emission from extragalactic sources, in particular blazars, is the interaction of ambient low-energy photons with the gamma-ray photons over cosmological distances (see Chapter 2). The measured VHE spectra of blazars obtained with the IACTs contain the intrinsic source spectra convoluted with the modification due to the infrared photons. Therefore, an accurate determination of the intrinsic spectral properties of blazar necessitates disentangling the effect of the absorption of the VHE gamma-rays. This poses an inherent challenge to our understanding the different emission mechanisms behind VHE emission from blazars since our knowledge of the background photon field is incomplete. Furthermore, it is likely that the original spectra of blazars may contain an intrinsic absorption-like feature such as a high-energy *cutoff*, at which where the accelerators run out of energy. This makes it particularly difficult to model the absorption of VHE gamma-rays as they travel over cosmological distance scales. Long-term studies involving the sampling of many more VHE blazar spectra over different redshift may allow us to better understand the absorption of gamma-rays due to a background infrared photon field. This, along with thorough studies of blazar spectra during periods of activity within the source such as flaring-states may provide invaluable insights into the fundamental physical processes responsible for the production of VHE gamma-rays in blazars. Therefore, a reliable method of measuring the VHE spectra of blazars as recorded by imaging Cherenkov telescopes is highly desired, and that is the subject of this thesis.

1.3 Dissertation Outline

The primary goal of the thesis is to describe a reliable method for estimating the energy spectra of VHE gamma-ray emitting blazars, specially in the context of the blazar 1ES 1218+304. A brief overview of the historical development of VHE gamma-ray astronomy is presented in this chapter. This chapter also outlines our current understanding of the VHE gamma-ray emission from AGNs with a particular emphasis on various acceleration models used to describe observational properties of the blazar subclass of AGN. Chapter 2 is devoted to the discussion of extragalactic background light. It also explores how the measured spectra of blazars at the highest energies may yield first observational evidence of the absorp-

tion of gamma rays in the intergalactic medium. In Chapter 3, I describe the physics behind the development of extended air showers in the atmosphere and the indirect detection of high energy particles striking the Earth using imaging atmospheric Cherenkov telescopes. I also briefly describe the main hardware elements of the VERITAS array in Chapter 3. A thorough description of the routines used for the reduction of raw data and procedures for the extraction of VHE spectrum is outlined in Chapter 4. In particular, analysis of a small Crab nebula data set is presented to serve as calibration of the data analysis chain utilized in this work. Chapter 5 is devoted to the analysis of VHE gamma-ray data from the blazar 1ES 1218+304 collected during the 2008-2009 season. This section also details the discovery of variable emission from 1ES 1218+304 during the same observing period and discusses the physical implications of the flux variability on blazar emission models. Finally, Chapter 6 presents the conclusion of this work. All the data that was used in this work is cataloged in Appendix A.

CHAPTER 2. EBL SIGNATURE IN VHE BLAZAR SPECTRA

2.1 The Extragalactic Background Light

Recently, gamma-ray observations have emerged as a viable cosmological tool for examining the thermal processes in the universe. In particular, the extinction of VHE gamma-ray photons via pair-production with the less energetic ambient photons over cosmological distances provides a unique opportunity to probe the intervening radiation field. The extragalactic space comprises of low density gases and radiation fields. The latter contains an imprint of all the electromagnetic radiation released as a result of structure formation since the decoupling of matter and radiation following the Big Bang (Hauser & Dwek, 2001). The initial radiative energy output resulting from the accumulation of matter into stars and galaxies was subsequently absorbed by dust and re-radiated at longer wavelengths. The reemission process accompanied by reddening due to cosmic expansion redistributed a substantial fraction of original radiative energy into infrared background radiation. Not surprisingly, the measurement and the explanation of this background radiation field at infrared (IR) wavelengths has become one of the fundamental topics in modern cosmology.

The ultraviolet/optical and IR portions of the diffuse background radiation ($0.1 - 1000$ μm) comprises what is conventionally known as the extragalactic background light (EBL). EBL is the second most dominant source of background radiation after the cosmic microwave background radiation. Figure 2.1(Top) shows contributions to the spectral energy distribution (SED) of the inter-galactic radiation fields at different wavelengths, from gamma-ray to radio. The typical spectrum of the EBL is characterized by a bi-modal distribution (Figure 5.22 (Bottom)). The first peak at UV/optical to near-IR (NIR) wavelength regime (blue shaded region) is primarily associated with the energy released during the formation of heavy elements in stars and the accretion of matter onto blackholes in AGN. The subsequent peak (red shaded region) consists of absorbed optical and UV radiation that is re-radiated by dust at mid-IR (MIR) wavelengths. The next section details the individual contributors to the EBL in more detail.

2.2 Spectral energy distribution of EBL

As noted earlier, the present make up of the SED of EBL (Figure 2.1(Bottom) corresponds to the integrated electromagnetic radiation from galaxies at the present epoch ($z = 0$). Subse-

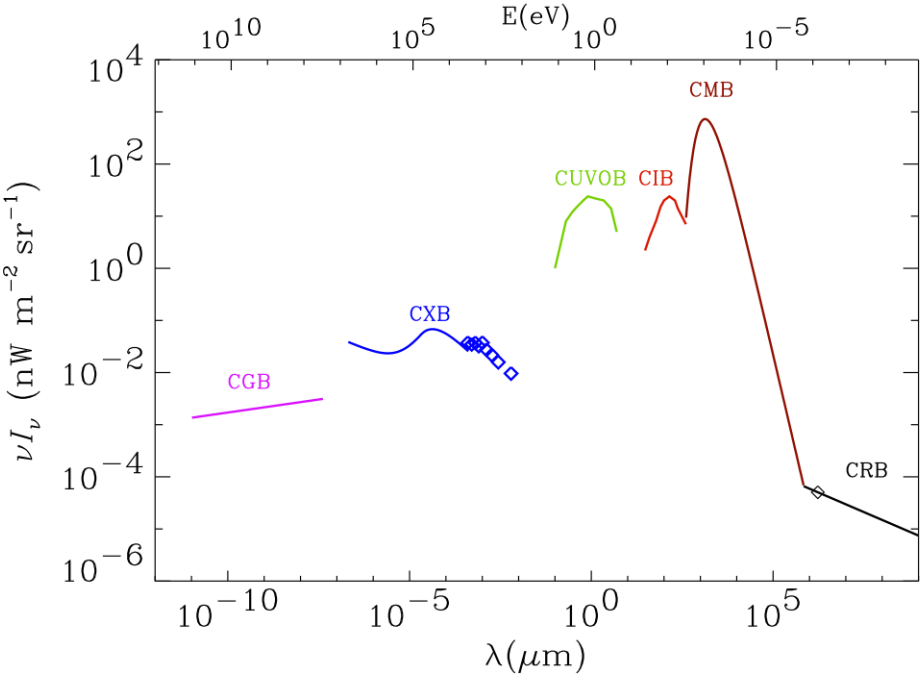

Figure 2.1 Spectral energy distribution of the inter-galactic radiation field at various wavelengths, from gamma ray to radio wavelengths. CRB- cosmic radio background, CMB- cosmic microwave background, CIB - cosmic infrared background, CUVOB - cosmic ultraviolet/optical background, CXB - cosmic x-ray background, CGB - cosmic gamma-ray background. The CIB+CUVOB constitutes the EBL. [from (Hauser & Dwek, 2001).]

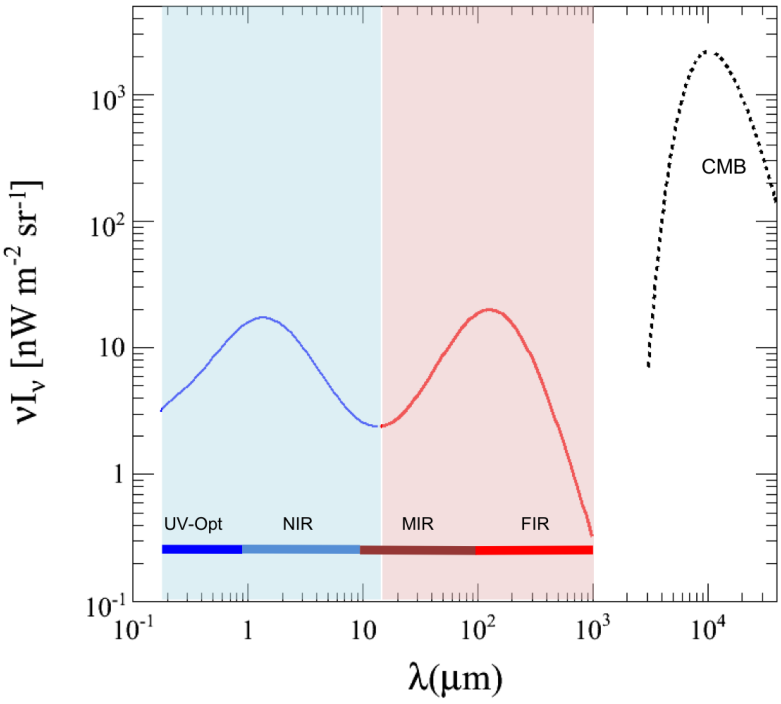

Figure 2.2 Schematic representation of typical spectral energy distribution of EBL. The first bump at UV-Optical-NIR wavelengths (*blue shaded region*) represent stellar emission via nucleosynthesis. The second bum at FIR wavelengths (*red shaded region*) corresponds to absorbed and re-radiated stellar emission by the interstellar dust particles. Also shown for comparison the CMB spectrum (*black dashed line*). See text for a detail description of the various processes contributing to the EBL spectral energy distribution.

quently, a complete analysis of the origin of the EBL must account for individual contributions from star formation activity, metallicity and dust content, all involving processes that are continually evolving in time. In addition, one must also consider the redshift of the radiation field due to the expansion of the universe. Figure 2.3 (Primack et al., 2005) gives a schematic representation of the evolution of the spectrum of EBL as a function of redshift, where the present EBL corresponds to a redshift of $z = 0$. Therefore, a detailed study of the EBL constraints both the intrinsic SED of sources and their distribution in redshift.

2.2.1 Stellar emission

The major contribution to the EBL comes from the nuclear energy released during the formation of stars in the galaxies, thus providing an ideal laboratory for nuclear physics and evolution theories. A significant fraction of the UV/optical luminosity of galaxies correspond

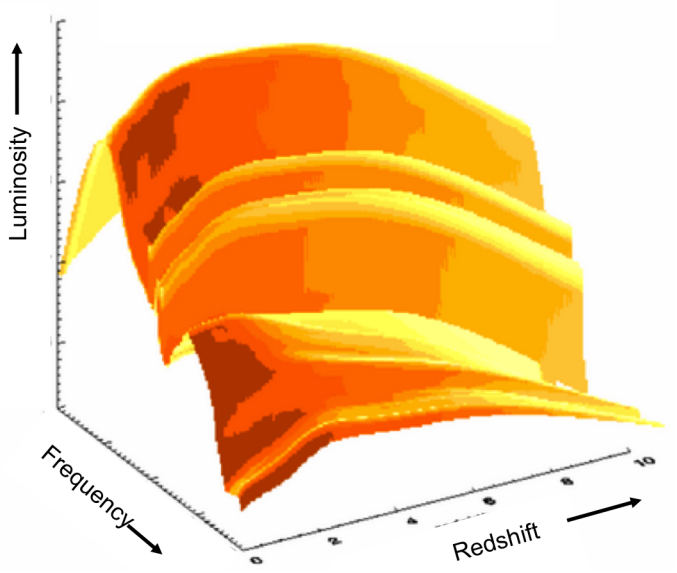

Figure 2.3 The evolution of the spectrum of the EBL as a function of redshift and wavelength [Adapted from (Primack et al., 2005)]

to the stellar emission from stars with a wide range of *metallicities*[1] or the abundance of heavy-elements. The first classification of stars is the spheroidal population or Population II (hereafter Pop II) stars. These low-mass, cooler and thus less luminous stars are often found in the galactic halos and the bulges. Studies of spectral lines and colors of distant galaxies indicate the relative lack of heavy elements in Pop II stars. Hence, present stellar evolution models suggest that these stars must have formed early in the galaxy's history before the gas settled into the galactic disks– produced from the synthesized nuclei in even earlier Population III (Pop III) stars with zero metallicity and the subsequent enrichment of the interstellar medium when the Pop III stars went supernovae.

Although the existence of Pop III stars is yet to be observationally verified, Pop II and III stars thought to contribute to the creation of metal-rich Population I (Pop I) stars. The last classification of both young and old Pop I stars predominantly found in the main disk is the spiral galaxies. A predominant production site for stellar formation in galaxies are regions of "starbursts" where interstellar gas is converted into stars at prodigious rates. The cumulative lifetime and emission profile of a star is primarily determined by its mass and original metallicity. Subsequently, massive stars ($M > 8\ M_{\odot}$) fuse hydrogen into helium at a furious rate, resulting in a much shorter life span ($\sim\ 10^7$ years) while emitting the bulk of its energy at UV wavelengths. On the other hand, intermediate-to-low mass stars undergo a more slow emission process as the balance between gravitational equilibrium and the core energy

[1] the *ratio* of elements heavier than He to hydrogen in the atmosphere of the star is commonly used to quantify the stellar composition.

production work together to keep the over-all stellar emission rate steady. The low-mass stars predominantly radiate in optical wavelengths. Therefore, to accurately model the contribution of stellar emission to the EBL density, the SED of individual starbursts must be averaged over the entire ensemble of galaxy populations.

2.2.2 Dust emission

The ubiquitous presence of dust forms one of the most fundamental constituents of the galaxy, and plays a major role in its evolution. In a conventional scenario, dust grains are created around giant stars which later drift into the ISM and subsequently are eroded by the hot components of the ISM and the energetic UV background. The interstellar dust is characterized by grains (mostly silicate and graphite) and Polycyclic Aromatic Hydrocarbons where the formation of the latter is triggered by Supernova. The exact details of the contribution of dust to the SED of the EBL depends on various details such as the optical properties of dust, its abundance and size distribution, the spatial distribution of dust relative to the radiation sources and the clumpiness of the ISM in galaxies (Dwek, 2001). Because the EBL spectrum represents time-integrated emission from galaxies, the study of dust's contribution to it is further complicated. In general, the dust particles in the ISM can most efficiently absorb and process a significant fraction of the galactic starlight. This is evidenced by the large presence of EBL radiation in the 10–1000 μm regime since only dust can efficiently re-emit processed starlight at infrared wavelengths. Furthermore, circumstellar dust produced as a result of mass loss from giant stars dominates the mid-IR emission. In fact, given the right environment, the re-radiated emission from dust is a substantial or even dominant fraction of the total luminosity associated with star formation (Kashlinsky, 2005). Observational studies show that the range of galaxy luminosities in the MIR to FIR greatly exceed that in the UV, optical and NIR where a tiny amount of dust has been shown to make the galaxy substantially brighter in the mid-IR to far-IR regime (Kashlinsky, 2005). Finally, a significant fraction of the radiative energy output from AGNs may be absorbed by the dusty torus around the central black hole and subsequently re-radiated at FIR wavelengths (Dwek, 2001).

2.2.3 Contribution from AGN

The combined energy output from AGN represent a significant fraction of the energy budget of the universe after nucleosynthesis. However, most current models assume a small contribution from AGN to the density of the EBL (Reyes, 2007). Madau & Pozzetti (2000) estimates that the total mean mass density of the massive black holes today to be $\rho_{BH} \backsimeq (3 \pm 2) \times 10^6 \mathrm{hM}_\odot\ \mathrm{Mpc}^{-3}$. This should have contributed a maximum of $\sim \frac{c}{4\pi}\epsilon\rho_{BH}c^2(1+z)^{-1}$ by accretion at redshift z to cumulative EBL flux observed in the present epoch. Assuming an average radiation efficiency to convert mass to radiation of ϵ of 6% and for a mean redshift distribution of AGNs at $< z > \sim\ 2$ (as suggested by observation), the contribution from AGN

is expected to produce less than $10 - 20\%$ of the total EBL (Madau & Pozzetti, 2000). Various authors have investigated the contribution of AGN to the net EBL budget by studying observational data from AGN and measurements at IR wavelengths (e.g., Malkan & Stecker, 1998; Lagache & Puget, 2000; Elbaz et al., 2002). They conclude that the AGN contribution to the EBL is relatively small compared to that of stars.

2.3 Summary of direct observations and limits of the EBL

Observationally, direct detection of the EBL is hindered by the fact that it lacks any intrinsic spectral signature. The observed EBL spectrum represents the emission characteristics of luminous sources, convolved with their cosmic evolution history and the nontrivial process of dust formation around these sources. Furthermore, direct measurements of the EBL spectral energy density (SED), particularly in the mid-IR, remain uncertain due to the presence of dominant foreground radiations. The intensity of the EBL is significantly weaker compared to many bright celestial contributors to the sky brightness (Hauser & Dwek, 2001). These include diffuse emission and scattered light from interplanetary dust (IPD), emission from unresolved stars and compact sources within galaxies, and dust emission from the surrounding ISM. As a result, observational determination of the EBL is hindered by the difficulty in separating the true extragalactic component from the above mentioned galactic foreground emission.

The spectral energy distribution of the residual signal compared to the different foreground emissions in Figure 2.4 [from Hauser et al. (1998)] illustrates the difficulty in eliminating the foreground emissions. The brightest contribution to the foreground comes from the zodiacal light which is sunlight processed by the IPD. In fact, the photon energy of the zodiacal light peaks around MIR wavelengths (between $10 - 20$ μm) and is expected to be roughly twice the size of the residual signal. At the NIR wavelength region ($1.25 - 3.5$ μm), there is a substantial contribution to the foreground from near-infrared galactic sources. Finally, diffuse emission from the ISM poses significant uncertainty in the measurement of EBL at Far-IR (FIR) wavelengths (> 50 μm). Therefore, a reliable estimate of the EBL spectrum requires that any significant contributions to the foreground radiations must be carefully modeled and subtracted from the measurements. Furthermore, any estimation of the residual signal from the EBL must be isotropic and relatively independent from the dominant foreground sources of infrared radiation (Hauser et al., 1998).

There have been several attempts to extract the isotropic component (mean level) of the EBL flux by directly detecting infrared photons from the Cosmic Infrared Background (CIB) (see Figure 2.1 left) using space-based instruments. The most notable of these experiments are the Diffuse Infrared Background Experiment (DIRBE) and Far Infrared Absolute Spectrometer (FIRAS), on board the COsmic Background Explorer (COBE) satellite. DIRBE was designed to map out the absolute brightness of the full sky in 10 photometric bands between $1.25 - 240$ μm. Following 10 months of observations, the DIRBE team claimed definitive detections

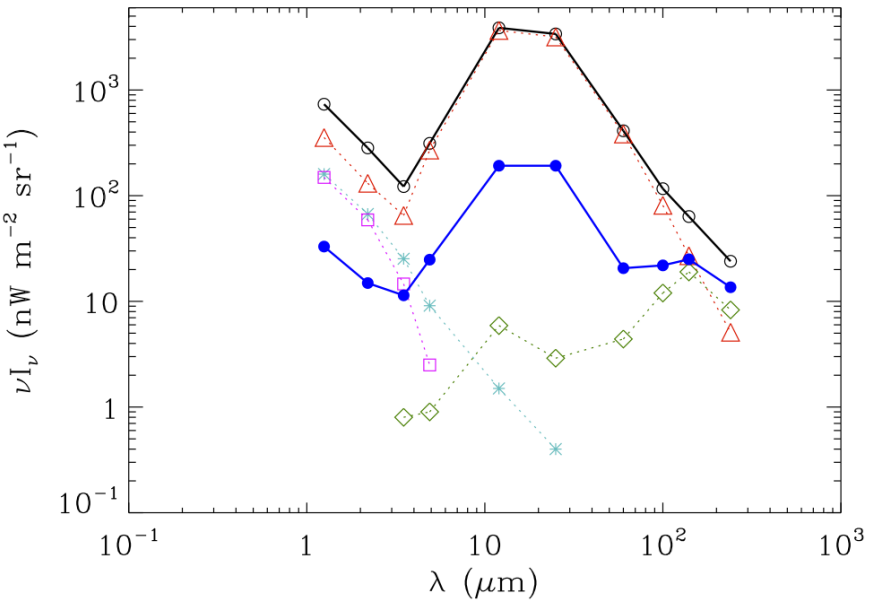

Figure 2.4 Different contributions to the foreground emissions for the measurements of the EBL. The most dominant component is the zodiacal light from IPD (red open triangles). Also shown is the residual emission corresponding to all foregrounds subtracted from the total sky brightness (filled circles). [adapted from (Hauser et al., 1998)]

at 140 and 240μm by requiring an isotropic residual signal at a 3σ confidence level (Hauser et al., 1998). Subsequent analysis of the DIRBE data also yielded upper limits between 1.25 and 60μm. Using similar approaches, FIRAS (Puget et al., 1996) obtained several upper limits on the EBL at higher wavelength between $125 - 2000\mu$m(Fixen et al., 1998). Alternatively, Kashlinsky & Odenwald (2000) pioneered the analysis of the CIB anisotropy in COBE data (fluctuation analysis) with minimal background subtraction which resulted in further upper limits in the infrared wavelength region.

Also, 24–band photometric data collected by the Near Infrared Spectrometer (NIRS) (Noda et al., 1994) on board the Infrared Telescope in Space (IRTS) yielded several measurements of the CIB in a wavelength range of 1.4 to 4 μm (Matsumoto et al., 2005). While the reported EBL intensity at around 2.2 and 3.5 μm is consistent with previously reported upper limits, detections by the NIRS at shorter wavelengths lie significantly above the lower limits. This near-infrared background excess (NIRBE) is considerably higher than the EBL density expected from galaxy source counts. Various authors (e.g. Salvaterra & Ferrara, 2003; Kashlinsky et al., 2005) have attributed this reported excess to emission from Pop III stars during the early history of the universe. This suggests that the EBL structure may reveal important

information about the formation and evolution of the Pop II stars. However, (Dwek et al., 2005) argued that the assumed contributions to the NIRBE by Pop III stars contradicts the stellar formation rates and baryon consumption rates typically predicted in stellar evolution models. Furthermore, (Dwek et al., 2005) and (Matsumoto et al., 2005) have explained that this excess may have resulted from inaccurate subtraction of the foreground emissions such as the zodiacal light. More recently, analysis of data collected by the Near Infrared Camera and Multi-Object Spectrometer (NICMOS) on board the Hubble Space have shown that emission from resolved galaxies and zodiacal light can account for the entire NIR flux of the EBL, once again contradicting the existence of NIR excess reported by NIRS (Thompson et al., 2007).

Finally, total flux from observed ordinary galaxy populations have been used to place lower limits on the EBL intensity by integrating flux from all galaxies down to a given flux limit. Recent estimates from a variety of galaxy counts data suggest that emission from the observed galaxy populations ($z \gtrsim 1-2$) most likely account for the EBL intensity at FIR wavelengths. Since the galaxies represent only one of many contributions to the EBL, these galaxy counts correspond to a strict lower limit on the total EBL. The total fluxes from galaxy counts at MIR wavelengths saturate at a levels which are just below the best current upper limits on the CIB, thus implying that galactic emission contributes at least a large fraction of the total energy budget of the EBL. At NIR wavelengths, the significantly lower level of contributions from the observed galaxy populations compared to the residual CIB signal points a substantial release of energy at a much earlier epoch than evident in the observed faintest galaxy population (Kashlinsky et al., 2005). Figure 2.3 presents a compilation of various limits and measurements of the EBL from different astronomical observations (Mazin & Raue, 2007). Although the collective limits on the EBL between the UV and FIR reproduce the expected bi-modal shape of the EBL SED, the measured data is plagued by systematic uncertainties described earlier. Consequently, the absolute EBL flux remain uncertain by roughly an order of magnitude. For a more comprehensive review of the measurements and implication of the CIB, see Hauser & Dwek (2001).

2.4 The absorption of VHE photons

Nikishov (1961) first considered the attenuation of high energy gamma rays in intergalactic space via pair production with low-energy photons. However, his early predictions dating before the discovery of the CIB overestimated the density of the intergalactic radiation field by three orders of magnitude. Following the detection of the CIB in late sixties, Gould & Schreder (1966) and Jelly (1966) explored the opacity of the low-energy extragalactic photon spectrum to VHE gamma rays from sources located at cosmological distances. In fact, Gould & Schreder (1967) later noted the importance of this astrophysical process and its great value for the understanding of cosmological origin of the universe, "Observations of cosmic photons in the region 10^{12} to 10^{23} eV would be of great value ... In fact, this may provide a means of

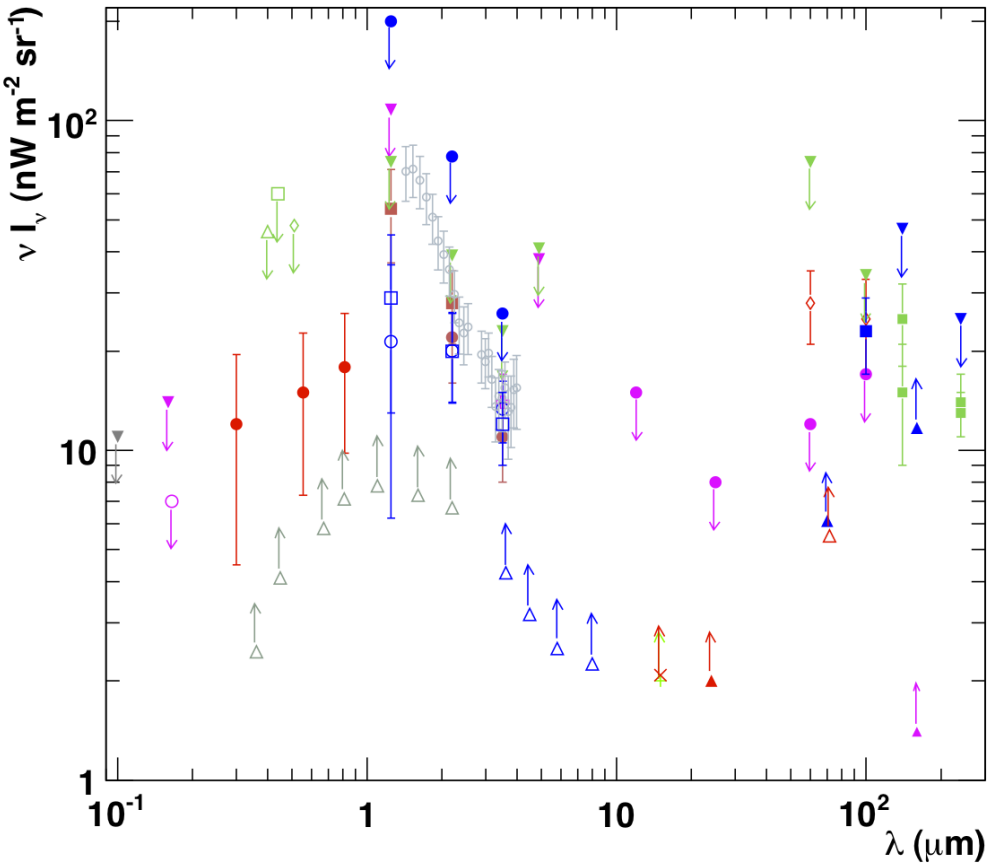

Figure 2.5 A summary of EBL measurements and limits compiled by Mazin & Raue (2007). Upper limits in the UV to optical: (Edelstein et al., 2000) (grey filled triangle), (Martin et al., 1991) (open pink circle), (Brown et al., 2000) (filled pink triangle), (Mattila, 1990) (open green triangle), (Toller, 1983)/(Leinert et al., 1998)(open green square), (Dube et al., 1979)/(Leinert et al., 1998) (open green diamond); Tentative detection in the UV/optical: (Bernstein et al., 2002, 2005) (filled red circle); Lower limits from source counts: (Madau & Pozzetti, 2000) (open grey triangles), (Fazio et al., 2004) (open blue triangles), (Elbaz et al., 2002) (green cross), (Metcalfe et al., 2003) (red ×), (Papovich et al., 2004) (filled red triangle), (Dole et al., 2006) (filled pink triangles), (Frayer et al., 2006) (open red triangle); detections in the near IR: (Dwek & Arendt, 1998) (open pink cross), (Gorjian et al., 2000) (filled brown circle), (Wright & Reese, 2000) (open blue squares), (Cambresy et al., 2001) (filled brown squares), (Matsumoto et al., 2005) (small open grey circles), (Levenson & Wright, 2007) (open blue circles); upper limits from direct measurements: (Hauser et al., 1998) (filled green triangles), (Dwek & Arendt, 1998) (filled pink triangles), (Lagache & Puget, 2000) (filled blue triangles); upper limits from fluctuation analysis: (Kashlinsky et al., 1996) (filled blue circles), (Kashlinsky & Odenwald, 2000)(filled pink circles); Lower limits from stacking analysis in the far-IR: (Dole et al., 2006) (blue triangles); detections in the far- IR: (Hauser et al., 1998) (filled green squares), (Lagache & Puget, 2000) (tentative, filled blue square), (Finkbeiner et al., 2000) (tentative, open red diamonds).

determining the optical photon density and testing cosmological models."

The subsequent discovery of TeV emission from the extragalactic source Mrk 421 by the Whipple observatory (Punch et al., 1992) opened up a real possibility of indirectly testing the transparency of the universe to VHE gamma ray photons that is not influenced by local sources of infrared radiation. In particular, Stecker & de Jager (1993) pioneered the method of using simultaneous measurement of GeV to TeV spectra of extragalactic sources to: determine the intrinsic source spectrum, understand the observational range of TeV photons and derive constraints to the EBL photons density (Stecker et al., 1996). In recent years, the continuing success of highly sensitive Imaging Atmospheric Cherenkov Telescopes (IACTs) such as VERITAS, H.E.S.S. and MAGIC has led to the discovery of many new extragalactic TeV emitters. These observations have in turn resulted in the calculation of several upper limits on the intensity of EBL. The derivation of limits to the EBL density from observations of TeV sources are discussed in Section 2.5.

2.4.1 Opacity to TeV photons

The most dominant form of absorption process for a VHE gamma ray traversing the extragalactic radiation field involves inelastic collision between two photons, resulting in an electron-positron pair.

$$\gamma_{\rm TeV} + \gamma_{\rm IR} \rightarrow {\rm e}^+ + {\rm e}^-$$

Consider a VHE photon $\gamma_{\rm TeV}$ with energy, E, interacting with a low-energy infrared photon $\gamma_{\rm IR}$ with energy ϵ. For the pair-production to continue, the the total available energy in the center-of-momentum frame must be $\geqslant 2m_e$. Following the parameterization in Vassiliev (2000), the spin-averaged pair-production cross section $\sigma_{\gamma\gamma}$ is given by:

$$\sigma_{\gamma\gamma}(q) = \frac{3}{8}\sigma_T f(q) \tag{2.1}$$

With

$$f(q) = q\Big[\Big(1 + q - \frac{q^2}{2}\Big)\ln\frac{1+\sqrt{1-q}}{1-\sqrt{1-q}} - (1+q)\sqrt{1-q}\Big] \tag{2.2}$$

and

$$q(E, \epsilon, \mu) = \frac{2m_e^2}{E\,\epsilon\,(1-\mu)} \tag{2.3}$$

where $\sigma_T = 6.67 \times 10^{-25}\,{\rm cm}^2$ is the Thompson scattering cross section, $m_e = 0.511$ MeV is the mass of the electron, and μ is the *cosine* of the collision angle between the incoming photons. For a VHE gamma ray photon with energy of 1 TeV, Figure 2.6 shows the functional dependence of $f(q)$ on the energy of the low energy photon. The function $f(q)$ roughly peaks at $q \sim 0.5$ in the case of a *head-on* collision ($\mu = -1$). This indicates that a 1 TeV photon has the highest probability for being absorbed by a soft photon with a wavelength $\lambda_{\rm IR}$,

$$\lambda_{\rm IR} = 2.41\,\mu{\rm m}\,\frac{\rm E}{1\,{\rm TeV}} \tag{2.4}$$

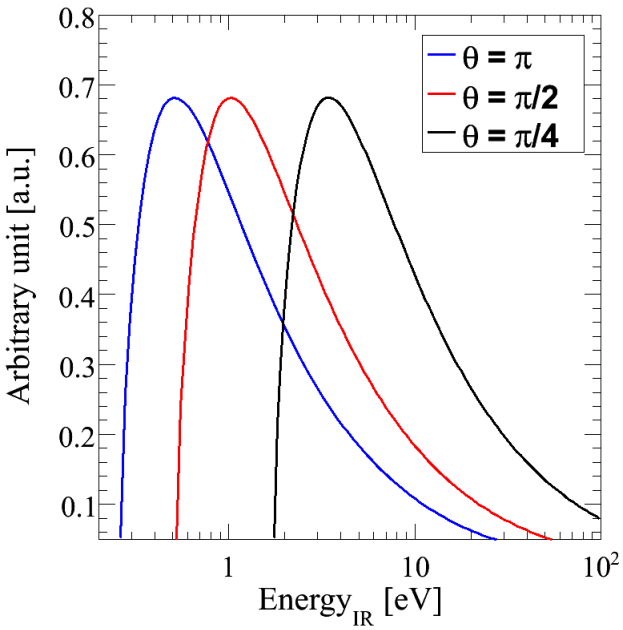

Figure 2.6 The functional behavior of $f(q)$ as a function of the infrared photon $\gamma_{\rm IR}$ for a gamma ray with E = 1 TeV. Plotted are $f(q)$ for the 3 different cases of $\mu = -1, 0$ and $1/\sqrt{2}$.

However, in the most general case of an energetic photon being absorbed in a diffuse isotropic background radiation field, the most effective attenuation of a 1 TeV gamma ray by a soft photon corresponds to a wavelength (Vassiliev, 2000),

$$\lambda_{\rm IR} = 1.33\,\mu{\rm m}\,\frac{\rm E}{1\,{\rm TeV}} \tag{2.5}$$

such that gamma rays with energies between 100 GeV and 10 TeV test attenuation by low energy photons in the range from 10 eV to 0.1 eV (or $1 - 10\,\mu$m).

For a source situated at a redshift of z and the observed gamma-ray with energy E, the EBL attenuation is generally characterized by the optical depth $\tau(E, z)$ parameter. Consequently, the survival probability, $\exp(-\tau(E, z))$ of the unknown intrinsic gamma-ray spectrum, $f_{\rm int}$, is related to the observed νF_ν spectrum, $f_{\rm obs}$ through the following relationship (Rybicki & Lightman, 1985),

$$f_{\rm obs} = e^{-\tau(E,z)}\, f_{\rm int} \tag{2.6}$$

Assuming an isotropic background radiation with particle density per energy per volume, $n(\epsilon)$, the optical depth or the absorption probability of a VHE gamma ray by the soft EBL photons is calculated to be (e.g., Peacock, 1999),

$$\tau(E_\gamma, z) = \int_0^z \left(\frac{{\rm d}l}{{\rm d}z'}\right) {\rm d}z' \int_{-1}^{+1} {\rm d}\mu\, \frac{1-\mu}{2} \int_{\epsilon'_{th}}^{\infty} {\rm d}\epsilon'\, n_\epsilon(\epsilon', z')\, \sigma_{\gamma\gamma}(E'_\gamma, \epsilon', \mu) \tag{2.7}$$

where $n_\epsilon(\epsilon', z')\,\mathrm{d}\epsilon'$ is the comoving number density of EBL photons with energies between ϵ' and $\epsilon' + \mathrm{d}\epsilon'$ at redshift z'. The lower limit on the $\mathrm{d}\epsilon'$-integral $\epsilon'_{th} = \epsilon_{th}(E'_\gamma, \mu) = \frac{2m_e^2c^4}{E'_\gamma(1-\mu)}$ corresponds to the threshold energy of the pair-production interaction. The dependence of the optical depth on the redshift of the source is given by,

$$\begin{aligned} \frac{\mathrm{d}l}{\mathrm{d}z} &= c\left(\frac{\mathrm{d}t}{\mathrm{d}z}\right) = \frac{\mathrm{R_H}}{(1+z)E(z)} \\ E(z) &\equiv \{(1+z)^2(\Omega_m z + 1) + z(2+z)[(1+z)^2\Omega_r - \Omega_\Lambda]\}^{1/2} \end{aligned} \tag{2.8}$$

where the matter and radiation energy density normalized to the critical density are given by Ω_m and Ω_r, respectively. $\Omega_\lambda = \lambda/3\mathrm{H}_0^2$ corresponds to the dimensionless cosmological constant such that $\Omega_\mathrm{m} + \Omega_\mathrm{r} + \Omega_\Lambda = 1$ for a flat universe. $\mathrm{R_H} \equiv c/\mathrm{H}_0$ is the Hubble radius, c is the speed of light, and H_0 is the Hubble constant.

The number density of EBL photons may be derived from the measured intensity or the specific comoving luminosity density at frequency ν and redshift z according to the following relation,

$$\begin{aligned} \epsilon^2 n_\epsilon(\epsilon, z) &= \left(\frac{4\,\pi}{c}\right)\nu I_\nu(\nu, z) \\ &= \int_z^\infty \nu' \mathcal{L}_\nu(\nu', z') \left|\frac{\mathrm{d}t}{\mathrm{d}z'}\right| \frac{\mathrm{d}z'}{1+z'} \end{aligned} \tag{2.9}$$

where $\epsilon = h\nu$ and $\nu' = \nu(1+z')$.

2.4.2 EBL models

The attenuation depends critically on the spectral energy density, $n(E, z)$, of the EBL photons. If the density is known, it is fairly straightforward to calculate the optical depth according to the recipe described above. Considering the uncertainty associated with direct measurements of the EBL intensity, several approaches have been developed to models of the SED of the EBL. This wide range of EBL models are constructed based on our knowledge of galaxy and star formation rate while incorporating observational constraints and data inputs. The EBL models are roughly categorized in two groups: backward and forward evolution models. The former models consider current IR observations of the spectral properties of local galaxies as function of luminosity and extrapolate them back in time using parametric models of the evolution of galaxies (e.g., Malkan & Stecker, 1998, 2001; Stecker et al., 2006). For different galaxy types, the EBL luminosity density is given by the convolution of the galaxy luminosity function with the integrated SED of galaxies. One clear advantage of the backward evolution models is their simplicity and they can be easily tested against observational data. However, these models fail to completely account for processes such as star and metal formation, and re-emission of radiated power by dust in galaxies (for a review of the models see Dwek & Arendt, 1998). The latter category of forward evolution models predict the temporal evolution

of galaxies forward in time assuming a fundamental theory of cosmology and star formation, provided the initial parameters do not conflict with current observational data (e.g., Somerville & Primack, 1999; Primack et al., 2005). These models have proven successful in reproducing the general characteristics of the observed EBL and may be used to test various astrophysical scenarios such as galaxy and star formation, as well as absorption and radiation of the light by dust.

2.5 EBL Constraints from Observations of VHE blazars

Recent observations of distant blazars from IACTs should allow us to characterize the effects of the EBL photons on the spectra of extragalactic gamma-ray sources. However, a severe limitation to the approach arises from our incomplete understanding of the emission mechanisms of gamma-ray and thus the intrinsic spectrum of blazars. Therefore, it is not straightforward to distinguish between the effects inherent to the source (such as the possibility of absorption inside the source, magnetics fields etc.) and the imprints of EBL absorption on the measured spectra of VHE sources. The presence of optical-infrared radiation field close to the source (Donea & Protheroe, 2003) may produce absorption effects that are completely independent of the EBL. Furthermore, a complex dependence of the EBL absorption on the energy of the high-energy gamma rays can lead to a degeneracy such that different EBL shapes can produce similar levels of EBL absorption. This results in further uncertainty in the measurements of EBL as the observed attenuation of the gamma-ray photons can not be uniquely ascribed to one particular EBL model.

Nevertheless, it possible to use measured VHE gamma-ray spectra of blazars to constrain the spectral distribution of the EBL by assuming an intrinsic spectrum (Stecker & de Jager, 1993). This approach assumes a particular shape of the EBL where the absolute normalization is left as a free parameter. Subsequently, de Jager (1994) and Dwek & Slavin (1994) used the spectrum of Mrk 421 to determine the EBL spectrum. However, the robustness of this method has come under criticism considering the critical assumptions made on the intrinsic source spectrum (Vassiliev, 2000). For example, the initial EBL limits derived by Stecker & de Jager (1993) was later subjected to revision (Stecker & de Jager, 1998) due to conflicts with direct measurements. Stanev & Franceschini (1998) later devised a more conservative approach to use the deviation, or lack thereof, of the data from an assumed intrinsic spectrum to derive an upper limit on a piecewise-flat EBL density, in a νF_ν representation. This technique was used by Biller et al. (1998) and Funk et al. (1998) to place upper limits on the EBL using observations of Mrk 421 and Mrk 501. This approach has come under similar scrutiny due to poorly motivated assumptions on the intrinsic source spectrum and Schroedter (2005a) cautions against the claims of upper limits through a small number of VHE gamma-ray observations as "over-optimistic.". [The reader is directed to Hauser & Dwek (2001) for a through review of various efforts to detect the EBL or to derive upper limits via the observations of VHE

gamma-ray objects up to 2001.]

More recently, efforts to obtain upper limits on the density of EBL has focused on the use of certain reasonable constraints on the intrinsic spectrum of the source. The origin of the observed VHE gamma-ray peak in typical blazar spectra is generally attributed to the inverse Compton up-scattering of UV/X-ray seed photons on ultrarelativistic electrons. Consequently, the resulting GeV–TeV intrinsic spectrum is expected to be smooth and consistent with the X-ray synchrotron peak; the spectra should not contain any "unphysical" behavior such as an exponential rise with energy or emission-like line features. Dwek & Krennrich (2005) applied a solid statistical method to a large sample of TeV spectra from Mrk 421, Mrk 501 and H 1426+478 to test the physical feasibility of a set of EBL shapes. EBL shapes, initially constructed based on limits and detections at various wavelengths, were subsequently ruled out, when, under the most conservative assumptions, the intrinsic spectra showed a significant exponential rise at high energies. Furthermore, the shock-accelerated electrons are unlikely to produce gamma-rays with spectral indices harder than $\Gamma = 1.5$ from Compton scattering. In a similar approach to the above, a certain EBL model that is consistent with EBL observations may be further constrained, by varying the normalization parameter until it fits the de-absorbed TeV blazar spectrum with a power law softer than $\Gamma_{\rm int} = 1.5$. Aharonian et al. (2006b) applied this "exclusion" criteria to the observed spectra of distant blazars 1ES 1101-232 and H 2356-309 from H.E.S.S.to derive strong upper limits on the normalization of EBL around $2\,\mu$m. The resulting EBL upper limits were found to be consistent with the lower limits from the integrated light of resolved galaxies. Krennrich et al. (2008) employed a similar technique to rule out EBL models which is inconsistent with the recent lower limits at 3.6 μm from galaxy counts (Levenson & Wright, 2008).

However, Mazin & Raue (2007) criticized the assumption of a particular shape of the EBL spectrum. They addressed the problem by devising a novel technique which scans over a large grid for every possible shape of the EBL density using spline functions. In this method, Mazin & Raue (2007)reconstruct the intrinsic spectra of all detected TeV blazars by considering any EBL shape that is compatible with the current limits from direct measurements and model predictions. Finally, they exclude the shapes for which the resulting de-absorbed gamma-ray spectra, when fit with a power-law, broken power-law, or power-law with an exponential cut-off, yields $\Gamma_{\rm int}$ greater than a certain value. The two constraints used by Mazin & Raue (2007) are $\Gamma_{\rm int} > 1.5$ and 0.75, respectively. Finally, the remaining allowed EBL shapes were combined into a single robust limit on the EBL intensity for a wide range of wavelengths.

Schroedter (2005b) developed a relatively straightforward technique to derive upper limits on the EBL by exploiting the fact that for a given gamma-ray energy, E_γ, the attenuation is maximized for a EBL photon with wavelength λ_0. Hence, if ones assumes that the total absorption at energy E_γ is solely caused by a monochromatic EBL with wavelength λ_0, the corresponding EBL density $n(\lambda_0)$ represents a conservative upper limit to the EBL at that

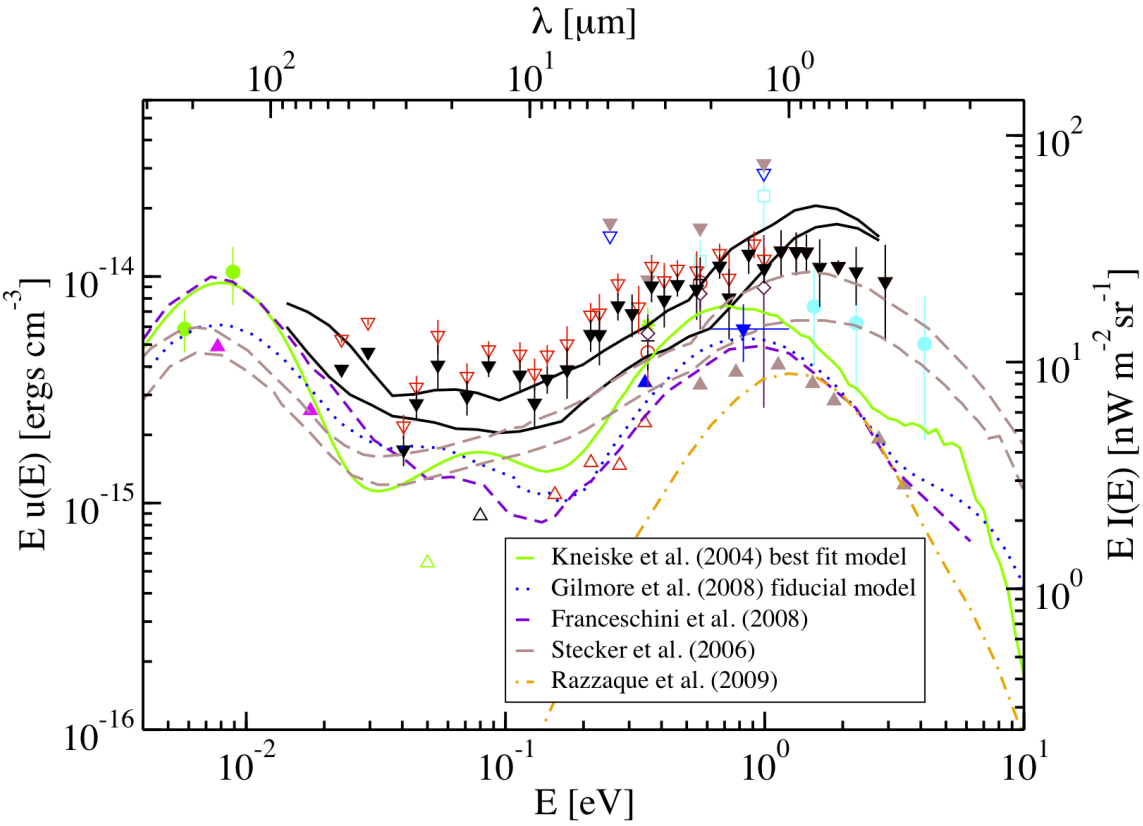

Figure 2.7 Measurements and constraints on the spectral distribution of EBL by (Finke & Razzaque, 2009). Measurements are from Bernstein et al. (2002, cyan points), Gorjian et al. (2000, empty red circles), Dwek & Arendt (1998, green asterisk), Cambresy et al. (2001, empty cyan square), Wright & Reese (2000, black cross), Levenson & Wright (2007, maroon diamonds), and Hauser & Dwek (2001, green filled circles). Lower limits are from Fazio et al. (2004, red empty triangles), Madau & Pozzetti (2000, brown filled triangles), Levenson & Wright (2008, blue filled triangle), Dole et al. (2006, magenta filled triangles), Metcalfe et al. (2003, black empty triangle), and Papovich et al. (2004, green empty triangle). Upper limits are from Hauser et al. (1998, brown filled inverted triangle), Dwek & Arendt (1998, blue empty inverted triangles), Aharonian et al. (2006b, blue filled inverted triangle), Mazin & Raue (2007, upper and lower black curves $\Gamma_{\rm int}^{\rm min} = 0.75$ and $\Gamma_{\rm int}^{\rm min} = 1.5$ upper limits, respectively), and Red empty and black filled inverted triangles are the $\Gamma_{\rm int}^{\rm min} = 1.0$ and $\Gamma_{\rm int}^{\rm min} = 1.5$ upper limits, respectively, derived by Finke & Razzaque (2009). Also plotted are several EBL models: the best fit model from Kneiske et al. (2004, solid green curve), the fiducial model from Gilmore et al. (2008, dotted blue curve), the model of Franceschini et al. (2008, short dashed violet curve), the baseline and fast evolution models of Stecker et al. (2006, lower and upper long dashed curves, respectively), and model B from Razzaque et al. (2009, dot-dashed orange curve).

wavelength. Schroedter (2005b) derived upper limits on the EBL density by utilizing a set of 6 well-measured TeV blazar spectra along with a conservative limit to maximum hardness of the intrinsic source spectrum, $\Gamma_{int} = 1.8$ (well justified by the observed data). Several key differences set this technique apart from the ones described earlier: this technique does not make assumptions about the shape of the EBL and it does not rely on a certain model to fit the de-absorbed spectrum. Finke & Razzaque (2009) recently extended the technique of Schroedter (2005b) to an up-to-date sample of TeV blazar spectra. The resulting upper limits are weaker and more conservative than limits derived from de-absorbing spectra with an assumed EBL model and fitting the intrinsic spectrum with a power law. Upper limits derived by Finke & Razzaque (2009) were found to be in reasonable agreement with limits from Mazin & Raue (2007). Figure 2.5 shows the constraints obtained by Finke & Razzaque (2009) along with other EBL measurements and constraints.

2.6 Possible EBL absorption feature in VHE blazar spectra

One of the major challenges to extracting information about the EBL from the observed spectra of TeV sources is our lack of knowledge about the intrinsic emission mechanism of the source. Not surprisingly, present attempts to probe the diffuse EBL radiation field rely on critical assumptions made about the source spectra. These assumptions depend on our theoretical understanding of particle acceleration and emission mechanism in blazar jets. However, an unambiguous EBL feature independent from source properties is highly desirable for getting a better understanding of the level of gamma-ray absorption on cosmological distance scales. This section briefly examines the possibility of identifying a unique signature in the observed spectra of blazars that is attributable to absorption by the EBL [2].

2.6.1 Spectral cutoff at 1 TeV

Figure 2.8 shows an example of a typical EBL model (in this case, Primack et al., 2005) and the corresponding opacity to VHE gamma rays calculated using Equation 2.7. We have already established that the cross section for the $\gamma_{\rm TeV} + \gamma_{\rm IR} \rightarrow e^+ + e^-$ interaction is highly sensitive to the energies of the incoming photons. As a result, the magnitude of the opacity to gamma rays depends on the intensity of the EBL. Moreover, the opacity varies as a function of the gamma-ray energy depending on the particular spectral shape of the EBL.

Consequently, changes in the slope of the EBL intensity with wavelength will give rise to changes in the slope of the gamma-ray opacity. In particular, the rise in the opacity curve (Figure 2.8) is marked by a softening around $\sim$ 1 and 5 TeV which results from the trough in the EBL spectral distribution between the stellar and dust emission peaks. According to Equation 2.5, $\sim$ 1 TeV photons are most effectively attenuated by $\sim$ 1 μm photons from

[2] Results from this work was published in Imran & Krennrich (2007)

the EBL. Therefore, the relative drop off in the EBL intensity between the NIR and MIR wavelength (1–15 μm) is expected to produce a change in the slope of the gamma-ray optical depth around $\sim$ 1 TeV. Physically, this is justified by the fact that the high energy photons have fewer EBL photons to interact with going from the NIR to the MIR range. Finally, a softening of the opacity could alter the TeV spectra of blazars around 1 TeV, potentially leading to a detectable spectral hardening of softening that is unique to the shape and intensity of the EBL.

A new generation of highly sensitive IACTs (VERITAS, MAGIC and H.E.S.S.) has successfully detected many new TeV blazars in the past 4–5 years. Moreover, the emission level of a number of these blazars are reported to highly variable on all timescales. Historically, variability in blazars is marked by changes of the emission level of the electromagnetic radiation by more than one order of magnitude. Flares with emission level as high as 10 times the Crab Nebula flux have been observed for the AGN Mrk 421 ($z = 0.03$). When correcting for distance, many blazars have been shown to emit high energy radiation at similar flaring levels: 1ES 1218+304 ($z = 0.182$ Acciari et al., 2010a), 1ES 1101-232 [$z = 0.186$][](Aharonian et al., 2006b), PKS 2155-304 ($z = 0.116$ Aharonian et al., 2007a), 1ES 1959+650 ($z = 0.047$ Daniel et al., 2005), and 1ES 2344+514 ($z = 0.044$ Aharonian et al., 1999a) Therefore, TeV observations of strongly flaring blazar may provide us with sufficient statistics to detect an EBL imprint in the measured spectra.

2.6.2 Template EBL spectra

In order to characterize the effect of the relative EBL intensity in the near and mid-IR regime, we apply a number of viale EBL scenarios to a set of simulated blazar spectra over a range of redshifts. Dwek & Krennrich (2005) provided a convenient parameterization of EBL scenarios and a wide range of EBL spectra. In this work, we considered a set of 12 different EBL realizations from Dwek & Krennrich (2005) which are consistent with observational limits in the near-IR, mid-IR and far-IR wavelengths. Dwek & Krennrich (2005) constructed these template EBL spectra by fitting polynomials to all extreme possible combinations of relative peak values for the following spectral contributions:

1. Three stellar components to the spectral distributions of the EBL. They are (a) *high-UV* contribution defined by the 0.1595 and 0.2365 μm data from Gardner et al. (2000) and Cambresy et al. (2001). These limits were derived using the Kelsall zodiacal light model (KZL) (Kelsall et al., 1998) to subtract the zodiacal foreground; (b) *mid-UV* contributions defined by the 0.1595 and 0.2365 μm data from Gardner et al. (2000) and the Wright (2001) determinations of the EBL intensity that employed the Gorjian zodiacal light model (GZL) (Gorjian et al., 2000) similar to the KZL; and (c) *low-UV* contributions defined by the 0.1595 and 0.2365 μm data from Gardner et al. (2000) and the galaxy number counts by Madau & Pozzetti (2000). The authors, Dwek & Krennrich

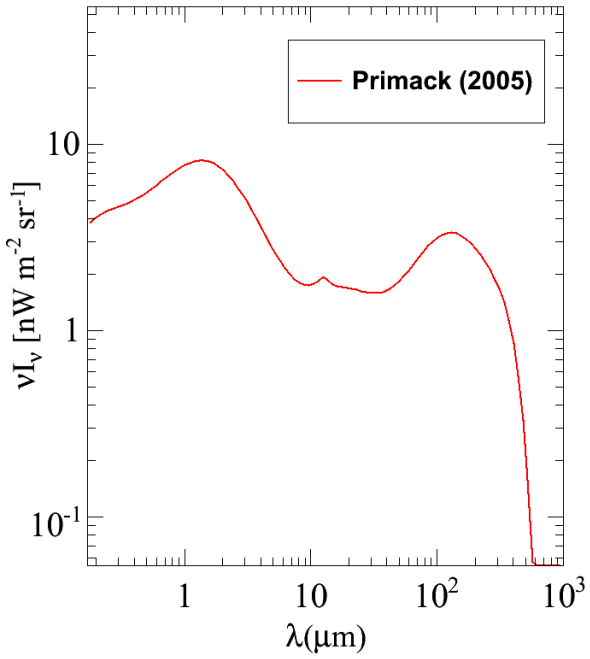

(a)

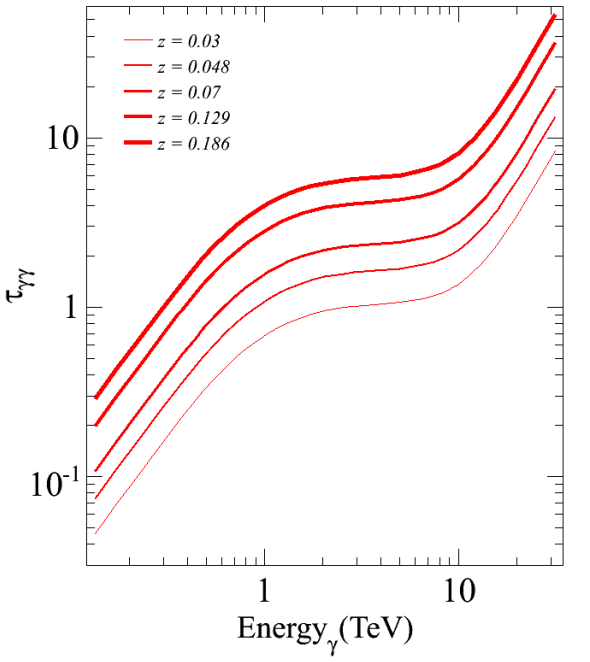

(b)

Figure 2.8 (a) A typical EBL model - Primack et al. (2005) model in this case. (b) Also shown for illustration is the corresponding opacity, τ_γ as a function of the energy, E_γ of gamma-ray photons for a range of redshifts, $z = 0.03$ to 0.186.

(2005), note that the determinations of three realizations of the stellar component are motivated by constraints at the near-IR, as well as at 0.1595 and 0.2365 μm. Furthermore, these limits were found to be consistent, within experimental uncertainties, with the claimed detection by Bernstein et al. (2002).

2. Two components at the mid-IR wavelengths, defined by the uncertainties in the measurements of the lower limits at 15 μm. The lower limits at the mid-IR were derived by Elbaz et al. (2002) from galaxy number counts obtained with the *Infrared Space Observatory* (ISO) satellite. The high mid-IR EBL intensity is given by the nominal 15 μm intensity added with a $+3\,\sigma$ excess from measurements. Similarly, the low mid-IR EBL intensity is obtained by subtracting $3\,\sigma$ from the nominal 15 μm intensity.

3. Two components at the far-IR wavelengths, defined by the two different calibrations of the DIRBE data at 100 and 240 μm. (Lagache & Puget, 2000; Hauser et al., 1998). For all wavelengths above 240 μm, the EBL intensities were derived from the FIRAS measurements by Fixen et al. (1998).

The combination of these EBL components gave rise to a total of 12 ($3\times2\times2$) different template EBL spectra. Dwek & Krennrich (2005) constructed an additional "average" EBL spectrum, which corresponds to a polynomial fit through the low-mid-IR component at 15 μm and the average UV and far-IR limits. The "average" EBL scenario is only meant to approximate the typical EBL intensity and excluded from final analysis.

Dwek & Krennrich (2005) devised a convenient nomenclature to represent the different EBL realizations by their relative intensities in the UV/optical, mid-IR and far-IR wavelength regime. The templates are referred to as XYZ, where X = H, M,or L represents the high, medium, or low intensity of the stellar component of the EBL. Similarly, Y = H or L represents the high or low flux of the mid-IR EBL intensity at 15 μm. Finally, Z = H or L corresponds to the high or low intensity of the EBL density at far-IR wavelengths. For example, HLH stands for an EBL scenario that is derived by a polynomial fit through high-UV, the low mid-IR, and the high far-IR intensities of the EBL. Figure 2.9 plots the different realizations of the EBL according to Dwek & Krennrich (2005). The three stellar components are represented in the figure by solid lines (high-UV), lines with connected dots (mid-UV), and the dashed lines (low-UV). The black lines correspond to EBL templates going through the high mid-IR and lines passing through the low mid-IR intensities are drawn in gray. All lines going through the high far-IR data are given by thick lines compared to the ones going through the low far-IR points. For comparison, the "average" EBL scenario is plotted in red in the figure. The data points used in the derivation of the template spectra and the coefficients of the polynomial fits can be found in Table 1 and Table 2, respectively, in Dwek & Krennrich (2005).

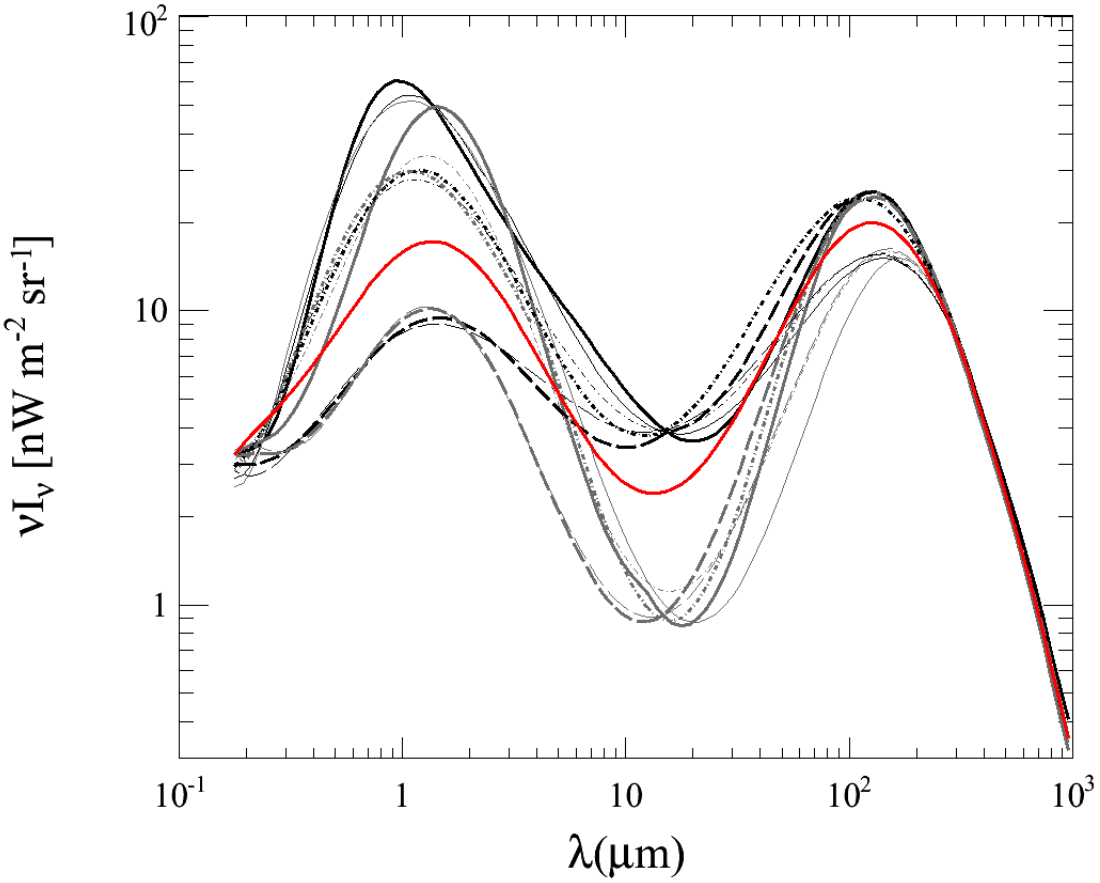

Figure 2.9 Template spectra representing different realizations of the EBL (adapted from Dwek & Krennrich (2005)). Three stellar components (high-UV, mid-UV, low-UV) are given by solid line, lines with connected dots, and dashed lines, respectively. The black lines represent EBL templates passing through the high mid-IR data, whereas gray lines depict templates passing through low mid-IR points. All lines going through the high far-IR data are thicker compared to the ones going through the low far-IR data points. The red line going through the nominal 15 μm data point represent the "average" EBL scenario.

2.6.3 Simulated blazar spectra

From our discussion of the dependence of the EBL opacity to the change in the slope of the EBL intensity between 1 and 15 μm, it is apparent that measured spectra of TeV blazars may contain a unique signature of EBL attenuation at around 1 TeV. In order to evaluate the prospect of finding an EBL induced absorption signature in the measured spectra of TeV blazars and to measure the sensitivity of the current generation of IACTs to such a spectral feature, we constructed a set of hypothetical "test" blazars. Emission from the test blazars are modeled as a single power-law such that the intrinsic spectra are represented by $(\mathrm{dN/dE})_{\mathrm{intrinsic}} \sim \mathrm{E}^{-\Gamma}$ where Γ correspond to the differential photon index.

We know from observations that the spectra of blazars can be characterized in the energy range $100\,\mathrm{GeV} \leqslant \mathrm{E} \leqslant 10\,\mathrm{TeV}$ by a single power law. Table 2.6.3 shows a compilation of the spectral slope of the reconstructed source-intrinsic spectra for a number of blazars detected by IACTs. The photon indices of the intrinsic spectra typically vary between $\Gamma = 1.4 - 3.3$. Aharonian et al. (2006b) attributes the exceptionally hard intrinsic spectrum for 1ES 1101-232 to the higher energy peak of the IC-peak beyond 1 TeV. Since the average observed photon index in BL Lac objects tend be around $\Gamma \sim 2.5$, the intrinsic power law slope of our simulated blazars are set at $\Gamma = 1.6$, 2.0, and 2.4, respectively. Our choice of intrinsic spectral indices for the test blazars adopts a generally accepted view of the emission model: the intrinsic TeV blazar spectrum can not be arbitrarily hard. Moreover, we chose a conservative approach where simple shock-acceleration scenarios precludes intrinsic spectrum harder than $\Gamma_{\mathrm{TeV}} = 1.5$.

The gamma-ray opacity due to the EBL photons vary as a function of the distance to the source. In order to account for the effect of the distance, the test blazars are placed at redshifts of $z = 0.03$, 0.048, 0.07, 0.116, 0.129 and 0.186. The choice for the values of distances are well-motivated by the distribution of redshifts for the observed TeV blazars.

In order to address the question of detectability of a spectral feature in the TeV regime due to attenuation by the EBL photons, the emission level of each of the test blazar is normalized to $\sim$ 4 times the Crab Nebula flux above 200 GeV when placed at a reference redshift of $z = 0.03$. This flux level corresponds to $\sim$ 10% of the Crab Nebula flux at a redshift of $z = 0.18$, which is typical for a number of historical TeV blazars observations particularly during emission in flaring states. In fact, recent observations by the VERITAS collaboration revealed similar emission level from the AGN 1ES 1218+304 ($z = 0.182$) (Acciari et al., 2010a). Moreover, report of a flare by th H.E.S.S. collaboration with PKS 2155-305 ($z \sim 0.1$) reaching 15 times the Crab Nebula flux makes our assumptions conservative. Given the sensitivity of the current generation of IACTs such as VERITAS, exposure times of 25–50 hours would enable us to detect sources at 10% Crab level and provide sufficient statistics to reconstruct the energy spectra.

We model the response of a typical IACT instrument for obtaining blazar spectra by folding in the statistical uncertainties, σ, associated with H.E.S.S. measurement of the AGN 1ES 1101-

Table 2.1 Measured VHE blazar spectra and reconstructed intrinsic spectral indices [Adapted from Wagner (2008)]. Γ denotes the reconstructed (intrinsic) VHE spectral power-law index at 500 GeV, calculated from the measured spectra assuming a Kneiske et al. (2004) 'low-IR' EBL density. [a]At an assumed $z = 0.1$. [b]At an assumed $z = 0.03$. [c]Spectrum measured during a flare state of the respective blazar. *References*: [1]Aharonian et al. (1999b), [2]Aharonian et al. (2001), [3]Albert et al. (2007a), [4]Albert et al. (2006b), [5]Albert et al. (2006c), [6]Albert et al. (2007b), [7]Superina et al. (2007), [8]Aharonian et al. (2005b), [9]Aharonian et al. (2005a), [10]Horan & Finley (2001), [11]Aharonian et al. (2002a), [12]Mazin & Raue (2007), [13]Aharonian et al. (2006b), [14]Albert et al. (2006a), [15]Aharonian et al. (2006b), [16]Aharonian et al. (2007b), [17]Albert et al. (2007c), [18]Albert et al. (2007d), [19]Albert et al. (2007d), [20]Krennrich et al. (2002), [21]Aharonian et al. (1999a), [22]Schroedter (2005b), [23]Daniel et al. (2005), [24]Aharonian et al. (2007a)

Object	Measured energy spectrum dF/dE ($\mathrm{TeV}^{-1}\,\mathrm{cm}^{-2}\,\mathrm{s}^{-1}$)	Intrinsic slope Γ	Reference
Mrk421	$(12.1 \pm 0.5)10^{-12}(\mathrm{E}/1.0\ \mathrm{TeV})^{-3.09\pm0.07}$	2.85 ± 0.58	1
Mrk501	$(8.4 \pm 0.5)10^{-12}(\mathrm{E}/1.0\ \mathrm{TeV})^{-2.76\pm0.08}$	2.49 ± 0.84	2
1ES2344+515	$(1.2 \pm 0.2)10^{-11}(\mathrm{E}/0.5\ \mathrm{TeV})^{-2.95\pm0.12}$	2.67 ± 0.21	3
Mrk180	$(4.5 \pm 1.8)10^{-11}(\mathrm{E}/0.3\ \mathrm{TeV})^{-3.3\pm0.7}$	3.06 ± 0.50	4
1ES1959+650	$(3.4 \pm 0.5)10^{-12}(\mathrm{E}/1.0\ \mathrm{TeV})^{-2.72\pm0.14}$	2.37 ± 0.29	5
BL Lacertae	$(1.9 \pm 0.5)10^{-11}(\mathrm{E}/0.3\ \mathrm{TeV})^{-3.64\pm0.54}$	3.17 ± 0.25	6
PKS0548–323	$(1.9 \pm 0.4)10^{-13}(\mathrm{E}/1.0\ \mathrm{TeV})^{-2.8\pm0.3}$	2.38 ± 0.28	7
PKS2005–489	$(1.9 \pm 0.7)10^{-13}(\mathrm{E}/1.0\ \mathrm{TeV})^{-4.0\pm0.4}$	3.52 ± 0.27	8
PKS2155–304	$(1.96 \pm 0.12)10^{-12}(\mathrm{E}/1.0\ \mathrm{TeV})^{3.32\pm0.06}$ E < 700 GeV, $(2.4^{+0.4}_{-0.3})10^{-12}(0.7 \pm 0.2)^{(3.79^{+0.46}_{-0.27}-3.15^{+0.10}_{-0.12})} \times(\mathrm{E}/1.0\,\mathrm{TeV})^{3.79^{+0.46}_{-0.27}}$ for E > 700 GeV	2.43 ± 0.64	9
H1426+429	$(2.9 \pm 1.1)10^{-11}(\mathrm{E}/0.43\ \mathrm{TeV})^{2.6\pm0.6}$	1.58 ± 0.23	10 11
1ES0229+200	$(2.34 \pm 0.37)10^{-14}(\mathrm{E}/3.0\ \mathrm{TeV})^{-2.5\pm0.2}$	1.39 ± 0.30	12
H2356-309	$(3.08 \pm 0.75)10^{-13}(\mathrm{E}/1.0\ \mathrm{TeV})^{-3.06\pm0.4}$	1.77 ± 0.37	13
1ES1218+304	$(8.1 \pm 2.1)10^{-11}(\mathrm{E}/0.25\ \mathrm{TeV})^{-3.0\pm0.4}$	1.97 ± 0.40	14
1ES1101–232	$(4.44 \pm 0.74)10^{-13}(\mathrm{E}/1.0\ \mathrm{TeV})^{-2.88\pm0.14}$	1.33 ± 0.37	15
1ES0347–121	$(4.52 \pm 0.85)10^{-13}(\mathrm{E}/1.0\ \mathrm{TeV})^{-3.10\pm0.23}$	1.76 ± 0.14	16
1ES1011+496	$(2.0 \pm 0.1)10^{-10}(\mathrm{E}/0.2\ \mathrm{TeV})^{-4.0\pm0.5}$	2.56 ± 0.29	17
PG1553+113[a]	$(1.8 \pm 0.3)10^{-10}(\mathrm{E}/0.2\ \mathrm{TeV})^{-4.21\pm0.25}$	3.68 ± 0.68	18
PG1553+113[b]	$(1.8 \pm 0.3)10^{-10}(\mathrm{E}/0.2\ \mathrm{TeV})^{-4.21\pm0.25}$	2.34 ± 0.46	19

Table 2.1 (Continued)

Object	Measured energy spectrum dF/dE ($TeV^{-1}\,cm^{-2}\,s^{-1}$)	Intrinsic slope Γ	Reference
Mrk421[c]	$(23.40 \pm 0.73)10^{-11}(E/1.0\ TeV)^{-2.32\pm0.03}$	2.09 ± 0.30	20
Mrk501[c]	$(2.50 \pm 0.16)10^{-10}(E/1.0\ TeV)^{-2.22\pm0.04}$	1.95 ± 0.41	21
1ES2344+515[c]	$(5.1 \pm 1.0)10^{-11}(E/1.0\ TeV)^{-2.54\pm0.17}$	2.20 ± 0.31	22
1ES1959+650[c]	$(1.23 \pm 0.25)10^{-10}(E/1.0\ TeV)^{-2.78\pm0.12}$	2.43 ± 0.29	23
PKS2155–304[c]	$(2.06 \pm 0.16)10^{-10}(E/1.0\ TeV)^{-2.71\pm0.06}$ E < 340 GeV, $(2.06 \pm 0.16)10^{-10}(0.430 \pm 0.022)^{(3.53\pm0.05)-(2.71\pm0.06)} \times(E/1.0\,TeV)^{-3.53\pm0.05}$ for E > 340 GeV	2.28 ± 0.40	24

232 (Aharonian et al., 2006b). Considering the relatively large redshift of 1ES 1101-232 ($z = 0.186$), we expect the VHE spectrum to be severely altered by the interaction of high-energy gamma rays with the low energy photons of the TeV. Moreover, the measured spectrum extends well beyond 1 TeV, with sufficient flux detection in the last bin at 5 TeV. Therefore, the errors in the measured flux of the 1ES 1101-232 represent a realistic simulation of both statistical and systematics uncertainties expected from the reconstruction of the observed VHE spectra of blazars.

Table 2.2 Spectral points of 1ES 1101-232 (Aharonian et al., 2006b).

Energy (TeV)	$E^2\,dN/dE$ ($TeV\,cm^{-2}\,s^{-1}$)	Error in $E^2\,dN/dE$ ($TeV^{-1}\,cm^{-2}\,s^{-1}$)
0.134	2.95×10^{-12}	1.17×10^{-12}
0.173	2.50×10^{-12}	0.89×10^{-12}
0.224	2.30×10^{-12}	0.65×10^{-12}
0.289	1.94×10^{-12}	0.56×10^{-12}
0.372	1.55×10^{-12}	0.45×10^{-12}
0.483	7.64×10^{-13}	4.90×10^{-13}
0.626	1.01×10^{-12}	0.38×10^{-12}
0.806	5.78×10^{-13}	4.23×10^{-13}
1.050	3.50×10^{-13}	2.70×10^{-13}
1.330	6.29×10^{-13}	3.90×10^{-13}
1.740	6.37×10^{-13}	3.31×10^{-13}
2.220	7.33×10^{-13}	3.80×10^{-13}
2.880	6.37×10^{-13}	4.20×10^{-13}

2.6.4 Cutoff strength

Figures 2.10 and 2.11 shows the effect of EBL induced attenuation in the case of a test blazar placed at $z = 0.048$. For a source with an intrinsic power law spectrum, $dN/dE \sim E^{-2.0}$, shown are each of the 8 viable EBL scenarios from Dwek & Krennrich (2005). We now discuss how the absorbed spectra of simulated blazars under different EBL templates can be tested for a spectral feature. We stipulated earlier that change in the slope of gamma-ray opacity can manifest as a spectral break in the observed blazar spectra at $\sim$1 TeV. The modulation is characterized by fitting the observed VHE spectrum with two simple power-law spectra, above and below 1 TeV, respectively. By assuming that a transition takes place around $E = 1\,\mathrm{TeV}$, the two power-law fits yields $\Gamma_{>1\,\mathrm{TeV}}$ and $\Gamma_{<1\,\mathrm{TeV}}$ to describe the changes to the measured spectrum around the transition region.

We introduce a new quantity *cutoff-strength*, $\Delta\Gamma$, to further quantify the change in the observed VHE blazar spectrum due to EBL absorption. $\Delta\Gamma$ is given by the difference in spectral indices from power-law fits to the measured spectrum above and below 1 TeV,

$$\Delta\Gamma = \Gamma_{>1\,\mathrm{TeV}} - \Gamma_{<1\,\mathrm{TeV}} \tag{2.10}$$

Figures 2.10 and 2.11 also show power-law fits to the absorbed spectra below and above 1 TeV. We clearly see that the magnitude of $\Delta\Gamma$ is mediated by the relative values of the EBL photons in the near, mid and far-IR wavelengths depending on the different EBL scenarios.

We also find that for a given redshift, the cutoff strength, $\Delta\Gamma$, essentially remains independent of the intrinsic source spectra. Our simple, mode-independent method only relies on the assumption that the spectral break at around 1 TeV is due to EBL pair production absorption. However, sources with intrinsic cutoffs may diminish our sensitivity to measurements of such spectral features because of rapidly decreasing flux points at higher energies, resulting in limited statistics. We argue that the best sources for searching for a measurable cutoff are HBLs with their characteristic IC luminosity peak extending well in to the multi-TeV regime. In fact, recently discovered HBLs such as 1ES 1218+304 (Acciari et al., 2009a), 1ES 0229+200 (Aharonian et al., 2007b) and RGB J0710+591 (Perkins et al., 2007) are particularly promising for carrying out a search for a spectral feature since these blazars have very hard intrinsic spectral slopes considering their redshifts ($z = 0.125 - 0.188$). Additionally, the high energy bumps in the observed TeV blazars spectra demonstrate a general hardening during flaring states (e.g., Albert et al., 2007e; Aharonian et al., 2009a). As a result, we expect TeV blazars in high states to provide further constraints to our measurement of the cutoff strength due to solid determination of the flux and spectral index.

Based on our analysis of EBL absorption on simulated blazar spectra, we find that the magnitude of $\Delta\Gamma$ has a strong dependence on distance to the source for competing EBL scenarios. Figure 2.12 show the distribution of $\Delta\Gamma$ for different template spectra as a function of redshifts. This is not particularly surprising considering the relative strength of the EBL

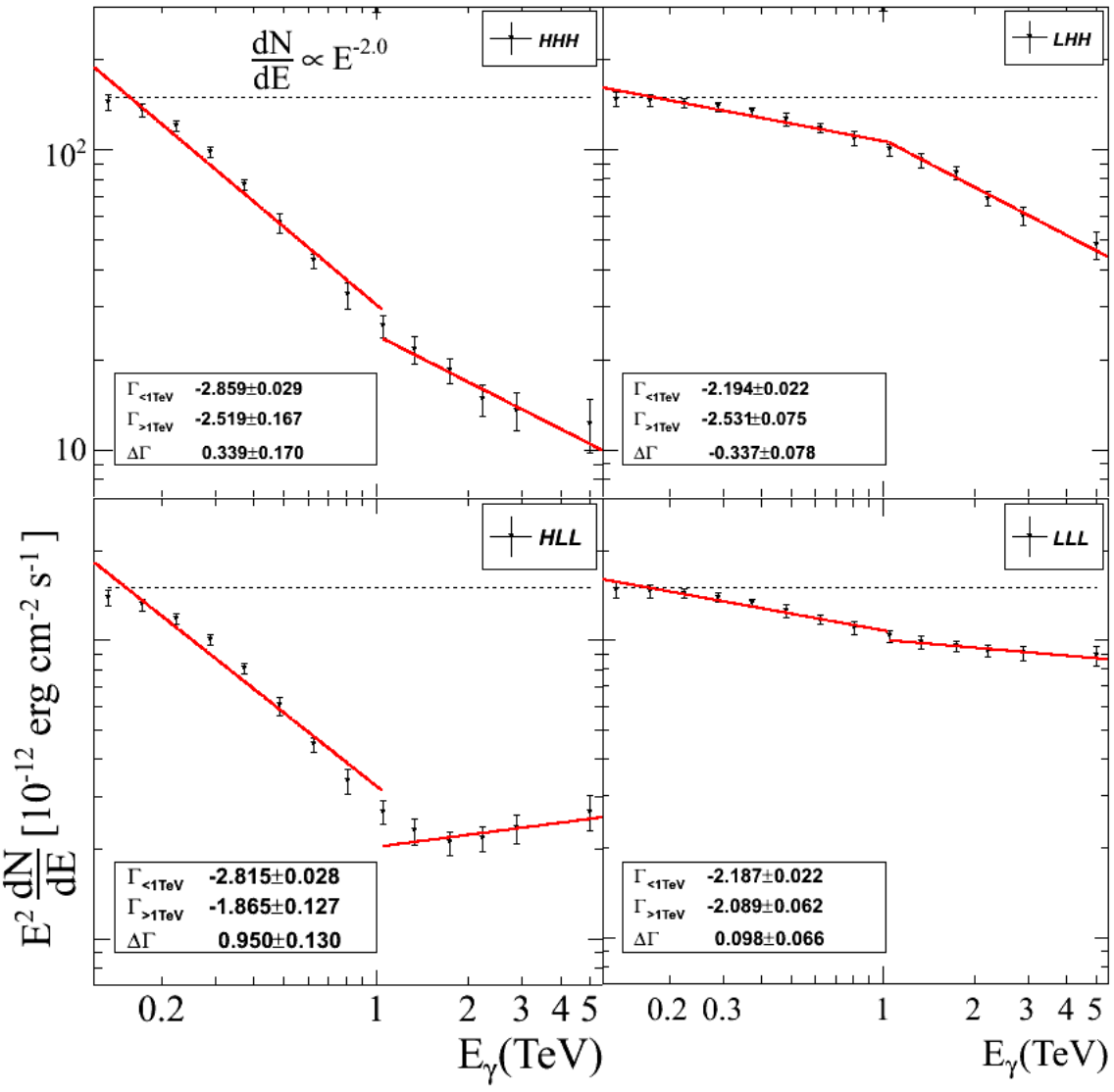

Figure 2.10 Absorbed energy spectra for the case of a test blazar with an intrinsic spectrum, $dN/dE \sim E^{-2.0}$, located at a redshift of $z = 0.048$. The affect of the EBL attenuation on the observed spectrum is shown for the following scenarios: a) HHH b) LLH, c) MLH, and d) HLH.

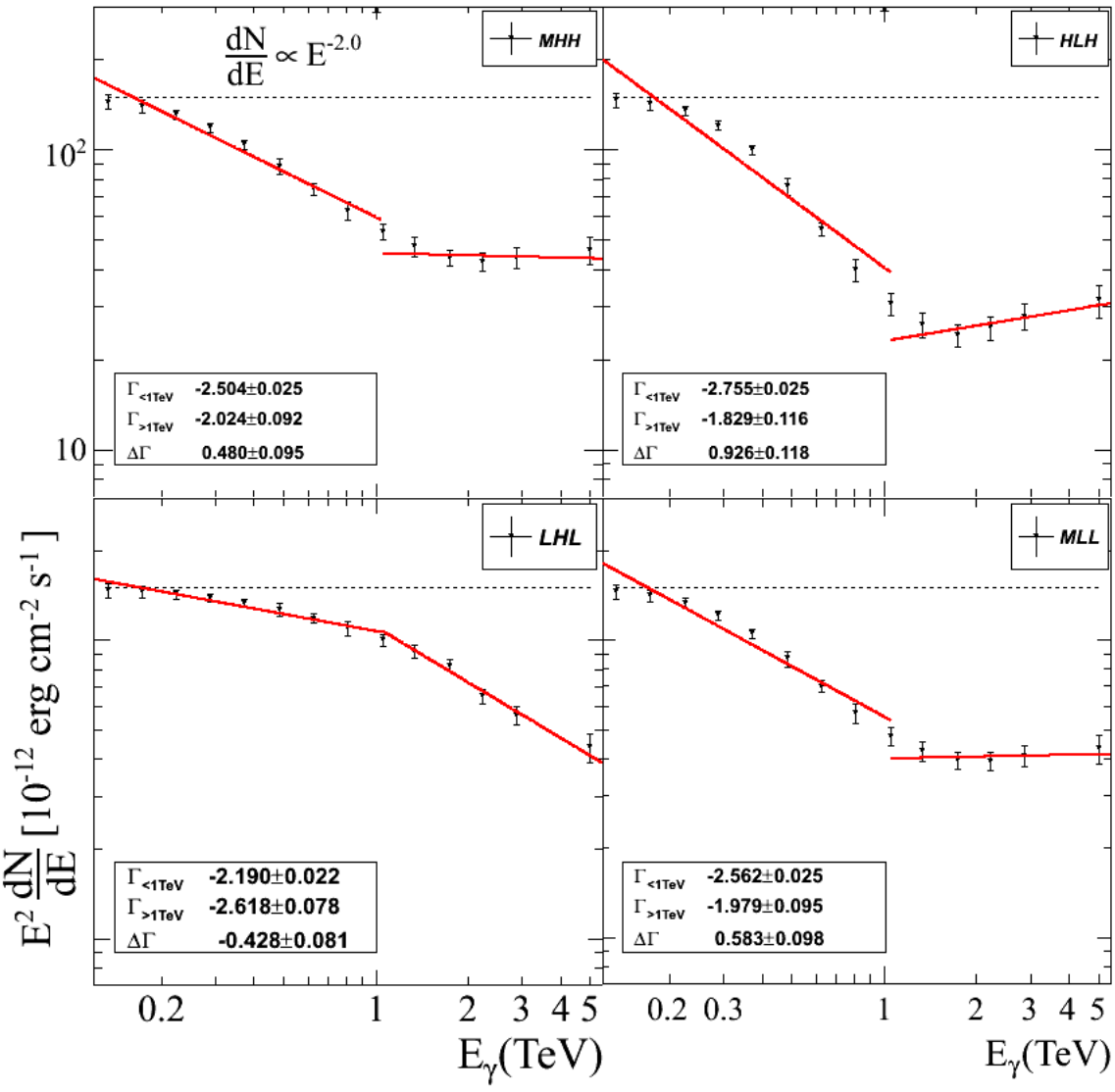

Figure 2.11 Absorbed energy spectra for the case of a test blazar with an intrinsic spectrum, $dN/dE \sim E^{-2.0}$, located at a redshift of $z = 0.048$. The effect of the EBL attenuation on the observed spectrum is shown for the following scenarios: a) LHL b) LLL, c) MLL, and d) HLL.

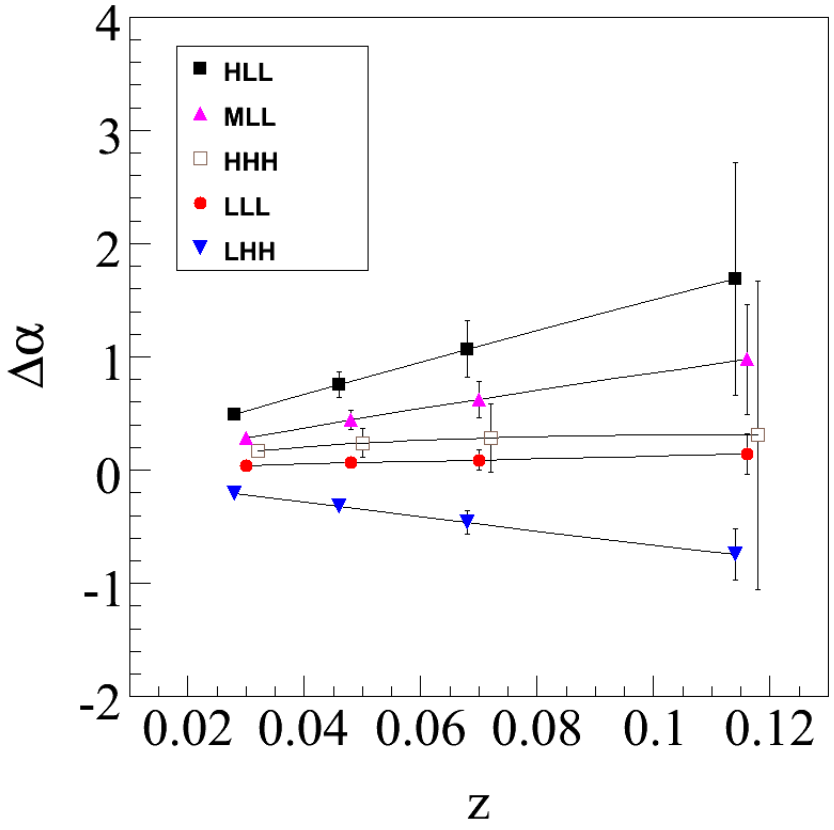

Figure 2.12 *Cutoff strength*, $\Delta\Gamma$, as a function of redshifts is shown for different EBL scenarios.

intensity at near-IR and mid-IR solely modulates the cutoff strength. Subsequently, the presence of a spectral feature is magnified with increasing distances as the high-energy gamma rays travel through greater path lengths . From our simple assumptions about the intrinsic flux levels of test blazars, we conclude that sources located at redshifts of $Z \sim 0.05$ to 0.13 are most promising for searching unveiling a spectral break.

2.7 EBL and hard spectra blazars

In recent years, the VHE gamma-ray sky has seen a dramatic increase in the number of sources, with over 2 dozens AGN[3] spanning redshifts of 0.0018 – 0.536. All except two are in the blazar class of AGN, which have been observed to emit E > 100 GeV gamma rays. The observed energy spectra of blazars have therefore passed through different path lengths in the

[3]For updates, see http://tevcat.uchicago.edu

extragalactic space resulting in different degrees of attenuation due to EBL pair-production interaction. From our earlier discussion, the measured TeV blazar spectrum may be used to constrain the spectral distribution of EBL since it contains unique information about the EBL intensity in the near-IR and mid-IR wavelength regime.

The discovery of gamma-ray emission from 1ES 1101-232, one of the most distant blazars, by the H.E.S.S collaboration yielded a well-measured energy spectrum up to 5 TeV. However, Aharonian et al. (2006b) found that the resulting upper limit to the EBL at optical/NIR wavelength lies very close to the lower limit given by the integrated light of resolved galaxies. The observed and the absorption-corrected spectrum are shown in Figure 2.13(a) by red squares and blue squares, respectively. The de-absorbed spectra are calculated from the EBL spectrum given in Figure 2.13(b), where P1.0, P0.55, and P0.55 correspond to the scaling factor applied to the EBL intensity by 100%, 55%, 45%, respectively. While P1.0 agrees with the EBL spectrum expected from galaxy emission (Primack et al., 2005), above derivation of the constraints to the EBL assumes that the intrinsic emission spectra of TeV blazars ($dN/dE \sim E^{-\Gamma}$) can not be any harder than 1.5. Consequently, the absorption-corrected energy spectrum of 1ES 1101-232 results in an "unusual" spectrum, i.e., $\Gamma < 1.5$ if the base spectral shape is scaled by any factor over 45%. Aharonian et al. (2006b) further concludes that any EBL scenario that includes all the NIR excess (Section 2.3) results in an unusual spectrum implying that the totality of the NIR can not be attributed to extragalactic origin alone.

In this section, we combine the recent estimate of the contribution of galaxies to the 3.6 μm intensity of the EBL with optical-NIR galaxy counts to set new limits on intrinsic spectra of some of the most distant TeV blazars, 1ES 0229+200, 1ES 1218+304, and 1ES 1101-232. The new lower limit on the 3.6 μm EBL flux is significantly higher than the previous ones set by the cumulative emission from resolved *Spitzer* galaxies. More importantly, revised EBL models derived from the limit on the 3.6 μm EBL intensity implies that the de-absorbed intrinsic spectra of the three blazar is 1.28 ± 0.20 or harder. Therefore, results based on our analysis question the reliability of recently derived upper limits on the NIR EBL intensity by Aharonian et al. (2006b) that are solely based on the assumption that intrinsic spectra should not be harder than 1.50. This work, conducted in collaboration with Frank Krennrich [4] and Eli Dwek [5], has been published in Krennrich et al. (2008).

2.7.1 Assumed theoretical limits on blazar emission models

The electromagnetic continuum spectra of blazars span many orders of magnitude from radio frequencies to muti-TeV energies. The non-thermal emission from blazar is typically characterized by two pronounced peaks in νF_ν representation of the observed spectra. The low energy peak, located between the IR and hard X-ray wavelengths is thought to arise from

[4]Dept. of Physics and Astronomy, Iowa State University, Ames, IA 50011
[5]NASA Goddard Space Flight Center, Greenbelt, MD 20771

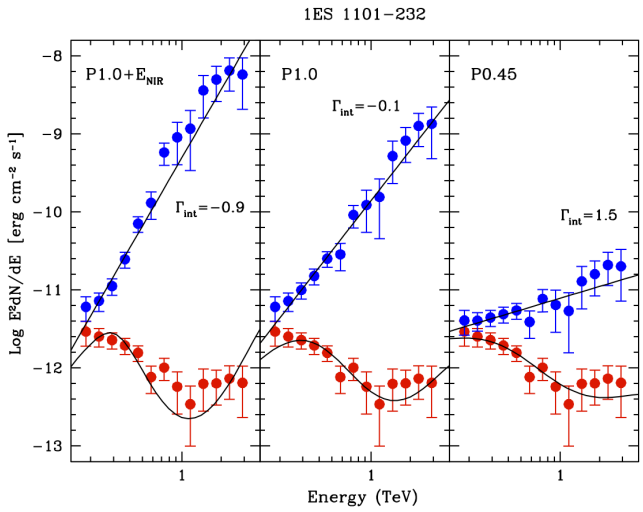

(a)

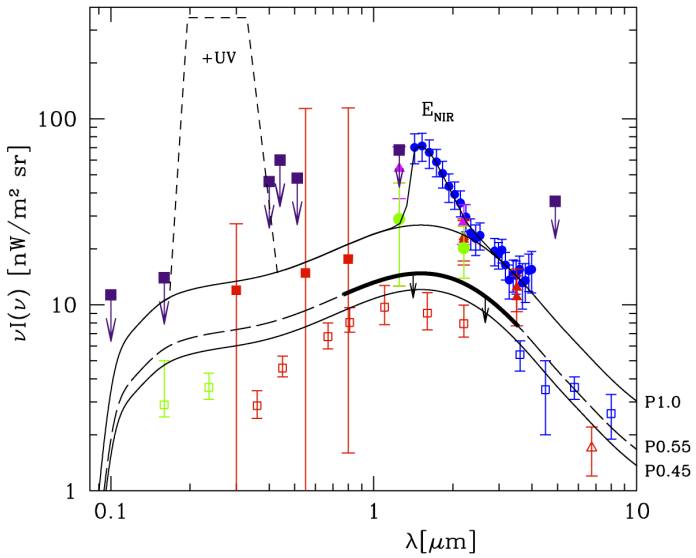

(b)

Figure 2.13 (a) The observed (*red*) and de-absorbed (*blue*) spectra of 1ES 1101–232 (Aharonian et al., 2006b). See text for The three different EBL scenarios used to unfold the intrinsic spectrum. The solid lines show best power-law fits to the spectra. (b) Limits on the SED of the EBL used in previous figure. The data points correspond to a compilation of direct measurements of the EBL (see for example Section 2.3). Note that the open symbols correspond to the integrated light from galaxy counts, and thus must be considered lower limits for the EBL. The curves show the EBL shapes used to reconstruct the intrinsic spectra in earlier figure where P1.0, P0.55, and P0.45 are the absolute normalization of the assumed EBL intensities. The thick line shows the range most effectively constrained by the HESS data. The short dashed line shows the additional UV component needed by P1.0 to obtain a "physical" intrinsic spectrum with spectra index no harder than Γ_i=1.5

synchrotron emission of ultrarelativistic electrons. The fast moving electrons are generated as a result of accelerated shocks moving along the jet at relativistic bulk speed. While the origin of the high energy peak at MeV to TeV energies is still being worked out, a generally accepted argument attributes the highest energy emission to IC upscattering of low-energy photons by electrons (leptonic model). The presence of the low-energy seed photons may be explained by synchrotron emission from the same population of electrons (synchrotron self Compton (SSC model, e.g.,) Maraschi et al., 1992) or an ambient thermal photon field (external IC models, e.g., Dermer & Schlickkeiser, 1994). Alternative emission scenarios involve hadronic interactions of highly relativistic jet outflow with ambient matter (Dar & Laor, 1997), proton-induced cascades producing neutral pions which decay into photons (Mannheim & Biermann, 1992) and proton synchrotron radiation (Aharonian, 2000).

In this general leptonic model for emission, the ultra high energy population of electrons are Fermi-accelerated with a differential particle spectrum of the form $dN/dE \sim E^{-\alpha}$, where the spectral index α is about 2. Based on rapid radiative cooling time of high energy electrons compared to the electrons at lower energies, the exponent α may be larger than 2 whereas current theories are challenged to produce an electron spectrum harder than 2. For a given particle spectrum of electrons, it is straightforward to evaluate the resulting synchrotron energy spectrum (Shu, 1991). The photon index of the synchrotron spectrum ($dN/dE_{sc} \sim E_{sc}^{\Gamma}$) is given by $\Gamma = \frac{\alpha+1}{2} = 1.5$. Moreover, this relation is identical for the energy spectrum of the IC photons on account of the close relation between the electron energy and the IC radiation. In fact, the IC emission spectrum is independent of the origin of the target photons if the scattering occurs in low-energy Thomson regime and the photon index increases (i.e. $\Gamma > 2$) in the Klein-Nishina regime (Raue, 2007). Therefore, the characteristic emission spectra of the VHE gamma rays due to IC upscattering is limited to a photon index of 1.5 or larger.

The photon index for the case of VHE gamma-ray emission via π^0 decay of high energy protons are complicated by the details of the underlying particle interaction. However, in this hadronic scenario, the resulting gamma-ray spectrum will generally follow a power-law distribution with $\Gamma = 4/3(\Gamma_p - 1)$ (e.g., Weekes, 2003), assuming a similar power-law distribution of protons with a spectral index of Γ_p. Hence, assuming a reasonable proton number distribution with $\Gamma_p \sim 2.5$, the observed VHE gamma-ray spectrum yields a photon index close to or above 2.

Subsequently, a number of recent studies (Aharonian et al., 2006b; Albert et al., 2007d) have attempted to constrain the EBL density based on the arguments that intrinsic photon index of TeV blazars can not be any harder than 1.5. In the proceeding sections, we derive a firm limit to the hardness of the energy spectra of some of the most distant TeV blazars. Our result for the intrinsic spectra of blazars is entirely based on observational data and therefore leads to much stronger constraints. Most importantly, our calculations indicate that the differential spectral index of the intrinsic spectrum of blazars can be harder than 1.5, thus

severely challenging the conventional blazar emission models discussed above.

2.7.2 Recent lower limits on EBL from galaxy counts

One of the "conventional" contributors to the EBL density is the emission of light from stars and galaxies. Experimental attempts to directly measure the EBL photons– particularly in the near and mid-IR wavelengths are greatly influenced by the presence of strong foreground emission from stars and dust within our own galaxy. Due to the challenge in distinguishing EBL from the generally brighter foreground, direct measurements are often plagued with large systematic uncertainties (Kashlinsky, 2005). The total flux from galaxies measured in deep count surveys provide yet another measure of the EBL density. Consequently, our knowledge of the EBL spectrum consists mostly of strict lower limits derived from ground- and space-based galaxy counts.

We have already established that the observed TeV spectra of blazars contain emission characteristics of the source convolved with the absorption due to the EBL in the NIR and MIR regions. Figure 2.15 presents the galaxy counts measured now to fairly faint limits at 0.36, 0.45, 0.67, 0.82, 1.1, 1.6, and 2.2 μm with observations coming from ground and Hubble Space Telescope observations (*filled triangles*). These data come from compilations summarized in Madau & Pozzetti (2000, labeled MP00 hereafter). The figure also shows the contributions to the EBL flux from faint galaxies at 3.6, 4.5, 5.8, and 8.0 μm (*open sqaures*) from three recent *Spitzer* IRAC surveys reported by Fazio et al. (2004) covering 3 independent fields with deep exposures extending up to $\sim$ 9 hours. Metcalfe et al. (2003) used ISOCAM observations of nearly 1000 galaxies at 15 μm to estimate the contribution to the EBL at that wavelengths from sources as faint as 30 μ Jy (*open circle*). Finally, *Spitzer*/MIPS 24 μm channel data has very good mid-IR resolution, allowing Papovich et al. (2004) to derive lower galaxy number counts from the *Spitzer* deep surveys (*diamond*) and probe a previously undetected population of very luminous galaxies at high z.

Table 2.3 provides a compilation of previous determination of the EBL at 3.5 and 3.6 μm from both direct measurements and galaxy counts. It is apparent that the direct determination of the EBL differ from the lower limits by as much as 2σ. In order to investigate this discrepancy, Levenson & Wright (2008) recently used *Spitzer* observations to estimate the EBL intensity at 3.6 μm. Furthermore, they employed a profile-fit photometry method to include light from faint fuzzy fringes to the total contribution of resolved galaxies. As a direct consequence of this work, Levenson & Wright (2008) reported an increase in the 3.6 μm lower limit from 5.4 to $9.0^{+1.7}_{-0.9}$ nW m^{-2} sr^{-}. This correction has brought the galaxies' contribution to the EBL to within $\sim 1\sigma$ of the EBL intensity determined from measurements made with the *COBE* satellite (Dwek & Arendt, 1998). In the following analysis, we treat the constraint by Levenson & Wright (2008, hereafter LW08) purely as a lower limit to the EBL at 3.6 μm.

We note the determination of the EBL intensities at shorter wavelengths may be underesti-

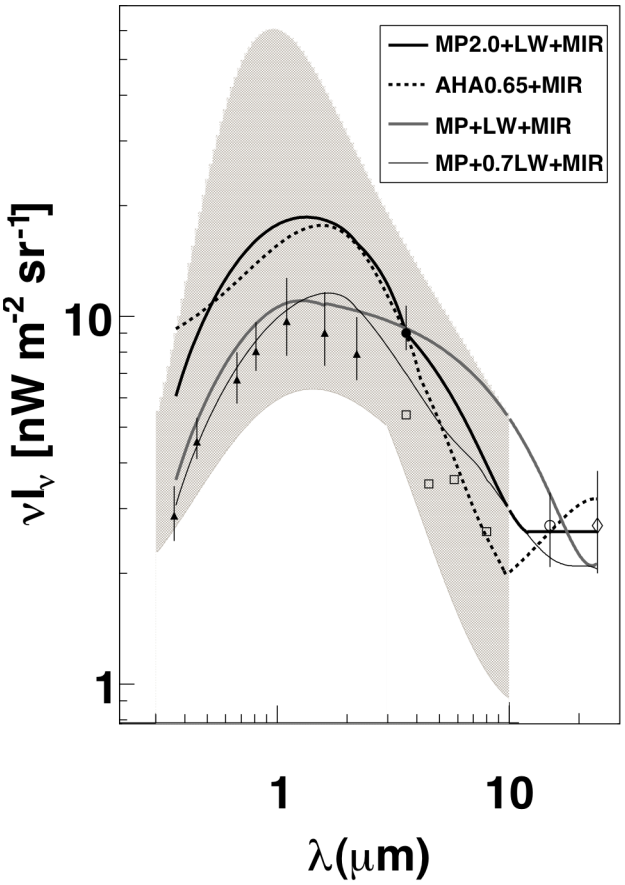

Figure 2.14 Selected EBL scenarios to find the softest possible intrinsic spectrum.

mated if the contributions from resolved galaxies do not account for faint fringes. As a result, similar profile-fitting techniques may apply to the calculation of total contribution from galaxies to the EBL via standard aperture photometry (Bernstein et al., 2002; Wright, 2001; Yoshi, 1993; Bernstein et al., 2007). This implies that the previously reported galactic contribution to the EBL could therefore be higher than the reported lower limits of MP00. Consequently, the new lower limit at 3.6 μm combined with possible higher limits at shorter wavelengths will produce increased attenuation for gamma-ray spectra at TeV energies and thus harder intrinsic spectra.

Table 2.3 Determinations of EBL at 3.5 and 3.6 μm [Adapted from Levenson & Wright (2008)]. Foreground subtracted intensities were measured in the DIRBE 3.5 μm band. Galaxy count intensities were measured in the *Spitzer* 3.6 μm band. These results do not distinguish between these almost identical wavelength bands.

Reference	EBL ($\mathrm{nW\,m^{-2}\,sr^{-1}}$)	Zodiac-Model
Dwek & Arendt (1998)	9.9 ± 2.9	Kelsall et al. (1998)
Gorjian et al. (2000)	11.0 ± 3.3	Wright (1998)
Wright & Reese (2000)	12.3 ± 3.2	Wright (1998)
Wright & Johnson (2001)	13.8 ± 3.4	Wright (1998)
Matsumoto et al. (2005)	14.5 ± 3.0	Kelsall et al. (1998)
Levenson & Wright (2007)	13.4 ± 2.8	Wright (1998)
Fazio et al. (2004)	> 5.4	N.A. (galaxy counts)
Levenson & Wright (2008)	$9.0^{+1.7}_{-0.9}$	N.A. (galaxy counts)

2.7.3 Sample of blazars with hard intrinsic spectra

We use the new lower limit at 3.6 μm to derive a range of possible intrinsic spectral indices of TeV blazars. Our goal is to use observational results to test the previously postulated theoretical paradigm, that the intrinsic spectra of blazars characterized by an energy spectrum of the form $\mathrm{dN/dE} \propto \mathrm{E}^{\Gamma}$ in the TeV regime can not exceed the hardness of $\Gamma_i = 1.5$. Given the limited availability of blazar spectra at TeV energy at sufficiently high redshift necessary for substantial absorption, we select the energy spectra of 1ES 1218+304 (Albert et al., 2006a) detected over the 0.08–0.7 TeV range along with the recent observations by VERITAS over an energy range of 0.18–1.5 TeV (Acciari et al., 2009a). We use the VERITAS spectrum since it extends to higher energies compared to that of MAGIC. We also consider the spectra of 1ES 1101–232 (Aharonian et al., 2006b) detected over the 0.18–2.9 TeV range, and 1ES 0229+200 (Aharonian et al., 2007c) detected over 0.16–11.5 TeV range.

It should be noted that 3C 279, the most distant blazar at a redshift of 0.536, has been observed by the MAGIC collaboration (Albert et al., 2008) over a limited spectral range from 0.08–0.485 TeV, and associated with considerably larger statistical uncertainties compared to the three blazars mentioned in the previous paragraph. Other blazars with adequately measured energy spectra are 1ES 1101+496 (Albert et al., 2007c) and 1ES 0347–121 (Aharonian et al., 2007b) with redshifts of $z = 0.212$ and 0.188, respectively. The measured spectra of 1ES 1101+496 is found to be extremely soft, with $\Gamma = 4.0 \pm 0.5$, and therefore not suitable in the search for a limit to the hardness of blazar spectra. On the other hand, the measured spectral index of 1ES 0347–121, $\Gamma = 2.10 \pm 0.23$, is slightly softer than 1ES 1101–232 and

covers essentially the same energy range, rendering it redundant. As a result, we restrict our selection of blazars primarily to 1ES 1218+304, 1ES 1101–232, and 1ES 0229+200. This set of three blazars constitute a representative sample of the most distant, well-measured blazar spectra that covers a wide range of energies where the data is obtained from three independent gamma-ray observatories (VERITAS, MAGIC and H.E.S.S). From our discussions earlier, the cross section for the $\gamma - \gamma$ interaction peaks at energies $\lambda_{\rm IR}[\mu{\rm m}] = 1.33\,{\rm E[TeV]}$. Hence, on account of the varying range of energy coverage, the intrinsic spectrum of each blazar will be constrained by different spectral regions of the EBL, thus allowing us to probe the intrinsic hardness of blazar spectra over a wide range of energies.

2.7.4 New limits on intrinsic blazar spectra

In this study, the unfolded intrinsic spectra of TeV blazars are derived by de-absorbing the measured energy spectra with a wide range EBL intensities, as shown in Figure 2.14 (*shaded region*). The variety of explored scenarios correspond to the Dwek & Krennrich (2005) parameterization of the EBL presented in Section 2.6.2. The lower limits from galaxy counts restrict the possible EBL density as a function of wavelength. However, the upper limits to the EBL are somewhat arbitrary since uniformly higher intensities will produce even harder intrinsic spectra and therefore are not relevant in to this study. The shaded area also correspond to the EBL densities that are most sensitive to the blazar energy spectra in question.

The EBL spectrum presented in Aharonian et al. (2006b), AHA, is also included in our study. This curve was constructed based on the general assumption that the EBL cannot be much higher than the previously determined lower limits from galaxy emission and therefore normalized to match the direct estimates of 26, 25, and 14 nW m^{-2} sr^{-1} at 1.25, 2.2, and 3.5 μm, respectively. Additionally, the normalization of the absolute EBL intensity (in νI_ν) is left as a free parameter to widen the range of possible EBL scenarios such that the scaling factor follows the name of the EBL model. Thus, AHA0.65 corresponds to AHA scaled by a factor of 0.65 to fit the $9.0^{+1.7}_{-0.9}$ nW m^{-2} sr^{-1} value at 3.6 μm reported by Levenson & Wright (2008). Finally, we also consider the effects on the intrinsic spectra resulting from lower limits at 15 and 24 μm. These scenarios are denoted by the suffix "MIR". Figure 2.14 illustrates the different EBL spectral slopes explored between the near-IR and mid-IR wavelengths. Hence, the MP + LW + MIR and the MP2.0 + LW + MIR show two different spectral sloples while both spectra intersect with the lower limits at 3.6 μm. The MP + 0.7LW + MIR scenario is also shown which falls substantially below the lower limit at 3.6 μm. Note that Figure 2.14 represents only a limited set of the explored scenarios, the ones that are most relevant to our investigation.

The resulting de-absorbed gamma-ray spectral indices Γ_i, for power-law fits to the unfolded energy spectra of 1ES 1101–232, 1ES 1218+304, and 1ES 0229+200 for a range of EBL scenarios are presented in Table 2.4. The scenarios marked with an asterisks represent EBL models

Table 2.4 Intrinsic spectra of 1ES 1101–232, 1ES 1218+304, and 1ES 0229+200 for competing EBL scenarios. Note that many scenarios contain a suffix that represents a scaling factor νI_ν. Also, scenarios marked with an asterisk are inconsistent the lower EBL limits.

	$\Gamma_{intrinsic}$		
Scenario	1ES1101	1ES1218	1ES0229
AHA0.45*	1.78 ± 0.20	1.86 ± 0.37	2.43 ± 0.13
LLH*	2.01 ± 0.22	2.07 ± 0.35	2.12 ± 0.20
LHL *	2.04 ± 0.20	2.08 ± 0.39	0.94 ± 0.32
LHL0.76*	2.23 ± 0.21	2.32 ± 0.37	1.30 ± 0.29
MHL0.70 *	1.26 ± 0.19	1.34 ± 0.36	1.35 ± 0.21
MP+0.7+MIR*	1.80 ± 0.21	1.82 ± 0.38	1.43 ± 0.16
LLL*	2.06 ± 0.16	2.20 ± 0.34	2.11 ± 0.20
HHH	-0.67 ± 0.12	-0.72 ± 0.29	0.90 ± 0.17
LLL2.4	1.10 ± 0.17	1.12 ± 0.34	1.67 ± 0.19
MHL1.10	0.40 ± 0.20	0.33 ± 0.36	0.70 ± 0.19
AHA0.65	1.28 ± 0.20	1.30 ± 0.38	2.40 ± 0.13
LHL1.25	1.85 ± 0.24	1.83 ± 0.40	0.59 ± 0.34
AHA0.65+MIR	1.29 ± 0.20	1.31 ± 0.38	1.70 ± 0.15
MP+LW+MIR	1.87 ± 0.22	1.77 ± 0.42	1.01 ± 0.17
MP2.0+LW+MIR	1.18 ± 0.20	1.20 ± 0.38	1.53 ± 0.15

that fall far below the galaxy counts, e.g., LLL case, and thus they are not viable. However, these templates serve to illustrate the dependence of the spectral indices on varying EBL scenarios. The models compatible with the galaxy count lower limits are given in the two lower sections of Table 2.4 (separated from the upper section by a double line). Finally, we show three additional scenarios (below the single line in Table 2.4) that takes into account lower EBL limits from galaxy counts at 15 and 24 μm. Therefore, the AHA0.65+MIR corresponds to the standard AHA0.65 scenario up to 10 μm with an additional MIR component consistent with lower limits. The MP+LW+MIR scenario is based on a fit through the MP00 data, the W08 data point, and the MIR data. The MP2.0+LW+MIR differs from the last case by its level in the near-IR with the MP00 values scaled up by a factor of 2.

The general strategy for finding a limit to the intrinsic spectra of the three selected blazars based on the EBL scenarios involves determining the hardest spectral index that any of these blazars show for a given EBL scenario. Afterwards we search for the EBL model that allows for the softest spectrum for the blazars. Since the selected blazars constrain the EBL in different wavelength regimes, therefore the combination of the three, simultaneously probing different EBL scenarios in the near-IR to mid-IR provides the strongest constraint to intrinsic spectra

of blazars. For example, when just considering 1ES 1218+304 by itself, its softest intrinsic spectrum among all EBL scenarios that obey galaxy count limits is described by a power law with an index $\Gamma_i = 1.83 \pm 0.40$ and corresponds to the LHL1.25 scenario. However, for the same scenario, the spectrum of 1ES 0229+200 would be extremely hard with a power law index of $\Gamma_i = 0.59 \pm 0.34$. Therefore, by searching for the combination of intrinsic spectra of these three sources that yield the softest spectral indices, one finds that the AHA0.65 scenario gives a spectral index of $\Gamma_i = 1.28 \pm 0.20$ for 1ES 1101–232, $\Gamma_i = 1.30 \pm 0.38$ for 1ES 1218+304, and $\Gamma_i = 2.40 \pm 0.13$ for 1ES 0229+200. The spectral index of $\Gamma_i = 1.28 \pm 0.20$ corresponds to the least hard spectral index of all EBL scenarios (*shaded region* in Figure 2.14) compatible with the lower limits. In other words, any other EBL scenario consistent with the lower limits from the galaxy counts results in any one of the three blazar to be harder than $\Gamma_i = 1.28 \pm 0.20$. Therefore, the lower limit at 3.6 μm by Levenson & Wright (2008) is an important constraint to the intrinsic spectra of blazars.

We also considered the contribution of an MIR component consistent with the 15 and 24 μm constraints but it does not have a significant impact on the result. Finally, we show the absorption-corrected energy spectra of 1ES 0229+200, 1ES 1218+204, and 1ES 1101–232 for the AHA0.65 scenario in Figure 2.15. Note the latter two spectra have been scaled in absolute flux for clarity.

Analysis of observational VHE data combined with a new lower limit to the EBL density at 3.6 μm provides a firm evidence that the intrinsic energy spectra of individual TeV blazars are extremely hard, exhibiting spectra with an index of $\Gamma_i = 1.28 \pm 0.20$ or harder. Moreover, the power-law indices of the blazar spectra of 1ES 1101-232, 1ES 1218+304 are well measured between gamma-ray energies of 0.18–3 TeV considering the statistical uncertainties associated with the corresponding measurements. Following Equation 2.5, the above energy range implies that the two spectra are mostly sensitive to the EBL densities between 0.2 and 4 μm. Similarly, the spectral range of 1ES 0229+200 between 1 and 4 TeV makes it sensitive to 1.3–13.3 μm. Therefore, simultaneous application of EBL scenarios to blazar spectra yields complementary spectral constraints with two over-lapping EBL regions. This combined with the new lower limit at 3.6 μm leads to much stronger and unambiguous constraints to the intrinsic spectra than any previous study.

Furthermore, consideration of faint and fuzzy fringes of resolved galaxies at shorter wavelengths may result in higher estimates for lower limits from MP00. If MP00 is scaled up by a factor as large as 2, then MP2.0+LW+MIR may be a more realistic EBL scenario. In such a case, the resulting intrinsic spectrum for 1ES 1101–232 is slightly harder with an index of $\Gamma_i = 1.18 \pm 0.20$ and none of the blazar spectra is softer than $1.29 \pm .20$ (AHA0.65+MIR). Consequently, our results based on the new lower limit of EBL poses a significant challenge to standard models of blazar emission that limits the hardness of intrinsic spectra to $\Gamma_i = 1.5$ or higher.

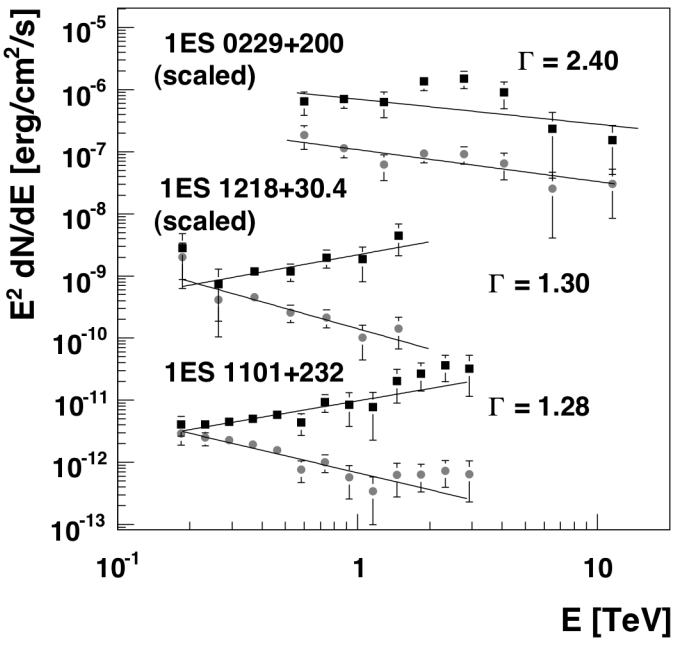

Figure 2.15 Shown are the measured (filled circles) and absorption corrected (filled squares) energy spectra of 1ES 1101-232 (Aharonian et al., 2006b), 1ES 1218+30.4 (Acciari et al., 2009a), and 1ES 0229+200 (Aharonian et al., 2007c) using the AHA0.65 EBL. Note that the latter two have been scaled in absolute flux for clarity. The intrinsic spectra of 1ES 1101+232 and 1ES 1218+30.4 are extremely hard, with G smaller than the limiting value of 1.5.

2.7.5 Hard spectra blazars

To date, blazars detected at VHE energies are predominantly high-frequency peaked BL Lacertae objects (HBLs). Nevertheless, a few objects with lower peak energies, namely low-frequency-peaked BL Lacertae (LBLs) (Albert et al., 2007d; Teshima et al., 2008) and intermediate-frequency-peaked BL Lacertae objects (IBLs) (Acciari et al., 2008a,b, 2009b; Ong et al., 2009a) were detected recently by IACTs at TeV energies. The gamma-ray luminosity of LBLs and IBLs generally peaks at sub-GeV to tens of GeV in energy and they are therefore easily detectable by Fermi while their detectability in the TeV regime by IACTs is more difficult due to their soft VHE spectra.

Among the HBLs, which are typically the domain of the TeV telescopes, a number of objects exhibit unusually hard intrinsic power law energy spectra ($dN/dE \sim E^{-\Gamma_i}$) after correcting for the $\gamma\,\gamma \;\rightarrow\; e^+\,e^-$ absorption by the cosmological diffuse EBL radiation field. While the

measured spectral indices, Γ_m, of these blazars (1ES 1101-232, 1ES 0347-121, 1ES 0229+200, 1ES 1218+304, RGB J0710+591) range from 2.5 to 3.1 (see Aharonian et al., 2006b, 2007c,b; Albert et al., 2006a; Acciari et al., 2009a; Perkins et al., 2007), the absorption-corrected spectral indices suggest very hard intrinsic source spectra in the VHE regime with $\Gamma_i \leq 1.28 \pm 0.28$ (Krennrich et al., 2008), based on recent lower limits to the EBL from galaxy counts (Levenson & Wright, 2008).

Similar hard energy spectra are found by Fermi, where, for example, the measured spectral indices for RGB J0710+591 and 1ES 1440+122 are found to be $\Gamma = 1.21 \pm 0.25$ and 1.18 ± 0.27 over energies from 0.2 GeV to tens of GeV (Abdo et al., 2009a). While the findings of very hard VHE spectra are based on EBL constraints from galaxy counts, the Fermi spectra directly resemble the intrinsic source spectra since absorption by the EBL is minimal for the covered energy range. The photon spectrum of 1ES 1218+304 measured by Fermi yields a spectral index of $\Gamma = 1.63 \pm 0.12$ between 0.2 GeV and ∼300 GeV, but absorption may already play a role at the high energy end (Abdo et al., 2009a).

Diffusive shock-acceleration theory, (for a review see Malkov & Drury, 2001), generally yields a limit to the spectral index of GeV to TeV photon spectra resulting from inverse Compton scattering of $\Gamma_i \geq 1.5$. Only recently, numerical studies by Stecker et al. (2007) indicate that sufficiently hard electron spectra could be generated by diffusive shock acceleration in relativistic shocks, for the production of photon spectra $1.0 < \Gamma_i < 1.5$. However, Böttcher et al. (2008) suggest that even for a hard-spectrum electron population, in the framework of a synchrotron self-Compton (SSC) scenario, the resulting GeV-TeV gamma-ray spectra should experience substantial softening from Klein-Nishina effects making gamma-ray spectra with $\Gamma_i < 1.5$ less likely.

Other approaches to explain the hard gamma-ray spectra are offered by ad hoc assumptions about the electron distribution, an additional absorption component in the source, or a postulate of new physics describing the propagation of gamma-rays on extragalactic distance scales. Katarzyński et al. (2006) invoke a high low-energy cutoff in the electron distribution that could give the appearance of a hard gamma-ray spectrum for a given energy regime. Aharonian et al. (2008) show that $\gamma\gamma$ absorption in the source due to a narrow-band emission component from the AGN could lead to unusually hard VHE spectra. Finally, Sánchez-Conde et al. (2009) suggested an axion like particle (ALP) that would distort the gamma-ray spectrum through ALP/photon mixing on cosmological distances in the presence of intergalactic magnetic fields.

A more easily testable model that involves known physics was recently proposed by Böttcher et al. (2008). The authors attribute the hard photon spectra to inverse-Compton up-scattering of ambient photons from the cosmic microwave background (CMB), occurring in a kiloparsec-scale jet. In this case, a substantial fraction of the jet power is transported by hadrons to the outer regions of the jet, where it is dissipated into ultra-relativistic electrons. Inverse Compton scattering in the Klein-Nishina regime is no longer the limitation at the highest

energies since low-energy target photons from the CMB are abundant. The low magnetic field in the large-scale jet also avoids an overproduction of synchrotron radiation and allows Compton emission to dominate. Furthermore, the synchrotron emission in the radio to X-ray wavebands is assumed to originate on sub-parsec scales. A similar mechanism was previously suggested to explain the hard X-ray spectra observed from the kiloparsec-scale jets of radio quasars (Tavecchio et al., 2007).

To date, all of the blazars exhibiting very hard spectra appear to emit at a baseline level that is consistent with this picture. However, it is also possible that the sensitivity of the current IACTs is the limiting factor in detecting day-scale variations, and that the underlying emission may contain flares. The question as to whether or not the gamma-ray emission from 1ES 1218+304 consists of flares or corresponds to a constant baseline emission level was one of the main motivations for VERITAS to monitor this object over a period of five months in the 2008/2009 season. The other motivation for deep exposures of relatively large redshift ($z = 0.1 - 0.2$) blazars at TeV energies is to provide better constraints on the EBL spectrum. The observed VHE photon spectrum can be used to constrain the EBL in the near to mid-IR. This is particularly promising for hard-spectrum blazars that provide the best sensitivity to any possible absorption feature.

CHAPTER 3. THE IMAGING CHERENKOV TECHNIQUE

The Earth is being constantly bombarded with cosmic ray particles and gamma-ray photons. However, the earth's atmosphere effectively blocks all electromagnetic radiation of energies greater than a few eV (Figure 3.1). Thus, the limited transmission probability of the atmosphere hampers the direct detection of high-energy electromagnetic radiation from the ground. While satellite experiments offer a viable alternative to directly measuring the gamma-ray radiation in space, the exponentially decreasing flux of gamma-ray photons together with the limited collection area of space-borne instruments restricts the effectiveness of this approach to detect a significant number of gamma-rays in a reasonable time scale. Fortunately, the ground-based Imaging Atmospheric Cherenkov technique has proven to be the most promising method in the recent decade for detecting gamma-ray above tens of GeV. Using the atmosphere as a giant calorimeter, this novel technique employs the detection of Cherenkov light emitted as a consequence of the interaction between primary gamma-ray photons (or charged cosmic ray particles) and the atmosphere. This section (very) briefly introduces the physics behind this interaction process and the subsequent production of Cherenkov light. Later, I outline the concept of the Imaging Atmospheric Cherenkov technique in the context of a specific instrument, the VERITAS telescopes that makes use of this technique.

3.1 Extended Air Showers

When a VHE particle (cosmic rays or gamma rays) strikes the earth's upper atmosphere, the kinetic energy of the primary particle is deposited in the atmosphere through interaction with atmospheric nuclei. The first interaction typically occurs at an altitude between 15-20 km above sea level (a.s.l). For a primary particle with energy greater than a few GeV, collision with the atmosphere creates a secondary particle which in turn interacts with the atmosphere to generate tertiary particles and so on, resulting in a cascade of particles. This avalanche of particles, also known as *extended air shower* (EAS), develops in the atmosphere as a function of the primary energy and highly depends on the various loss mechanisms governing the interaction of particles.

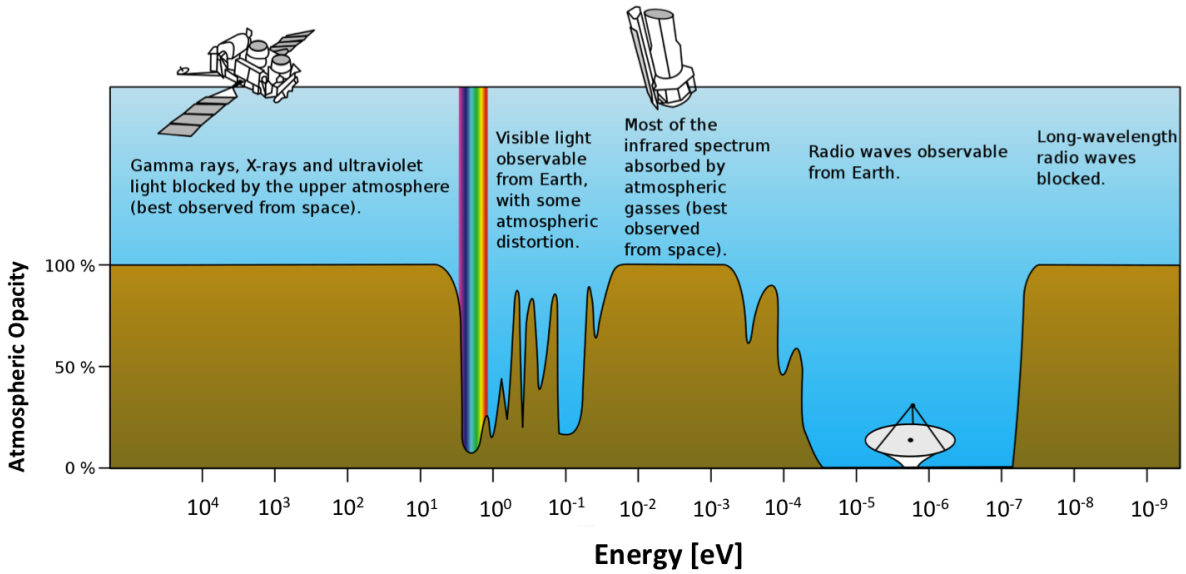

Figure 3.1 Limited transmission probability of the earth's atmosphere at different energies [adapted by the author]. *Credit*: NASA

3.1.1 Development of air showers

In the case of primary gamma-rays, the predominant interaction mechanisms that lead to the development of EAS in the atmosphere are pair-production and bremsstrahlung while cosmic ray particles (mainly charged protons) undergo hadronic interactions producing pions and other nucleon secondaries. In the following, we discuss the two flavors of EAS produced by electrons/positrons and charged cosmic rays, respectively– electromagnetic showers and hadronic showers:

Electromagnetic showers

For gamma-rays of energies greater than 10 MeV, pair-production is the main particle production mechanism as the energetic photons enter the atmosphere. If the photon energy is at least equal to $2m_ec^2$ [1], the photon can decay into an electron-positron pair. However, this process can only take place when photons pass through matter due to consideration for energy and momentum conservation. Subsequently, as the electrons and positrons pass through the atmosphere, they interact with air molecules to produce secondary gamma-ray photons by bremsstrahlung radiation. An energetic charged particle passing through matter will slow down or be deflected on account of the Coulomb field of a nucleus. The deflection or retardation produces bremsstrahlung radiation where the energy loss is proportional to the energy of the charged particles. In addition, energy loss by bremsstrahlung is more significant for electrons

[1] $m_e = 0.511$ keV is the rest mass of an electron.

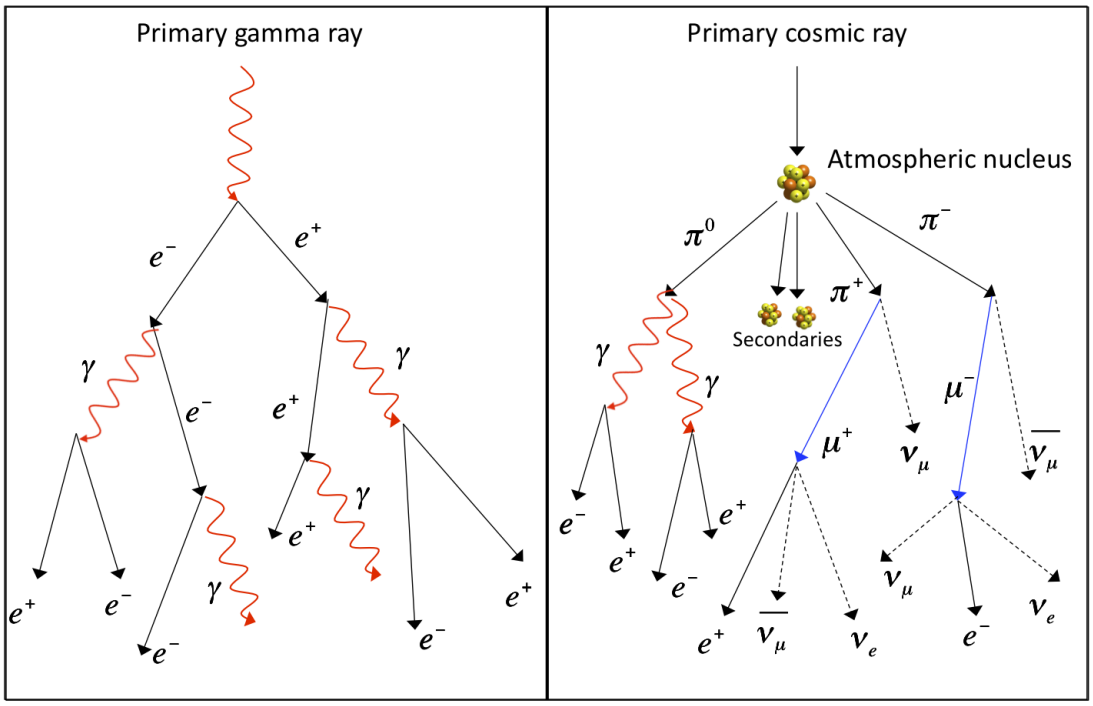

Figure 3.2 A schematic development of cascades in the atmosphere. *Left*: A gamma-ray shower. *Right*: A Cosmic ray shower

(or positrons) compared to protons due to an inverse relationship with the mass of the particle. The resulting radiation is strongly beamed in the direction of the particle. The number of particles in the cascade continues to grow exponentially until the average energy of the particles reach a critical value, $E_c \sim 100$ MeV (in air). If the particle energy falls below E_c, energy loss by ionization begins to dominate losses from bremsstrahlung and the cascade dies out rapidly. At this point in the development of the cascade, commonly referred to "shower maximum", the number of charged particles in the shower is the greatest. The higher the energy of the primary particle, the further the air shower penetrates into the atmosphere. For a typical 100 GeV gamma-ray, the shower maximum occurs at 8-10 km a.s.l. Figure 3.3(a) and 3.3(b) shows the longitudinal distribution of charged particles in the atmosphere initiated by two primary gamma-ray photons: the first shower from a 100 GeV photon dies out before it reaches the ground while local muons in the air-shower from a 1 TeV photon effectively reaches the ground level.

Hadronic showers

In contrast to the purely electromagnetic showers, the shower development for cosmic rays impinging on the earth's atmosphere is dominated by hadronic components produced

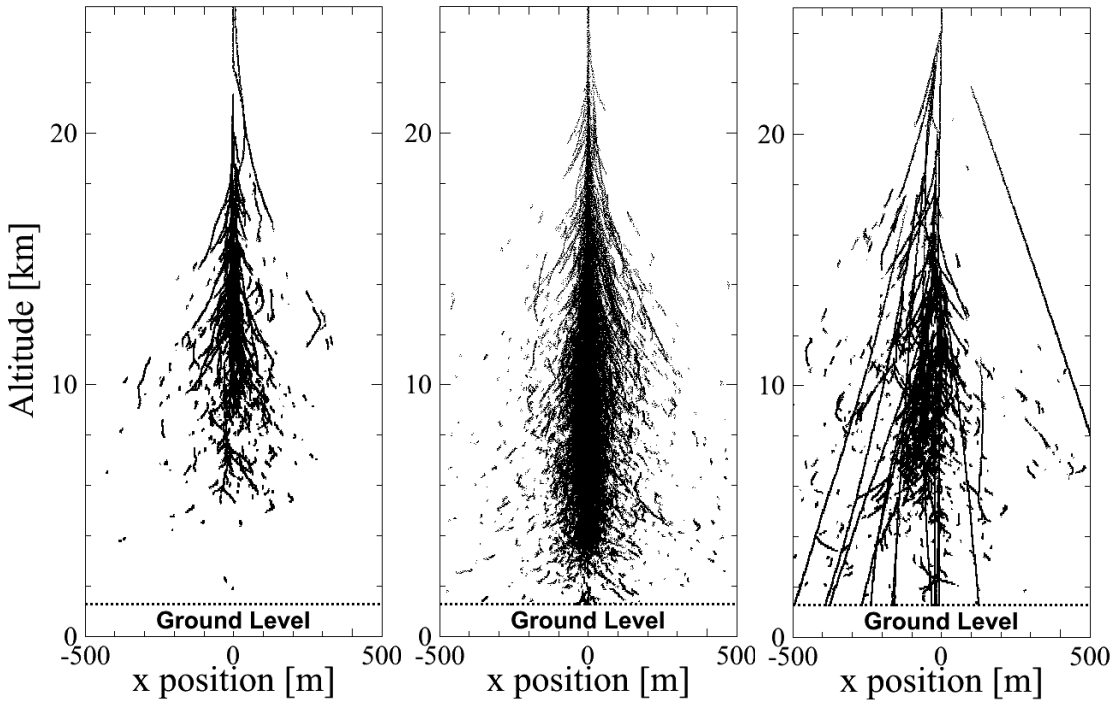

Figure 3.3 Longitudinal profile of the development of electromagnetic and hadronic showers in the atmosphere where the primary particle is a: (a) 100 GeV photon, (b) 1 TeV photon, and (c) 1 TeV proton.

during the interaction with atmospheric nuclei. Regulated by strong interaction forces, the collision between the primary hadrons and particles in the earth's atmosphere mainly produces neutral and charged pions. Other significant end products of hadronic collisions in the core of the cascade include kaons and light baryons such as neutrons and protons. These secondary particles along with fragments of the target nucleus continues to undergo further hadronic interactions until the energy per nucleon reaches the pion production threshold of ($\sim 1GeV$). The neutral pion decays into a pair of gamma-rays ($\pi^0 \rightarrow \gamma\ \gamma$) which then generates an electromagnetic cascade as described above. Each hadronic interaction roughly imparts a third of its energy into the neutral pion. Since most hadrons eventually re-interact, most of the primary energy of the cosmic ray particle is used to replenish the electromagnetic component as the shower develops. On the other hand, the charged pions decay into muon/muon-neutrinos pairs. Muons can either decay into $e^{\pm}\nu\overline{\nu}$ or lose energy by ionization. Due to high initial energy, these secondary muons only lose energy relatively slowly by ionization in the atmosphere, thus they reach the ground without further interaction. As a result, muons make up the most *penetrating* part of the cosmic ray induced cascade.

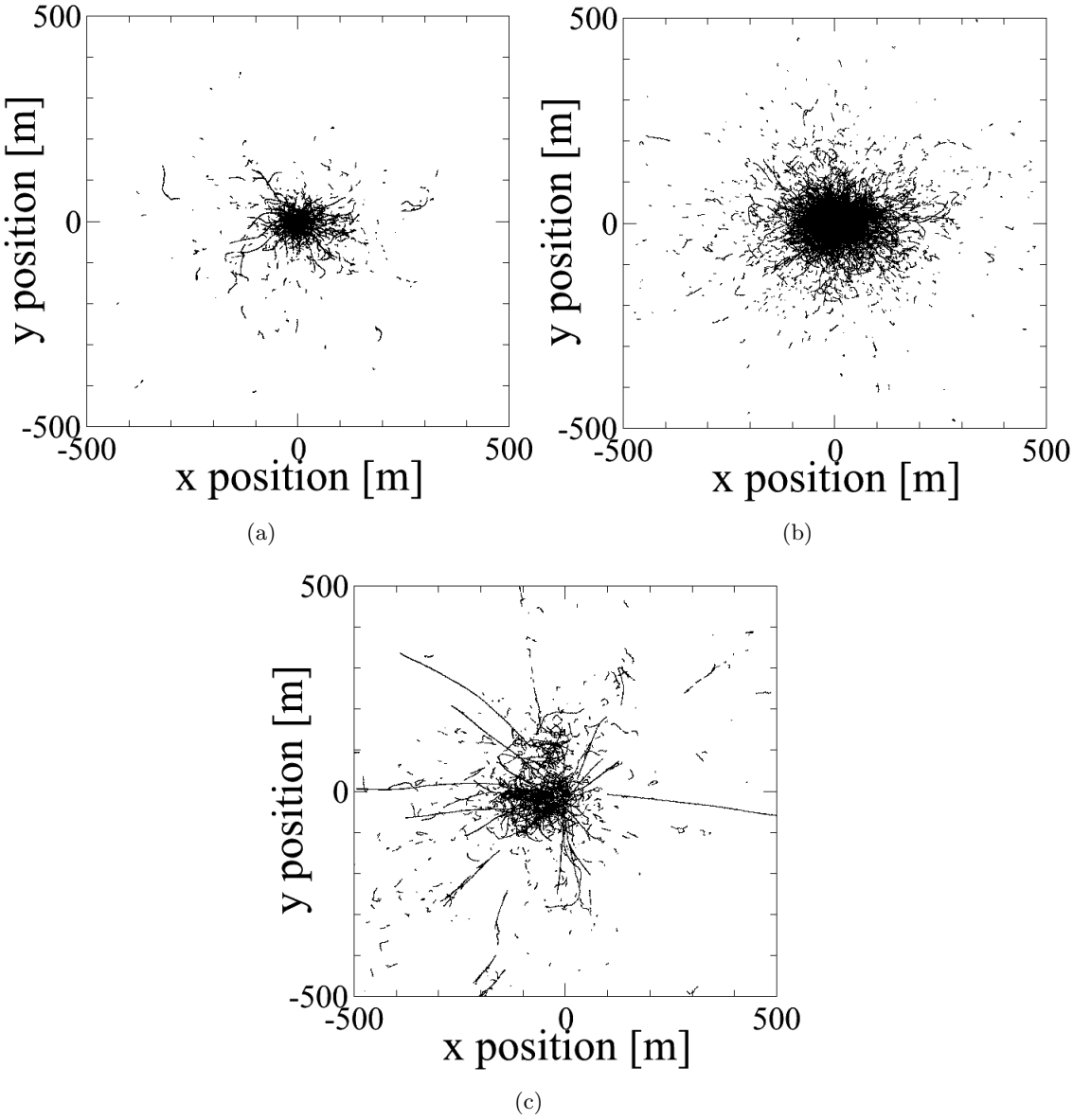

Figure 3.4 Lateral profile of electromagnetic and hadronic showers in the atmosphere where the primary particle is a: (a) 100 GeV photons, (b) 1 TeV photon, and (c) 1 TeV proton.

Difference between hadronic and electromagnetic showers

The longitudinal development and the lateral structure of the hadronic showers are more complex than for the gamma-ray induced showers largely due to the strong interactions involved. However, hadronic showers also contain a strong electromagnetic component as described above. Therefore, the difference between the showers are often difficult to distinguish (Jelly & Porter, 1963). Nevertheless, a suppression of the cosmic ray dominated background based on the difference between the two showers is desired for a successful detection of gamma-ray source in the sky. Here we list a few key difference between the two types of showers:

- The absorption length for hadronic interactions is considerably longer than that for electromagnetic interactions. As a result, hadronic showers are more penetrating and develop deeper into the atmosphere compared to gamma-ray induced showers with comparable primary energies.
- Hadronic interactions impart a larger transverse momentum to secondary particles compared to collisions in electromagnetic cascades. The resulting hadronic cascade is broader and more scattered.
- An important feature of the electromagnetic shower is the rarity of muons compared to an hadronic shower. An electromagnetic shower contains less than 5% of the number of muons in a hadron-induced shower with comparable energy. This arises from a very high probability for a photon to pair-produce electron-positron pair than any other decay channel.
- In strong hadronic interactions, a considerable portion of the energy of the primary particle is fed into muons. Therefore, hadronic showers are typically smaller than those produced by gamma-ray photons of the same energy.
- Due to the various complex, multi-particle scattering processes involved in the development of the hadronic shower and the larger interaction length, hadronic showers are accompanied by larger fluctuations compared to electromagnetic shower.

3.1.2 Cherenkov light emission in the atmosphere

A charged relativistic particle traveling through the atmosphere at a velocity v exceeding the phase velocity of light c in air will emit Cherenkov radiation. As the charged particle traverses through a dielectric medium (in this case *air*), molecules surrounding the particle are polarized. For a relativistic particle, non-uniform polarization of molecules across the medium results in a coherent and constructive interference of electromagnetic wave or Cherenkov light (Frank & Tamm, 1937). The resulting Cherenkov light is beamed on a narrow cone at a

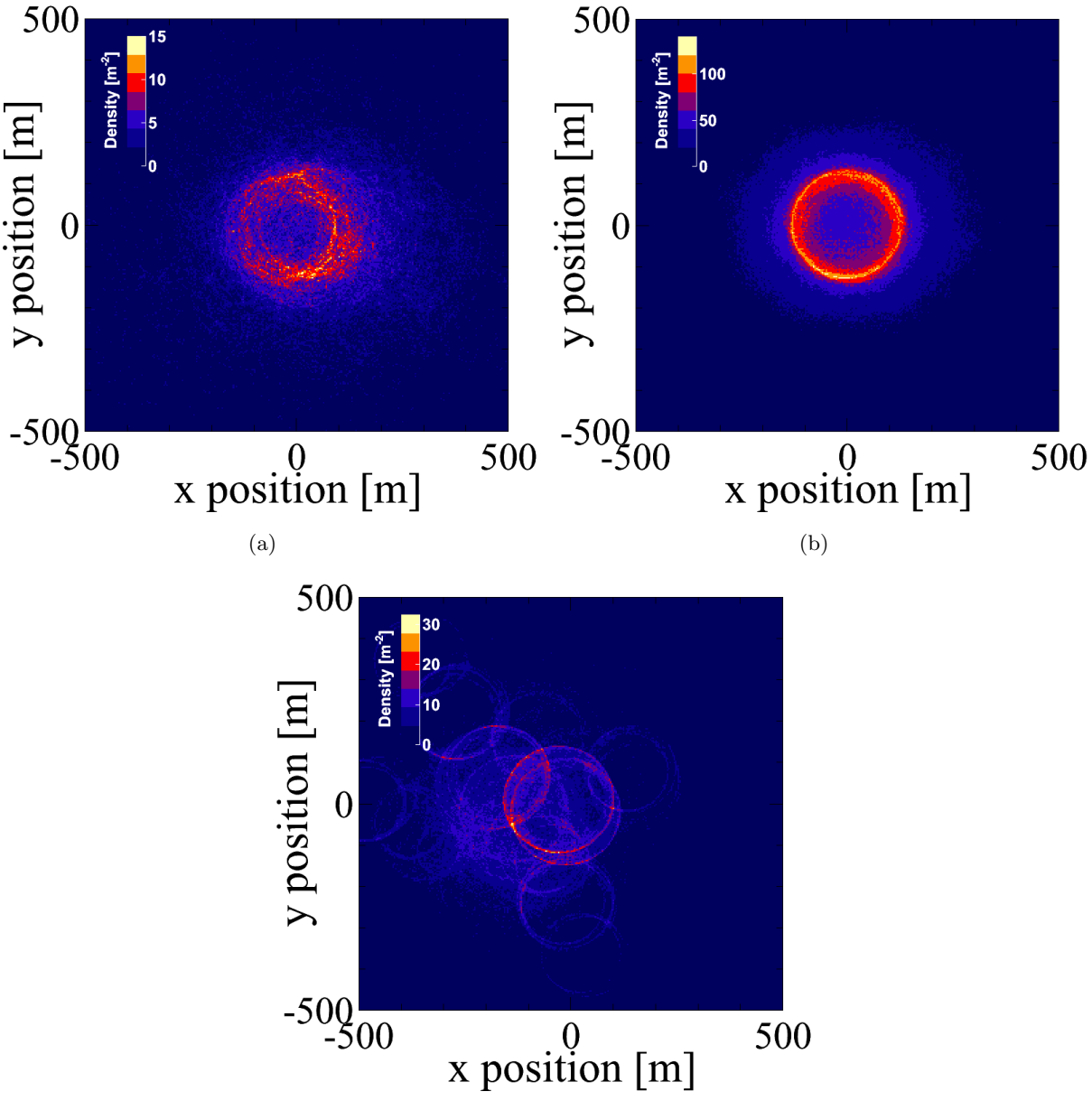

Figure 3.5 Distribution of Cherenkov photons on the ground resulting from electromagnetic and hadronic showers in the atmosphere. The primary particle is a: (a) 100 GeV photon, (b) 1 TeV photons, and (c) 1 TeV proton.

characteristic angle Θ_c with respect to the path of the charged particle. The angle of emission is given by,

$$\cos\Theta_c = \frac{1}{\beta n} \tag{3.1}$$

Where β is the velocity of the particle in units of the speed of light in a vacuum and n is the refractive index of the dielectric medium(≈ 1 for air). With increasing energy of the particle, the characteristic angle reaches a maximum at $\beta \simeq 1$:

$$\Theta_{c,max} = \cos^{-1}\left(\frac{1}{n}\right) \tag{3.2}$$

This allows us to calculate the threshold kinetic energy for a particle to produce Cherenkov light below which radiation is not emitted,

$$E_{min} = \gamma_{min} m_0 c^2 = \frac{m_0 c^2}{\sqrt{1-n^2}} \tag{3.3}$$

This implies that the emission of Cherenkov light is dominated by low mass particles (e.g, electrons). The number of Cherenkov photons N produced per unit length l and per unit wavelength λ along the track of an electron is given by,

$$\frac{\mathrm{d}^2 N}{\mathrm{d}l\mathrm{d}\lambda} = \frac{2\pi\alpha}{\lambda^2} \cdot \left(1 - \frac{1}{\beta^2 n^2(\lambda)}\right) \tag{3.4}$$

Where the fine structure constant $\lambda \approx 1/137$. Since N varies as $1/\lambda^2$, the number density of Cherenkov photons peaks at UV wavelengths. However, the atmosphere is a strong absorber of UV radiation as a result of the Rayleigh-scattering in the atmosphere. This causes the most of the Cherenkov light to appear at the blue ($300-320$ nm) part of the electromagnetic spectrum instead.

The intensity of the Cherenkov light scales linearly with the atmospheric depth ρ while the characteristic angle scales as square root of ρ,

$$I \quad \propto \rho \qquad\qquad 0.3 - 1.4^\circ \tag{3.5}$$

$$\Theta_c \quad \propto \rho^{1/2} \qquad\qquad 2 - 30 \text{ photons} \tag{3.6}$$

As the atmospheric depth changes with the height, the intensity of the Cherenkov light is modified along with the Cherenkov emission angle. This produces a focusing of the Cherenkov light on the ground such that an enhancement or hump in the photon density occurs at ~ 120 m away from the impact location of the primary particle (Figure 3.6). The number density of Cherenkov photons is roughly proportional to the energy of the primary particle as the number of charged particles increases and the resulting shower extends closer to the ground. Beyond ~ 120 m the density of photons is dominated by contributions from secondary particles with large scattering angles relative to the direction of the shower core.

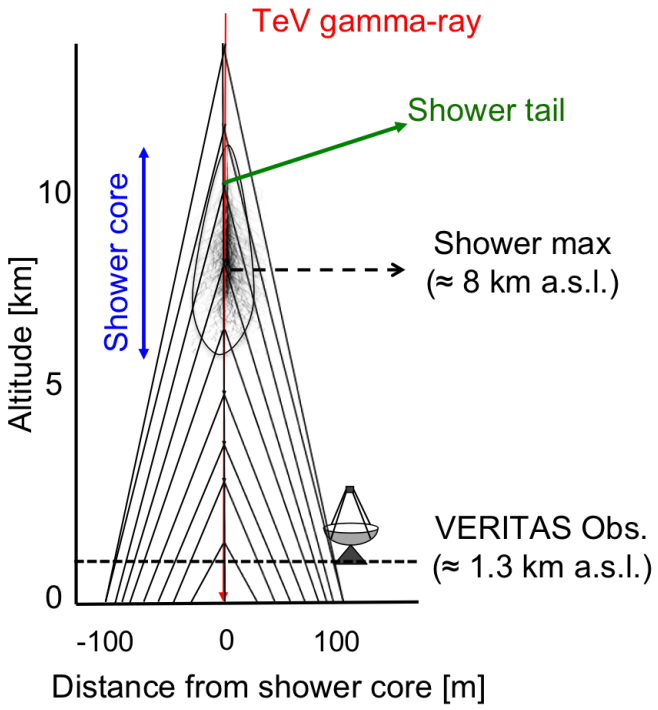

(a)

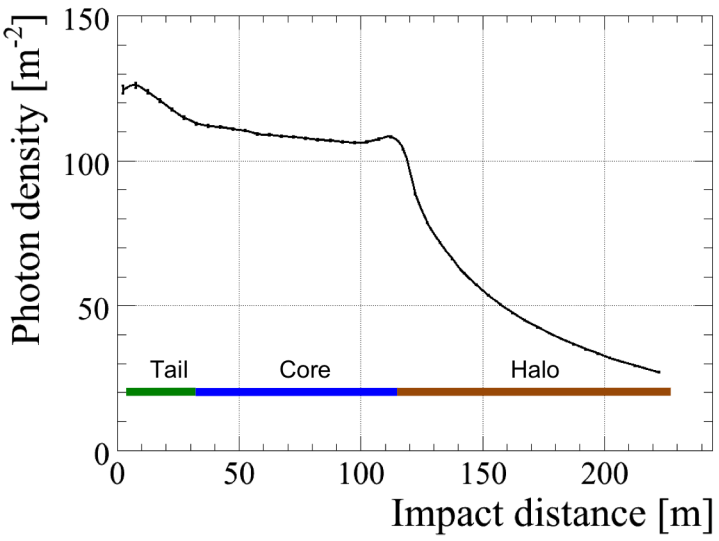

(b)

Figure 3.6 Schematic view of Cherenkov emission from different parts of a photon-induced EAS. The corresponding lateral Cherenkov photon density distribution for a 500 GeV gamma-ray initiated shower at an altitude of 1300 m a.s.l is shown in the inset– (a) Photons collected at distance < 30 m from the shower core are mainly collected from from the tail of the shower. (b) For a distance < 120 m, most of the light originates from the shower core, (c) Secondary particles with large scattering angles w.r.t to the shower core produces majority of the Cherenkov light on the ground beyond 120 m. Note the enhancement of photons at 120 m due to focusing effect of photons with varying emission angle.

3.2 Imaging Atmospheric Cherenkov technique

The design of the earliest Cherenkov detector began with a simple idea of using the earth's atmosphere as a calorimeter to sample the Cherenkov light from air showers (Galbraith & Jelly, 1953, 1955). This concept was strongly motivated by the fact that a sufficiently large and sensitive detector placed anywhere in the $45,000$ m^2($\pi 120^2$ m^2) Cherenkov light pool is capable of detecting the primary particle. The success of the early atmospheric Cherenkov instruments were largely limited by the overwhelming cosmic ray background until the development of the imaging technique by the Whipple Collaboration. This novel technique exploited the differences in the images of Cherenkov light pool to discriminate between gamma-ray showers and the hadronic background. The lateral distribution of Cherenkov photons from a gamma-ray initiated cascade tends be more compact than that of hadronic cascades due to the physics described earlier (Section 3.1.1). In contrast, the image from a hadronic shower will be broader and more irregular. Moreover, the time spread of the Cherenkov light pulse from hadronic showers ($\sim$ 10 ns) is slightly longer than that from an electromagnetic cascade ($\sim 3-5$ ns). This broad spread arises because the hadronic shower contains many more penetrating particles and the resulting Cherenkov light arrives early compared to the rest of the shower. Another powerful feature of electromagnetic shower image is that they arrive from the same direction as the putative source direction, whereas cosmic ray showers are highly isotropized due to deflections from the interstellar magnetic field. Background rejection based on differences in respective shower images led to Whipple's discovery of the first astronomical VHE gamma-ray source, the Crab nebula in 1989 (Weekes et al., 1989).

Significant improvement in sensitivity, energy resolution, and hadron discrimination was achieved in the last generation of IACT by HEGRA Collaboration (Daum et al., 1997) with the introduction of stereoscopic observations. In this scheme, multiple telescopes are simultaneously used to record Cherenkov photons from the same air shower so that coincident triggers between telescopes helps lower the background rate. At lower energies, prevalent local muon events from cosmic rays are almost completely suppressed with trigger multiplicity which reduces the energy threshold of the system. Stereoscopy also allows a determination of the distance to the shower core and hence the shower maximum. Since the number of secondary particles in the air shower at shower maximum is a good measure of the energy of the primary photon, stereo observations significantly improve the energy resolution of the instrument. Simultaneous images of the same air shower can also be used to pinpoint the location of the source with better accuracy leading to overall improvement in angular resolution. Finally, multiple telescopes separated by distances of the same order as the lateral spread of the Cherenkov light pool ($\sim$ 120 m) provides a much larger collection area $\sim 10^5$ m^2. for detection of particles.

The latest generation of IACTs employs stereoscopic observations combined with large mirror areas and fast electronics to achieve unprecedented gamma-ray sensitivity over a wide range of energies. The major stereoscopic IACT observatories currently operational across the globe

Figure 3.7 The 4-telescope VERITAS array in Southern Arizona, USA (2010). *Credit:* N. Gallante/VERITAS

are: H.E.S.S (Aharonian et al., 2006a), VERITAS (Holder et al., 2006), and CANGAROO-III (Kubo et al., 2004). In addition, the MAGIC telescope gained stereoscopic capabilities in 2009 with the addition of a second IACT (Moralejo et al., 2009).

3.3 The VERITAS experiment

The VERITAS (Very Energetic Radiation Imaging Telescope Array System) Collaboration operates an array of 4 identical 12m IACTs at the base camp of the F. L. Whipple Observatory in Southern Arizona (31.68° N, 110.95° W, 1275 m above sea level) (Figure 3.7). The first VERITAS telescope was commissioned in 2004 as a proto-type and the complete array with 4 telescopes became operational in 2007. In Summer of 2009, Telescope 1 was relocated to arrange the telescopes in a square with a typical baseline of $\sim$ 100 m. All data used in this dissertation work were obtained with the VERITAS array prior to the Telescope 1 move, Designed to detect VHE gamma-rays in the energy range between 100 GeV and 10s of TeV, VERITAS is the most sensitive IACT system in the world at the time of this publication.

The VERITAS telescopes are constructed following a tessellated Davies-Cotton reflector design with a 12 m aperture reflector and a focal length of 12 m. The reflector consists of 350 hexagonal mirror facet, each with an area of 0.322 m^2 resulting in a total mirror area of $\sim$ 110 m^2. The glass mirror facets are ground and polished by *Displays & Optical Technoliges Inc* (Roundrock, Texas) before being cleaned, aluminized, and anodized at the VERITAS optical coating laboratory. The aluminized coating ensures that the peak reflectivity response of mirror facets match the peak intensity of Cherenkov radiation at the observing altitude. The average reflectivity of the mirrors is $>$ 90% for a wavelength of 320 nm. The mirrors are mounted on the optical support structure using a triangular frame with three adjustment screws to enable accurate alignment. The individual facets are manually aligned by using a laser-based alignment system and the resulting optical point spread function (PSF) of $\sim 0.6°$ (Ong et al., 2009b) is well contained with in the size of photomultiplier tubes (see below).

The VERITAS camera

Each of the VERITAS focal plane instruments or the cameras has a 3.5° field of view (FOV) and consists of 499 photomultiplier tubes (PMTs). The cameras are located 12 m from the central mirrors of the telescope, housed in a durable light-tight and water-tight focus box (Figure 3.8) to protect its contents from the natural elements. Inside the focus box, the PMTs are supported on a hexapod structure which allows fine adjustments of the position and tilt of the focal plane. The PMTs installed on the VERITAS cameras are Photonis XP 2970/02-hemispherical UV sensitive, 10 gain-stage bi-alkali photocathodes with a quantum efficiency of $> 20\%$ at 300 nm. With a diameter of 28.6 mm, these PMTs are packed hexagonally to give a net angular spacing of 0.15°. Locally designed and fabricated light concentrators (Winstan light cones) are laid over the PMT assembly to further reduce the dead space between pixels by 25%. These highly reflective ($\sim 85\%$) light cones increase light collection while reducing the ambient photons by limiting the acceptance angle of PMTs to the solid angle of the detector. The cones have been reported to increase the light collection efficiency by a factor of up to 20% (Jordan & Krennrich, 2004).

A multichannel modular commercial power supply (CAEN) is used to control the high voltage to each individual PMT. The high voltages are typically set to allow the PMTs to be operated at a gain of $\sim 2 \times 10^5$. Each PMT unit is fitted with a custom-built preamplifier to boost the signal before it travels to a dedicated *fast analog to digital converter* (FADC). The high-bandwidth preamplifiers are adjusted to match the dynamic range of the FADCs. Finally, the PMTs are connected to the telescope trigger and data acquisition electronics using 50 m of 75 Ω coaxial cable.

VERITAS trigger system

The sensitivity of the VERITAS array to VHE gamma rays are limited by fluctuations in the night sky background (NSB) and single muon events from hadronic showers. Background suppression is particularly desirable at lower energies close to the threshold of the VERITAS array. At present, VERITAS uses a three-level trigger system to reduce the rate of these background events. The first level (L1) trigger consists of a custom-designed constant fraction discriminator (CFD) for each PMT pixel in a telescope camera (Vassiliev et al., 2003). Thus, if the sum of the voltages from the PMT pulse and a time-delayed copy exceeds a certain threshold, a trigger pulse is issued. At first glance, lowering the CFD threshold may seem like a reasonable approach to reducing the energy threshold of the telescope. However, the NSB increases exponentially with decreasing CFD trigger threshold. To address high NSB rate, a multiplicity trigger can be used by requiring more than one CFD signal to be coincident within a fixed time window, Therefore, the CFD output is sent to the second level (L2) trigger which is a pattern selection trigger (PST) system. The PST contains a memory look-up on a chip that can be promptly programmed to recognize patterns of multiple triggered pixels within the camera,

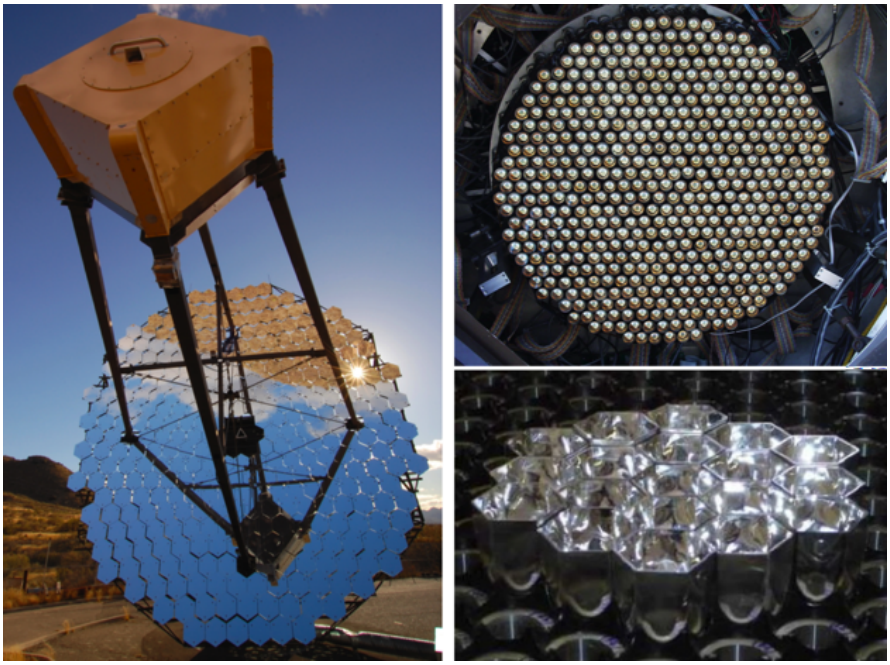

Figure 3.8 *Left:* Picture of the VERITAS focus box in the foreground. *Right:* Top panel shows the 499 PMT-assembly without light-cones. Bottom panel shows a group of light cones laid over the PMTs. *Credit:* S.Fegan/T. Nagai/VERITAS

In standard operation mode, each VERITAS camera is configured to issue a trigger if CFD triggers arrive in three adjacent pixels within a time coincidence window of ~ 10 ns. Triggers due to the NSB are largely random in nature which imply that pattern triggers preferentially selects compact Cherenkov signals from gamma-ray induced showers. The final trigger level (L3) consists of an array trigger that is used to identify events simultaneously observed by multiple telescopes. At lower energies, hadronic background consists of a large number of "local" muons. Therefore, by requiring multiple telescopes to trigger a substantial fraction of the background events are removed. For VERITAS, the standard telescope coincidence requirement is any two telescopes triggering within a ~ 100 ns time window.

The following chapter discusses in detail, the digitization of the analog data from the telescope array and the subsequent analysis of VERITAS data.

CHAPTER 4. VERITAS DATA ANALYSIS

This chapter presents a summary of the analysis chain developed here at ISU to analyze data taken with the VERITAS telescopes. A brief discussion of the processing of the VERITAS raw data is given in Section 4.2. Afterwards, I give an overview of the Hillas parameterization of the Cherenkov images along with the development of cuts to preferentially select gamma-ray induced events over background events. In addition, I describe the generation of a large database of Monte Carlo simulated gamma rays to in order to perform spectral analysis. Finally, the data analysis chain is evaluated on a small Crab nebula database. The resulting differential energy spectrum of the Crab nebula is found to be in good agreement with previous measurements by different experiments.

4.1 Observations

The VERITAS telescopes are operated under a strict set of observing guidelines to ensure the collection of quality data. In order to protect the sensitive photomultiplier tubes and reduce the noise in the system, observations are done on clear, moonless, , and dark nights. As a result, the observing sessions are divided into 2 to 3 consecutive weeks of moonless nights, called "dark runs". While some data is periodically collected under moonlight conditions with modified trigger settings, the dataset used in this dissertation excludes all moonlight data. The telescopes are typically shut down for a two month period during the summer monsoon season in Southern Arizona. This avoids damage to the sensitive electronic equipments due to excessive humidity and frequent lightning storms.

It is also important to constantly monitor the real time weather for cloud cover, excessive wind or humidity during the observations. Cloud cover not only blocks the source flux but also helps scatter the ambient light. The latter may give rise to strong fluctuations in the trigger rate. Thus, observers usually rate the sky conditions for every data run on a scale of A to F, where A is ideal and F is an extremely poor condition. For a more accurate measurement, a Far-Infrared (FIR) Pyrometer was installed at the VERITAS site to detect cloud cover. The FIR instrument measures the infrared radiation reflected by clouds. It is highly sensitive to the change in temperatures due to clouds passing through its field of view. In addition, a weather station located near the VERITAS facility is used to monitor the wind speed, temperature and the humidity. These data along with the FIR information is recorded and stored in the

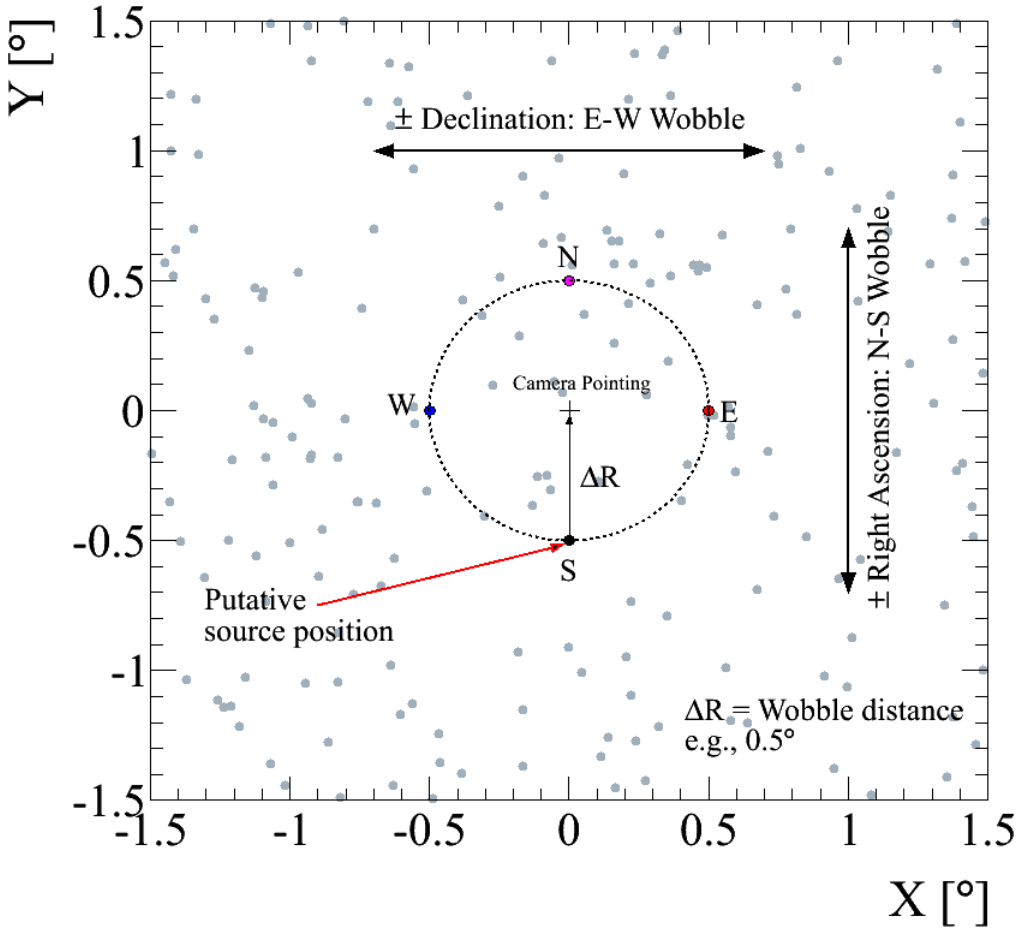

Figure 4.1 A schematic description of the *wobble* observation mode. The telescope is typically pointed at $\sim 0.5°$ away from the putative source position in right ascension or declination.

VERITAS database for each observing run. Subsequently, data obtained with poor sky quality or under extreme weather conditions may be discarded during offline analysis.

The VERITAS telescopes are operated mainly in two different observation modes: *ON/OFF* mode or *wobble* mode, each offering a slightly different method for estimating the background (see Section 4.4.3).

1. *ON/OFF* mode : In this observation mode, the source region (*ON*) is placed directly in the center of FOV of the camera and tracked for a given length of time, typically 28 sidereal minutes. Since the *ON* scan measures the gamma-ray flux combined with the background rate, an independent estimate of the background is required to calculate the source flux. Following the *ON* scan, the telescopes are slewed back to a background region (*OFF*) that corresponds to the same declination as the source but separated in right ascension by the duration of the *ON* scan. Thus, the *ON/OFF* scans cover

identical part of the sky, in both azimuth and elevation. This method is largely limited by low duty cycles since half of the observing time is spent tracking an empty part of the sky. Moreover, changes to the weather conditions in between the scans may lead to an inaccurate estimation of the background.

2. *wobble* mode : The more widely used observation strategy is the *wobble* mode (Fomin et al., 1994). In this method, the source is offset by a distance of 0.5° from the center of FOV of the camera. During each data run, the offset is alternated between a positive and negative declination (or right ascension). Each *wobble* run typically lasts 20 minutes. An advantage to this method is that there is no need for an additional (*OFF*) run. To estimate the background, several *off* regions are chosen in the camera with the same offset as the source but symmetrically away from the source region (see Figure 4.1). Consequently, the *wobble* mode allows us to simultaneously calculate the background. This is described in greater detail in Section 4.4.3.

4.2 Data Analysis Chain

This section briefly outlines the analysis used to search and extract the gamma-ray signal from a source region in the sky. A simplified schematic of the different parts of the analysis chain is shown in Figure 4.2. Many details of this analysis have been presented in other forms (Holder et al., 2006; Cogan, 2006). The primary steps involved in the analysis of data collected by ground-based Cherenkov telescopes are as follows:

- The Cherenkov photons recorded in each pixel are calibrated and converted in to photo-electrons (pe). This involves the normalization of the gain of each PMT with respect to the others. In addition, corrections must be applied to account for timing offsets due to the different pulse arrival times between FADCs.
- To remove the night-sky-background (NSB) noise, recorded images are cleaned. Image cleaning algorithms allow us to isolate pixels containing significant fractions of Cherenkov photons and remove tubes containing primarily NSB or noisy PMTs from the final analysis.
- Each cleaned image is parameterized and reduced to a set of interesting variables that sufficiently describe the image.
- The shower images recorded by the VERITAS telescopes are primarily images of the hadronic cosmic ray events. Gamma-ray events are separated from the background events by applying suitable cuts to the image parameters.

The VERITAS Collaboration has a number of software packages available for performing routine offline data analysis. At Iowa State University (ISU), the *Event Display* analysis

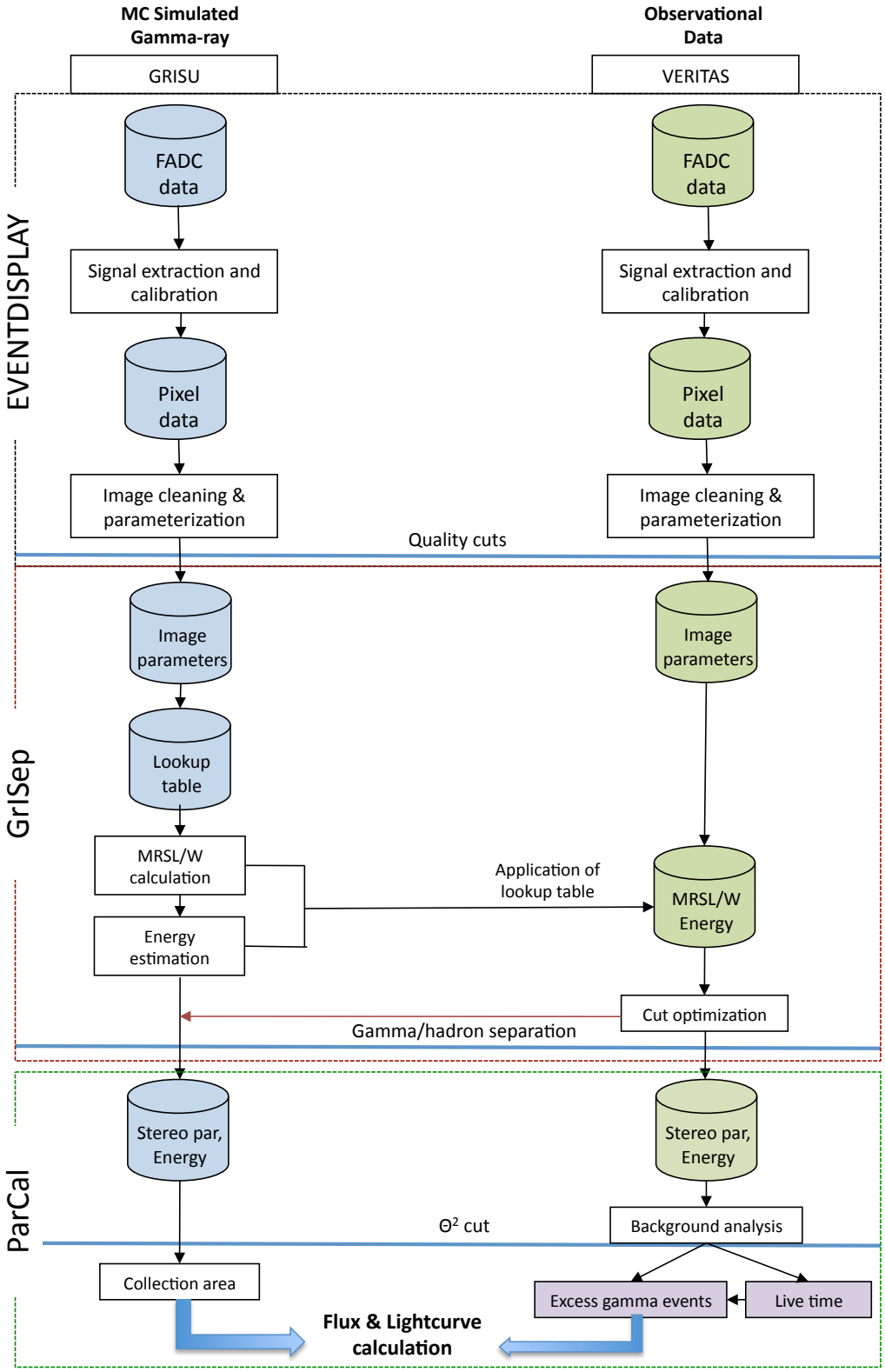

Figure 4.2 Outline of the analysis chain used in this work.

package (Maier , 2007) is used for data reduction and analysis. Developed mostly by Gernot Maier, *Event Display* is written in C++ and based on the ROOT[1] framework. Being entirely independent of VEGAS (Daniel et al., 2007), the VERITAS standard analysis package, *Event Display* provides a completely independent cross-check and confirmation on the different stages of data analysis.

At the end of each nightly observing session, the data from the VERITAS Observatory is sent to be archived at the University of California at Los Angeles (UCLA) repository. The data is stored in a custom designed binary format, VERITAS Bank Format (VBF), where they are uniquely identified with a run number. Afterwards, the relevant data is downloaded to local ISU RAID storage. The process of retrieving UCLA data has been automated by the author to reduce any delay or redundancy.

The VERITAS group at ISU maintains a mini-cluster of Quad-Core Intel Xeon processors with over 25TB of data storage. Following a thorough check on the data quality, each data run is promptly analyzed with *Event Display* and the results are saved into a corresponding ROOT binary data file.

4.2.1 Calibration

Initially, the raw data collected by the VERITAS cameras are translated into a more useful form with the offline analysis package, *Event Display*. The goal of this multi-step process is to extract all possible meaningful information such as flux, spectrum and morphology of the gamma-ray source. Incident Cherenkov photons are converted to photoelectrons (pe) by the photo-cathode in the PMT, producing a measurable current in the system. The total induced charge in the PMT is a function of the number of photons originally collected by the PMT. The resulting current is sampled and digitized with a dedicated 500 MHz flash ADC (FADC) unit. The FADCs are programmed to a 24 sample readout window corresponding to a total duration of 48 ns. Each successive 2 ns time bins or FADC "slices" represent the digitized signal amplitude measured in digital counts (d.c). The first step in data analysis involves determining the charge-to-pe conversion factor as well as characterizing the arrival time for the signal at each pixel.

Figure 4.3 shows an example trace of the FADC signal for a cosmic ray event in a certain signal channel. The simplest method for calculating the total charge deposited at the PMT is to integrate the area under the entire FADC trace. This is complicated by the fact that the digitized signal contains a persistent contribution from the NSB. To improve the signal to noise ratio, an optimum integration window must be found which covers a significant fraction of the signal due to Cherenkov photons. *Event Display* uses the *fixed window* method with 10 sample (20 ns) integration window to calculate the charge. Due to a gradient in the arrival times of the FADC signals in the pixels, a time T_{zero} is evaluated for the start of the integration. T_{zero}

[1] http://root.cern.ch

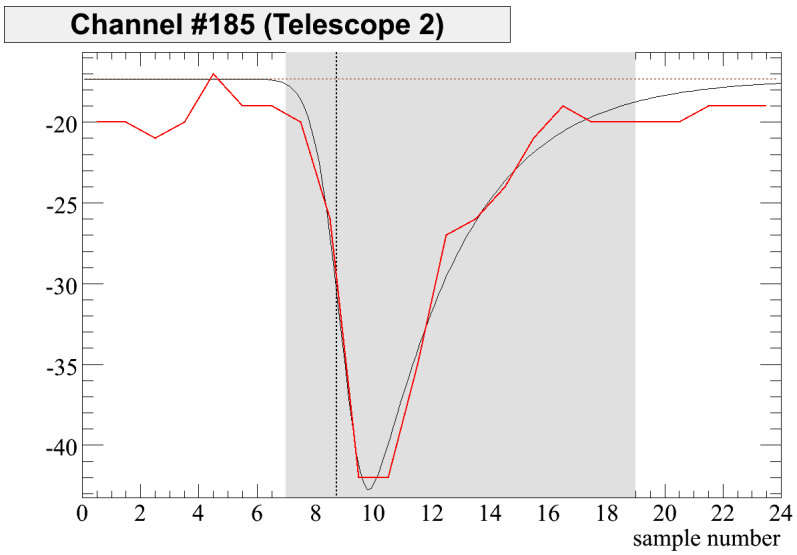

Figure 4.3 Example of a FADC trace from a cosmic ray event. The vertical line denotes the arrival time of the pulse, T_{zero}. The dashed horizontal line gives the electronic pedestal level. The integration region with a width of 20 ns (10 samples) is given by the shaded region.

is defined as the time on the rising edge of the FADC trace where the signal amplitude reaches half of its peak value after subtraction of the pedestal (see below) baseline (Cogan, 2006). Since T_{zero} depends on hardware configurations such as cable length, high voltage settings and FADC look-back time, it is averaged over many events to calculate a relative timing offset, T_{offset}, between pixels. Finally, the T_{offset} is used to correct the arrival timing information and reposition the integration window.

The calibration of the charge-to-pe conversion factor in the electronics requires measuring the average FADC signal amplitude in d.c. as a result of a single photoelectron hitting the PMT (Holder et al., 2006). To achieve this, a blue nitrogen laser (400 nm) is used to uniformly illuminate the cameras. Afterwards, the intensity of the laser is adjusted until each PMT face receives an average of $\sim$ 1 photoelectron. The corresponding FADC readout is integrated to calculate the average conversion factor: 5.26 ± 0.55 digital counts per photoelectron. The distribution of FADC counts for a single PMT is shown in Figure 4.4.

In order to ensure uniform response across the cameras, individual pixels must be calibrated. This reduces hardware dependency of the recorded data and eliminates systematic uncertainties arising from the varying responses of the different sub-systems in the camera. Data collected by the IACTs are dominated by NSB events. In order to efficiently subtract this background from the data, the fluctuations in the NSB must be evaluated. To achieve this, the telescopes

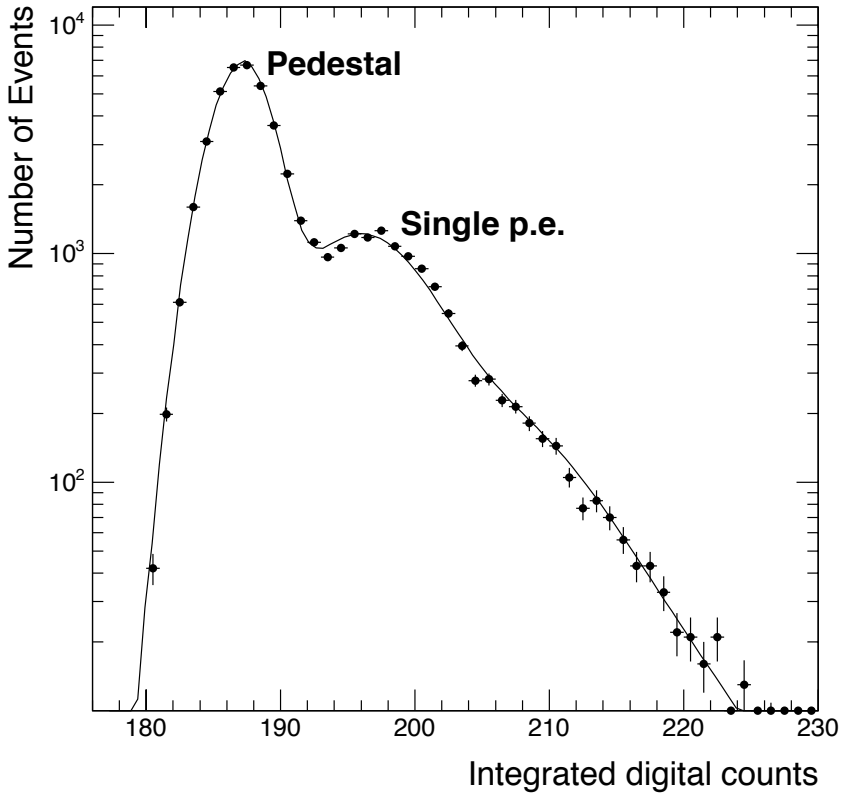

Figure 4.4 Histogram of FADC counts in response to a single photoelectron. The average charge-to-pe conversion factor over all PMTs is found to be 5.26 ± 0.55 d.c./pe. [From Holder et al. (2006)]

are artificially triggered at a rate of 3 Hz during the regular observation in order to sample the background events without any Cherenkov light. The resulting histogram of the integrated FADC charge characterizes the NSB. The mean of the distribution of integrated charge from NSB is defined as the *pedestal* and the associated RMS is referred to as the *pedvar*. The *pedvar* represent the background noise that must be subtracted from data during analysis. While the NSB level varies with changing FOV and weather, the *pedvar* is calculated every three minutes during a data run to maintain an acceptable data acquisition rate. Figure 4.5(a) shows the distribution of mean *pedvar* averaged from all channels in Telescope 1 during a typical Crab observation.

Finally, a relative calibration is performed to flat-field the response of the camera such that each signal channel produces roughly equal amount of light in response to the same air shower. Ideally, at the beginning of each observing session, a 5 minute *laser* run is performed. During the laser run, the VERITAS cameras are uniformly illuminated with multiple bright, time-

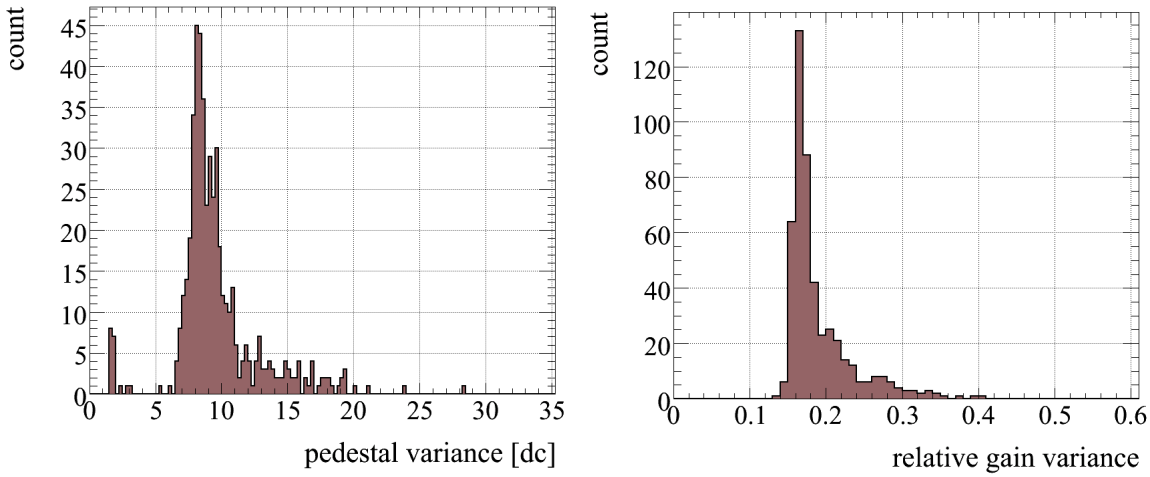

(a) (b)

Figure 4.5 For a selected data run (Run #37195) and Telescope 3, shown are the distributions of *Left: pedvar*, and *Right: gain*.

coincident light pulses running at 10 Hz. For each laser pulse, the distribution of integrated charge in each pixel is compared to the average integrated charge across the camera. Assuming the laser delivers same number of photons over each pixel, a difference in the integrated charge for an individual pixel with respect to the others in the entire camera establishes a calibration for the relative gain of pixels. The relative gain factor is applied to each pixel in order to correct for any non-uniformity in the cameras. A distribution of relative gains for a typical channel is shown in Figure 4.5(b). The arrival time of laser pulses in each FADC trace allow us to perform a correction for relative time offsets T_{offset} in each channel.

4.2.2 Image cleaning

Following the calibration of the light intensity distribution of shower images in the camera, a cleaning algorithm is applied to select pixels with residual intensities related to the Cherenkov image. The motivation for this is two folds: As a direct consequence of the air shower geometry only a small number of the image pixels contain light from the shower. Therefore, it is desirable to only use these pixels containing a significant fraction of Cherenkov photons. Secondly, image cleaning removes pixels containing spurious signals due to photomultiplier noise or the NSB. Using the default configuration in *Event Display*, the image cleaning process is carried out by a *two-pass* method. In the first pass, pixels containing an integrated signal greater than 5 times their pedvars are selected. The pixels passing the first step are referred to as the *Picture* tubes. The second pass of the cleaning procedure selects pixels directly adjacent to the *Picture* tubes, provided that the integrated charge in these *Boundary* tubes exceeds 2.5 times their pedvars. The second pass operates under the assumption that the *Boundary* pixels

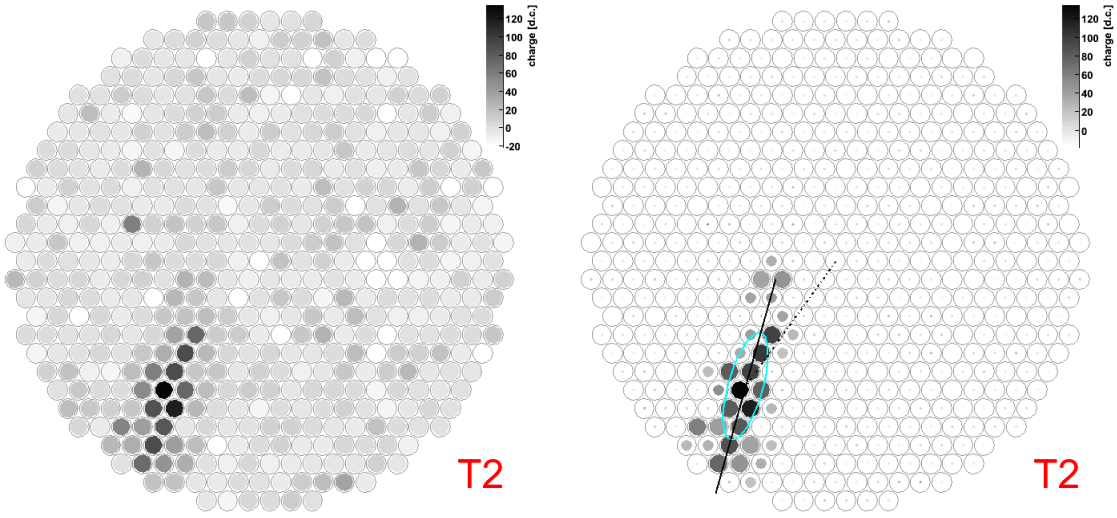

(a) (b)

Figure 4.6 *Left*: The distribution of charge across the camera for a gamma-ray candidate event. The gray scale denoted the charge for each pixel in digital counts. *Right*: The same image after image cleaning with the two-pass methods.

adjacent to the *Picture* tubes are more likely to be part of the shower images even if they contain a relatively smaller fraction of light. Finally, the charges in all remaining tubes are set to zero and discarded from subsequent image analysis. Figure 4.6 shows a camera image for a gamma-ray candidate event before and after image cleaning. The image cleaning removes a substantial number of pixels from the final image.

4.2.3 Image parameterization

After removing noise from pixels, the resulting cleaned images are characterized by the standard *Hillas parameterization* (Hillas, 1985a). The brightness, shape and orientation of the light intensity distribution in the camera are subsequently parameterized by calculating the first three statistical moments of the image. The reader is referred to e.g., Reynolds et al. (1993) for a complete description of the derivation of different Hillas parameters. In the first approximation, the Cherenkov light intensity distribution may be described as an ellipse. Figure 4.7 shows the characterization of an image with the different Hillas parameters.

The total amount of light present in the image is represented by the *size* parameter, which is a measure of the brightness of the shower. The parameters *length* and *width* measure the images' major axis and the minor axis, respectively. *Length* and *width* correspond to the longitudinal and lateral development of the shower. The position of the shower with respect

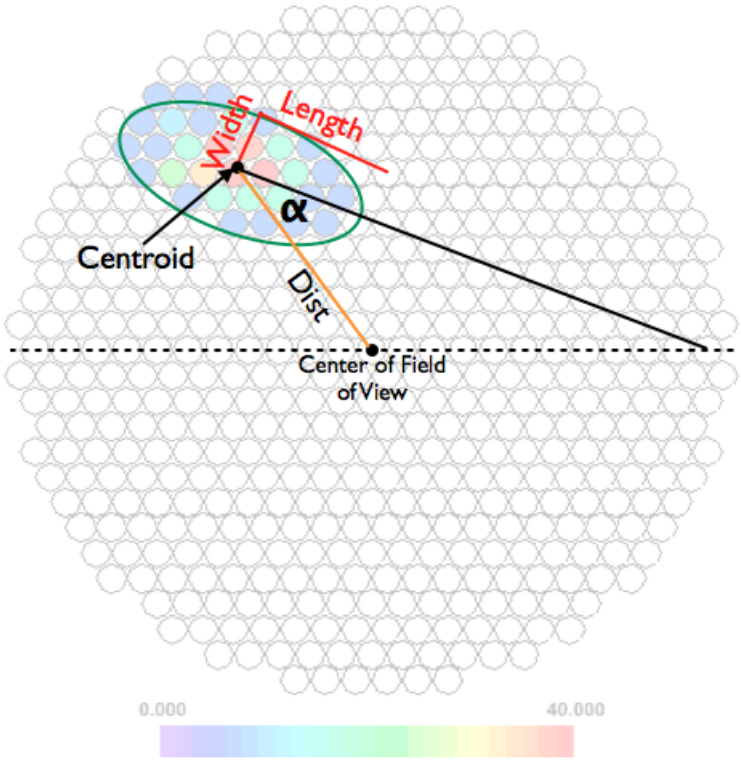

Figure 4.7 Graphical description of Hillas parameters.

to the telescope location on the ground is specified by the *distance* parameter, the angular separation between the image centroid and the center of the FOV. Hillas (1985a) demonstrated that these and other single-telescope image parameters can be used to discriminate gamma-ray induced electromagnetic showers from cosmic ray air showers. For stereo analysis involving multiple telescopes, scaled parameters (Section 4.4.2) derived from these Hillas parameters have proven to be even more powerful at gamma-hadron separation and discussed in detail in the following sections.

4.2.4 Shower reconstruction

The use of more than one telescopes has significantly improved the sensitivity of ground-based IACTs to gamma-ray sources in the sky. Single telescope analysis is limited in its ability to determine the arrival direction of the shower. For each shower the source is assumed to lie somewhere along the major axis of the ellipse. Hence, there is inherent ambiguity in the source location with respect to the camera FOV without stereoscopic imaging. The situation is greatly improved with the aid of stereoscopic techniques, where Cherenkov light from air

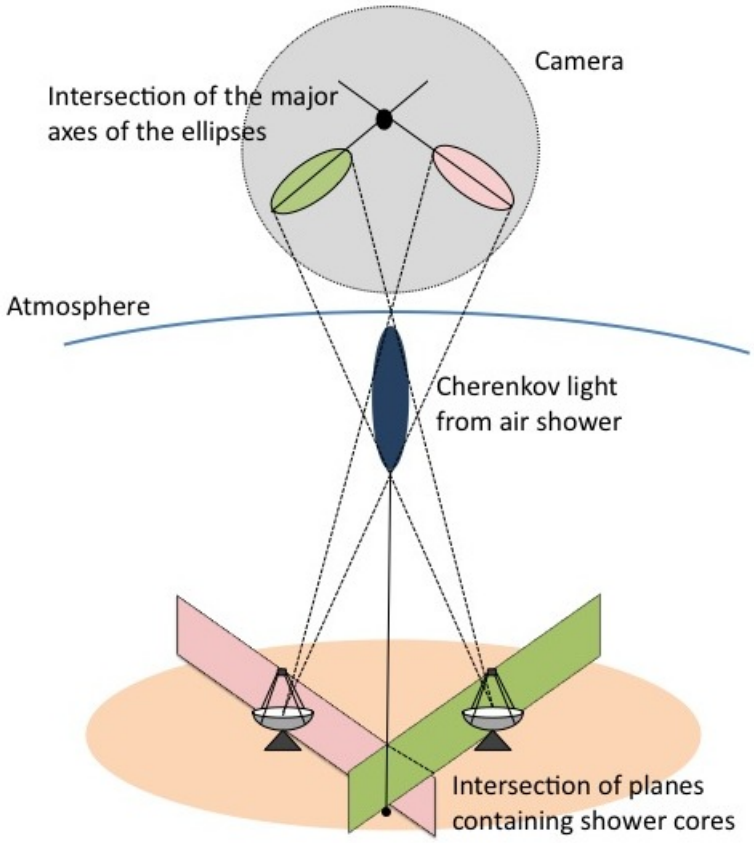

Figure 4.8 Principle of stereoscopic reconstruction [adapted from Funk (2005)]

showers can be simultaneously viewed from multiple angles. Afterwards, a simple intersection of the major axis of the ellipses from the different cameras allow us to accurately determine the *source location* in the camera (Figure 4.8).

A similar approach also enable us to determine the location of the impact point of the shower on the ground (*shower core*). Each shower image specifies a shower plane perpendicular to the camera plane. The shower plane contains the shower axis along the path of the primary particle. Therefore, an intersection of two or more shower planes uniquely determine the shower axis (Figure 4.8). By projecting the reconstructed shower axis to the ground plane, we can locate the position of the *shower core* on the ground. Figure 4.9 shows the error in reconstructed core location in the shower plane based on Monte Carlo simulated gamma-ray showers. Typical angular resolution of VERITAS array for core reconstruction has been found to be on the order of $\sim$ 10 m from simulated gamma rays. Thus, we can now define an additional stereo parameter *impact distance* which specifies the perpendicular distances between the *shower core* and individual telescopes on the ground. This parameter is extensively used later in analysis for generating lookup-table to calculate shape cuts and estimate energies of the primary gamma-

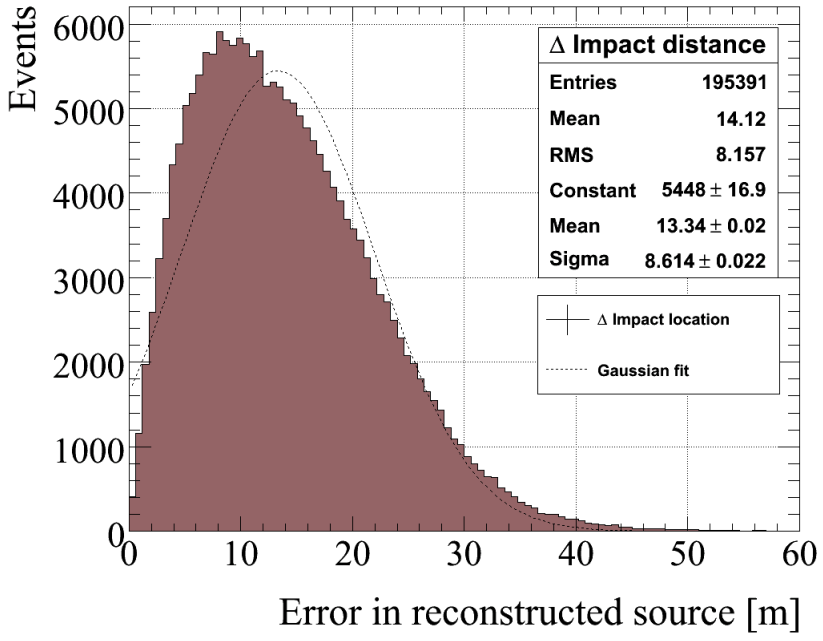

Figure 4.9 Error in the reconstruction of the core location in the shower plane based on Monte Carlo generated showers.

ray particles. Finally, stereoscopic reconstruction further allow us to estimate the height of the shower maximum, $h_{\max}$ for each telescope. The single Hillas *distance* parameter gives

$$\begin{aligned} \frac{impact\ distance}{h_{\max}} &= \tan(distance) \approx distance \\ \Rightarrow h_{\max} &\approx \frac{impact\ distance}{distance} \end{aligned} \tag{4.1}$$

4.3 Monte Carlo Simulation

In the absence of a natural or artificial VHE gamma-ray calibrator in the sky, Monte Carlo (MC) simulation is an essential tool for deriving the energy spectra of gamma-ray sources. An accurate model of the telescope must be constructed in order to predict the detector's response to the Cherenkov light produced by the air showers particles. This section details the MC simulation database developed at ISU for the spectral analysis of the Crab nebula and the blazar, 1ES 1218+304. The simulation process primarily consists of (i) production of the particle cascade, (ii) Cherenkov light generated by charged particles in the cascade, and (iii) the response to the Cherenkov light by the VERITAS telescopes.

4.3.1 Simulation of the air shower

There are a variety of programs available for simulating the production of atmospheric particle cascade from VHE gamma-rays. Most popular among them are KASCADE (Kertzman & Sembroski, 1994), CORSICA (Heck et al., 1998) and MOCCA (Hillas, 1985a). For our work, MC simulations of particle showers were generated using the KASCADE code, available as part of the Grinnell-ISU-Utah (GrISUtah)[2] air shower and detector simulation package. Written in Fortran, KASCADE uses available cross-section measurements to produce secondary particles from the primary cosmic ray or gamma-ray. A three-dimensional model of the air shower is created as secondary particles are allowed to interact with the atmosphere. Individual particles in the shower are tracked as the EAS develops in the atmosphere. Finally, the associated radiation and absorption processes such as Compton scatter, bremsstrahlung, pair production, multiple Coulomb scattering and ionization losses are simulated for appropriate particles types. The "U.S. Standard Atmosphere, 1976" was used in order to model the pressure, density, and temperature of the atmosphere as a function of altitude.

4.3.2 Cherenkov light production

The emission of Cherenkov light by ultra-relativistic charged particles in the atmosphere is simulated with *Cherenk*, also included in GrISUtah. For every shower particle track in KASCADE, Cherenkov light is produced if the particle energy is above the Cherenkov energy threshold (Section 3.1.2). In our database the Cherenkov threshold is set at 25 MeV. A Poisson deviate with a mean given by the Jelly formula is used to calculate the number of Cherenkov photons produced in a given shower segment (Mohanty, 1995). The wavelength of the photons are randomly distributed in a Cherenkov wavelength band from 185 nm to 685 nm. In order to speed up the computation, only photons striking within a detector radius of 9 m is tracked. The final output from the program is a list of photons from each shower segment along with various appropriate quantities, such as the impact position on the ground, direction cosines, relative timing information and wavelength, etc.

4.3.3 Detector model

We used the GrISUDet program to model the response of the VERITAS telescopes to Cherenkov photons. It simulates the propagation of the Cherenkov photons through the optical system. This process accounts for the various properties associated with the telescopes including mirror reflectivity, aberration and misalignment. The output photons from *Cherenk* are traced through the mirrors on to a matrix of 499 PMTs. GrISUDet also models the increased light collection efficiency due to the light cones (Jordan & Krennrich, 2004) by appropriately scaling the effective photosensitive area of the PMT cathode.

[2] http://www.physics.utah.edu/gammaray/GrISU

Afterwards, the responses of the camera and the associated electronics are simulated. Cherenkov photons hitting a PMT generates a single photoelectron pulse convolved with electronic noises and loss due to signal transmission. The detector-specific parameters are defined in a ascii configuration input file. In addition to the geometrical characteristics of the telescopes, this file includes PMT quantum efficiency, trigger settings and a scaling factor for converting photoelectrons to digital units. This provides a great flexibility in tuning the detector response. For every pixel containing a triggered event, GrISUDet produces a corresponding FADC trace at that pixel. The GrISUDet output can be readily processed with *Event Display* thus allowing us to treat the simulations and real data in an identical manner.

4.3.4 ISU database

Table 4.1 details the various initial parameters used in our simulation of the particle shower. The VERITAS array configuration and the details pertaining to individual telescope used for the MC simulation correspond the status of the array in October, 2008. A total of 30 million gamma-rays were injected at a depth of 1.1 g/cm^2. The energy of the primary particles were drawn from a Crab-like power-law spectrum with a differential index of -2.5. The energy of primary particles ranged between 50 GeV and 20 TeV. The shower core of the particles were uniformly scattered in a circle of radius 400 m in a plane perpendicular to the direction of the primary photon. The simulated primary particles were incident at a fixed zenith angle of 20°, which is roughly close to the average elevation of the 1ES 1218+304 dataset. The arrival direction of the simulate showers were randomized between 0° and 360°. In the final analysis, the azimuthal direction was restricted to a range corresponding to that of the real data.

To simulate electronic noise in the PMTs and noise due to the NSB, the simulated showers were processed with artificial noise. For our simulation database, the level of NSB noise was adjusted to match the observed pedestal variations. We used two different noise levels with values of 120 and 200 pe/ns/m^2/sr, corresponding to extra-galactic and galactic observing conditions respectively. The geomagnetic field was modeled as a magnetic dipole with a field strength of 0.5 G and a dip angle of 30°, appropriate for the location of the VERITAS observatory.

For the sake of completeness, it should be noted that our MC simulations were produced with the following simplifications:

1. All telescopes are exactly the same.
2. The constant fraction discriminator (CFD) is not simulated. Instead, we assume a simple threshold trigger.
3. There are no misaligned mirrors.
4. All cameras are considered to be perfectly focused.

Table 4.1 A table of initial parameters for the ISU MC database.

Number of particles	14 Million
Differential index	-2.5
Energy range	50 GeV – 20 TeV
Elevation	70°
Thrown radius	400 m
Observatory depth	888.7 g/cm^2
Configuration file	`v4bc_AI_415_L20_16Oct2008DB.cfg`

4.4 Gamma-Hadron separation

Most of the triggered events ($\sim$ 99.9%) in the VERITAS data are cosmic ray events. Therefore, it is crucial to develop a set of criteria or cuts to allow us to distinguish the gamma-ray events from the background dominated data. Moreover, a set of highly efficient cuts must be available to successfully perform sensitive measurement of VHE gamma-ray emission from weak candidate objects. As noted in Chapter 3, air-showers from hadronic primaries tend to be wider than the gamma-ray induced showers. Consequently, the separation procedure hinges on the intrinsic differences between the shower properties of gamma rays and hadrons. This section briefly introduces the *mean-reduced-scaled* shape parameters primarily used for selecting gamma-ray events. In addition, we outline the two specific techniques used in this thesis to estimate the background level in our data. Finally, a summary of the cut optimization procedure aimed at extracting signal from faint sources is presented.

4.4.1 Image quality cuts

In the standard VERITAS analysis a set of image quality cuts are applied to the data prior to the stereo-reconstruction of individual telescope images. The main motivation behind these cuts is to reject poorly reconstructed events. As a result, we impose a minimum image intensity (given by *size* parameter) requirement in each camera for a successful reconstruction. The *size* cut also helps avoid possible fluctuations from hardware trigger affects at the expense of a higher energy threshold. We also require a minimum of 2 telescope for image reconstruction. Similarly, we discard pairs of images that are nearly parallel in the array plane due to the resulting uncertainties in the reconstruction of the source location and shower impact point on the ground. For events with large *impact distances* or high primary energies, the resulting images tend to suffer truncation at the camera edge. This effect is mitigated by applying an upper bound on the *distance* parameter. Finally, the arrangements of the VERITAS telescopes prior to the relocation of T1 in the summer of 2009 was asymmetric. The close proximity of Telescope 1 and 4 reduced the triggering efficiency for the array. Hence, events solely triggered by this pair of telescopes (T1 and T4) were excluded from analysis. Table 4.2 shows the sets

of image quality cuts applied to the analysis described in this work. Collectively, these sets of cuts are also known as *pre-reconstruction* cuts.

Table 4.2 *Pre-reconstruction* cuts employed in the standard analysis of VERITAS data in 2007-2009.

Parameter	Quality cuts
size	> 400 d.c.
distance	$\leqslant 1.4^{\circ}$
Number of triggering pixels	$\geqslant 4$
Number of telescopes for successful reconstruction	$\geqslant 2$
Image angle between telescope	$\geqslant 10^{\circ}$
Remove telescope pairs	T1+T4
Picture threshold	5.0 σ
Border threshold	2.5 σ

4.4.2 Mean scaled parameters

The HEGRA Collaboration successfully pioneered the use of the *mean-scaled-width*and -*length* parameters for separating the gamma-ray signal from the hadronic background (Daum et al., 1997). Also known as shape parameters, these parameters have been found to be highly efficient at selecting gamma-ray events. To derive the shape parameter we exploit the correlation between the distribution of light intensity of gamma rays on the ground (i.e., *size* and *imapct distance*) and the corresponding single-telescope image parameters *width* and *length*. Following Aharonian et al. (2004), we construct a slightly modified version of the scaled from a general formula,

$$RSP_i = \frac{p_i - \overline{p}(s,i)}{\sigma_i(s,i)} \tag{4.2}$$

where p_i is the single-telescope parameters to be studied, such as *width* or *length*. It is compared with the mean of the expected distribution $\overline{p}(s,i)$ for the same event parameter. Now, $\overline{p}(s,i)$ is dependent on the image amplitude *size* and impact parameter *impact distance*. It is estimated from the Monte Carlo generated simulation of the gamma-ray events processed with identical image quality cuts. The averaged quantities are calculated in advance by constructing a two-dimensional grid or a lookup-table in *size* and *distTelCore*. The Monte Carlos are used to fill up the table and the averaged results are accumulated from many simulated events. Subsequently, the difference between the image parameter from data and the predicted value from MC, $(p_i - \overline{p}(s,i))$, is scaled by the standard deviation of the corresponding bin in the lookup-table. During the final step, the *mean-reduced-scaled width* (MRSW) and the *mean-reduced-scaled length* (MRSL) is calculated by taking a simple or weighted average of the quantity in

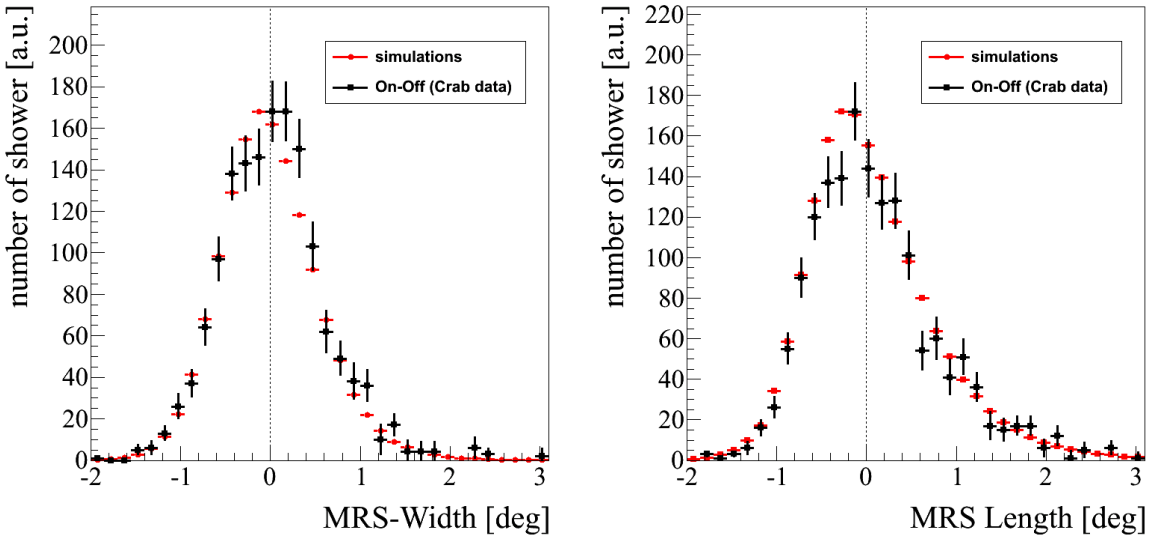

Figure 4.10 Distribution of MRSW (*Left*) and MRSW (*Right*) for Monte Carlo simulated gamma-ray events (red solid line), excess events (black solid line) and for real background events (black circles) from Crab data in 2007-2008. The vertical lines show the corresponding lower and upper bounds on the respective distributions for the hard cuts.

Equation 4.2 over all telescopes passing the *pre-reconstruction* cuts for any given event,

$$MRSW = \frac{1}{N_{\rm tel}} \sum_{i}^{N_{\rm tel}} RSP_i \cdot w_i \tag{4.3}$$

where $N_{\rm tel}$ is the total number of triggered telescopes after cuts and w_i is the corresponding weighting factor. Figure 4.10 shows the distribution of MRSW and MRSL for Monte Carlo simulated gamma-ray events at 20° zenith angle. Also shown for comparison are the corresponding distributions from the excess gamma-ray like events in Crab nebula data after passing all other cuts (see Table 4.3). A reasonable agreement between the simulated events and the excess event distribution imply the MC simulation of gamma rays is well understood.

Finally, we apply a directional cut on the θ^2. The angular difference between the reconstructed source position and the putative source position in the camera is denoted by θ. Applying a cut on θ is akin to placing a circular bin around the source position and only accepting events falling inside this circular region. More commonly, one plots the distribution of the variable θ^2 since it provides a constant solid angle on the sky per angular bin. For a point gamma-ray source in the sky, the incoming particles are ideally clustered around the true source location with the resulting θ^2 distribution peaking around 0. This is markedly different in the case of cosmic ray particles which are isotropically distributed in the sky. Consequently, the θ^2 distribution for cosmic-rays is roughly uniform across the camera. As a result, cuts on

the angular position or the θ^2 provides another powerful criterion for discriminating gamma-ray like events from the residual hadronic background. Figure 4.12 shows the θ^2 distribution for Monte Carlo simulated gamma-rays compared with that from a Crab nebula data for suitable cuts on MRSL and MRSW only (Section 4.4).

With an established a set of image parameters valuable for separating gamma rays from the background, we must determine a set of useful cuts to efficiently reject the background in our data while keeping most of the gamma-ray initiated events. The cuts were found to be sensitive to the strength of the candidate source. Moreover, the cuts also depend on the intrinsic characteristics of the source, such as the spectral index. Therefore, a rigorous cut optimization procedure was attempted to derive cuts with the following goals in mind:

- Cuts for detecting faint/weak sources in the sky by maximizing the sensitivity of the detector to gamma-rays.
- Cuts for spectral analysis aimed at reducing the systematic errors in the energy spectrum measurement.

Briefly, the cut optimization was carried out with a set of 11 good-quality 4-telescope Crab runs taken at low zenith angles with 0.5° wobble offset. To derive cuts for detecting faint sources, the Crab data was scaled down to a flux level corresponding to 10% of the original Crab flux. Initially, cuts on the MRSW and MRSL parameters were simultaneously optimized by scanning a finely binned two-dimensional grid in MRSW/MRSL. The strategy for finding the optimum cuts was to maximize the significance of detection or sensitivity (Section 4.4.4). Afterwards, a cut on the angular direction is optimized by varying the value of θ^2 for the "best" value for MRSW and MRSL parameters. Three different sets of cuts were obtained for this work, *standard*, *spectrum-I* and *spectrum-II* cuts. Table 4.3 summarizes the three cuts. The *standard* cut primarily differs from the other two *spectrum* cuts in the value of the θ^2 cut used. The primary advantage for the *standard* cut is the substantial reduction in the background, thus yielding a optimum sensitivity for the discovery of weak sources. On the other hand, the *spectrum* cut has the benefit of retaining a higher number of gamma-ray like events in addition to reducing the systematic uncertainties associated with the Monte Carlo detector model. Additionally, *spectrum-I* cut has been optimized for the spectral analysis of a strong source (e.g. Crab) while the *spectrum-II* cut is more suitable for deriving the energy spectrum of a source with $\sim 10\%$ of the Crab nebula flux.

4.4.3 Background estimation

The data may yet contain a significant fraction of the background events after image selection cuts. Following the application of the image quality cuts and gamma-hadron separation cuts, we are left with gamma-ray candidate events such that these events look like gamma rays based on cuts on the image parameters. Therefore, the remaining background level needs to

Table 4.3 Summary of the set of Optimized cuts for MRSW, MRSW and θ^2.

Cuts	MRSW		MRSL		θ^2	Image size	Distance
	Min	Max	Min	Max	Max [deg.^{2}]	Min [d.c]	Max [deg.]
Standard	–1.76	0.6	–1.6	0.5	0.0225	400	1.4
Spectrum-I (*Crab*)	–2.00	0.6	–2.0	0.5	0.035	400	1.4
Spectrum-II (*1ES 1218*)	–1.76	0.6	–1.6	0.5	0.03	400	1.4

be carefully determined in order to calculate the total number of excess events over residual contamination from the background. With a reliable estimate of the background, we can finally evaluate the statistical significance of the detection of gamma ray signal in our data. Following Aharonian et al. (2004), two separate background estimation techniques were employed in this work, each serving a unique purpose:

1. *Reflected background model*- In this method, the signal region is described by a circular area surrounding the target location on the camera. The optimum size of the signal region is given by the angular cut on the θ^2 parameter. With the VERITAS array, most observations are carried out in the wobble mode (Section 4.1), where the pointing of the telescope is offset by ΔR (usually $\pm 0.5^\circ$) in right ascension (declination) with respect to the source position. In the simplest scheme, the background is estimated from a region with same shape and size, located directly opposite relative to the center of the FOV from the signal region (see Figure 4.11 gray circles). In order to increase the statistics, multiple backgrounds may be positioned on a circle with radius ΔR around the center of the camera. The maximum number of permissible circular regions for background estimation depend on the values for ΔR and θ. However, caution must be exercised to prevent overlapping of background regions as this may lead to over-sampling of the background level. Similarly, the signal and background regions should not overlap to avoid the contamination of the signal region by background events. Typically, the acceptance of gamma-ray showers on the camera varies as a function of the position on the camera, zenith angle and the exposure time. Since the background regions are located at the same radial distance as the signal region, we can neglect the effect of camera acceptance for *Reflected background model*. Hence, the normalization factor α for scaling the background is simply given by $1/n$, the reciprocal of the total number of background regions, n. The systematic effects arising from non-radial acceptance in the camera can be minimized by choosing runs that are evenly distributed in all four *wobble* directions. In addition to signal search, this particular method is most commonly used for selecting events for spectral analysis due to the simplicity of the technique combined with the ease of implementation.

2. *Ring-background model* - This method is particularly suited for deriving two-dimensional maps of excess gamma rays in a certain region on the sky. For each point in the sky map, a circular signal or on-source region is constructed with the θ cut (region O in Figure 4.11). A circular annulus (ring) with an inner radius r_L and an outer radius r_U, centered around the source is chosen to be the background region (see Figure 4.11). Typical mean radius of the annulus is set at 0.5°. Any events with reconstructed source direction falling into the ring region is considered as a background event. Since the ring region covers different offset position relative to the observation position, the acceptance of the ring region can not be assumed to be uniform. Therefore, the normalization factor α for proper weighting of the background events is evaluated as a function of the radial position on the camera. The scaling factor for a given test point situated at a radial distance Δr away from the center of the FOV is given by the ratio of the integrated acceptance for the signal region to the integrated acceptance of the ring background region corresponding to the test location.

$$\alpha(\Delta r) = \frac{\sum\limits_{r\in\text{circle}} accp_\gamma(\Delta r)}{\sum\limits_{r\in\text{ring}} accp'_\gamma(\Delta r)} \tag{4.4}$$

where $accp_\gamma(\Delta r)$ and $accp'_\gamma(\Delta r)$ are the acceptances of gamma-ray like events in the circular on-source region and the background region, respectively. To accurately model the acceptance of the camera, any potential source for gamma rays in the camera FOV must be excluded from the acceptance calculation. The obvious advantage of the *ring-background model* is that it may be used to estimate the background for any sky positions in the sky, including the center of the camera. Therefore, the method has been successfully used in survey analysis of the galactic center where the distribution of potential sources and their extensions are not a priori known.

4.4.4 Significance calculation

The application of the image selection cuts and the background modeling allow us to determine the number of excess gamma-ray event N_γ above the cosmic ray dominated background level. As previously mentioned, the typical circular signal region or ON region (defined by θ) contains N_{on} events. Depending on the specifics of a particular background model, we can estimate the number of events in a certain background region as αN_{off}. With the assumption that N_{on} contains both gamma-ray signal and background events, the excess N_γ is given by

$$N_\gamma = N_{\text{on}} - \alpha N_{\text{off}} \tag{4.5}$$

where the background normalization factor is given by α. The normalization factor is required to account for the differences in the solid angle of observation and the exposure time for the

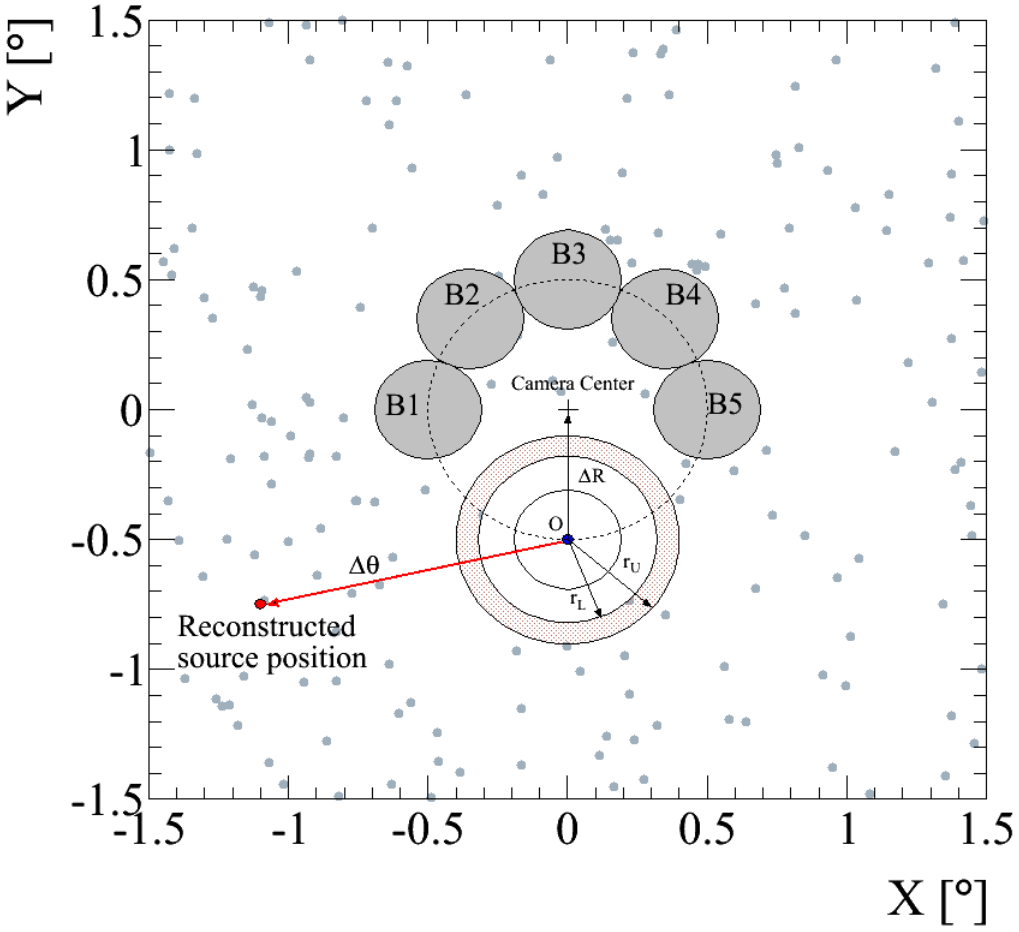

Figure 4.11 Description of the background estimation techniques used in this thesis. The locations and shapes of the signal region and the background region are defined for two methods, (i)*Reflected background model*: For a source region O, the background is estimated from several background regions $(\mathrm{B1}, \mathrm{B2}, \ldots, \mathrm{B5})$ located at the same distance from the camera center and with the same size as O. The number of maximum background regions depend on the position of S relative to the camera center and the exact size of SO(given by cut on θ). (ii) *Ring background model*: For a circular source region O about any test location on the camera, the background is defined to be a annulus with inner and outer radii of r_i and r_I, respectively. For accurate determination of the acceptance rate across the camera, all potential sources of gamma-rays must be excluded from the acceptance calculation.

ON and the OFF counts. The recipe for estimating the appropriate scaling factor is described in the preceding section. Finally, the statistical significance S of the gamma-ray signal above the background is given in Li & Ma (1983)

$$S = \sqrt{2}\left(N_{\rm on}\ln\left(\frac{(1+\alpha)N_{\rm on}}{\alpha(N_{\rm on}+N_{\rm off})}\right) + N_{\rm off}\ln\left(\frac{(1+\alpha)N_{\rm off}}{N_{\rm on}+N_{\rm off}}\right)\right)^{1/2} \tag{4.6}$$

For the total live time of observation $t_{\rm live}$, the gamma-ray detection rate from the source R_γ is given by

$$R_\gamma = \frac{N_\gamma}{t_{\rm live}} \pm \frac{\sqrt{N_{\rm on}+\alpha^2 N_{\rm off}}}{t_{\rm live}} \tag{4.7}$$

4.4.5 Angular resolution

A key characteristic for describing the performance of an IACT experiment is the angular resolution of the detector. It is a measure of the telescope's ability to effectively localize the source of gamma-ray signals in the sky, and it is of particular importance for the search of point gamma-ray sources. We have derived the angular resolution of the VERITAS array using Monte Carlo simulations of a point-source of gamma rays. Figure 4.12 (red circles) shows the distribution of the squared angular distance θ^2 between the reconstructed and the true source location of the Monte Carlo gamma rays. As a canonical value, the 68% of the containment radius of the θ^2 distribution is used to describe the angular resolution of the system. Commonly referred to as the Point Spread function (PSF), the 68% containment radius of this histogram is estimated by fitting the θ^2 distribution with a sum of two one-dimensional Gaussian functions,

$$\mathrm{PSF} = A_{\rm abs}\left[\exp\left(\frac{-\theta^2}{2\,\sigma_1^2}\right) + A_{\rm rel}\,\exp\left(\frac{-\theta^2}{2\,\sigma_2^2}\right)\right] \tag{4.8}$$

Where the absolute amplitude $A_{\rm abs}$ scales with the number of events in the θ^2 histogram. The figure of merit or the PSF is given by the standard deviation σ_2. After applying *standard* cuts, the θ^2 distribution from the Monte Carlos at 20° zenith angle was fitted with Equation 4.8, yielding a best fit value of $\theta_{68\%} = 0.124°$. To check the accuracy of our modeling of the PSF, the PSF fit to the Monte Carlo simulation was applied to a Crab nebula dataset by fixing all parameters except for $A_{\rm abs}$ (Figure 4.12 solid black line). The resulting best fit has a $\chi^2/\mathrm{ndf} = 110.3/96$ with a probability of 0.15. A reasonable agreement between real data and the model PSF fit confirms the reliability of our detector simulation along with the effectiveness of our gamma-hadron separation cuts.

4.5 Spectral analysis

Once a source of gamma ray has been successfully identified we can attempt to derive its energy spectrum. The GrISEp software package is used to carry out the main steps involved in the derivation of the energy spectrum of the excess gamma ray events:

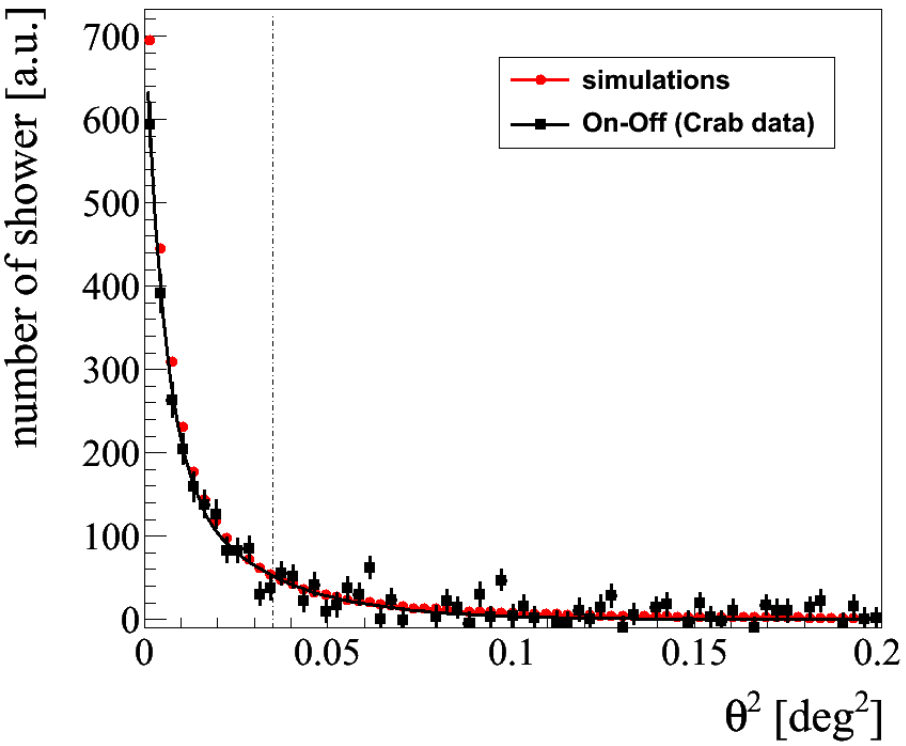

Figure 4.12 θ^2 distribution for the Crab nebula dataset fit with PSF simulated γ-rays at 20° zenith angles.

- Select gamma ray events from data using a set of optimized cut while efficiently rejecting cosmic ray initiated showers.
- Derive the gamma ray collection area for the VERITAS array.
- Reconstruct the primary energy for each particle based on the observed image parameters.
- Determine the gamma ray flux.

In the absence of a gamma-ray source with a known spectrum in the sky, the relation between the particle's energy and the recorded signal must be carefully evaluated using Monte-Carlo simulations in order to calculate the gamma-ray flux. This section outlines the method for measuring the gamma-ray flux and the energy spectrum of VHE gamma-ray sources. The method is later evaluated by applying it to the Crab Nebula observation (Section 4.6). The resulting differential energy spectrum is found to consistent with previous measurements of the Crab nebula, giving confidence in our calibration and data reduction methods.

4.5.1 GrISEp package

One of the key goals for the analysis of the VERITAS data is to extract the energy spectrum of the primary gamma ray particles. To this effect, we have made extensive use of the

Grinnell-ISU Energy-estimation Package (GrISep) to derive the VHE spectra of astrophysical sources. Developed in collaboration with the Grinnell College, GrISep is a self-contained software package that is implemented on top of C++ and ROOT. GrISep was primarily designed to allow fast, easy development and implementation of new analysis algorithms. The highly modular nature of the code allows for a highly flexible analysis chain while keeping down the code-overhead at runtime.

Developed on the *factory design pattern* (Gamma et al., 1994), GrISep consists of several independent classes (illustrated schematically in Figure 4.2) for precessing configuration parameters, calculating image parameters, implementing cuts, generating lookup tables and estimating energies. Various initial steering parameters can be specified in plain ascii input files. This provides for a highly customizable interface to change parameters and algorithms, thus allowing easy automation of the analysis.

As an input, GrISep is equipped to read the standard "Hillas" type image parameters from each triggered telescopes. These initial parameters may be calculated from any of the several different analysis routines currently used by the VERITAS collaboration, e.g, Event Display, VEGAS and GrISU. Subsequently, reconstructed shower parameters for the triggering events may be computed with GrISep. This flexibility for accepting calibrated data from different analysis package allows us to conduct several analysis in parallel for further tests and evaluation.

4.5.2 Energy estimation

The energies of the selected gamma-ray particles are not a priori known and must be deduced from the image parameters. It is generally assumed that the energy of the primary gamma-ray is characterized by detailed intensity structure of the telescope images. Therefore, one of the most useful criterion for determining the initial gamma ray energy is the total image amplitude, *size*, seen in any given shower. This is motivated by the fact that as the energy of the primary particle increases, its subsequent interaction with the atmosphere gives rise to more secondary electrons and positrons in the resulting particle cascade. The higher number of secondary particles translate to a larger amount of Cherenkov being produced in the air shower. Although only a tiny fraction of the primary energy is actually emitted as Cherenkov light, the observed light is an indirect measure of the primary energy. Figure 4.13 illustrates the dependence of *size* on the energy of the shower, where *size* scales proportionally with the energy of the primary gamma-ray events.

The total amount of Cherenkov light collected is also affected by the position of the shower cores relative to the individual telescopes, given by *impact distance* (Section 4.2.4). The light is seen by a larger fraction of the photomultiplier tubes when the shower is propagating closer to the telescope's pointing axis. Thus a greater amount of the Cherenkov light illuminates the camera. The reverse is true for showers hitting the ground farther away from the telescope, where the detectors only sample a portion of the Cherenkov light pool from the shower. This

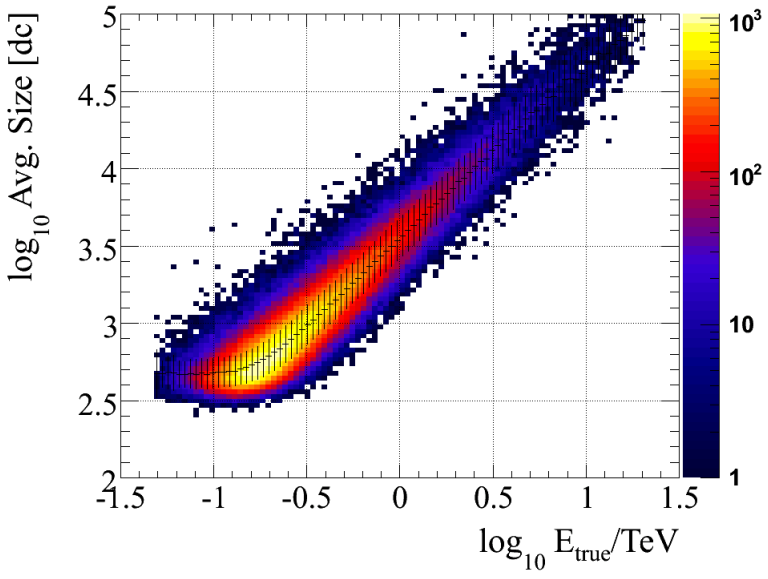

Figure 4.13 Profile histogram of size vs. energy.

not only reduces the light being deposited on the camera but may cause the corresponding shower images to truncated in the camera. Therefore, both the *size* and the *impact distance* parameters are expected to be reasonable estimators of the primary gamma-ray energy.

The standard energy estimation method for VERITAS utilizes lookup-tables created from MC simulations. A prescription for reconstructing the primary energy consists of creating tables with a two-dimensional binning in $log(size)$ and *impact distance* for each telescope. Separate tables are generated for every sets of zenith angles and azimuth angles using GrISep. The choice for the logarithmic *size* bin is motivated by the wide energy range.

Afterwards, the lookup-tables are trained with the MC simulation. During the training phase, the energy, E_{true}, for each telescope images passing the selection cut is used to fill up the tables. As a result, individual table bins accumulate the mean of $\log(E_{\text{true}}/\text{TeV})$ and the corresponding standard deviation for the simulated showers. In order to ensure a reasonable standard deviation of the estimated energy, we require at least 3 events in the addressed bin for a successful energy estimation.

Application of the lookup-table to the data yields an estimate of the particle's energy, $\log(E_{\text{est}}/\text{TeV})$ for each telescope as a function of the image amplitude and the impact parameter. Finally, the energy of the observed gamma-rays are calculated using a simple or weighted mean of the energies independently estimated for each telescopes, i.e.,

$$E_{\text{est}}(size, impact\ distance) = \frac{1}{N}\sum_{i=1}^{N} E^{i}_{\text{est}} \cdot w_i \tag{4.9}$$

where, i represents the telescope number, N is the total number of telescopes present in the reconstructed event and w_i denotes the corresponding weighting factor. Figure 4.14 shows an

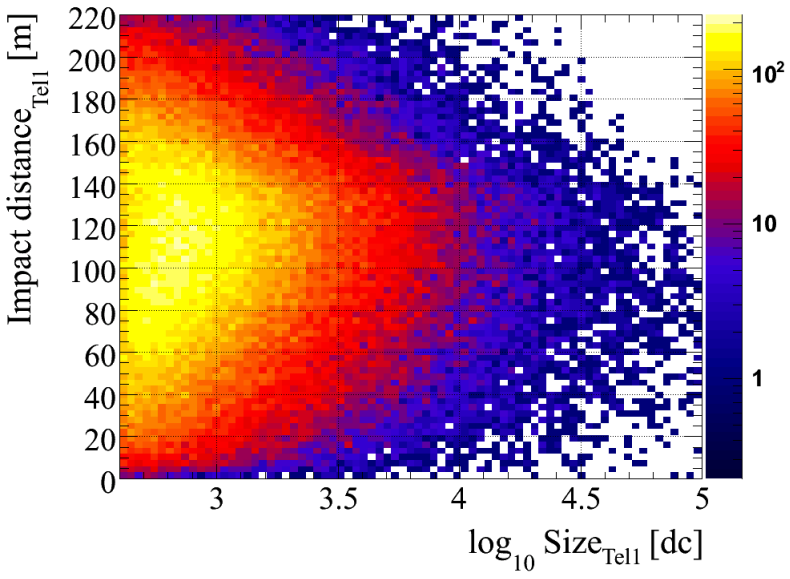

Figure 4.14 Lookup table binned in *size* vs. *distTelCore*.

example of a lookup-table for the energy of a single telescope image at a zenith angle of 20°. For a given bin in $log(size)$ and *impact distance*, the plot shows the total number of events present in each bin.

The energy resolution or the mean relative error for measuring an energy E_{est} when the true energy is E_{true} is given by,

$$\Delta E = \frac{E_{\text{est}} - E_{\text{true}}}{E_{\text{true}}} \tag{4.10}$$

The energy resolution is determined from the Monte-Carlo simulations by comparing the estimated energy with the true energy. Figure 4.15(a) shows the distribution of the difference between the log of the estimated energy and the log of the energy of the simulated gamma rays for the *spectrum-I* cuts described in the previous sections. The residual, $(\log E_{\text{est}} - \log E_{\text{true}})$ is approximately normally distributed and the RMS of the distribution is closely related to the energy resolution,

$$E_{resol}(\%) = 100 \cdot \ln(10) \cdot RMS_E \tag{4.11}$$

A Gaussian fit to the residual gives an energy resolution of 23% above $E_{\text{true}} > 250$ GeV at this zenith angle. The resolution is close to 20% at higher energies. The energy resolution typically depends on the energy. Figure 4.15(b) shows the distribution of $\Delta \log E$ as a function of the simulated energy E_{true}. It shows that the energy reconstruction gets better with increasing energy. This dependence is to be expected since collection of more light in each camera leads to smaller statistical fluctuations in the image size. Moreover, the intrinsic shower fluctuations also decrease with increasing energy of the primary gamma-ray. A reliable measure of the energy resolution is key to determining the minimum energy width of a resolvable spectral

structure for a particular analysis. It also provides the optimal binning for spectral reconstruction (Section 4.5.4). It should be noted that the energy resolution depends on the selection cuts and the quality cuts. The cuts introduced in Section 4.4 were primarily optimized for the analysis of 1ES 1218+304 along with Crab nebula observational data.

The energy bias of the spectral analysis is defined as the mean value of the fractional error, ΔE in the reconstructed energy. The mean value of the distribution of ΔE is shown as a function of the $E_{\rm true}$ in Figure 4.15(c). For a robust measurement, a relatively bias-free energy estimate is desired, i.e., the average energy of the estimated gamma ray event for a given bin be equal to the average energy of the true energies. However, for energies close to the threshold there is an unavoidable bias due to the selection affect. In the case of gamma-ray events with low energies, a sharp image cut in *size* preferentially selects events with larger reconstructed energies, which leads to a positive bias. The opposite is true at higher energies where the bias is negative as images of large energy events are truncated at the edge of the camera FOV. As a result, the reconstructed energies are systematically lower than the true energies of the gamma-ray events. Hence, to reduce large bias in the reconstructed energies, a energy threshold cut with $|\text{bias}| < 10\%$ is applied to the data. Following Aharonian et al. (2004), we compute a safe energy threshold, $E_{\rm safe}$ by simply increasing the energy threshold in the bias histogram by a factor of 10%.

4.5.3 Collection area

The energy dependent collection area characterizes the efficiency with which gamma rays are detected by the IACTs. It is also a measure of the area over which gamma rays triggers the telescopes. The collection area is modeled from the Monte-Carlo simulated events as a function of energy E and zenith angle Θ. The prescription for the derivation of the collection area is as follows: Simulated gamma ray showers drawn from a power law distribution (with a spectral index Γ) are injected into the atmosphere. The showers are randomly distributed over a circular region with radius a R_0 (typically $\sim$ 400 m) around the center of the array. This sufficiently large area ($\sim 10^5$ m^2) encompasses the typical impact parameter range of triggered showers ($\sim 0 - 250m$). The collection area, $A(E, \Theta)$, is then calculated as the fraction of the simulated gamma-ray events which trigger the detector and pass the selection cuts multiplied by the area over which the photons were thrown. Therefore, $A(E, \Theta)$ is given by

$$A(E, \Theta) = \pi\, R_0^2\, \frac{N_{\rm triggered}(E, \Theta)}{N_{\rm simulated}(E, \Theta)} \tag{4.12}$$

Where $N_{\rm simulated}(E, \Theta)$ represents the total number of simulated gamma-ray events and $N_{\rm triggered}(E, \Theta)$ gives the number of events that both trigger the detector and pass the gamma/hadron selection cuts.

The collection area is estimated as a function of the Monte-Carlo energy of the simulated events ($A_{\rm true}$). Due to the finite energy resolution and the limited detection efficiency of our

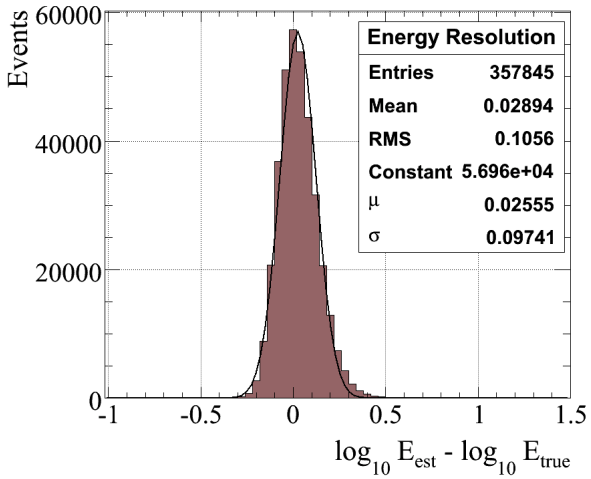

(a)

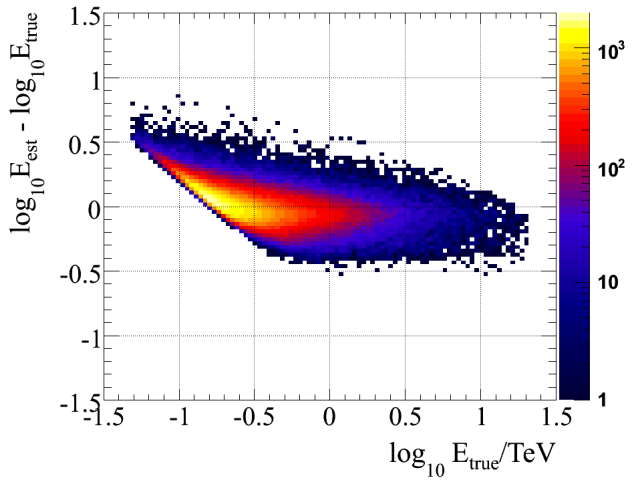

(b)

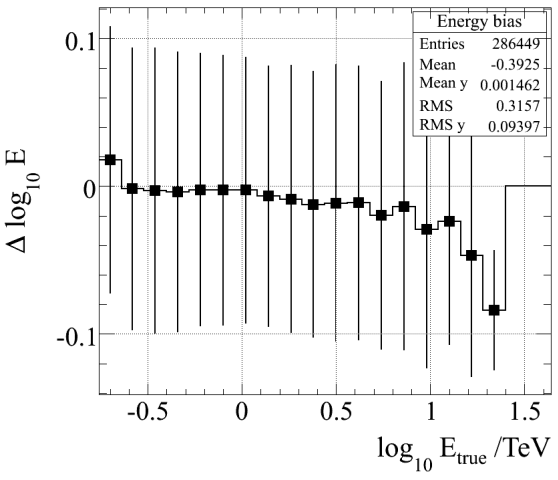

(c)

Figure 4.15 (a) Distribution of residual, (log $E_{\rm est}$ – log $E_{\rm true}$) for all energies for spectrum cuts, along with Gaussian fits to the distribution. The mean and rms for the residual is 0.0022 ± 0.0002 and 0.0093 ± 0.0001, respectively (b) The distribution of $\log_{10} \Delta$E as a function of the true energy. (c) Energy bias is shown as a function of the simulated true energy for 20° zenith angles. It is a profile plot of the distribution shown in the middle panel giving the mean of the ΔE distribution.

detector system, there exists the possibility for a spill-over where an event with a true energy, E_{true} may be misclassified as having energy E_{est}. To compensate for this effect, a modified collection area (A_{mod}) is defined which is a convolution of the collection area and the energy resolution of the detector. The modified collection area is computed by weighing the collection area in Equation 4.12 with the incident power law spectrum of the Monte-Carlo simulations and using the estimated energies, E_{est} instead of the true simulated energies, E_{true}.

Figure 4.16(a) shows both the collection area and the modified collection area at 20° zenith angle for the 2008-2009 VERITAS array configuration. To account for the weak dependence on the azimuthal angle via the geo-magnetic field, we generated one set of collection area for the northernly and one set for the southernly direction. The collection areas also depend on the position of the source in the camera due to the inhomogeneity of the response across the FOV. Therefore, the simulated source was placed at a wobble offset of 0.5°, which reflects the typical observational conditions. For the spectral measurements of the Crab, the area as derived using the *spectrum-I]* cuts assuming a source with a power law index of $\Gamma = 2.5$, which is consistent with previous measurements. Notice the fall in the collection areas at higher energies. As previously mentioned, higher energy showers with large impact parameters result in truncated images in the camera's FOV. As a result, an upper bound on the *distance* parameters preferentially rejects these high energy gamma-ray events, causing a drop-off in the collection area. It should be pointed out that the collection area (a function of the true energy E_{true}) is independent of the simulated spectrum. This is in contrast to the modified collection area which is sensitive to the source spectrum as shown in Figure 4.16(b).

While not directly relevant to the derivation of the energy spectrum, the collection area allows us to determine the effective energy threshold of a detector. Mohanty (1995) defines the energy threshold, E_{th} as the peak in the differential rate vs. the energy curve, $\mathrm{d}\,R/\,\mathrm{d}\,E$. The differential rate is calculated by folding the collection area of the detector (as shown in Figure 4.16) with the expected differential energy spectrum of the simulated gamma-ray source.

$$\frac{dR}{dE} = A(E,\Theta)\,\frac{dN}{dE} \tag{4.13}$$

The differential trigger of the VERITAS detector for a source with Crab-like source spectrum ($dN/dE = E^{-2.5}$) at 20° zenith angle is shown in Figure 4.17 where $E_{\text{th}} \sim 160$ GeV.

4.5.4 Flux and spectral measurements

Before the final derivation of the flux and the energy spectrum can be attempted, both simulated and real data are processed and reduced in an identical fashion as outlined in the previous sections. The number of gamma-ray candidate events received from the source region (ON), N_{on} and the background region (OFF), N_{off}, is determined for each sets of gamma/hadron separation cuts (Table 4.3). In order to estimate the background we use the *reflected-region* background method with 3 background regions. Following a successful energy reconstruction,

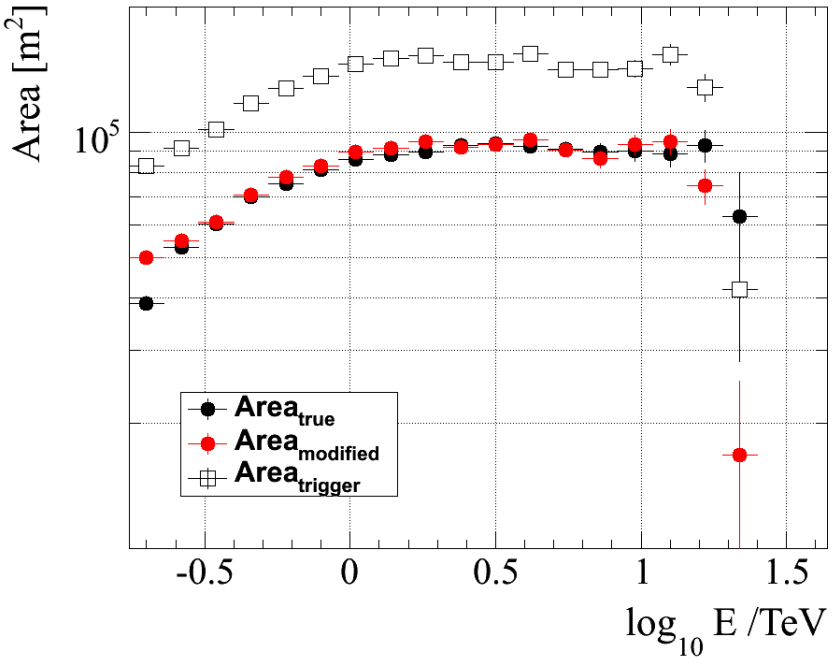

(a)

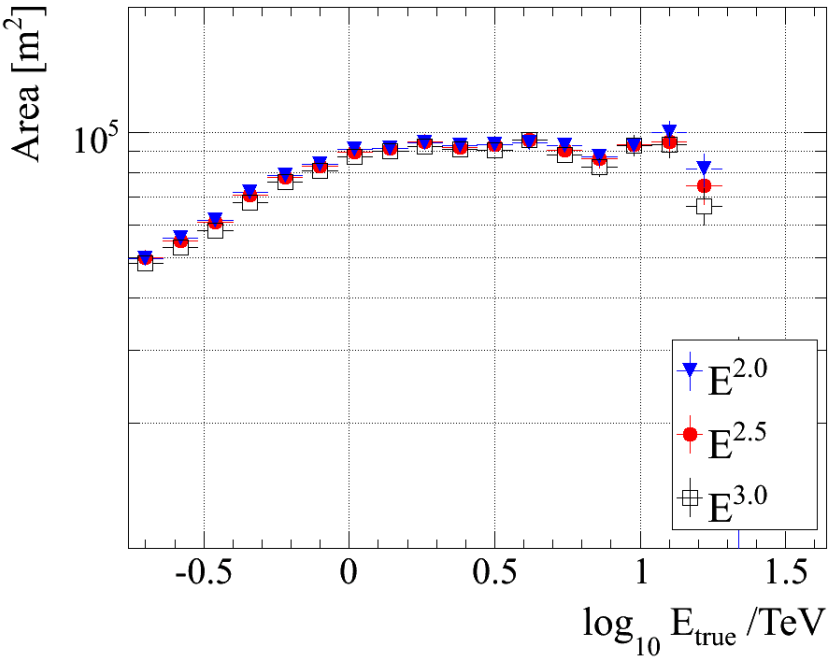

(b)

Figure 4.16 (a) Collection area (black line) and the modified collection area (red line) for the 2008-2009 VERITAS array configuration. The areas were derived using the spectrum cuts and correspond to a simulated source at 20° zenith angle with a power law index, $\Gamma = 2.5$. Also shown for comparison, the trigger collection area (open circle)(b) The dependence of the modified area on the spectral index of the simulated source.

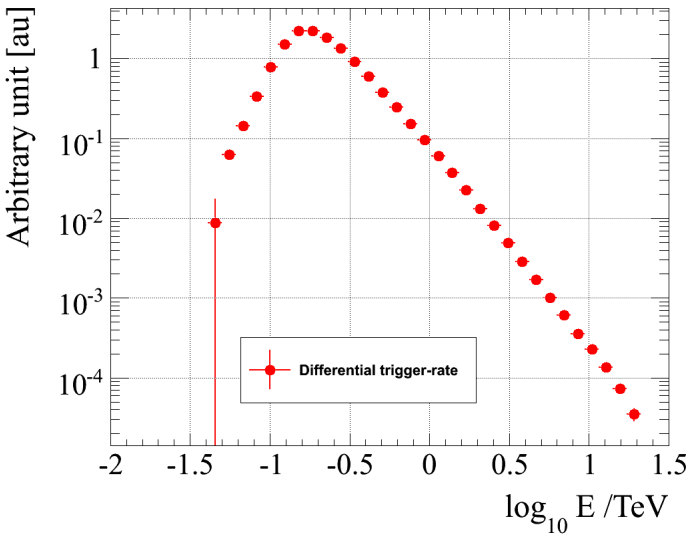

Figure 4.17 The differential trigger rate of the VERITAS array. The peak response at $\sim$ 160 GeV corresponds to the energy threshold for the hardware.

the events are binned in logarithmic energy bins of width $\Delta log(E)$. Finally, the differential gamma-ray flux, $F(E)$, for each energy bin is given by

$$F(E) = \frac{1}{t_{\rm live}\,\Delta E}\left\{\sum_{i=1}^{N_{\rm on}}\frac{1}{A_{\rm mod}(E,\Theta)} - \alpha\sum_{j=1}^{N_{\rm off}}\frac{1}{A_{\rm mod}(E,\Theta)}\right\} \tag{4.14}$$

where $t_{\rm live}$ is the total live time for the analysis and α provides the normalized acceptance factor for the background events (0.33 in this case). The finite energy resolution and the acceptance of the VERITAS detector is given by the modified collection area, $A_{\rm mod}(E,\Theta)$, as a function of energy and zenith angle of observations for the data.

For the spectral analysis, a bin size of $1/8^{th}$ per decade in $\log(E/\text{TeV})$ was chosen to account for the width of the resolution function (see for detail Mohanty, 1995). For a given run only events with an energy above $E_{\rm safe} \sim 200$ GeV are considered. We also require a significance of $> 1.5\ \sigma$ in each energy bin for the calculation of the spectrum. The significance of the excess events in each bin is given by

$$\sigma_{\rm excess} = \frac{(N_{\rm on} - N_{\rm off})}{\sqrt{\sigma_{\rm on}^2 + \sigma_{\rm off}^2}} \tag{4.15}$$

where $\sigma_{\rm on}$ and $\sigma_{\rm off}$ are the associated statistical errors for the ON and OFF data, respectively. The distribution of the ON and OFF counts roughly follow a Poisson statistics for data dominated by cosmic ray background events. Hence, for discreet bins with low counts, we can approximate $\sigma_{\rm on} = \sqrt{N_{\rm on}}$ and $\sigma_{\rm off} = \sqrt{N_{\rm off}}$, respectively. The errors in the flux measurement is

estimated using standard error propagation and it does not include the error in the calculation of the collection area.

A differential energy spectrum, usually a simple power law, of the form

$$F = I_o \times \left[\frac{E}{N\,\mathrm{TeV}}\right]^{-\Gamma} \tag{4.16}$$

is fitted to the discreet measurements of the flux and the associated errors. Here I_o is the flux normalization constant at an arbitrary energy N and Γ is the spectral index. In the case of the Crab Nebula spectrum, we set N at 1 TeV. We stress that the modified collection area is sensitive to the initial input spectrum of the Monte-Carlo simulation. As a result, an iterative approach to matching the simulated spectrum to the measured spectrum becomes necessary if there is significant deviation between the two spectra. For a power-law spectrum. the process usually converge within one iteration.

The best fit for a power law spectrum to the measured spectral points are determined using a χ^2 minimization method. For a flux $F(E_i)$ in a certain energy bin E_i and the corresponding error $\sigma(E_i)$, we define a χ^2 such that,

$$\chi^2 = \sum_{i=1}^{N} \left\{\frac{F(E_i) - I_0\,(E_i)^{-\Gamma}}{\sigma_i}\right\}^2 \tag{4.17}$$

Afterwards, the χ^2 is minimized by varying the flux normalization constant (I_o) and the spectral index (Γ) until the best fit to the power law in Equation 4.16 is achieved.

4.6 Crab Nebula Spectrum

A young supernova remnant, the Crab nebula is one of the most frequently studied objects in the gamma ray sky. First detected at TeV energies by the Whipple 10 m telescope in 1989 (Weekes et al., 1989), the VHE spectrum of the Crab nebula between 100 GeV and 50 TeV has been extensively measured by ground-based IACTS. In more popular emission scenarios, the VHE gamma rays originate from the inverse Compton (IC) scattering of shock-accelerated electrons on low-energy seed photons. The production of seed photons are mostly due to the synchrotron emission from the same population of relativistic electrons. There may also be an external contribution to the seed photons from a combination of the cosmic microwave background and local dust and starlight. The Crab nebula is commonly referred to as the 'standard candle' in TeV astronomy due to its steady IC emission along with a persistent high flux. Therefore, the observations of the Crab nebula can be used to test the reliability of both new and existing analysis methods in IACTs. In this section, I present the results of the measurement of the energy spectrum from the 2007-2008 Crab nebula database. Observations of the Crab nebula with the VERITAS array is used to test the analysis chain outlined in the previous sections. Afterwards, our results are compared with recent results from HEGRA, MAGIC and H.E.S.S.

4.6.1 Observations

The Crab nebula is routinely observed with the VERITAS array during the fall season between September and December. In addition to characterizing the emission properties of the source, these observation are essential to the study of the performance and the calibration of the detector. For the data analysis of the Crab nebula, a group of 11 20-minute data runs were chosen. These observations were carried out over a period of several dark periods during 2007 and 2008. The zenith angle of observation for the dataset ranged between 3° and 25° with a mean of 20°. A rigid quality cuts were used to select data collected under good weather conditions with stable rates and free of hardware anomalies. Each run was collected with the full array of 4 telescopes using 0.5° wobble offset in the camera FOV. The total live time for the observation was 220 minutes.

The data was processed with *Event Display* and the spectral analysis was performed with the *GrISep* package. We used the quality cuts and the shape cuts (*spectrum-I*) specified in Table 4.3 to select the gamma-ray candidate events. For the derivation of the energy spectrum, we used the *reflected* background method with 3 background regions to estimate the background. Listed in Table 4.4 are the results from the analysis of the Crab dataset including duration, the number of excess events and the significance of observations for the combined data set (See Appendix A.1 for a similar table of values for individual runs).

Table 4.4 Summary of results including excess, rates, and significance from the analysis of 2007-08 Crab nebula data set.

	Duration [min.]	ON	OFF	Excess	Rate [min^{-1}]	Significance σ	Sensitivity $\sigma/\sqrt{h}$
Crab	220	2769	1645	2214.6	10.1 ± 0.3	52.5	27.4

4.6.2 Comparison between data and simulations

For the spectral analysis, the gamma-ray simulations described in Section 4.3 were processed in the same manner as the data. In order to mimic the night-sky noise for the Crab nebula, a galactic source, an artificial noise of 200 photoelectron/ns m^2 sr were applied to the Monte-Carlo simulations. For Telescope 3, Figure 4.18 shows a comparison of "Hillas" parameters, such as *width*, *length* and *distance*, between MC and Crab data. Similar control plots were generated for each telescope in order to ensure good agreement between the MC simulation and the real data.

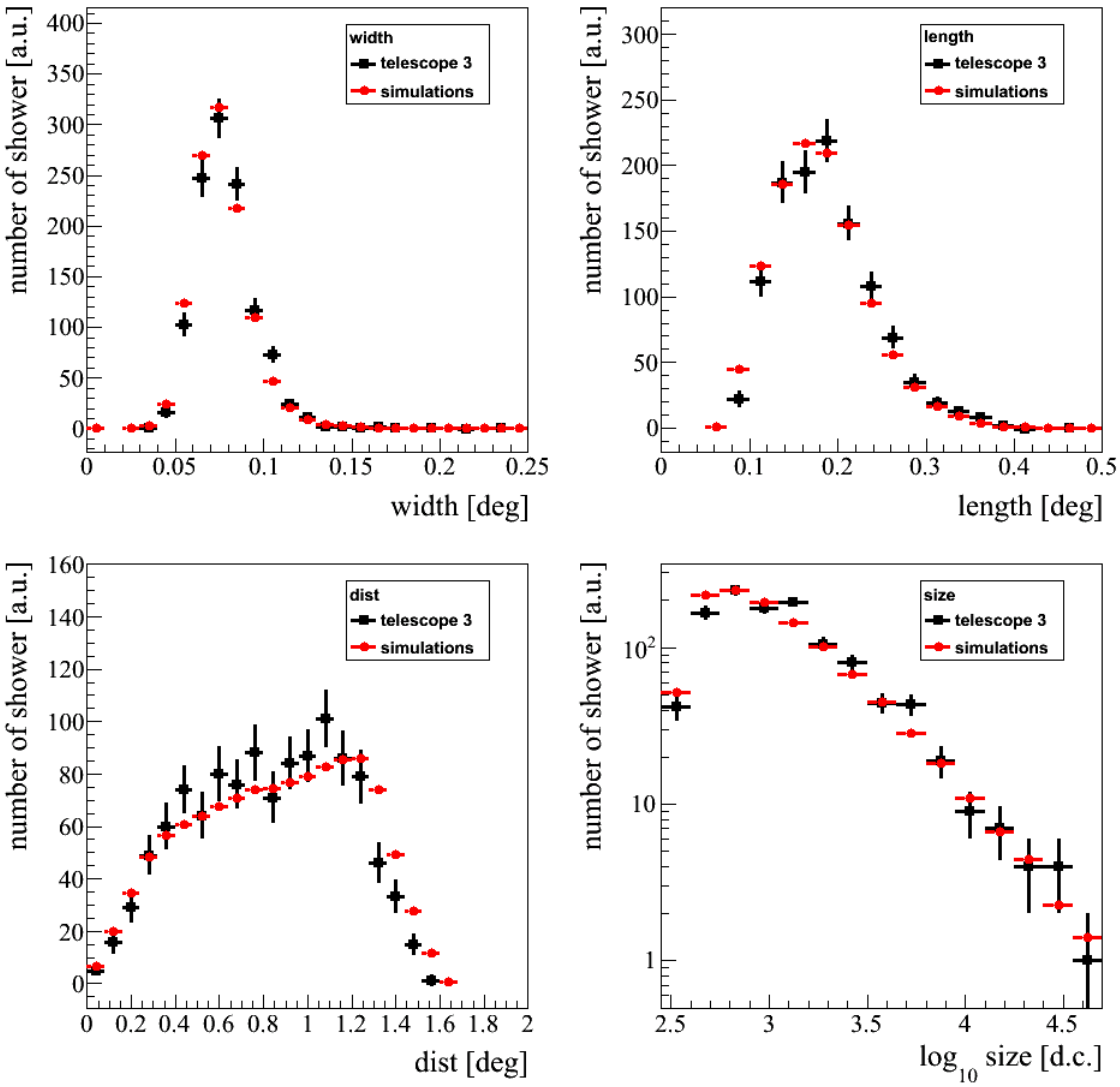

Figure 4.18 Comparison of data and the Monte-Carlo parameter distributions. The data is given by the black circles and the Monte–Carlos with solid line. The simulations are drawn from a -2.5 power law spectrum. The MRSL (MRSW) distribution was created with a cut on θ^2 and MRSW (MRSL) only. For the θ^2 distribution only MRSL and MRSW cuts were applied.

4.6.3 Energy spectrum

We derived the energy spectrum of the Crab nebula for the 2007-2008 data using the methods described in the previous sections. A summary of results from the best power law fit to the energy spectrum is shown in Table 4.5. Listed in the table are the number of excess events, significance, fluxes and the associated errors for the particular set of *spectrum-I* cuts. The energy spectrum of the Crab nebula for the VERITAS 2007-2008 dataset is shown in Figure 4.19(a) along with the residual of the fit (Figure 4.19(b)) . Also shown are past measurements of the energy spectrum with the Whipple 10m in 1994-1995, MAGIC in 2005, and H.E.S.S in 2003-2005 (Aharonian et al., 2006a). Shown in Figure 4.20 are the 68%, 95%, and the 99% confidence interval of the χ^2 minimization for the fitted Crab spectrum. The power law fit to the Crab nebula spectrum over the energy range from 0.2 TeV to 7 TeV is given by

$$\frac{dN}{dE} = (3.2 \pm 0.12_{\rm stat}) \times 10^{-11} \left(\frac{E}{1.0{\rm TeV}}\right)^{-2.43 \pm 0.03\,{\rm stat}} \ {\rm cm}^{-2}{\rm s}^{-1}{\rm TeV}^{-1} \tag{4.18}$$

The quality of the best fit is given by $\chi^2 = 8.3$, with a probability of 0.76 for 12 degrees of freedom.

Table 4.5 Crab nebula flux from 2007-08 dataset using the *spectrum-I* cut optimized for a strong source.

Energy [TeV]	Excess	σ	Actual Flux [TeV^{-1} cm^{-2} s^{-1}]	Fitted Flux [TeV^{-1} cm^{-2} s^{-1}]	Error [TeV^{-1} cm^{-2} s^{-1}]
0.2	493	18.0	1.51×10^{-09}	1.60×10^{-09}	8.39×10^{-11}
0.26	415	18.0	8.74×10^{-10}	8.45×10^{-10}	4.85×10^{-11}
0.35	294	15.7	4.25×10^{-10}	4.10×10^{-10}	2.71×10^{-11}
0.46	245	14.4	2.32×10^{-10}	2.11×10^{-10}	1.61×10^{-11}
0.6	162	11.8	1.05×10^{-10}	1.11×10^{-10}	8.88×10^{-12}
0.79	127	10.7	5.88×10^{-11}	5.67×10^{-11}	5.50×10^{-12}
1.05	98	9.5	3.18×10^{-11}	2.84×10^{-11}	3.33×10^{-12}
1.38	54	6.8	1.31×10^{-11}	1.46×10^{-11}	1.92×10^{-12}
1.82	43	6.3	7.53×10^{-12}	7.47×10^{-12}	1.20×10^{-12}
2.4	26	4.9	3.59×10^{-12}	3.81×10^{-12}	7.26×10^{-13}
3.16	23	4.8	2.37×10^{-12}	1.95×10^{-12}	4.98×10^{-13}
4.17	10	3.1	7.62×10^{-13}	9.96×10^{-13}	2.42×10^{-13}
5.5	7	2.5	4.07×10^{-13}	5.08×10^{-13}	1.63×10^{-13}
7.24	4	2.0	1.95×10^{-13}	2.61×10^{-13}	9.78×10^{-14}

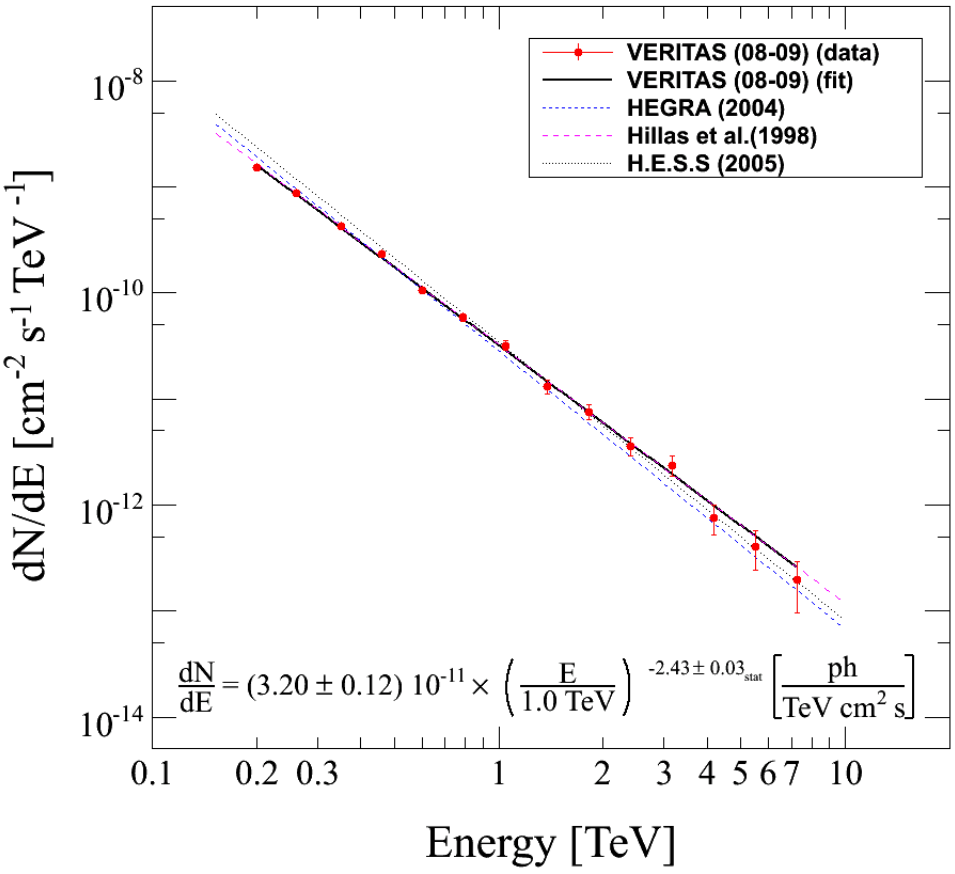

(a)

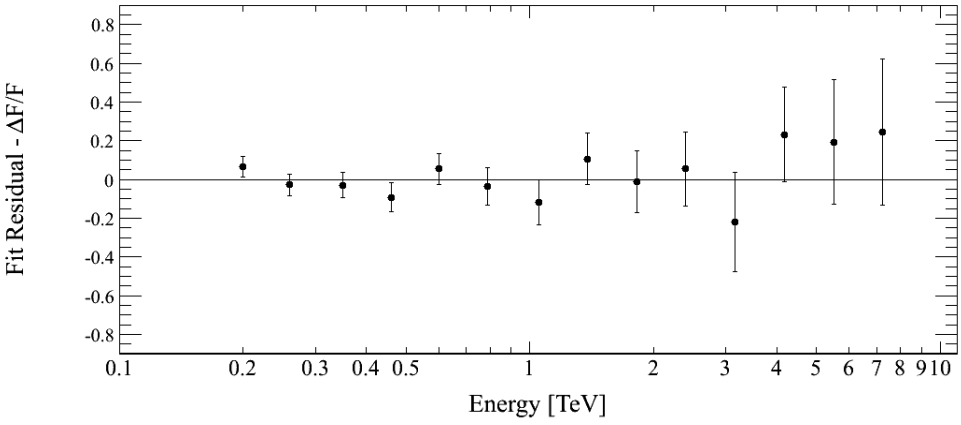

(b)

Figure 4.19 (a) VHE gamma-ray spectrum of the Crab nebula with the VERITAS array in 2007-2008 using two sets of cuts. (b) Residual of the power law fit.

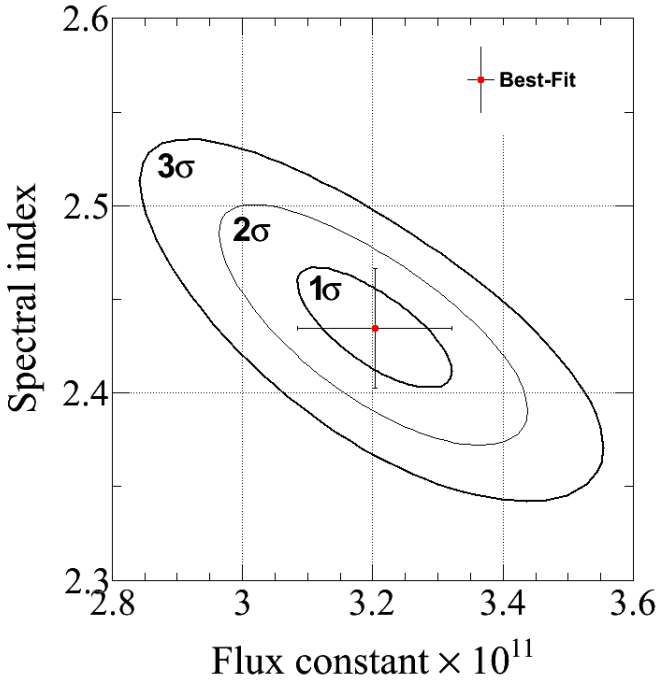

Figure 4.20 Contour plot of the 68%, 95%, and 99.9% confidence region from the χ^2 fit to a power law for the Crab nebula data set using spectrum cut. The best fit value is shown by the red point.

4.6.4 Systematic uncertainties

In addition to statistical errors, the reconstructed energy is affected by systematic uncertainties. However, most of these affects are often difficult to evaluate and only a rough estimate can be given. In this chapter, we discuss the various contributing factors in order to estimate the systematic uncertainties in the absolute flux (I_0) and the photon index Γ for best power-law fits to the reconstructed energy spectrum. The most important systematic effects are:

1. **Photon losses in the optical system**: The telescope optical system consists of mirrors and Winston light cones. The overall mirror reflectivity is assumed to be $\sim$ 85% in our MC data which agrees reasonably well with measurements. However, in the desert climate of Southern Arizona, the mirrors are prone to accumulate dirt/dust leading to a degradation in reflectivity with aging. Additional optical parameters such as the mirror alignment on the PSF and photon losses in the light cones contribute to the systematic error on the absolute flux measured. We make a reasonable guess to estimate the systematic error due to these effects to be approximately $\pm$5%.

2. **Detector model**: One of the most crucial sources of systematic errors arises from the uncertainties in the overall charge-to-photoelectron conversion factor. This quantity is

dominated by a combination of factors including the geometry of the PMT surface, poor knowledge of the PMT signal-to-noise ratio, photocathode uniformity (i.e., variation of the output signal as a function of the photocathode position), non-linearity in PMT gain, the amplifiers, light collection efficiency of the first PMT dynode, the spread in quantum efficiency of PMT, and number of dead or inactive PMTs in the camera. As a consequence of changes to the overall calibration of pixel intensities, the Hillas *size* parameter for triggered events might be over/under estimated, and thus affecting both absolute flux and the spectral index of the spectrum. We estimate the systematic error due to uncertainties in the charge-to-pe conversion factor by artificially scaling up (or down) the *size* parameter in the MC simulation. The resulting uncertainties are estimated to be on the order of $\pm 15\%$ on I_0 and ± 0.1 on Γ. Additional uncertainties in the trigger inefficiencies are caused by variations in the CFD settings and electronics along with integration window for the FADC pulse. These factors primarily affect the energy threshold of the instrument but their affects may be neglected due to the application of efficient software cuts during offline analysis.

3. **Variations in the atmospheric conditions**: The atmospheric model used in the MC simulation (the U.S. standard atmosphere 76) does not address variations in the real weather conditions such as the humidity, high clouds, atmospheric temperature and pressure. Our limited ability to model the day-to-day environmental conditions e.g., presence of dust and aerosol in the air, also produces uncertainty in the experiment. In general, atmospheric and environmental parameters may lead to an underestimation of the measured flux. For reasonably small zenith angles, the resulting systematic effect on the flux level is estimated to be $\pm 5\%$ (see e.g., Krennrich et al., 1999).

4. **Difference between MC simulation and data**: Systematic differences between simulated and real gamma-ray data may affect the efficiency of the selection and gamma/hadron separation cuts in the analysis. Consequently, events may be misclassified or assigned wrong energy leading to systematic errors on the determination of the effective collection areas and thus on the flux and the spectral index. In the absence of a straightforward method to evaluate the systematic uncertainties due to the possible difference MC and data, we estimate the errors by varying the cuts on *mrs*-parameters and θ^2 about the optimized cut values. We conclude the systematic errors due to these effects to be ± 10 on the flux and ± 0.1 on the spectral index.

The overall systematic uncertainty to the flux is estimated from the above list by adding different sources of error in quadrature and found to $\sim 20\%$. Similarly, the net systematic uncertainty in the calculation of the spectral index is found to be ± 0.14. We note that most of the relevant contributors to the systematic error produce an underestimation of the measured gamma-ray rate or lead to an overestimation of the efficiency of the system. The overall effect

is an underestimation of the flux. Therefore, large systematic errors affecting the measurements may be minimized or yet better understood by carrying out more detailed studies of MC simulations. Furthermore, careful measurements with routine monitoring of the different telescope subsystems should pursued to reduce the influence of the systematic errors on our measurements.

CHAPTER 5. VHE GAMMA-RAY FLARE FROM 1ES 1218+304

This chapter details the observations which led to the discovery of a prominent VHE gamma-ray flare from the blazar 1ES 1218+304. Beginning December 2008 till May 2009, the VERITAS Collaboration led an intensive monitoring campaign of the distant BL Lac object, 1ES 1218+304. The majority of the data was collected during the month of January through April in 2009. In January 2009, VERITAS detected an increased VHE gamma-ray emission from 1ES 1218+304 showing significant day-scale flux variations. This chapter presents the analysis of these data collected by VERITAS. The derivation of the energy spectrum of the source is also outlined. Finally, the implications of the observed flux variability is discussed for shock acceleration scenarios in relativistic jets, and in particular the viability of kiloparsec-scale jet emission scenarios. The discovery of variable VHE gamma-ray emission from 1ES 1218+304 with the VERITAS telescopes was published in Acciari et al. (2010a).

5.1 Overview

First detected by the Ariel-5 X-ray satellite (Cooke et al., 1978), 1ES 1218+304 was one of the earliest BL Lac objects to be discovered based on its X-ray emission (Ledden et al., 1981). Initially identified with the high galactic-latitude X-ray source 2A 1219+305, the object was later classified as a BL Lac object using optical and radio counterparts (Wilson et al., 1979). The source has been the subject of extensive multiwavelength campaigns, and for the purpose of this thesis, the common name 1ES 1218+304 from the Einstein Slew Survey is adopted (Elvis et al., 1992).

Located at a redshift of $z = 0.182$ (Bade et al., 1998; White et al., 2000), 1ES 1218+304 resides in an elliptical host galaxy with luminosity $M_R = -23.56$ with a super-massive black hole mass of $\log(M_{BH}/M_{\odot}) = 8.58$ (Urry et al., 2000). The source morphology has been closely studied in the optical to near-infrared band by different observatories (Falomo et al., 1999; Kotilainen et al., 2004). Optical observations using the Hubble Space Telescope (HST) (Woo & Urry, 2002) have resolved the host galaxy and found that the BL Lac nucleus is well centered in the main body of the host galaxy (Falomo et al., 2000). Long-term optical monitoring of the source (Figure 5.1) has revealed that optical emission from 1ES 1218+304 typically varies on the timescale of months (Pica et al., 1988).

In the radio wavelengths, VLA maps (Figure 5.2(a)) of the object (Laurent-Muehleisen et

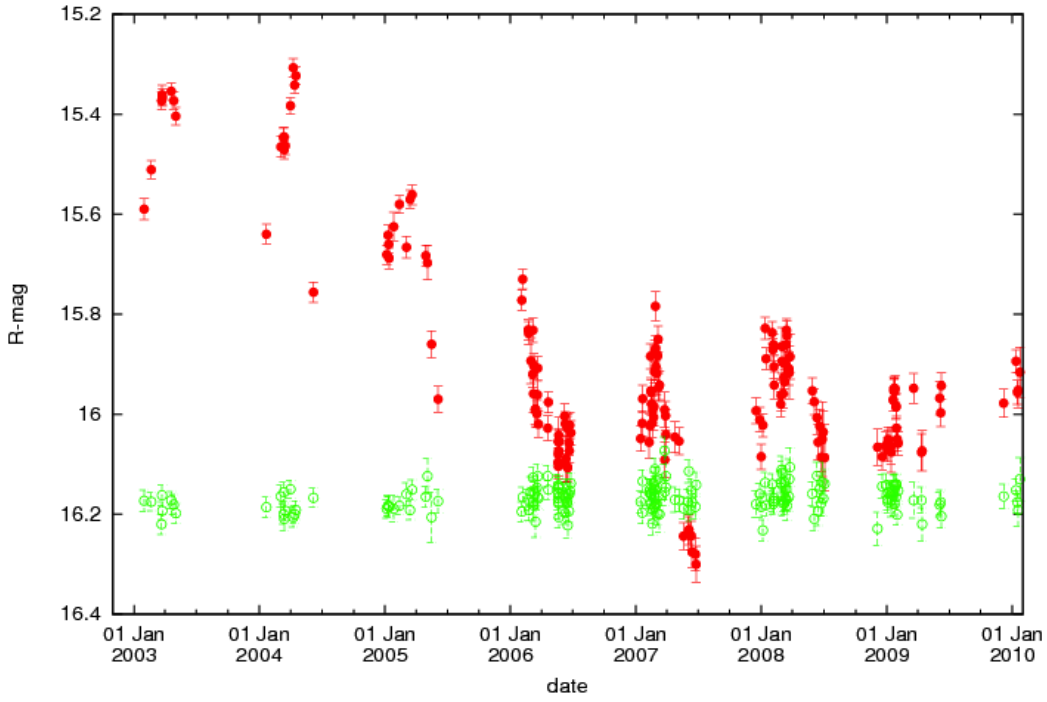

Figure 5.1 Long-term optical monitoring of 1ES 1218+304 reveals variations over timescale of months. (Pica et al., 1988)

al., 1993) along with VLBA observations (Figure 5.2(b) have confirmed (Giroletti et al., 2004) that the source is compact on kiloparsec scales. Giroletti et al. (2004) places an upper limit on the size of the jet at 0.7 kpc and deduces the Doppler factor to be in the range of $\delta = 1.9 - 3.7$. The radio properties of the jets of AGN are a valuable tool for constraining the bulk Lorentz factor and the jet angle with respect to the observer's line-of-sight.

The blazar 1ES 1218+304 is particularly well-studied in the X-rays. Moreover, frequent target of opportunity (ToO) observations are carried out by the *Swift* and the *RXTE* observatories. The *Beppo*SAX X-ray Astronomy Satellite observed the source on 12 July 1999 and measured a 2-10 keV flux about 1.5×10^{-11} erg cm^{-2} s^{-1} with a peak energy of $E_p = 0.7$ keV (Giommi et al., 2005). The *Beppo*SAX spectral data is well described by a log-parabolic model and gives a curvature $b = 0.37 \pm 0.03$.

In October 2005, 1ES 1218+304 was observed twice by the *Swift* Satellite yielding a flux level similar to that observed by *Beppo*SAX (Tramacere et al., 2007). Despite limited statistics, power law best fits to the *Swift* data shows a decrease in the flux level by 35% and points to a variation of the photon index. Figure 5.3 (Blustin et al., 2004) shows the 2-10 keV fluxes of 1ES 1218+304 observed with various different X-ray observatories.

The *Suzaku* X-ray satellite observed 1ES 1218+304 later in May 2006 for a total of 79.9 ks with the XIS and HXD instruments. During observation, *Suzaku* detected a prominent flare

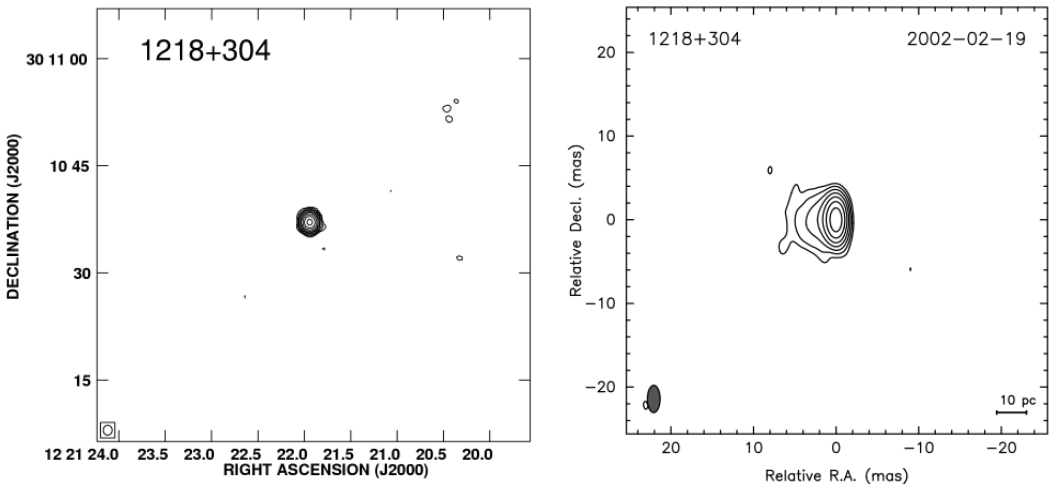

(a) (b)

Figure 5.2 Images of 1ES 1218+304 from (a) VLA and (b) VLBA observations respectively. (Laurent-Muehleisen et al., 1993; Giroletti et al., 2004)

in the 5-10 keV flux where the flux changed by a factor of ∼2 over a timescale of 5×10^4 s (Sato et al., 2008). More interestingly, the hard X-ray variation during the large flare clearly lagged behind that in the soft X-rays. This is a clear deviation from past observations where soft X-rays usually lagged behind the hard X-ray. The authors attribute the time difference to the energy dependence of the electron's acceleration time. The non-contemporaneous spectral energy distribution of 1ES 1218+304 with currently available data set including the *Suzaku* observations (Sato et al., 2008) is presented in Figure 5.4. Given the synchrotron peak in the SED of 1ES 1218+304 is located in the hard X-ray, the source is, therefore, classified as high-frequency peaked BL Lac (HBL)object (Donato et al., 2001).

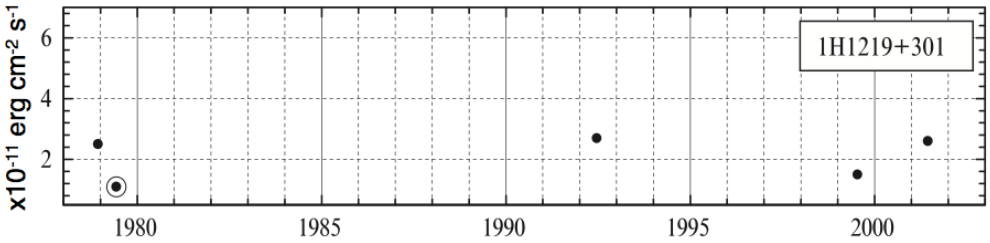

Figure 5.3 10 keV fluxes of 1ES 1218+304 observed with Einstein, ROSAT, BBXRT, ASCA, BeppoSAX and XMM-Newton. The circled points correspond to observations where intrinsic absorption was reported.

5.2 Gamma-ray Observations

1ES 1218+304 was observed by the EGRET experiment on board the CGRO between 1991 and 1992. Subsequent non-detection placed the EGRET 95% confidence upper limit for 1ES 1218+304 at (>100 MeV) 1.7×10^{-7} cts. cm^{-2} s^{-1} (Lin et al., 1996). The source was later followed-up with the Whipple Observatory between 1995 and 2000 without a successful detection. An upper limit on the integral flux above an energy threshold of 350 GeV of 8.3×10^{-8} cts. cm^{-2} s^{-1} (corresponding to 8% of the Crab Nebula flux) was reported by Whipple (Horan et al., 2004). Observation of 1ES 1218+304 by the HEGRA Collaboration also resulted in an 99% upper limit on the integral flux F(>840 GeV) = 2.67×10^{-12} cts. cm^{-2} s^{-1} (corresponding to ∼12% of the Crab Nebula flux), considerably higher than previous upper limits (Aharonian et al., 2004).

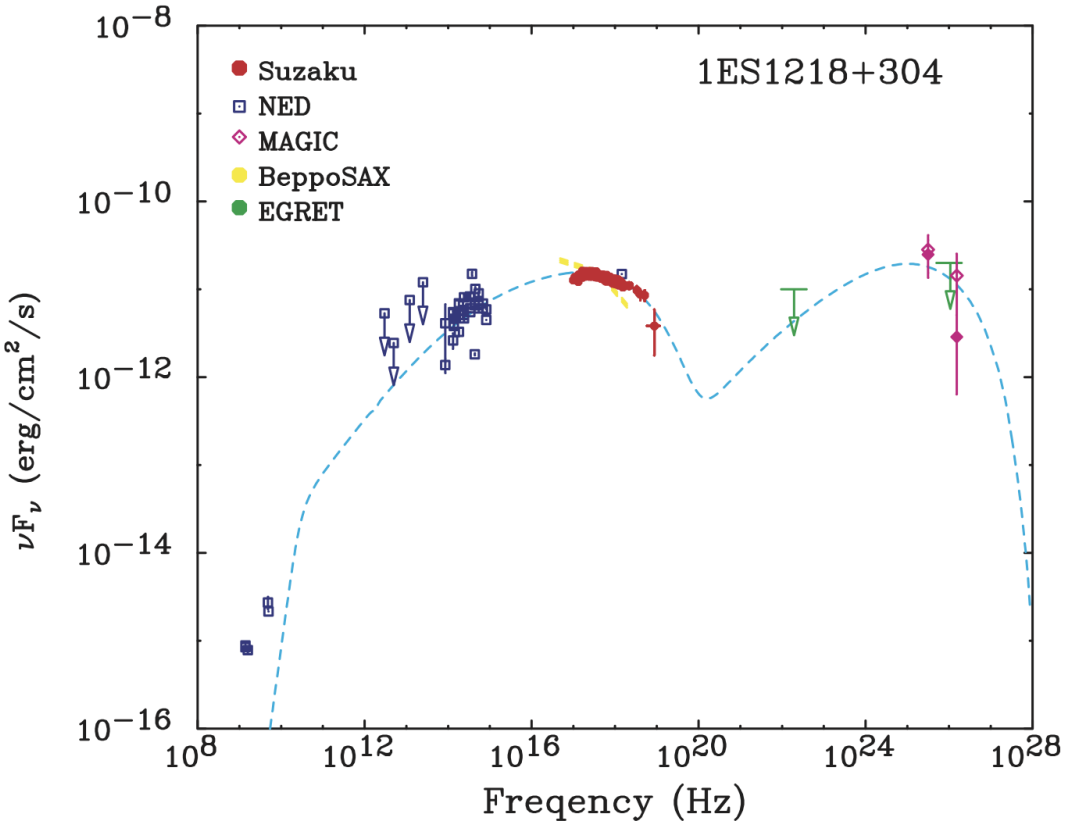

Figure 5.4 Broadband SED of 1ES 1218+304 (Sato et al., 2008). Filled circles represent *Suzaku* data. The EBL corrected TeV data is given by the open diamond symbols. The spectral fit corresponds to a one-zone SSC model.

Based on its typical broadband characteristics with high radio and X-ray fluxes, various authors (e.g., Fossati et al., 1998; Costamante & Ghiselellini, 2002) have suggested 1ES 1218+304

as a promising candidate for detection at VHE gamma-ray with ground-based detectors. By requiring sufficient number of energetic electrons and a high density of seed photons in order to produce TeV photons via inverse Compton process, (Costamante & Ghiselellini, 2002) predicted an integral flux F($>$ 300GeV) = 1.6×10^{-12} cts. cm^{-2} s^{-1} (corresponding to $\sim$1.3% of Crab Nebula flux) based on SED modeling of the source.

In 2005 January, the MAGIC Collaboration reported the first clear detection of VHE gamma-ray emission from 1ES 1218+304 with an energy threshold of 120 GeV (Albert et al., 2006a). After 8.2 hours of observation over a period of 6 days, gamma-ray signal was detected at a level of 6.4 standard deviations σ. The integral flux above 100 GeV was found to be F($>$ 100GeV) = $(8.7 \pm 1.4) \times 10^{-7}$ photons m^{-2} s^{-1}, substantially smaller than the upper limits calculated by either Whipple or HEGRA. The resulting gamma-ray light curve did not indicate any significant time variability from the source. The measured differential energy spectrum could be described by a simple power law with a photon index of -3.0 ± 0.04,

$$\frac{dN}{dE} = (8.1 \pm 2.1) \times 10^{-7} \left(\frac{E}{250\text{GeV}}\right)^{-3.0 \pm 0.4\,\text{stat}} \text{ m}^{-2} \text{ s}^{-1} \text{ TeV}^{-1} \quad (5.1)$$

During the MAGIC observations, 1ES 1218+304 was simultaneously monitored at optical wavelengths by the 1.03 m telescope at the Tuorla Observatory, Finland and the 35 cm telescope at KVA Observatory on La Palma, Canary Island, Spain. However, optical observations did not yield any signs of variability from the source.

The VERITAS collaboration later confirmed the MAGIC detection in 2007 (Acciari et al., 2009a). 1ES 1218+304 was observed as part of the blazar monitoring program to measure the intensity and spectrum of the extragalactic background light. A total of 17.4 hours of observations of 1ES 1218+304 were carried out between 2006 and 2007. The main results of which are summarized in Table 5.1. The source was detected with a statistical significance of 10.4 σ. Figure 5.5(a) (right panel) shows the distribution of θ^2 for excess VERITAS events from the source during the 2006-2007 season. The light curve of the integral photon flux above 200 GeV for the source is shown in Figure 5.5(b) (left panel). Each point corresponds to one observation night. The average integral flux ($\phi > 200$ GeV) for the source was calculated to be $(12.2 \pm 2.6) \times 10^{-12}\,\text{cm}^{-2}\,\text{s}^{-1}$, which corresponds to $\sim$6% of the Crab Nebula flux. During three months of observations in 2006-2007, VERITAS did not detect any evidence for time variability in the VHE gamma-ray emission from the source. The resulting differential energy spectrum of 1ES 1218+304 between $\sim$160 GeV and $\sim$1.8 TeV is given by,

$$\frac{dN}{dE} = (7.5 \pm 1.1_{stat} \pm 1.5_{sys}) \times 10^{-12} \left(\frac{E}{500\text{GeV}}\right)^{-3.08 \pm 0.34\,\text{stat} \pm 0.2\,\text{sys}} \text{ cm}^{-2} \text{ s}^{-1} \text{ TeV}^{-1} \quad (5.2)$$

The results from the VHE observations of 1ES 1218+304 by VERITAS was found to be statistically consistent with measurements carried out by the MAGIC collaborations (Acciari et al., 2010a).

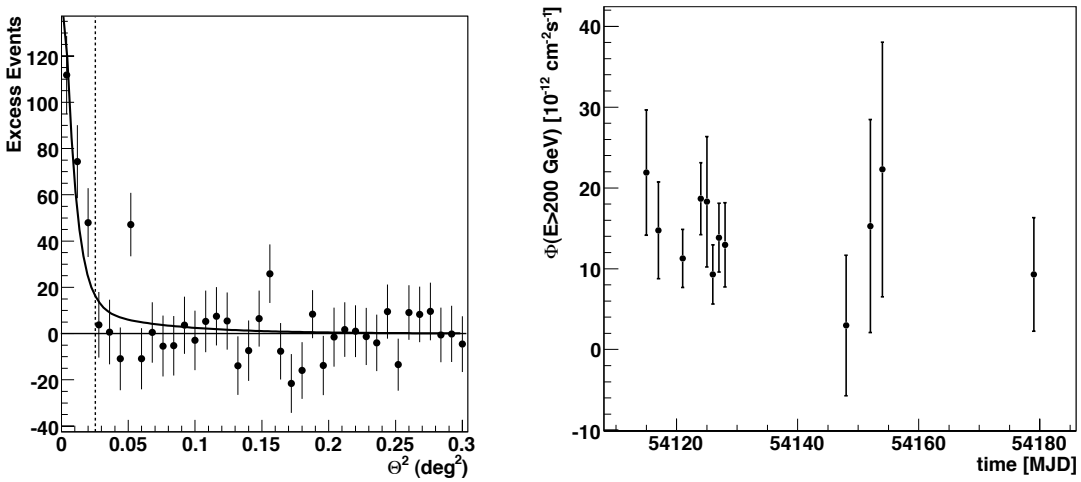

(a) θ^2 plot

(b) Light curve

Figure 5.5 (a) θ^2 plot for 1ES 1218+304 during the 2006-2007 season. (b) Light curve of the integral photon flux above 200 GeV for the source 1ES 1218+304. The individual data points correspond to the averaged daily flux assuming a spectral shape of $dN/dE \propto E^{-\Gamma}$ with $\Gamma = 3.08$ (Acciari et al., 2009a)

5.3 Observations and Results (2008-2009)

As part of the Key Science Project in 2008-2009, the VERITAS Time Allocation Committee granted $\sim$ 45 hours for an intensive joint monitoring campaign of the known TeV blazars 1ES 1218+304 and W Comae. Since the sources are separated by only 2° in the sky, an observation strategy involving alternating the *wobble* direction between the two source was recommended. Both sources were observed from December 24, 2008 through May 18, 2009. Beginning January 25, 2009, a preliminary analysis indicated that the blazar 1ES 1218+304 was in an elevated state. Subsequently, the focus of the joint campaign shifted to an extensive targeted monitoring of 1ES 1218+304. During the months of January and February in 2009, 1ES 1218+304 was given an additional 10 hours of observing time from the Director's discretionary time budget. Considering the indications of a heightened emission from 1ES 1218+304, a contemporaneous multiwavelength observations with the *RXTE* satellite was invoked from 2009 February 1 through February 3 for a total of $\sim$ 138 minutes. Later, the source was followed up with *RXTE* from 2009 February 21 to 2009 March 6 as part of a pre-organized multiwavelength campaign.

In this section the first detection of variable VHE gamma-ray emission from 1ES 1218+304 is described in detail. A complete description of the data sample (Section 5.3.2) along with

Table 5.1 Summary of observations and analysis of 1ES 1218+304. Shown are the integral flux above 200 GeV in 2008-09 assuming a spectral index of $\Gamma = 3.16$, and the corresponding flux in units of the Crab nebula flux over 200 GeV. [a]See Acciari et al. (2009a).

Observation period	Live Time hr	Zenith deg.	Significance σ	$\phi(> 200$ GeV) 10^{-12} cm^{-2} s^{-1}	Unit of Crab nebula Flux(E > 200 GeV)
2008-2009	26.7	2–30	23.3	$20.5 \pm 1.0_{stat}$	0.09 ± 0.004
2006-2007[a]	17.4	2–35	10.4	$12.2 \pm 2.6_{stat}$	0.05 ± 0.011

the selection criteria applied to ensure the analysis of good quality data is presented. In the following section (Section 5.3.3), I will examine the results from of the VERITAS analysis of 1ES 1218+304 during the 2008-2009 observing season. Finally, the derivation of the energy spectrum of 1ES 1218+304 for the most recent observations is discussed in Section 5.3.4.

5.3.1 Observations

1ES 1218+304 is best viewed between December and June. Figure 5.6 shows the visibility plot for 1ES 1218+304 from the VERITAS observatory. In 2008 and 2009, a total of 131 observing runs were attempted on 1ES 1218+304 with the full VERITAS array. On a few occasions, data was collected with only two telescopes. To simplify the data analysis and to remove any systematic affects, the final dataset was restricted to data collected with three or more telescopes.

The source was observed at zenith angles between 2° and 36°. Figure 5.7 shows the distribution of zenith angles and azimuthal angles for all the data surviving the quality cuts. The majority of the runs were observed for a duration of 20 minutes. The individual observation time for all runs surviving the quality cuts is tabulated in Appendix A. All observations were performed in the *wobble* mode (Section 4.1) with a 0.5°, which allows for simultaneous background estimation. To reduce bias and to ensure uniform response across the camera, great care was taken to collect data with an even distribution of all the 4 wobble directions (North, South, East, and West).

5.3.2 Data sample

In order to reject runs affected by poor weather conditions and other anomalies, quality selection cuts were routinely applied to the data. This is necessary to reduce the systematic effects on the measured flux and the energy spectrum of the source. Every data run in the 1ES 1218+304 dataset was checked against the available FIR data. Runs with highly fluctuating FIR readings were discarded as this indicates significant cloud cover in the sky. An example

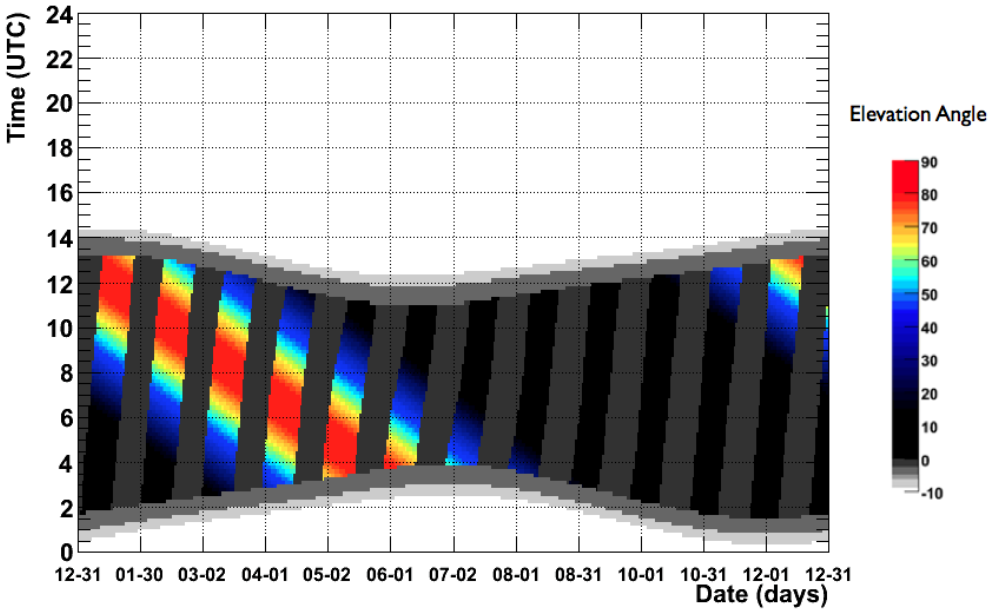

Figure 5.6 Yearly visibility plots for the VERITAS Observatory location. *Courtesy*: TeVCat - http://tevcat.uchicago.edu

of a data run with irregular FIR rate is shown in Figure 5.8(a). Note the sudden increase in FIR temperature 8 minutes into the bad run as clouds move in over the cameras. This was later confirmed by the observer's log detailing the accounts of the night. Contrast this with a good quality data characterized by a stable FIR temperature throughout the duration of the run (Figure 5.8(b)). In addition, only nights rated B (Section 4.1) or betters were used for final analysis. This excluded runs taken under extreme weather conditions, e.g., hazy sky or gusty weather.

The trigger rates were closely verified during the collection of data. Unusual rate dips or spikes in the trigger rate often point to hardware or software issues. Moreover, the estimation of the effective live-time for an observation is sensitive to the trigger rate. In particular, the L3 rate was carefully monitored to ensure that the mean rate stayed close the predicted value (around 250–300 Hz for four telescope data). Since runs with significant variations in the L3 rates point to problem with the data acquisition system, such run were removed from final analysis. Figure 5.9(a) compares stable rates with an instance where the data acquisition system went offline for a brief 30 second (Figure 5.9(b) period during the course of a run. For quality selection, the author routinely followed-up on various hardware reports in order to remove data collected in non-optimal conditions. This involves discarding data from those rare nights when the system is plagued by substantial hardware troubles such as faulty preamps or DAQ failure.

The individual PMTs in the VERITAS cameras are programmed to be switched off in the

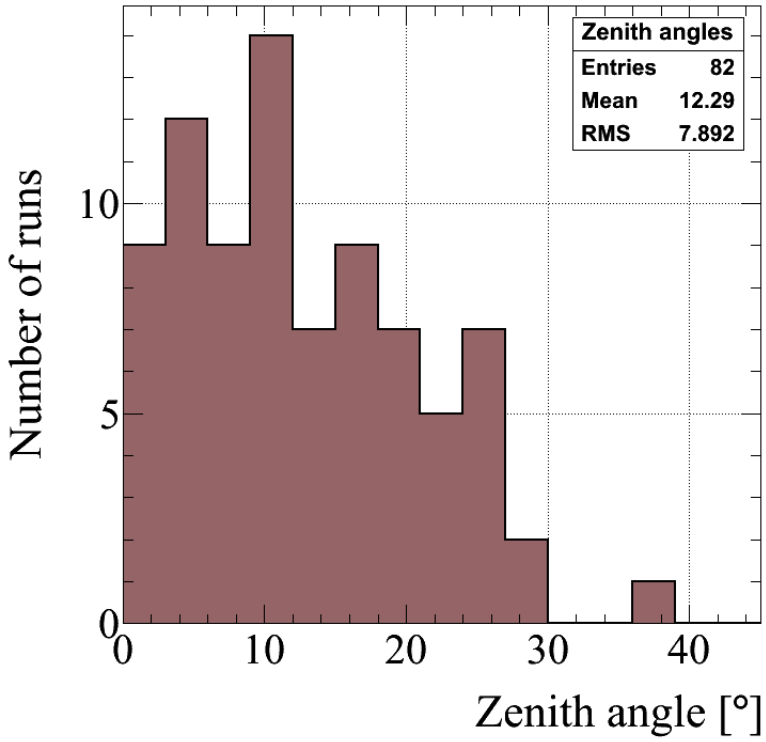

Figure 5.7 Zenith distributions

presence of over-current at the PMT cathode. This is often the case when an especially bright star image crosses the FOV of the camera. While the PMTs are brought back online as soon as the star transits through the PMT, unexpected phenomena such as lightning, airplane or satellite passing through the FOV may cause the PMT to be inactive for the remainder of the run. Therefore, a quality cut has been adopted to reject runs with more than 10% of the PMTs missing at any one time. Fortuitously, no runs were lost due to the PMT selection cut in the case of 1ES 1218+304. We also note that on January 27, the laser system for gain calibration was found to be broken. Later, the local observers discovered that the photo-diode relay fiber for one of the telescopes (T2) was substantially damaged. The laser system was later brought back online the following week after repair. Therefore, the laser run collected on the night of January 24 was used to calibrate data from all subsequent nights through February 5, 2009.

In the 2008-2009 1ES 1218+304 dataset, a total of 82 runs survived the quality selection cut (labeled 08-09 data thereafter). This corresponds to a total live-time of 27.2 hours for signal search and spectral analysis. The zenith angle of observation for the quality dataset ranged between 2° and 30°, with a mean of 12°. A detailed description of the quality dataset along with the corresponding laser runs may be found in Tables A.

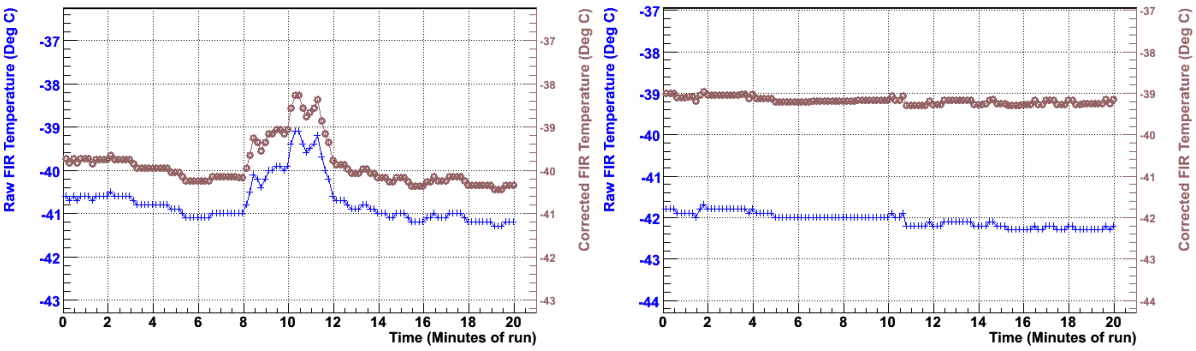

(a) Poor FIR reading

(b) Stable FIR reading

Figure 5.8 The FIR temperature data for a bad run is compared with that of good run. (a) An Unstable FIR reading indicates the presence of cloud in the FOV of the camera. (b) shows stable FIR readings for a good quality run

5.3.3 Results

The raw data from 08-09 dataset was processed with *Event Display* (version 3.30) following the methods described in Chapter 4. Following calibration and cleaning, shower images recorded by the individual telescopes were parameterized with a Hillas-type (Hillas, 1985a) second-moment analysis. Afterwards, the shower direction and the projected shower impact point on the ground are determined using stereoscopic reconstruction of the air shower. MC simulations were treated in an identical fashion.

Cuts on the image intensity (*size*), mean scaled shower parameters (MRSL, MRSW), and θ^2 were applied to reject background events and maximize the detection significance. For the purpose of the source search in the sky, the gamma/hadron cuts were optimized a priori for a source with a 10% of Crab Nebula flux (Section 4.4). ON source events were estimated using a circular region of radius θ around the nominal source position as described in Section 4.4.3. Finally, the background or OFF source counts were estimated using off-source *reflected regions*.

Two sets of cuts were considered for this work, *standard* and *spectrum-II* cuts. Table 4.3 details the different values used for both sets of cuts. While the MRSL and MRSW values are the same for both the cuts, they differ in the θ^2 cut used. In addition, the number of off-source regions used in the *standard* and *spectrum-II* cuts are 7 and 3, respectively. The *standard* cuts are optimized for greatest source significance by maximizing the background rejection. However, for an established source the θ^2 cut (*spectrum-II* cut) was relaxed in order to retain a higher number of gamma-ray candidate events. Subsequently, the number of OFF source regions were reduced to 3 in order to prevent contamination from the ON source region. The *spectrum-II* cut has the advantage of a reduced energy threshold compared to the *standard*

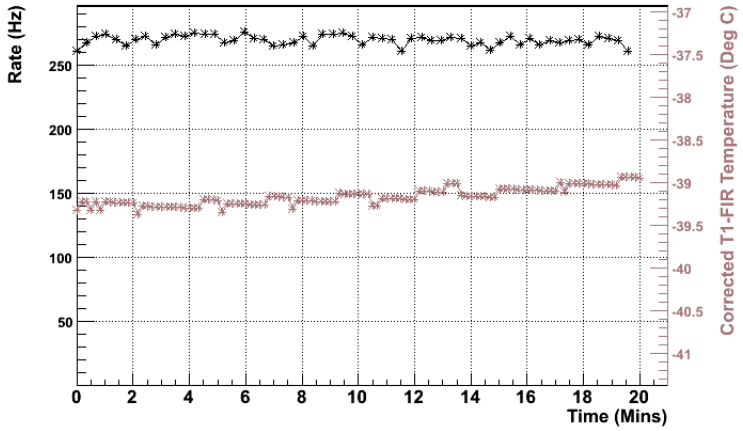

(a) stable L3 rate

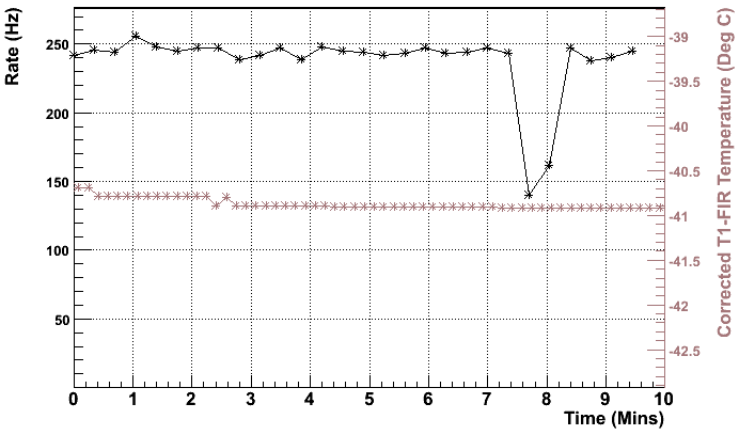

(b) unstable L3 rate

Figure 5.9 A comparison of the L3 rates for a good and bad run. (a) Good: The trigger rate is stable for the entire duration of the run. (b) Bad: A sudden drop in the L3 rates resulted from the *EventBuilder* system going offline for 30 seconds.

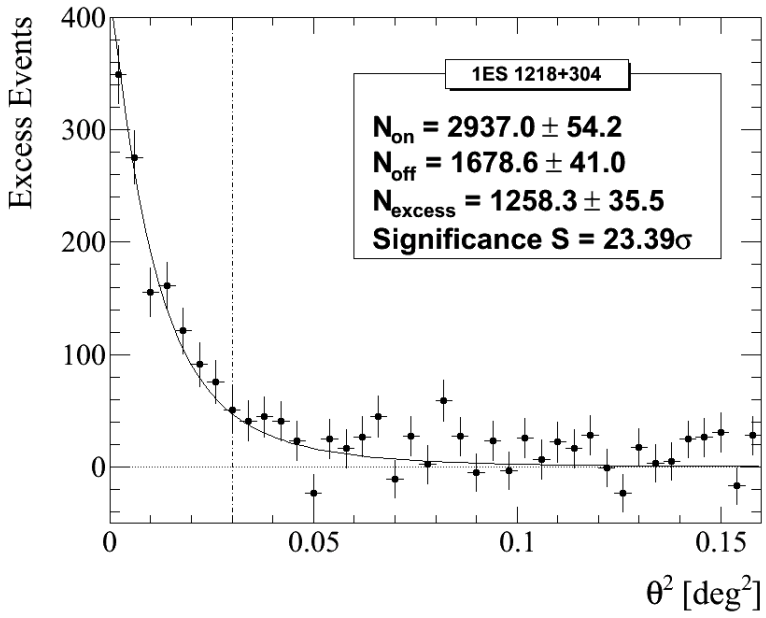

Figure 5.10 Distribution of θ^2 for excess events ON-OFF from the observations of 1ES 1218+304. The dashed-dotted line shows the boundary of the signal region for the spectrum cuts ($\theta^2 = 0.03°$). The solid curve indicates the expected θ^2 distribution from a point source and provides a good fit to the data.

cut. The slightly wider cuts also reduce the systematic uncertainties associtated with the MC detector since the analysis is less susceptible to fluctuations in the optimized set of cut values. Therefore, the *spectrum-II* cut is particularly suitable for the determination of the energy spectra.

In this work we exclusively focus on the *spectrum-II* cuts. Table 5.2 shows the corresponding number of excess and background events for this particular set of cuts. Also shown on the same table are significances of observation along with corresponding gamma-ray rate. We only report the significances determined from the *reflected regions* analysis in the above table since *ring background model* is not suitable for spectral analysis (Section 4.4.3). The significance was calculated following Equation (17) in (Li & Ma, 1983). We, however, note that both the standard cuts and the spectrum cuts yield consistent results with a slightly higher gamma-ray rate reported in the latter due to wider acceptance window in θ.

When all of the data taken on the source are combined, the total significance amounted to 23.3 σ with a gamma-ray rate of 0.78 ± 0.04 γ per minute. Figure 5.10 shows the distribution of the squared angular distance, θ^2, between the reconstructed and the nominal source position for the excess events. A clear excess is visible for an angular cut of 0.15°indicating a point-like gamma-ray source in the sky. In the same figure, we show the expected θ^2 distribution for a

Table 5.2 Summary of results including excess, rates, and significance from the analysis of 1ES 1218+304 in 2008-2009

	Duration min.	ON	OFF	Excess	Rate γ/min	Significance σ	Sensitivity $\sigma/\sqrt{h}$
1ES 1218+304	1606	2937	5036	1253.9	$0.78 \pm 0.0.04$	23.3	4.5

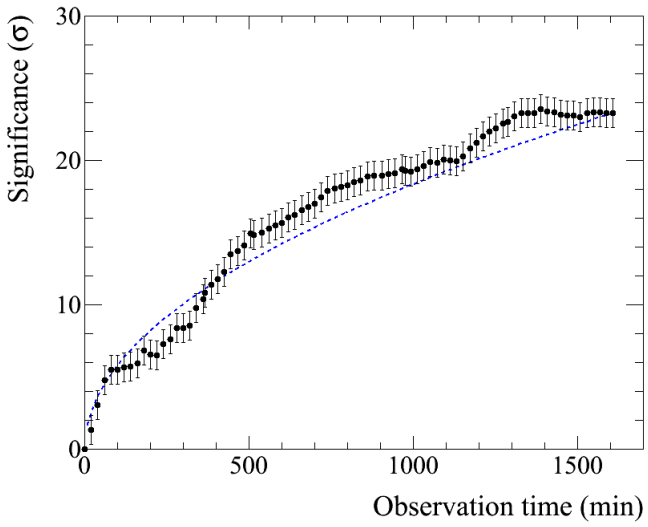

Figure 5.11 Cumulative significance as a function of time for the 08-09 dataset.

MC simulated point source, which is comparable to the real data. Also shown in Figure 5.11 is the significance of detection for 1ES 1218+304 as a function of time. For a steady source the increasing significance is expected to scales as $\sqrt{time}$, given by the dashed blue line. We see a marked deviation in the total significance build up during the period of increased gamma-ray emission from the source.

Finally, Figure 5.12 shows the gamma-ray rate curve from the AGN 1ES 1218+304 for the 08-09 dataset. The rates are binned by single day of observation. We clearly see hints of heightened emission beginning January 30, 2009 (MJD = 54860). This increased gamma-ray rate prompted an intensive monitoring of 1ES 1218+304 for the next 3 months in 2009.

Results from two-dimensional analysis of the 08-09 dataset is presented in Figure 5.13. This analysis was performed using the *ParCalReader* package developed at ISU by the author. The 2D significance map was constructed with the *ring-background* model analysis (see Section 4.4.3). A visible excess of gamma-ray events is seen at the center of the location of 1ES 1218+304. This map is created by reconstructing the arrival direction of the shower images

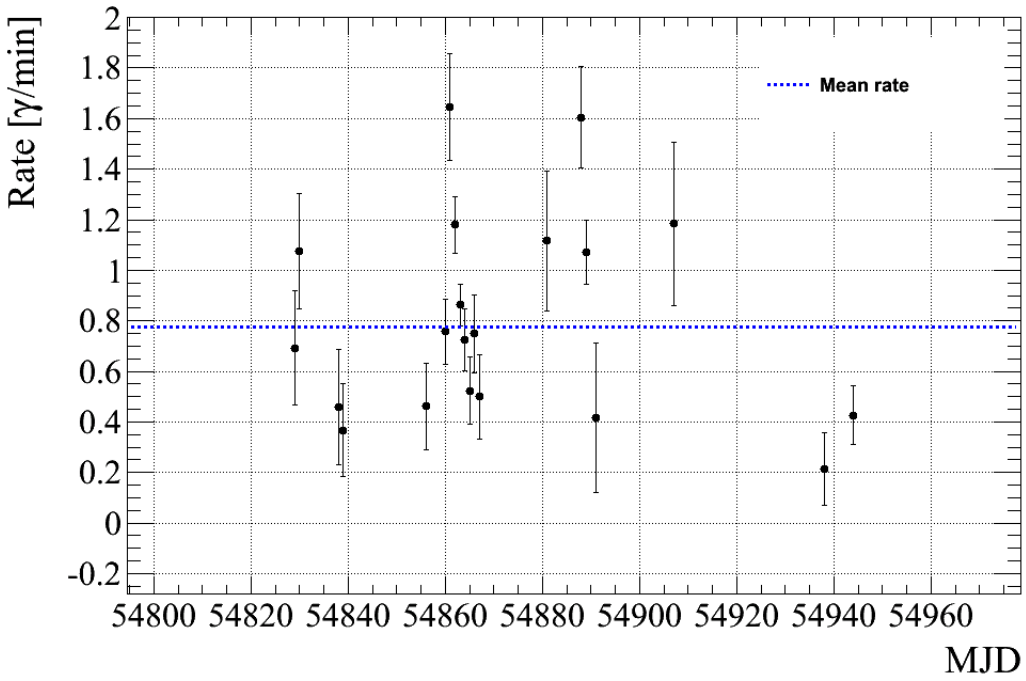

Figure 5.12 The rate curve for the 1ES 1218+304 data during 2008-2009. The dashed line shows a straight line fit through the data.

in the camera coordinates and transforming them into celestial coordinates. The significance map is subsequently smoothed using a Gaussian smoothing function with $\sigma_{2D} = 0.124°$, corresponding to the PSF of the telescopes (see Section 4.4.5). Figure 5.13(b) shows the distribution of significances per bin in an uncorrelated significance map. The excess in the distribution confirms the presence of a gamma-ray source in the sky. We also find that a fit to the background distribution of significances can be approximated by a Gaussian with zero mean and unity dispersion, which is expected for pure statistical noise.

5.3.4 Energy spectrum

One of the key motivations for the observations of 1ES 1218+304 was to derive an energy spectrum extending up to multi-TeV regime. An accurately measured source spectrum is particularly valuable for constraining the spectrum of the EBL. Previous observations of 1ES 1218+304, an HBL, revealed a very hard TeV spectrum with a luminosity peak in the TeV regime. Therefore, it is particularly well suited for the study a possible spectral break ∼1 TeV in the observed energy spectrum due to the absorption of TeV photons by the ambient EBL radiation field (see Section 2). This section describes the estimation of energies for the primary gamma rays and the calculation of the differential energy spectrum of 1ES 1218+304.

MC simulations were used to generate a two dimensional lookup table in image size and

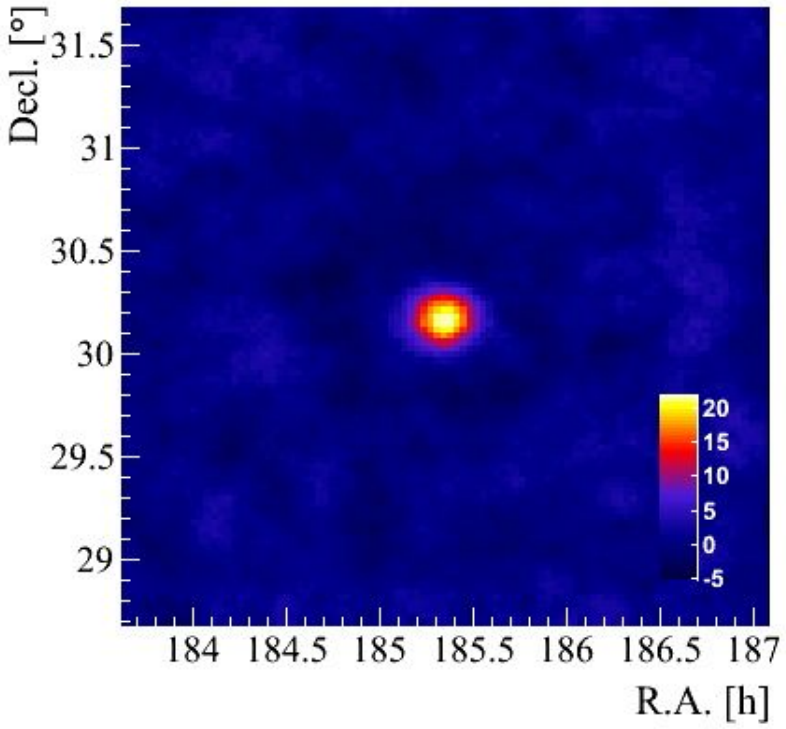

(a) Significance map

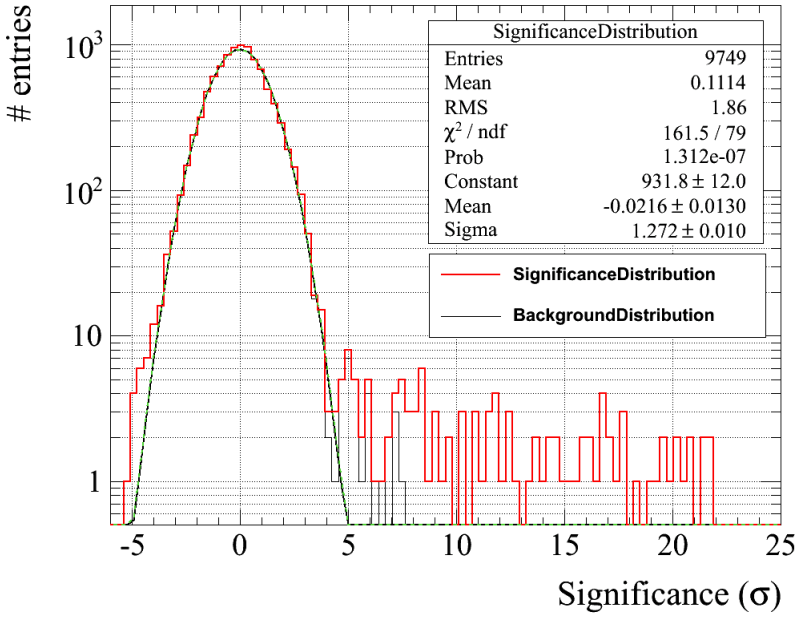

(b) Significance distribution

Figure 5.13 Two dimensional analysis

impact distance of individual showers from each telescope. Afterwards, the lookup table was used the estimate the energy of each candidate gamma-ray events. The spectral reconstruction was carried out using the methods outlined in Section 4.5.2. The distribution of the energy residual ($\log E_{\rm est} - \log E_{\rm true}$) is approximately normally distributed and shown in Figure 5.14. The corresponding energy resolution for the 1ES 1218+304 analysis is described by the RMS width of the above distribution (Equation 4.11), and it ranges between 19% and 26% over a energy range of 200 GeV to 2 TeV. Figure 5.14 shows the energy resolution plots for two separate energy bands with an effective resolution of 19% above a TeV.

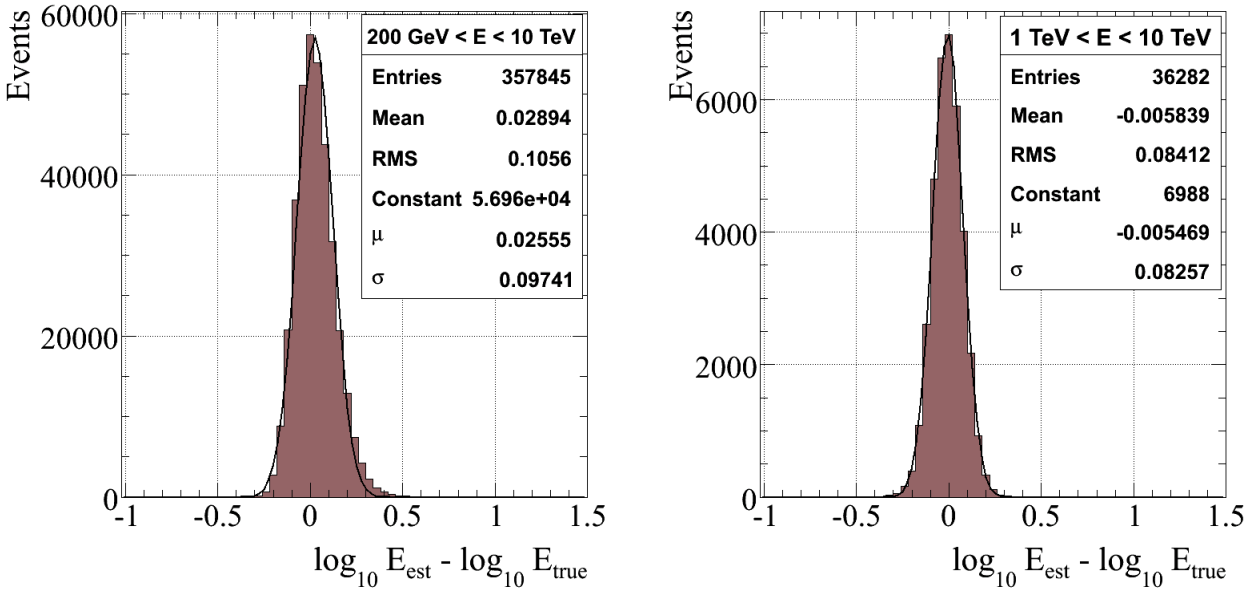

Figure 5.14 Energy resolution plot for different energy bands.

The relative energy bias *bias* at a zenith angle of $z = 20°$ is shown in Figure 5.15 as a function of the estimated energies of the gamma-ray events. An additional selection cut with $|\text{bias}| \leq 10\%$ is applied to the data in order to remove large uncertainties in the energy reconstruction.

Figure 5.16 shows the modified collection (see Section 4.5.3) area as a function of the estimated energy. The modified collection area has been generated from MC simulated gamma rays that were incident at a zenith angle of 20°. The simulated showers were thrown over an effective radius of 400 m around the center of the telescope array with a 0.5° pointing offset on the camera. In order to mimic the sky condition for an extragalactic source, the MC simulations were processed with a lower NSB noise (120 pe/ns/m^2/sr) in comparison to the data analysis of galactic sources (the Crab nebula) in the previous Chapter.

The *spectrum-II* selection cuts were used to measure the energy spectrum of 1ES 1218+304. Given that the acceptance of the camera may not be uniform across the camera, we deliberately chose to use the *reflected regions* model over the *ring background* model for background

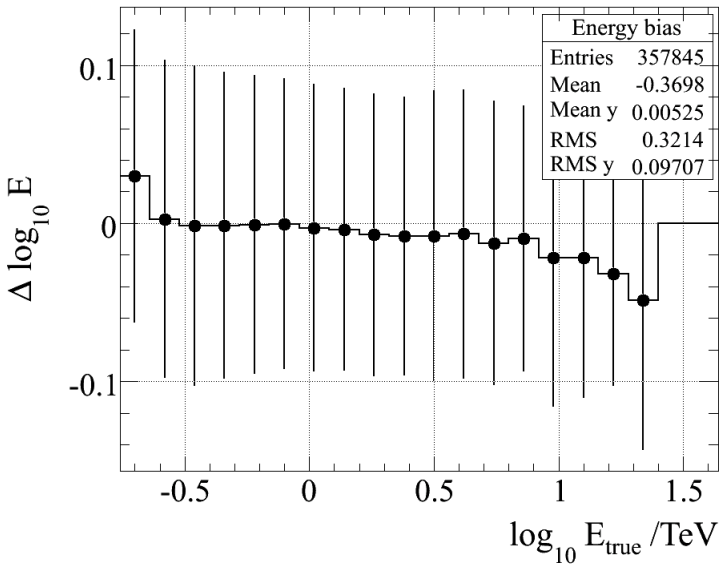

Figure 5.15 Energy bias

estimation. The application of the *reflected regions* model also proved to be relatively straight forward during the course of the analysis. Finally, Table 5.3 lists for each estimated energy bins: the excess event counts, the significance of the excess, the calculated differential flux, the fitted differential flux and the statistical error in the actual differential flux. For the flux calculations, the excess events are binned in 9 logarithmic energy bins, ranging from 200 GeV up to 1.8 TeV. To calculate the flux, the energy dependent modified collection area is applied following Equation 4.14 to the excess. The resulting time-averaged differential energy spectrum for the 08-09 dataset is shown in Figure 5.17(a). The data points can be fitted with a power law function of the form $I_0 \left(\frac{E}{500\ \mathrm{GeV}}\right)^{-\Gamma}$. The best fit to the measured energy spectrum for the 08-09 dataset, with 1-σ statistical errors, is given by:

$$\frac{dN}{dE} = (12.7 \pm 0.7) \times 10^{-12}\ (\frac{E}{500\mathrm{GeV}})^{-3.16 \pm 0.09\,\mathrm{stat}}\ \mathrm{cm}^{-2}\mathrm{s}^{-1}\mathrm{TeV}^{-1} \tag{5.3}$$

For the fitted spectrum, the overall value of χ^2 for 7 degrees of freedom, is 10.1. The χ^2 probability that this data would randomly result from the power law fit is 0.18. Also shown in Figure 5.17(a) is the differential energy spectrum for the 2006-2007 dataset. We note that the two spectra differ by an overall flux normalization constant. This is not surprising since the most recent 08-09 dataset represent data collected during increased emission from 1ES 1218+304. However, we conclude that the overall spectral indices are compatible within statistical errors for the two datasets. Figure 5.17(b) shows the corresponding residuals for the power-law fit to the 08-09 energy spectrum. The fit also allows us to calculate the integral flux above the energy threshold of the spectral analysis, namely 200 GeV. It is found to be $\Phi(\mathrm{E} > 200\ \mathrm{GeV}) = (20.5 \pm 1.0_{\mathrm{stat}}) \times 10^{-12}\ \mathrm{cm}^{-2}\ \mathrm{s}^{-1}$ corresponding to ∼9% of the Crab Nebula flux. A summary of results obtained for the spectral measurements on 1ES 1218+304 for data

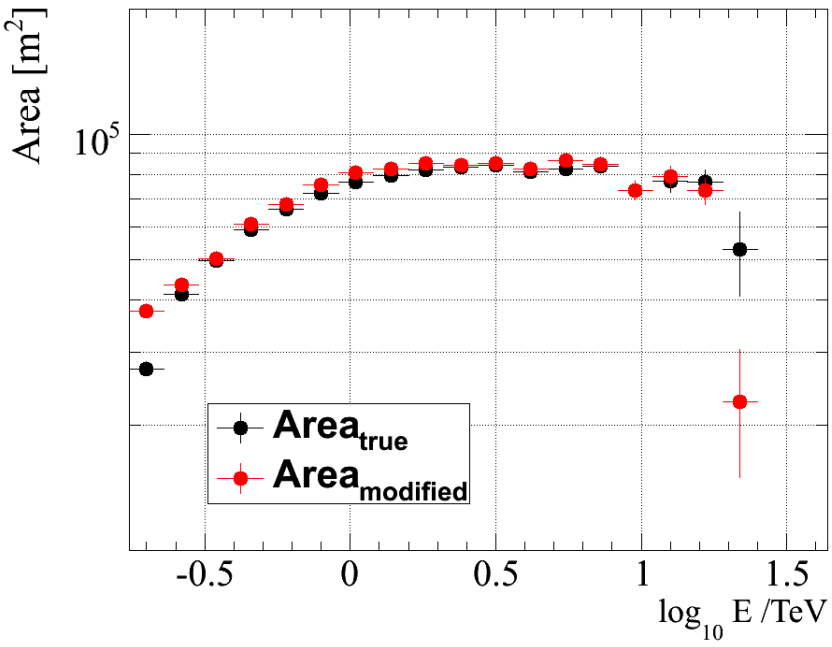

Figure 5.16 Modified collection area

taken during 2008-2009 observing seasons is given in Table 5.3 Figure 5.18 shows a contour plot derived from the χ^2 fit errors in flux normalization I_0 and the photon index Γ for the 08-09 dataset using the *spectrum-II* cuts.

5.4 Gamma-ray Light Curve

The observations of 1ES 1218+304 in 2008-2009 was marked by a remarkable VHE gamma-ray flare (Figure 5.12). During this period, we witnessed day-scale changes in flux by factors >3. In the following section, a derivation of the VHE gamma-ray light curve from 1ES 1218+304 is presented. This allows us to carry out a detailed investigation of the time variability of gamma-ray emission from the source. The light curve shows the time dependence of the integral flux. Initially, the 08-09 dataset is binned by time into a single night of observations. For each nightly bin, the time is represented by the *Modified Julian Day* (MJD) of the observation. Gamma-ray events were selected using Spectrum cuts. The time dependent integral flux, $\phi_{E>E_{th}}(t)$, above the energy threshold of the analysis is given by:

$$\phi_{E>E_{th}}(t) := \int_{E_{th}}^{\infty} \phi(E,t)\, dE \tag{5.4}$$

Where $\phi(E,t)$ is the differential energy flux for energy E and time t. However, it is not always possible to compute the $\phi(E,t)$ due to poor statistics arising from the limited observing time. Lack of sufficient excess events in short time bins may prevent us from deriving the differ-

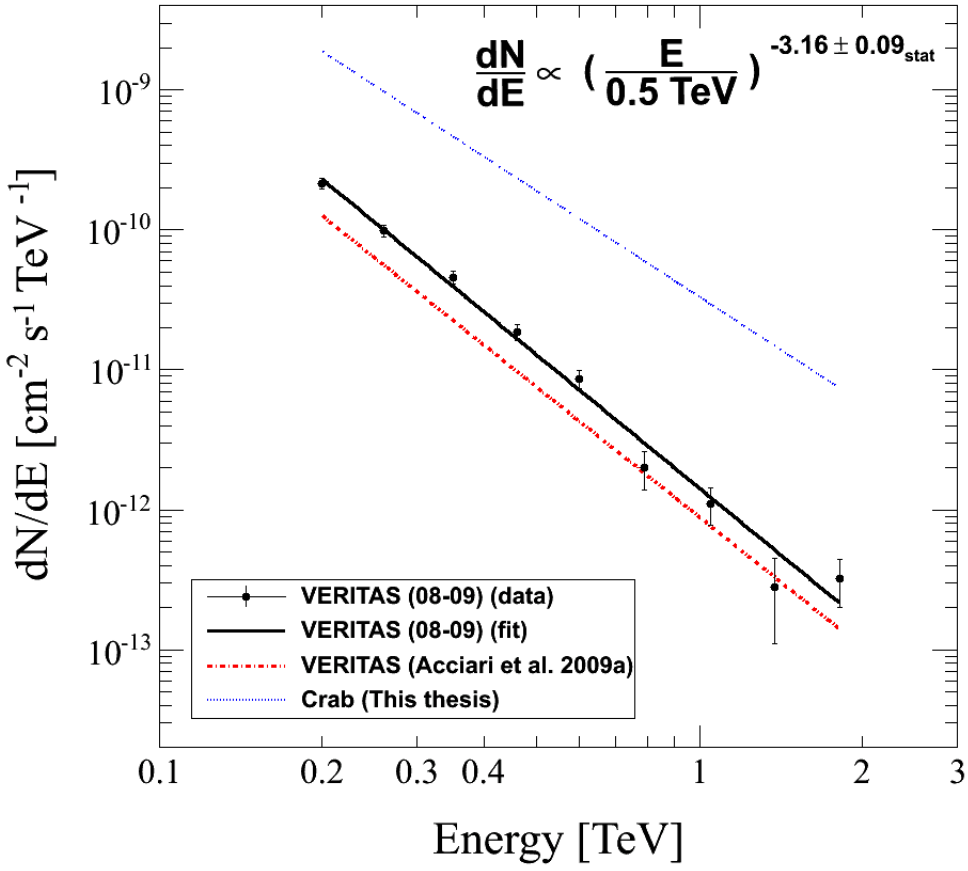

(a)

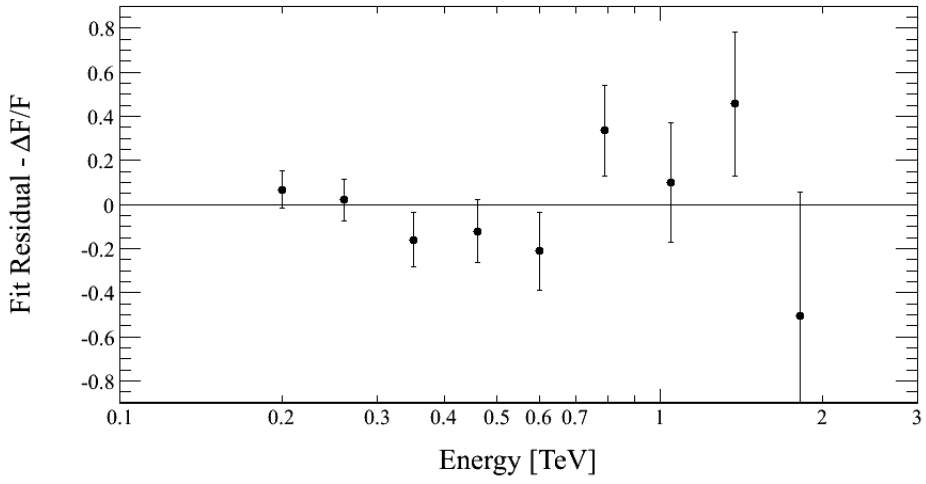

(b)

Figure 5.17 *Top*: Differential energy spectrum 1ES 1218+304 from the total 2008-09 data set compared to past measurements by VERITAS and MAGIC. *Bottom*: Residual of the power law fit.

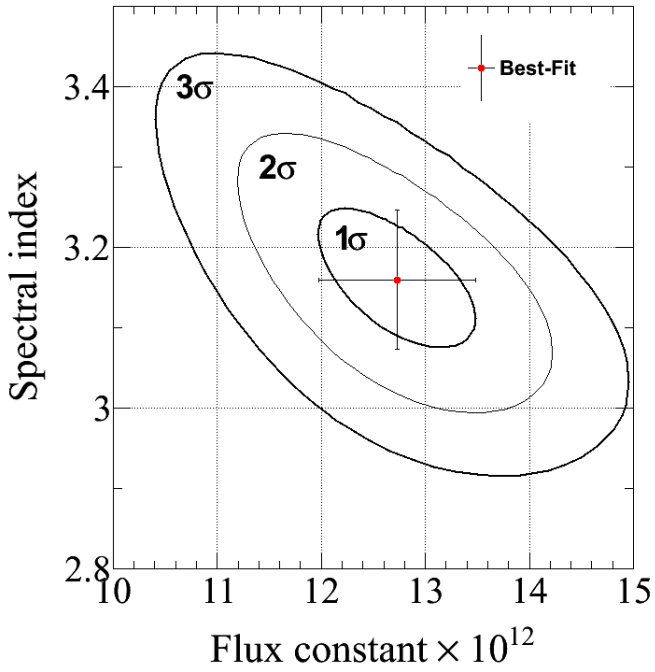

Figure 5.18 Contour plot of the 68%, 95%, and 99.9% confidence region from the χ^2 fit to a power law for the 1ES 1218+304 data set using spectrum cut. The best fit value is shown by the red point.

ential energy spectrum, $\phi(E,t)$ for the corresponding bin. Therefore, $\phi_{E>E_{th}}(t)$ is indirectly calculated using the measured gamma-ray counts above the same energy threshold.

The prescription for the derivation of the light curve is as follows. For an azimuth (Φ) and zenith ($\mu = \cos(\Theta)$) angle dependent modified collection area $A(E,\Phi,\mu;t)$, the measured gamma-ray rate is give by:

$$\frac{dN}{dt}_{E>E_{th}} = \int_{E_{th}}^{\infty} A(E,\Phi,\mu;t)\,\phi(E,t)\,dE \tag{5.5}$$

This allows us to calculate the integral photon flux as

$$\begin{aligned}\phi_{E>E_{th}}(t) &= \frac{\frac{dN}{dt}_{E>E_{th}} \int_{E_{th}}^{\infty} \phi(E,t)\,dE}{\int_{E_{th}}^{\infty} A(E,\Phi,\mu;t)\,\phi(E,t)\,dE} \\ &\approx \frac{\frac{dN}{dt}_{E>E_{th}} \int_{E_{th}}^{\infty} \phi(E)\,dE}{\int_{E_{th}}^{\infty} A(E)\,\phi(E)\,dE}\end{aligned} \tag{5.6}$$

The simplification in the last line of Eq. 5.6 assumes that the shape of the spectrum does not vary significantly in time but changes only in the flux normalization. We also use a collection area averaged in azimuthal angle (Φ) to account for the time dependence. For the derivation of the integral flux, we apply a collection area derived from the simulated MC showers at a

Table 5.3 1ES 1218+304 flux from the 2008-2009 data set using the *spectrum* cut optimized for a weak source with a 5% of the Crab nebula flux..

Energy TeV	Excess	σ	Actual Flux TeV^{-1} cm^{-2} s^{-1}	Fitted Flux TeV^{-1} cm^{-2} s^{-1}	Error TeV^{-1} cm^{-2} s^{-1}
0.2	387	10.9	2.15×10^{-10}	2.30×10^{-10}	1.97×10^{-11}
0.26	280	10.5	9.84×10^{-11}	1.01×10^{-10}	9.40×10^{-12}
0.35	190	0.0	4.56×10^{-11}	3.93×10^{-11}	4.79×10^{-12}
0.46	124	7.9	1.86×10^{-11}	1.66×10^{-11}	2.36×10^{-12}
0.6	85	6.8	8.67×10^{-12}	7.16×10^{-12}	1.27×10^{-12}
0.79	29	3.2	1.99×10^{-12}	3.00×10^{-12}	6.16×10^{-13}
1.05	22	3.3	1.10×10^{-12}	1.22×10^{-12}	3.29×10^{-13}
1.38	8	1.7	2.80×10^{-13}	5.15×10^{-13}	1.69×10^{-13}
1.82	12	2.7	3.23×10^{-13}	2.15×10^{-13}	1.20×10^{-13}

zenith angle of 20°. Since the collection area scales inversely with the cosine of the zenith angle ($\propto 1/\mu$), this particular choice is well justified considering the distribution of the zenith angles for the 08-09 dataset (Figure 5.7).

5.4.1 Day scale variability

Table A.3 lists the nightly averaged gamma-ray rates and integral fluxes for the 08-09 dataset. The light curve shows strong nightly variations between January 25, 2009 and February 5,2009. The highest gamma-ray flux was observed on MJD 54861 (January 30, 2009). The highest observed flux corresponds to $\sim$ 24% of the Crab Nebula flux. Solid detection of the source as evidenced by the strong signal to background ratio allow us to search for day-scale variability in the observed data. Figure 5.19 shows a light curve of 1ES 1218+304 integral flux above 200 GeV from VERITAS observations during 2008-2009.

In order to test the stability of the daily integral flux we begin with the assume that 1ES 1218+304 is a steady source and employ a χ^2-test to check our hypothesis. For a given photon flux $\phi_i \pm \sigma_i$, we define a χ^2 sum as,

$$\chi^2 = \sum_{\mathrm{i}=1}^{\mathrm{N}} \frac{(\phi_\mathrm{i} - \overline{\phi})^2}{\sigma_\mathrm{i}^2} \tag{5.7}$$

The weighted mean of the photon fluxes $\overline{\phi}$ is given by,

$$\overline{\phi} = \frac{\sum_{\mathrm{i}=1}^{\mathrm{N}} (\phi_\mathrm{i}/\sigma_\mathrm{i}^2)}{\sum_{\mathrm{i}=1}^{\mathrm{N}} (1/\sigma_\mathrm{i}^2)} \tag{5.8}$$

A fit to a constant flux over the entire dataset is shown by a blue dashed line. The overall χ^2 for the constant fit is 106 for 106 degrees of freedom. The corresponding χ^2 probability

is exceedingly small ($\sim 10^{-13}$). This confirms that the variations in the flux are not merely statistical. We conclude, the 08-09 dataset indicates a day-scale variable emission from the blazar 1ES 1218+304.

In order to quantify the time scales for the flux variations, we apply a simple flare model to the data. Therefore, flux during the flare is described by an exponential function of the form,

$$\phi(\mathrm{t}) = \mathrm{A}\exp^{-|(\mathrm{t}-\mathrm{t}_{\mathrm{max}}|)/\sigma_{\mathrm{r,d}}} \tag{5.9}$$

Where the initial normalization constant A is set to the averaged integral flux, $A = (20.5 \pm 1.0) \times 10^{-12}$. The t_{max} is the time of the highest emission in our data (MJD 54861); The rise ($t < t_{max}$) and decay ($t > t_{max}$) time constant are give by σ_r and σ_d, respectively. The best fit of the flare model to the data (Figure 5.19, inset) yields $\sigma_r = 1.26$ days ($\chi^2/\mathrm{dof} = 16.8/6$) and $\sigma_d = 2.5$ days ($\chi^2/\mathrm{dof} = 0.25/2$). The rise and decay time, from half to the maximum amplitude is given by:

$$\tau_{\mathrm{r,d}} = \ln(2) \times \sigma_{\mathrm{r,d}} \tag{5.10}$$

Therefore, we can estimate the characteristic flux doubling time, τ_{var} to be on the order of ~ 1 day or shorter. The inset within Figure 5.19 shows the light curve above 200 GeV for nights with the highest flux. The fitted flare models showing the rapid rise and decay time for the VHE gamma-ray emission from 1ES 1218+304 are given by black dashed lines.

We also show the normalized daily gamma-ray rate distribution from the data collected during the 2008-2009 season in Figure 5.20. Also shown on the same plot is the expected profile distribution of daily rate from a non-variable source in the sky. For a standard normally distributed variate $\Phi_i = (\phi_i - \overline{\phi})/\sigma_i$, the width of the distribution is expected to have a standard deviation of unity for a non-variable source. The width of the distribution from observed data is clearly greater than a 1σ. Therefore, it strongly suggests that the measured fluctuations in the rate are not statistical and the source is indeed variable.

Figure 5.21 shows the 2008-2009 light curve combined with previous VERITAS measurements in 2006-2007. While the two measurements correspond to observations carried out under very different conditions, the yearly light curve suggests an underlying constant emission component from 1ES 1218+304. Except for the flaring states, the gamma-ray emission over the two seasons are relatively constant and the daily integral photons fluxes are found to be reasonably agreeable to each other.

5.4.2 Flaring spectrum

It is not uncommon to find significant variations in the observed energy spectra from blazars during the flaring states. In the most famous case of a nearby blazars Mrk 421, its spectra is reported to harden considerably with increasing flux (Krennrich et al., 2002). Similar instances of spectral variations have been reported during the exceptional gamma-ray flare of PKS 2155-304 in 2006 (Aharonian et al., 2009a). In oder to investigate possible changes to the spectral

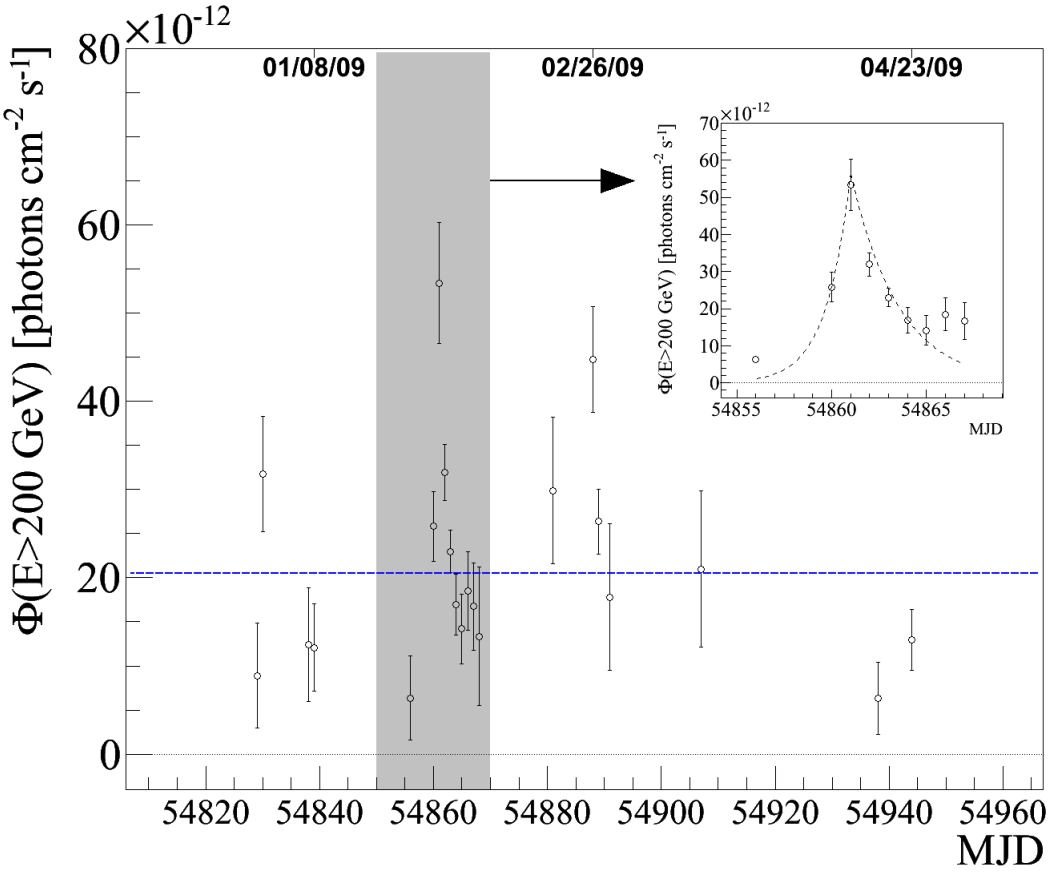

Figure 5.19 Night-by-night VHE light curve for 1ES 1218+304 is shown as measured from December 29, 2008 (MJD 54829) to April 23, 2009 (MJD 54944). The open circles represent the integral flux above 200 GeV, $\phi(E > 200\text{GeV})$ from 1ES 1218+304 assuming a spectral shape, $dN/dE \propto E^{-\Gamma}$ with $\Gamma = 3.16$. The dashed-dotted line corresponds to the average integral flux, $\phi(E > 200\text{GeV}) = (20.5 \pm 1.0) \times 10^{-12}$ cm^{-2} s^{-1}. The inset shows the flux variations for the flaring nights in more detail. An exponential function, $e^{\lambda t}$ (dashed line) is used to describe the rise and fall time for flux variations giving $\lambda_{\text{rise}} = 0.79$ ($\chi^2/dof = 16.8/6$) and $\lambda_{\text{rise}} = -0.40$ ($\chi^2/dof = 0.25/2$, respectively. The characteristic flux doubling time, t_{var} is estimated to be on the order of ~ 1 day).

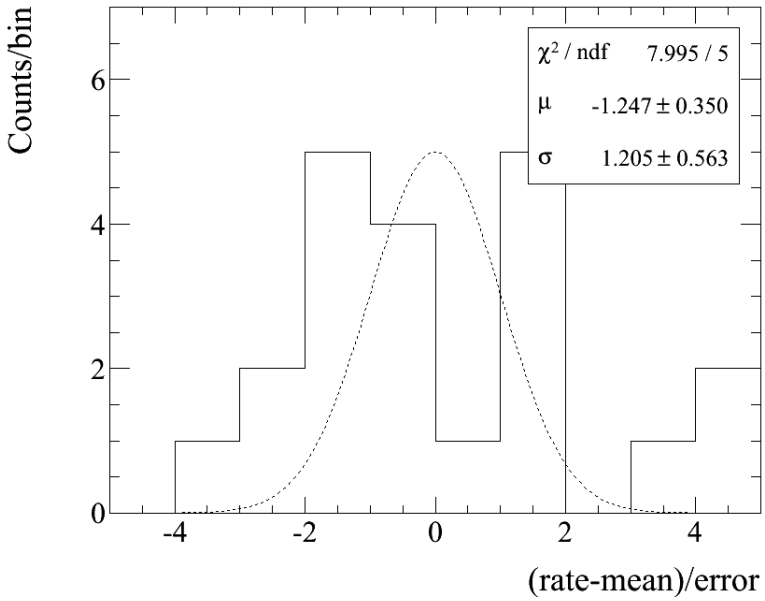

Figure 5.20 Normalized daily rate distribution for the 08-09 data. Also shown in black dashed line is the expected profile from a non–variable gamma-ray source.

shape during the flaring activity, the 08-09 dataset is divided into high-state and low-state samples. The two nights with the highest flux during the flaring period (January 30 and 31) are considered be the high state, while the remaining nights are considered the low state. Afterwards, the energy spectra for both samples are derived following the spectral analysis methods outlined in the previous sections. Figure 5.22 shows the resulting differential energy spectra for the two cases. Both the high-state and the low-state spectra are well described by a power law of the form $dN/dE = f_0 \, (\frac{E}{0.5TeV})^{-\Gamma}$. Table 5.4 summarizes the spectral results for the two data samples. While the two spectra obviously differ in the flux normalization, we see no evidence for a significant change to the spectral index during the period of increased gamma-ray emission from 1ES 1218+304.

Table 5.4 High-state and the Low-state Data during 2008-2009.

State	Excess	σ	Rate γ/min^{-1}	$\phi(>200\mathrm{GeV})$ 10^{-12} cm^{-2} s^{-1}	I_0 10^{-12} TeV^{-1} cm^{-2} s^{-1}	Γ	χ^2/ndf
High	251	13.1	1.28 ± 0.11	35.8 ± 2.9	21.2 ± 2.4	3.10 ± 0.15	6.9/6
Low	1003	19.9	0.71 ± 0.39	18.6 ± 1.0	11.6 ± 0.8	3.17 ± 0.10	5.8/7
Avg	1696	23.4	0.8 ± 0.04	20.5 ± 1.0	12.7 ± 0.8	3.16 ± 0.86	10.1/7

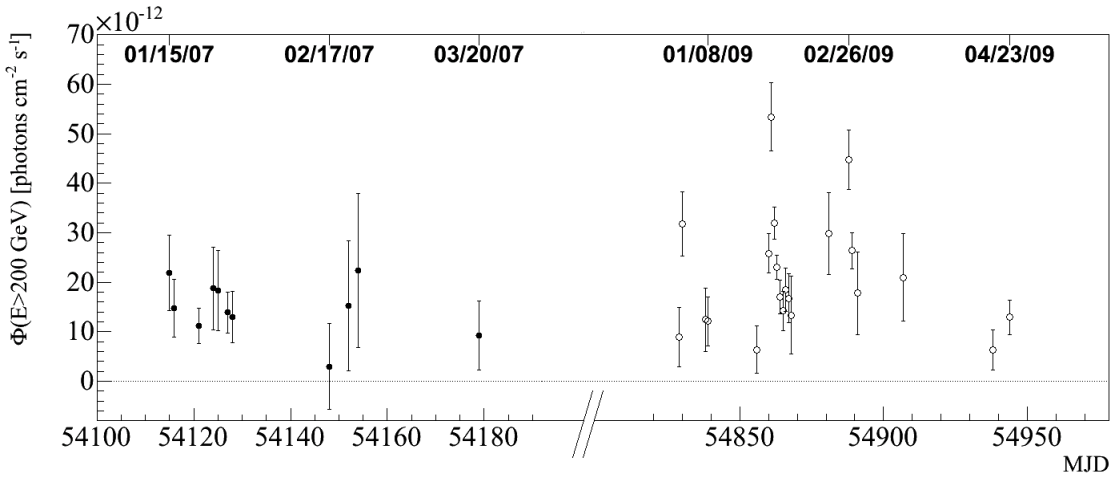

Figure 5.21 Yearly light curve in units of integral flux above 200 GeV from 1ES 1218+304. The data is binned by day. The filled circles correspond to VERITAS data from the 2006-2007 epoch. The open circles represent the most recent data from the 2008-2009 season.

5.5 Discussion and results

A prominent feature in the emission properties of blazars is the observed variability on time scales ranging from minutes to years. In 2006, *Suzaku* detected a prominent X-ray flare from 1ES 1218+304 revealing a hard-lag variation in the X-rays (Sato et al., 2008). While 1ES 1218+304 was flagged as variable in the Fermi bright source catalog (Abdo et al., 2009b), no variability was detected in the Fermi light curve (Abdo et al., 2009a). The increased flux measured by VERITAS is the first significant observation of flaring activity in the VHE emission from 1ES 1218+304. Among the other hard-spectrum VHE blazars (1ES 1101-232, 1ES 0347-121, 1ES 0229+200, 1ES1218+304, RGB J0710+591) measured to date, 1ES 1218+304 is the first clear example of significant VHE variation from a baseline flux. Consequently, the strong flare will challenge existing spectral models of 1ES 1218+304 that assume a constant VHE emission from the source (see for example Rüger et al., 2009).

5.5.1 Size of gamma-ray emission region

It is generally assumed that the VHE emission from blazars is produced in the relativistic jet where the highly collimated and Doppler-boosted emission is responsible for the high luminosities and short variability timescales. We can place an upper limit on the size of the emission region by considering the relativistic causality argument. Since the time for light to cross a homogeneous region must be less than the variability time scale, we can constrain the

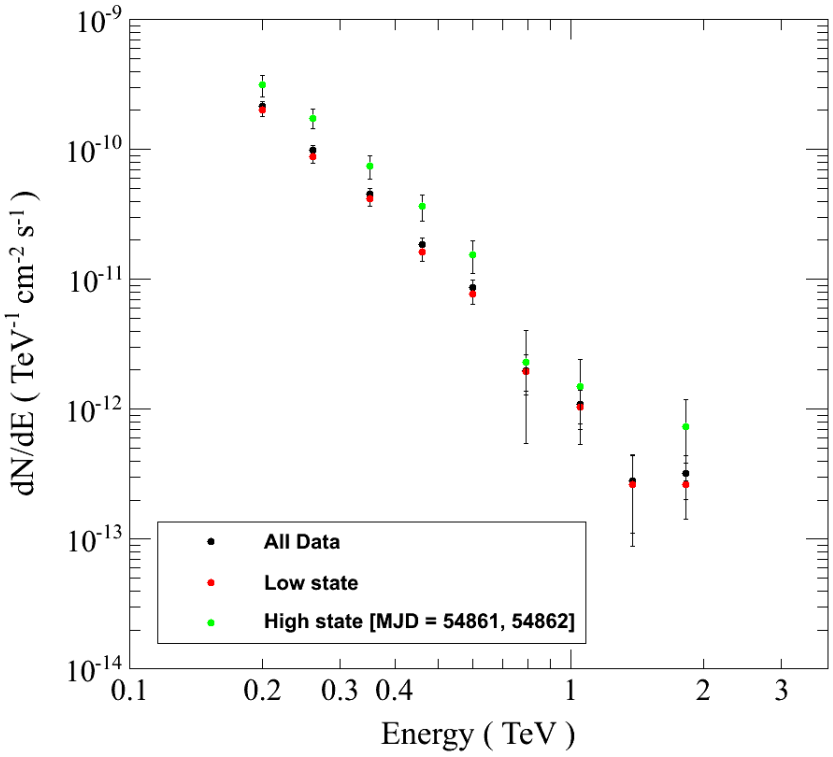

Figure 5.22 Energy spectra for the High-state and the Low-state.

size of the emission region, R by,

$$R \leq c\, t_{var}\, \frac{\delta}{1+z} \tag{5.11}$$

Where δ is the relativistic Doppler factor and t_{var} is the observed gamma-ray variability timescale. In the case of 1ES 1218+304, $z = 0.182$. Therefore, the estimated flux-doubling time $t_{var} \lesssim 1$ day (see Figure 5.19) limits the size of the emission region to

$$\begin{aligned} R/\delta &\leq 2.19 \times 10^{15} \text{ cm} \\ &\sim 0.71 \times 10^{-3}\ pc \end{aligned} \tag{5.12}$$

The Doppler factor ($\delta \sim 20$) typically derived for blazars (Marscher, 2006) implies that

$$R \lesssim 4.38 \times 10^{16} cm \tag{5.13}$$

5.5.2 Extended kiloparsec jet model

While the hard emission spectrum during the quiet state is consistent with the CMB-inverse-Compton interpretation, the requirement for a large emission region (∼pc scale) predicted by the model is excluded by the $R \lesssim$ 0.01 pc constraint imposed by the variability.

Therefore, the flaring behavior from 1ES 1218+304 implies that the CMB-inverse-Compton model of emission in the kpc-scale extended jet is unlikely to be the sole explanation for the extreme hardness in the intrinsic spectrum of 1ES 1218+304.

Although our observations of 1ES 1218+304 are consistent with a baseline level of VHE emission that could have its origin in an extended emission region, the variability described here indicates that comparable flux with a comparably hard spectrum is emitted from the compact regions of this source. Further observations of 1ES 1218+304 are required to determine if the hard-spectrum emission can be explained as originating from the kpc extended jet via the CMB-inverse-Compton model. Consequently, long-term VHE monitoring with ground-based gamma-ray telescopes may be crucial to unraveling the emission mechanism in distant the hard-spectrum VHE blazars.

CHAPTER 6. CONCLUSIONS

This thesis details the analysis of VHE gamma-ray data obtained with the VERITAS array in Southern Arizona. The analysis led to the discovery of variable emission from the hard spectrum blazar 1ES 1218+304. Furthermore, I explored a novel method to search for the first observational evidence of the absorption of gamma-ray photons in the intergalactic space. Finally, this work utilized measured spectra of distant, hard spectrum blazars along with new EBL lower limits from galaxy counts to derive a strong observational constraints to the intrinsic spectral hardness of blazars.

Possible signature of EBL absorption in VHE blazar spectra

In modern cosmology, a clearer understanding of the EBL is highly desirable since it encapsulates a significant fraction of the structure formation history of our universe. In VHE gamma-ray astronomy, a reliable measurement of the spectral energy density of the EBL is equally crucial to the determination of the intrinsic spectrum of blazars at very high energies. Gamma-ray photons are attenuated by the ambient photon field over cosmological distance where the level of absorption is strongly modulated by the exact intensity profile of the EBL as a function of wavelength. Direct measurement of the SED of EBL remain largely uncertain particularly in the near-to-mid infrared regime due to the presence of strong foreground emission from within our own galaxy. On the other hand, EBL limits derived by integrating light from resolved galaxies are only lower limits and may not account for dim and/or diffuse sources. Thus, VHE spectra of blazars provide an elegant but indirect too tool to probe the EBL. This process is highly iterative since our understanding of the blazars and their emission is far from complete. In this thesis, I developed an independent EBL code to test the absorption of gamma rays for varying models of the EBL. I used different EBL models that are consistent with direct observations to show that absorption due to EBL may lead to a measurable change in the spectra of blazars at 1 TeV. In addition, the spectral change is mediated by the relative intensity of the EBL between near and mid IR wavelength. An observation of such a spectral feature would not only be the first direct evidence for absorption of gamma ray in intergalactic medium, but it would also provide a strong constraints to the EBL at near- and mid-IR.

I also took part in a study to use the new lower limits on the EBL at 3.6 μm from galaxy counts to impose constraints to the intrinsic spectral hardness of blazars. In the rapidly growing field of ground based imaging Cherenkov telescopes, improved sensitivity combined

with better energy resolution have enabled us to peer further out in distance, in search for new blazars. Not surprisingly, the total number of confirmed blazars have swelled past 30. A few of these blazars have been shown to emit VHE gamma rays with a remarkably hard energy spectrum which is beginning to test our current models for VHE emission from these sources. While standard emission models predict that the intrinsic blazar spectra cannot be any harder than 1.5, our work present strong observational evidence otherwise. By utilizing the measured energy spectra of the blazars 1ES 11101–232, 1ES 1218+304, and 1ES 1011+496 from three separate IACTs covering different energy regimes, we are able to show that the intrinsic spectrum of blazar can be at least as hard as 1.28 ± 0.24.

Data analysis

A significant fraction of my research work was devoted to the analysis of VHE gamma-ray from blazars collected with the VERITAS array. To this effect, I developed an independent data analysis chain at Iowa State University. This was strongly motivated by the daily analysis of data from blazars, a key component of the VERITAS discovery program. I also collaborated with colleagues at ISU and Grinnell College to develop the GrISep *toolkit*, used throughout this work for the estimation of primary energies from blazars. The design, development, implementation, and testing of this software was an integral part of this dissertation. As an important part of data analysis, I devoted a large fraction of my effort to generating a database of Monte Carlo simulations. I made careful efforts to verify and test all the important initial parameters that were used in the MC simulations. Additionally, I wrote independent software to perform optimization of gamma/hadron separation cuts crucial for the detection and measurements of energy spectrum of blazars. Optimization of scaled length, scaled width, and the size of signal region (θ^2) resulted in two sets of cuts were for the analysis of both strong and weak sources of gamma rays.

In order to test the robustness of this analysis chain, it was applied to a small data set of the observations of the Crab nebula. The optimization led to an achievement of a sensitivity corresponding to 27.2 $\sigma/\sqrt{\text{hour}}$ on the Crab. The final measured value of the spectrum of the flux from Crab, using a *spectrum* cut optimized for strong source is given by:

$$\frac{dN}{dE} = (3.2 \pm 0.12_{\text{stat}} \pm 0.64_{\text{sys}}) \times 10^{-11} \, (\frac{E}{1.0\text{TeV}})^{-2.43 \pm 0.03_{\text{stat}} \pm 0.14_{\text{sys}}} \, \text{cm}^{-2}\text{s}^{-1}\text{TeV}^{-1} \quad (6.1)$$

where the two quoted error for the flux normalization and the spectral index are the statistical error and the estimated systematic error, respectively. The measured spectra of the Crab nebula has been found to be in good agreement with previously published values by the Whipple Collaboration, H.E.S.S and MAGIC.

Variable VHE emission from 1ES 1218+304

The optimized data analysis chain was finally used in the daily data analysis of the blazar 1ES 1218+304. Initially discovered in the VHE gamma-ray by the MAGIC Collaboration in 2005, the relatively distant 1ES 1218+304 was among a group of TeV blazars that were found to exhibit surprisingly hard source spectra considering their redshifts. In an attempt to characterize the emission properties of this group of blazars, VERITAS initiated a 4 month long observing campaign to monitor 1ES 1218+304 in 2008-2009. I performed the official next-day analysis of the source as part of the monitoring campaign. Beginning January 25, 2009, 1ES 1218+304 was found to be in a heightened flux state based on daily gamma-ray rate. The highest measured flux corresponds to $\sim$ 24% of the Crab nebula flux. The initial report prompted an intensive observing of the source for the next 2 months, yielding a total of 27.2 hours of usable observations. In addition to deriving the spectrum of the flux from 1ES 1218+304, I also analyzed the flare data from the source. My analysis revealed the first evidence for flux variability from 1ES1218+304, over times scale of a day. Subsequent analysis of the flare data showed no variation to the energy spectrum during the period of increased emission. Analysis of the entire data set resulted in a 23.3 σ detection of the source corresponding to a sensitivity of 4.5 $\sigma/\sqrt{hour}$. The time-averaged differential energy spectrum of the flux from 1ES 1218+204 as observed for the 2008-2009 season, using the *spectrum* cut optimized for a weak source is given by:

$$\frac{dN}{dE} = (12.7 \pm 0.7_{\,\mathrm{stat}}) \times 10^{-12} \, (\frac{E}{500\mathrm{GeV}})^{-3.16 \pm 0.09\,_{\mathrm{stat}}} \ \mathrm{cm}^{-2}\mathrm{s}^{-1}\mathrm{TeV}^{-1} \qquad (6.2)$$

A possible explanation for the production of VHE gamma rays with a hard intrinsic spectrum was offered by Böttcher et al. (2008). In this model, shock-accelerated electrons were thought to efficiently inverse-Compton scatter CMB photons to TeV energies which would account for an additional hard component to the intrinsic spectrum. In order to sufficiently accelerate the electrons to ultrarelativistic energies and suppress the synchrotron cooling over CMB-Compton emission imply a parsec scale emission region that is situated at kiloparsec distances away from the central engine. A key prediction in this model is that the additional hard component is very slowly varying. However, this is in direct conflict with the observed rapid flux variability from 1ES 1218+304. As a result, we can rule out CMB-Compton emission as the sole explanation for the intrinsic spectral hardness of the blazar. However, it is very possible that the 'quiet' emission from 1ES 1218+304 does indeed contain a CMB-Compton emission and may account for the baseline flux levels observed in the many hard spectrum blazars.

APPENDIX A. CRAB AND 1ES 1218+304 DATABASE

2007-2008 Crab Database

Table A.1 List of data runs used to derive the energy spectrum of Crab nebula for 2007-2009.

Date	Run	Laser	Pointing Dir.		Zenith Angle[°]	Duration min	Rate γ/min	σ
20071014	37195	37177	0.5°	S	77	20.0	9.85 ± 0.82	15.4
20071015	37230	37228	0.5°	S	78	20.0	10.58 ± 0.85	15.9
20071020	37438	37433	0.5°	N	77	20.0	8.97 ± 0.82	13.7
20071114	37947	37955	0.5°	E	78	20.0	9.73 ± 0.82	15.2
20071114	37948	37955	0.5°	W	80	20.0	11.05 ± 0.85	16.9
20071114	37950	37955	0.5°	S	78	20.0	9.93 ± 0.82	15.4
20071117	38031	38046	0.5°	W	63	20.0	7.71 ± 0.71	14.0
20071118	38061	38076	0.5°	N	65	20.0	10.43 ± 0.83	16.1
20080111	38722	38731	0.5°	W	68	20.0	10.40 ± 0.82	16.5
20080112	38764	38786	0.5°	W	75	20.0	12.24 ± 0.87	19.0
20080130	38958	38968	0.5°	W	80	20.0	9.86 ± 0.80	16.1

2008-2009 1ES 1218+304 Database

Table A.2 List of data runs used to derive the energy spectrum of the blazar 1ES 1218+304 for 2008-2009

Date	Run	Laser	Pointing Dir.		Zenith Angle[°]	Duration min	Rate γ/min	σ
20090107	43957	43959	0.5°	N	88	20.0	0.52 ± 0.34	1.6
20090108	43967	43970	0.5°	N	85	20.0	0.13 ± 0.17	0.8
20090108	43968	43970	0.5°	S	88	20.0	0.60 ± 0.35	1.8
20090125	44151	44139	0.5°	N	85	20.0	1.12 ± 0.36	3.5
20090125	44153	44139	0.5°	N	84	20.0	0.00 ± 0.25	0.0
20090125	44159	44139	0.5°	S	70	20.0	0.28 ± 0.33	0.9
20090129	44275	44174	0.5°	N	85	20.0	1.05 ± 0.33	3.7
20090129	44276	44174	0.5°	S	80	20.0	0.65 ± 0.30	2.3
20090129	44277	44174	0.5°	E	76	20.0	1.19 ± 0.34	4.0
20090129	44278	44174	0.5°	W	71	20.0	0.33 ± 0.31	1.1
20090129	44279	44174	0.5°	N	67	20.0	0.50 ± 0.31	1.7
20090130	44313	44174	0.5°	N	73	20.0	1.83 ± 0.38	5.9
20090130	44314	44174	0.5°	S	69	20.0	1.15 ± 0.36	3.6
20090130	44316	44174	0.5°	N	66	5.0	2.87 ± 0.88	4.2
20090131	44345	44174	0.5°	N	71	20.0	1.07 ± 0.34	3.6
20090131	44346	44174	0.5°	S	75	20.0	0.97 ± 0.34	3.2
20090131	44347	44174	0.5°	N	79	20.0	1.07 ± 0.35	3.5
20090131	44348	44174	0.5°	S	83	20.0	2.27 ± 0.41	6.8
20090131	44349	44174	0.5°	N	88	20.0	0.68 ± 0.31	2.4
20090131	44353	44174	0.5°	N	72	20.0	0.95 ± 0.33	3.3
20090131	44354	44174	0.5°	S	68	20.0	1.78 ± 0.39	5.4
20090131	44355	44174	0.5°	N	64	10.0	0.13 ± 0.39	0.3
20090201	44375	44174	0.5°	S	54	25.0	0.63 ± 0.29	2.4
20090201	44378	44174	0.5°	N	66	20.0	0.85 ± 0.35	2.7
20090201	44379	44174	0.5°	S	71	20.0	0.80 ± 0.32	2.8
20090201	44380	44174	0.5°	N	75	20.0	0.63 ± 0.32	2.2

Table A.2 (Continued)

Date	Run	Laser	Pointing Dir.		Zenith Angle[°]	Duration min	Rate γ/min	σ
20090201	44381	44174	0.5°	S	80	20.0	1.18 ± 0.37	3.7
20090201	44383	44174	0.5°	E	88	20.0	0.69 ± 0.30	2.5
20090201	44384	44174	0.5°	W	84	20.0	0.97 ± 0.32	3.5
20090201	44385	44174	0.5°	W	80	20.0	0.73 ± 0.32	2.5
20090201	44386	44174	0.5°	N	76	20.0	0.78 ± 0.32	2.7
20090201	44387	44174	0.5°	S	72	20.0	1.28 ± 0.34	4.4
20090201	44388	44174	0.5°	N	67	20.0	1.10 ± 0.32	3.9
20090201	44389	44174	0.5°	S	64	20.0	0.67 ± 0.27	2.8
20090202	44427	44174	0.5°	N	70	20.0	0.60 ± 0.34	1.9
20090202	44429	44174	0.5°	E	81	20.0	0.77 ± 0.36	2.3
20090202	44430	44174	0.5°	S	86	20.0	0.82 ± 0.31	3.0
20090202	44431	44174	0.5°	N	88	20.0	0.52 ± 0.29	1.9
20090202	44439	44174	0.5°	N	74	20.0	0.95 ± 0.33	3.3
20090202	44443	44174	0.5°	N	66	20.0	0.65 ± 0.33	2.1
20090203	44457	44174	0.5°	S	85	25.0	0.33 ± 0.27	1.3
20090203	44459	44174	0.5°	S	84	20.0	0.55 ± 0.30	2.0
20090203	44460	44174	0.5°	N	74	20.0	0.58 ± 0.34	1.8
20090203	44464	44174	0.5°	S	66	20.0	0.98 ± 0.33	3.4
20090203	44465	44174	0.5°	N	63	10.0	0.10 ± 0.39	0.3
20090204	44475	44174	0.5°	N	78	17.0	0.33 ± 0.33	1.1
20090204	44476	44174	0.5°	N	83	20.0	0.77 ± 0.33	2.5
20090204	44478	44174	0.5°	S	87	20.0	0.82 ± 0.33	2.7
20090204	44479	44174	0.5°	N	81	20.0	1.02 ± 0.35	3.3
20090205	44491	44174	0.5°	S	83	20.0	0.30 ± 0.30	1.0
20090205	44492	44174	0.5°	N	79	20.0	0.90 ± 0.33	3.0
20090205	44493	44174	0.5°	S	74	20.0	0.30 ± 0.29	1.1
20090206	44508	44509	0.5°	N	63	20.0	0.17 ± 0.27	0.6
20090219	44587	44577	0.5°	N	78	20.0	1.12 ± 0.32	4.0
20090226	44704	44691	0.5°	S	86	20.0	1.88 ± 0.43	5.0
20090226	44706	44691	0.5°	N	81	20.0	1.33 ± 0.37	4.2
20090226	44707	44691	0.5°	S	77	20.0	1.60 ± 0.40	4.6
20090227	44730	44721	0.5°	N	74	20.0	1.22 ± 0.36	3.9
20090227	44731	44721	0.5°	S	78	20.0	1.13 ± 0.39	3.2
20090227	44732	44721	0.5°	N	83	20.0	1.43 ± 0.40	4.1
20090227	44733	44721	0.5°	S	87	16.0	0.75 ± 0.40	2.0

Table A.2 (Continued)

Date	Run	Laser	Pointing Dir.		Zenith Angle[°]	Duration min	Rate γ/min	σ
20090227	44735	44721	0.5°	S	86	20.0	1.42 ± 0.36	4.7
20090227	44736	44721	0.5°	N	80	20.0	1.10 ± 0.37	3.3
20090227	44737	44721	0.5°	N	75	20.0	0.38 ± 0.33	1.2
20090301	44795	44789	0.5°	N	79	20.0	0.42 ± 0.31	1.4
20090317	44907	44897	0.5°	N	82	20.0	1.18 ± 0.37	3.7
20090326	45152	45163	0.5°	S	88	20.0	0.13 ± 0.26	0.5
20090417	45528	45539	0.5°	N	81	20.0	0.35 ± 0.31	1.2
20090417	45529	45539	0.5°	S	85	20.0	0.08 ± 0.26	0.3
20090417	45530	45539	0.5°	N	88	20.0	0.15 ± 0.30	0.5
20090417	45531	45539	0.5°	S	84	20.0	0.42 ± 0.31	1.4
20090423	45695	45708	0.5°	N	88	20.0	0.13 ± 0.31	0.4
20090423	45696	45708	0.5°	S	85	20.0	1.17 ± 0.35	3.8
20090423	45697	45708	0.5°	N	81	20.0	0.50 ± 0.30	1.8
20090423	45698	45708	0.5°	S	77	20.0	0.35 ± 0.31	1.2
20090423	45701	45708	0.5°	N	69	20.0	0.13 ± 0.23	0.6
20090423	45702	45708	0.5°	S	64	18.0	0.28 ± 0.31	0.9

2008-2009 Daily Integral Flux for 1ES 1218+304

Table A.3 For 1ES 1218+304, the daily gamma-ray rates and the integral fluxes, $\phi(E > 200$ GeV), binned by day.

MJD	Rate γ/min	$\phi(>200$GeV) 10^{-12} cm^{-2} s^{-1}
54829	0.69 ± 0.23	8.90 ± 6.0
54830	1.08 ± 0.23	31.8 ± 6.5
54838	0.46 ± 0.23	12.4 ± 6.4
54839	0.37 ± 0.18	12.1 ± 5.0
54856	0.46 ± 0.17	6.36 ± 4.8
54860	0.76 ± 0.13	25.8 ± 3.9
54861	1.64 ± 0.21	53.4 ± 6.8
54862	1.18 ± 0.11	31.9 ± 3.2
54863	0.86 ± 0.08	23.0 ± 2.4
54864	0.72 ± 0.12	16.9 ± 3.4
54865	0.52 ± 0.13	14.2 ± 4.0
54866	0.75 ± 0.15	18.5 ± 4.4
54867	0.50 ± 0.17	16.7 ± 5.0
54881	1.12 ± 0.28	29.9 ± 8.3
54888	1.61 ± 0.20	44.7 ± 6.0
54889	1.07 ± 0.13	26.4 ± 3.7
54891	0.42 ± 0.29	17.8 ± 8.3
54907	1.18 ± 0.32	21.0 ± 8.9
54938	0.21 ± 0.14	6.36 ± 4.1
54944	0.43 ± 0.12	12.9 ± 3.5

BIBLIOGRAPHY

Abdo, A.A., et al.(2009a), "Fermi Observations of TeV-Selected Active Galactic Nuclei," ApJ, **707**, 1310

Abdo, A.A., et al. (2009b), "Fermi/Large Area Telescope Bright Gamma-Ray Source List," ApJS, **183**, 46.

Acciari, V.A., et al. (2008a), "VERITAS Discovery of $>$ 200 GeV Gamma-Ray Emission from the Intermediate-Frequency-Peaked BL Lacertae Object W Comae," ApJ, **684**, L73.

Acciari, V.A., et al. (2008b), "Veritas Observations of a Very High Energy γ-Ray Flare From the Blazar 3C66A," ApJ, **693**, L104.

Acciari, V., et al. (2008c), "Observation of Gamma-Ray Emission from the Galaxy M87 above 250 GeV with VERITAS," ApJ, **679**, 397A

Acciari, V., et al. (2009a). "VERITAS observations of the Bl Lac object 1ES 1218+304," ApJ, **695**, 1370.

Acciari, V., et al. (2009b), "Multiwavelength Observations of a TeV-Flare from W Comae," ApJ, **707**, 612.

Acciari, V. et al. (2009c). "Radio Imaging of the Very-High-Energy γ-Ray Emission Region in the Central Engine of a Radio Galaxy," Science, **325**, 444.

Acciari, V. et al. (2009d). "Observation of Extended Very High Energy Emission from the Supernova Remnant IC 443 with VERITAS," ApJ, **698**, 133.

Acciari, V. et al. (2009e), " A connection between star formation activity and cosmic rays in the starburst galaxy M82," Nature, **462**, 770.

Acciari, V., et al. (2010a). "Discovery of Variability in the Very High Energy $\gamma-$Ray Emission of 1ES 1218+304 with VERITAS," ApJ, **709L**, 163.

Acciari, V. et al. (2010b), "Observations of the Shell-type Supernova Remnant Cassiopeia A at TeV Energies with VERITAS," ApJ, **714**, 163.

Acciari, V. et al. (2010c). "VERITAS 2008 - 2009 monitoring of the variable gamma-ray source M87," ApJ, **716**, 819.

Aharonian, F., et al. (1999a), "The temporal characteristics of the TeV gamma-radiation from MKN 501 in 1997. I. Data from the stereoscopic imaging atmospheric Cherenkov telescope system of HEGRA, " A&A, **342**, 69.

Aharonian, F., et al. (1999b), "Observations of MKN 421 during 1997 and 1998 in the energy range above 500 GeV with the HEGRA stereoscopic Cherenkov telescope system," A&A, **350**, 757.

Aharonian, F.,(2000), "TeV gamma rays from BL Lac objects due to synchrotron radiation of extremely high energy protons," New Astronomy, **5**, 377.

Aharonian, F., et al. (2001), "The TEV Energy Spectrum of Markarian 501 Measured with the Stereoscopic Telescope System of HEGRA during 1998 and 1999," ApJ, **546**, 898.

Aharonian, F., et al. (2002a), "TeV gamma rays from the blazar H 1426+428 and the diffuse extragalactic background radiation," ApJ, **384**, L23.

Aharonian, F., et al. (2002b), "Variations of the TeV energy spectrum at different flux levels of Mkn 421 observed with the HEGRA system of Cherenkov telescopes," A&A, **393**, 89.

Aharonian, F., et al. (2003), "Detection of TeV gamma-rays from the BL Lac 1ES 1959+650 in its low states and during a major outburst in 2002," A&A, **406**, 9.

Aharonian, F., et al. (2004). "Observations of 54 Active Galactic Nuclei with the HEGRA system of Cherenkov telescopes," A&A, **457**, 899.

Aharonian, F., et al. (2005a), "H.E.S.S. observations of PKS 2155–304," A&A, **430**, 865.

Aharonian, F., et al. (2005b), "Discovery of VHE gamma rays from PKS 2005–489," A&A, **436**, L17.

Aharonian, F., et al. (2005c), "Discovery of Very High Energy Gamma Rays Associated with an X-ray Binary," Science, **309**, 746.

Aharonian, F., et al. (2005d), "A search for very high energy gamma-ray emission from the starburst galaxy NGC 253 with HESS," A&A, **442**, 177.

Aharonian, F., et al.(2005e). "The unidentified TeV source (TeV J2032+4130) and surrounding field:Final HEGRA IACT-System results," A&A, **431**, 197.

Aharonian, F., et al. (2006a). "Observations of the Crab Nebula with HESS," A&A, **421**, 529.

Aharonian, F., et al. (2006b). "A low level of extragalactic background light as revealed by γ-rays from blazars," Nature, **440**, 1018.

Aharonian, F., et al. (2007a). "An Exceptional Very High Energy Gamma-Ray Flare of PKS 2155–304," ApJ, **664**, L71.

Aharonian, F., et al. (2007b). "Discovery of VHE γ-rays from the distant BL Lacertae 1ES 0347–121," A&A, **473**, L25.

Aharonian, F., et al. 2007c, "New constraints on the mid-IR EBL from the HESS discovery of VHE γ-rays from 1ES 0229+200," A&A, **475**, L9.

Aharonian, F., et al. (2008), "Formation of hard very high energy gamma-ray spectra of blazars due to internal photon-photon absorption," MNRAS, **387**, 1206.

Aharonian, F., et al. (2009a). "Simultaneous multiwavelength observations of the second exceptional gamma-ray flare of PKS 2155-304 in July 2006," A&A, **502**, 749.

Aharonian, F., et al. (2009b), " Detection of Gamma Rays from a Starburst Galaxy," Science, **326**, 1080.

Albert J., et al. (2006a). "Discovery of very high energy gamma rays from 1ES 1218+30.4," Astronom. J., **642**, L119.

Albert, J., et al. (2006b), "Discovery of Very High Energy γ-Rays from Markarian 180 Triggered by an Optical Outburst," ApJ, **648**, L105.

Albert, J., et al. (2006c), "Observation of Very High Energy Gamma-Ray Emission from the Active Galactic Nucleus 1ES 1959+650 Using the MAGIC Telescope," ApJ, **639**, 761.

Albert, J., et al. (2006d), "Variable Very-High-Energy Gamma-Ray Emission from the Microquasar LS I +61 303," Science, **312**, 1771

Albert, J., et al. (2007a), "Observation of Very High Energy γ-Rays from the AGN 1ES 2344+514 in a Low Emission State with the MAGIC Telescope," ApJ,**662**, 892.

Albert, J., et al. (2007b), "Discovery of Very High Energy γ-Ray Emission from the Low-Frequency-peaked BL Lacertae Object BL Lacertae," ApJ,**666**, L17.

Albert, J., et al. (2007c), "Discovery of Very High Energy γ-Rays from 1ES 1011+496 at $z = 0.212$," ApJ,**667**, L21.

Albert, J., et al. (2007d), "Detection of Very High Energy Radiation from the BL Lacertae Object PG 1553+113 with the MAGIC Telescope," ApJ,**654**, L119.

Albert, J., et al. (2007e). "Observations of Markarian 421 with the MAGIC Telescope," ApJ, **663**, 125.

Albert, J., et al. (2008). "Very-High-Energy gamma rays from a Distant Quasar: How Transparent Is the Universe?," Science, **320**, 1752.

Angel, J. R. P., & Stockman, H. S.,(1980). "Optical and infrared polarization of active extragalactic objects," ARA&A, **18**, 321.

Bade. N., et al. (1998). "On the evolutionary behaviour of BL Lac objects," A&A, **334**, 459.

Bednarek, W.,(1993). "On the gamma-ray emission from 3C 279," MNRAS, **402**, 29.

Bednarek, W., & Prothroe, R. J., (1997). "Modulation of AGN gamma-rays by interaction with X-rays from an accretion disc hotspot," MNRAS, **290**, 139.

Begelman, M. C., Blandford, R. D., & Rees, M. J.(1984). "Theory of extragalactic radio sources," Rev. Mod. Phys. **56**, 255.

Bernstein, R. A., Freedman, W. L., & Madore, B. F. (2002). "The First Detections of the Extragalactic Background Light at 3000, 5500, and 8000 Å. I. Results," A&A, **571**, 56

Bernstein, R. A., Freedman, W. L., & Madore, B. F. (2005). "Corrections of Errors in "The First Detections of the Extragalactic Background Light at 3000, 5500, and 8000 Å. I, II, and III" (ApJ, 571; 56, 85, 107 [2002])," ApJ, **632**, 713

Bernstein, R. A.,et al. (2007). "The Optical Extragalactic Background Light: Revisions and Further Comments," ApJ, **666**, 663.

Biermann, P. L., et al. (2003). "Single and binary Black Holes and their active environment," in Proc. to the 7th. Paris Cosmology Colloquium, Eds. N. Sanchez and H. de Vega.

Biller, S. D., et al. (1998). "New Limits to the Infrared Background: Bounds on Radiative Neutrino Decay and on Contributions of Very Massive Objects to the Dark Matter Problem," Phys. Rev. Lett., **80**, 2992.

Blandford, R. D., & Eichler, D., (1987). "Particle acceleration at astrophysical shocks: A theory of cosmic ray origin," PhR, **154**, 1.

Błażejowski, M., et al. (2000). "Comptonization of Infrared Radiation from Hot Dust by Relativistic Jets in Quasars," ApJ, **545**, 107.

Bloom, S. D., & Marscher, A. P., (1996). "An Analysis of the Synchrotron Self-Compton Model for the Multi–Wave Band Spectra of Blazars," ApJ, **461**, 657.

Blustin, A. J., et al. (2004). "Intrinsic absorbers in BL Lac objects: The XMM-Newton view," A&A, **417**, 60.

Böttcher, M., & Chiang, J.(2002). "X-Ray Spectral Variability Signatures of Flares in BL Lacertae Objects," ApJ, **581**, 121.

Böttcher, M.(2007). " Modeling the emission processes in blazars," Astrophys. Space Sci., **309**, 95.

Böttcher, M., Dermer, C., & Finke, J. (2008). "The Hard VHE γ-Ray Emission in High-Redshift TeV Blazars: Comptonization of Cosmic Microwave Background Radiation in an Extended Jet?," ApJ, **679**, L9.

Briggs, M. S., et al. (1996). "BATSE Observations of the Large-Scale Isotropy of Gamma-Ray Bursts," ApJ, **459**, 40.

Brown, T. M., Kimble, R. A., Ferguson, H. C., et al. (2000). "Measurements of the Diffuse Ultraviolet Background and the Terrestrial Airglow with the Space Telescope Imaging Spectrograph," Astronom. J., **120**, 1153

Cambresy, L., Reach, W. T., Beichman, C. A., & Jarrett, T. H. (2001). "The Cosmic Infrared Background at 1.25 and 2.2 Microns Using DIRBE and 2MASS: A Contribution Not Due to Galaxies?," ApJ, **555**, 563

Celotti, A., Ghisellini, G., & Chiaberge, M.(2001). "Large-scale jets in active galactic nuclei: multiwavelength mapping," MNRAS, **321**, L1

Cheng, K. & Ruderman, M. A., (1986). "Energetic radiation from rapidly spinning pulsars. I - Outer magnetosphere gaps. II - VELA and Crab," ApJ, **300**, 500.

Cogan. P., (2006). "Nanosecond samplings of atmospheric Cherenkov radiation applied to TeV gamma-ray observations of blazars with VERITAS," Ph.D Thesis, University College Dublin, Ireland.

Cooke, B. A., et al. (1978)."The Ariel V /SSI/ catalogue of high galactic latitude /absolute value of B greater than 10 deg/ X-ray sources," Royal Astronomical Society, **182**, 489.

Coppi, P. S., & Aharonian, F., (1999). "Simultaneous X-Ray and Gamma-Ray Observations of TEV Blazars: Testing Synchro-Compton Emission Models and Probing the Infrared Extragalactic Background," ApJ, **521**, 33.

Costamante, L. & Ghiselellini, G., (2002). "TeV candidate BL Lac objects," A&A, **384**, 56.

Daniel, M., et al. (2005). "Spectrum of Very High Energy Gamma-Rays from the blazar 1ES 1959+650 during Flaring Activity in 2002," ApJ, **621**, 181.

Daniel, M. et al. (2007), "The VERITAS Standard Data Analysis," in Proc. to the 30th ICRC, Merida.

Dar, A., & Laor, A.,(1997). "Hadronic Production of TeV Gamma-Ray Flares from Blazars," ApJ, **478**, L5.

Daum, A., et al. (1997). "First results on the performance of the HEGRA IACT array," Astropart. Phys., **8**, 1D.

de Jager, O. C., Stecker, F. W., & Salamon, M. H.(1994). "Estimate of the intergalactic infrared radiation field from γ-ray observations of the galaxy Mrk 421," Nature, **369**, 294.

Dermer, C., & Schlickkeiser, R., (1993). "Model for the High-Energy Emission from Blazars," ApJ, **416**, 458.

Dermer, C., & Schlickkeiser, R., (1994), "On the location of the acceleration and emission sites in gamma-ray blazars," ApJS, **90**, 945.

Dermer, C., Sturner, S. J., & Schlickkeiser, R.(1997). "Nonthermal Compton and Synchrotron Processes in the Jets of Active Galactic Nuclei," ApJS, **109**, 103.

Djannati-Ataï, A., et al. (1999). "Very High Energy Gamma-ray spectral properties of MKN 501 from CAT Čerenkov telescope observations in 1997," A&A, **350**, 17.

Dole, H., Lagache, G., Puget, J.-L., et al. (2006). " The cosmic infrared background resolved by Spitzer. Contributions of mid-infrared galaxies to the far-infrared background," A&A, **451**, 417

Domingo-Santamaria, E., & Torres, D. F. (2005). "High energy -ray emission from the starburst nucleus of NGC 253," A&A, **444**, 403.

Donato, D., et al. (2001). "Hard X-ray properties of blazars," A&A, **375**, 739.

Donea, A. C.,& Protheroe, R. J.(2003). " Radiation fields of disk, BLR and torus in quasars and blazars: implications for γ-ray absorption," APh, **18**, 377.

Donnnarumma, I, et al. (2009). "The June 2008 Flare of Markarian 421 from Optical to TeV Energies," ApJ, **691**,13

Drury, L. O., Aharonian, F. , & Völk, H. J., (1994). "The gamma-ray visibility of supernova remnants. A test of cosmic ray origin," A&A, **287**, 959.

Dube, R. R., Wickes, W. C., & Wilkinson, D. T. (1979). " Upper limit on the extragalactic background light," ApJ, **232**, 333

Dwek, E. & Arendt, R. G. (1998). "A Tentative Detection of the Cosmic Infrared Background at 3.5 μm from COBE/DIRBE Observations," ApJ, **508**, L9.

Dwek, E., & Slavin, J.(1994). "On the determination of the cosmic infrared background radiation from the high-energy spectrum of extragalactic gamma-ray sources," ApJ, **436**, 696.

Dwek, E., (2001). "The Role of Dust in Producing the Extragalactic Diffuse Background," in Proc. of IAU Symposium, The Extragalactic Infrared Background and its Cosmological Implications, **208**, 389.

Dwek, E., Arendt, R. G., & Krennrich, F. (2005). "The Near-Infrared Background: Interplanetary Dust or Primordial Stars?" ApJ, **635**, 784.

Dwek, E., & Krennrich, F.,(2005). "Simultaneous Constraints on the Spectrum of the Extragalactic Background Light and the Intrinsic TeV Spectra of Markarian 421, Markarian 501, and H1426+428," ApJ,**618**, 657.

Edelstein, J., Bowyer, S., & Lampton, M.(2000). "Reanalysis ofVoyager Ultraviolet Spectrometer Limits to the Extreme-Ultraviolet and Far-Ultraviolet Diffuse Astronomical Flux," ApJ, **539**, 187.

Elbaz, D., Cesarsky, C. J., Chanial, P., et al. (2002). "The bulk of the cosmic infrared background resolved by ISOCAM," A&A, **384**, 848

Elvis, M., et al. (1992). "The Einstein Slew Survey," ApJS, **80**, 257.

Falomo, R., et al. (1999). "Optical imaging of the host galaxies of X-ray selected BL Lacertae objects," A&A, **352**, 85.

Falomo, R., et al. (2000). "The Hubble Space Telescope Survey of BL Lacertae Objects. III. Morphological Properties of Low-Redshift Host Galaxies," ApJ, **542**, 731

Fazio, G. G., Ashby, M. L. N., Barmby, P., et al. (2004). "Number Counts at $3\mu\text{m} < \lambda < 10\mu\text{m}$ from the Spitzer Space Telescope," ApJS, **154**, 39.

Finkbeiner, D. P., Davis, M., & Schlegel, D. J. (2000). "Detection of a Far-Infrared Excess with DIRBE at 60 and 100 Microns," ApJ, **544**, 81

Finke, J. D.& Razzaque, S.(2009). "Constraints on the Extragalactic Background Light from Very High Energy Gamma-Ray Observations of Blazars," ApJ, **698**, 1761.

D.J. Fixsen et al. (1998). "The Spectrum of the Extragalactic Far-Infrared Background from the COBE FIRAS Observations," ApJ, **508**, 123.

Fomin, V. P., et al. (1994). "New methods of atmospheric Cherenkov imaging for gamma-ray astronomy. I. The false source method," Astropart. Phys., **2**, 137.

Fossati, G., et al. (1998). "A unifying view of the spectral energy distributions of blazars," MNRAS, **299**, 433.

Franceschini, A., Rodighiero, G., & Vaccari, M.(2008). "Extragalactic optical-infrared background radiation, its time evolution and the cosmic photon-photon opacity," A&A, **487**, 837.

Frank, I. M. & Tamm, Ig., (1937). C. R. Ac. Sci., USSR. **14**, 109.

Frayer, D. T., Huynh, M. T., Chary, R., et al. (2006). "Spitzer 70 Micron Source Counts in GOODS-North," ApJ, **647**, L9

Funk, B., et al. (1998). "An upper limit on the infrared background density from HEGRA data on MKN 501," Astropart. Phys., **9**, 97.

Funk, S. (2005). "A new population of very high-energy gamma-ray sources detected with H.E.S.S in the inner part of the Milky Way," Ph.D. Thesis, University of Heidelberg, Germany.

Gaidos, J. A., et al. (1996). "Extremely rapid bursts of TeV photons from the active galaxy Markarian 421," Nature, **383**, 319.

Galbraith, W., & Jelly, J. G.,(1953). "Light Pulses from the Night Sky associated with Cosmic Rays," Nature, **171**, 349.

Galbraith, W., & Jelly, J. G.,(1955). Journal of Atmospheric and Terrestrial Physics, **250**, 304.

Gamma, E., Helm, R., Johnson, R., & Vlissides, J. M. (1994). "Design Patterns: Elements of Reusable Object-Oriented Software," McGraw-Hill, New York.

Gardner, J. P., Brown, T. M., & Ferguson, H. C.(2000). "Ultraviolet Galaxy Counts from Space Telescope Imaging Spectrograph Observations of the Hubble Deep Fields," ApJ, **542**, L79.

Gehresl, N, Macomb, D. J., Bertsch, D. L., Thompson, D. J., & Hartman, R. C. (2000). "Discovery of a new population of high-energy gamma-ray sources in the Milky Way," Nature, **404**, 363.

Ghisellini, G., & Madau, P., (1996). "On the origin of the gamma-ray emission in blazars," MNRAS, **280**, 67.

Gilmore, R. C., Madau, P., Primack, J. R., & Sommerville, R. S.(2008). "Modeling Gamma-Ray Attenuation in High Redshift GeV Spectra," in American Institute of Physics Conference Series, **1085**, 577.

Giommi, P., et al. (2005). "The sedentary survey of extreme high energy peaked BL Lacs," A&A, **434**, 385.

Giroletti,, M., et al. (2004). "A Sample of Low-Redshift BL Lacertae Objects. I. The Radio Data," ApJ, **613**, 752.

Ginzburg, V. L., & Syrovatskii, S. I. (1963). "Origin of Cosmic Rays" Macmillan, New YorK, 1964.

Gorjian, V., Wright, E. L., & Chary, R. R. (2000). "Tentative Detection of the Cosmic Infrared Background at 2.2 and 3.5 Microns Using Ground-based and Space-based Observations," ApJ, **536**, 550

Gould, R. S., & Schreder, G. (1966). "Opacity of the Universe to High-Energy Photons," Phys. Rev. Lett., **16**, 252.

Gould, R. S., & Schreder, G. (1967). "Opacity of the Universe to High-Energy Photons," Phys. Rev. Lett., **155**, 1408.

Grenier, I. A.,(2002). "Unidentified EGRET sources in the Galaxy," in Proc. to XXI Texas Symposium on Relativistic Astrophysics, Italy, p.397 - 404, World Scientific Publishing, ISBN 981-238-580-0,

Harding, A., (1996). "Inverse-Compton Gamma-Rays from Plerions," Space Sci. Rev., **75**, 257

Hartman, R. C, Bertsch, D. L., & Bloom, S. D., et al. (1999). "The Third EGRET Catalog of High-Energy Gamma-Ray Sources," ApJS, **123**, 79.

Hauser, M., et al. (1998). "The COBE Diffuse Infrared Background Experiment Search for the Cosmic Infrared Background. I. Limits and Detections," ApJ, **1998**, 508.

Hauser, M. & Dwek, E., (2001), "The Cosmic Infrared Background: Measurements and Implications," ARA&A, **39**, 249.

Heck, D., et al. (1998), "Corsika: A monte carlo code to simulate extensive air showers," Technical Report FZKA **6019**.

Hillas, M.(1985a). "Electromagnetic and muonic structure of showers initiated by gamma-rays and by hadrons," Proc. 19th ICRC (La Jolla), **3**, 445.

Hillas, A. M., (1985b), "Cerenkov light images of EAS produced by primary gamma,". Proc. 19th ICRC (La Jolla), **1**, 155.

Holder, J., et al. (2006). "The first VERITAS telescope," Astropart. Phys., **25**, 391.

Horan, D., & Finley, J. P., (2001). in Kampert K. H. Heinzelmann G., Spiering, C., eds, Proc 27th ICRC, Copernicus Gesellschaft, Hamburg, p. 2622.

Horan, D., et al. (2004). "Constraints on the Very High Energy Emission from BL Lacertae Objects," ApJ, **603**, 51.

Imran, A., & Krennrich, F.(2007). "Detecting a unique EBL signature with TeV gamma rays," in Proc. to the 30th IRCR, Merida, Mexico

Ito, C. et al. (2002). "Detection of diffuse TeV gammaray emission from the nearby starburst galaxy NGC 253," A&A, **396**, 1.

Jakobson, P., et al. (2006). " A mean redshift of 2.8 for Swift gammaray bursts," A&A, **447**, 897.

Jelly, J. G., & Porter N. A., (1963). "Čerenkov Radiation from the Night Sky, and its Application to γ-Ray Astronomy," Quart. J. R. Astron. Soc., **4**, 275.

Jelley, J. V. (1966). "High-Energy γ-Ray Absorption in Space by a 3.5°K Microwave Field." Phys. Rev. Lett., **16**, 479.

Jordan, P., & Krennrich, F. (2004), "The Design of Light Concentrators for a 12m Cherenkov Telescope," Internal memo for the VERITAS collaboration.

Kaaret, P., Cusumano, G., & Sacco, B., "X-ray timing of the 34 millisecond binary pulsar SAX J0634+0533," ApJ, **542**, 41.

Kashlinsky, A., Mather, J., Odenwald, S., & Hauser, M. (1996). "Clustering of the Diffuse Infrared Light from the COBE DIRBE Maps. I. C(0) and Limits on the Near-Infrared Background," ApJ, **470**, 681.

Kashlinsky, A., & Odenwald, S. (2000). "Clustering of the diffuse infrared light from the COBE DIRBE maps. III. Power spectrum analysis and excess isotropic component of fluctuations," ApJ, **528**, 74.

Kashlinsky, A.,(2005), "Cosmic infrared background and early galaxy evolution," Physics Report, **409**, 361.

Kashlinksy, A., Arendt, R. G., Mather, J., & Moseley, S. H. (2005). "Tracing the first stars with fluctuations of the cosmic infrared background," Nature, **438**, 45.

Katarzyński, K., et al. (2006). "Hard TeV spectra of blazars and the constraints to the infrared intergalactic background," MNRAS Letters, **368**, L52.

Kelsall, T., et al. (1998). "The COBE Diffuse Infrared Background Experiment Search for the Cosmic Infrared Background. II. Model of the Interplanetary Dust Cloud," ApJ, **508**, 44.

Kertzman, M. P., & Sembroski, G. H. (1994). "Computer simulation methods for investigating the de- tection characteristics of TeV air Cherenkov telescopes," Nuclear Instrumentation and Methods in Physics Research A, **528**, 629.

Kneiske, T. M., Bretz, T., Mannheim, K., & Hartmann, D. H., (2004). "Implications of cosmological gamma-ray absorption. II. Modification of gamma-ray spectra," A&A, **413**, 807.

Kotilainen, J. K, et al. (2004). "The optical-near-infrared colour of the host galaxies of BL Lacertae objects," A&A, **424**, 107.

Koyama, K., et al. (1995). "Evidence for shock acceleration of high-energy electrons in the supernova remnant SN1006," Nature, **378**, 255.

Krawczynski, H., Coppi, P. S., Maccarone, T., & Aharonian, F., (2000). "X-ray/TeV-gamma-ray observations of several strong flares of Mkn 501 during 1997 and implications," A&A, **353**, 97.

Krawczynski, H., et al. (2001). "X-ray/TeV-gamma-ray observations of several strong flares of Mkn 501 during 1997 and implications," ApJ, **559**, 187.

Krawczynski, H., Coppi, & Aharonian, F.,(2002). "Time-dependent modelling of the Markarian 501 X-ray and TeV gamma-ray data taken during 1997 March and April," MNRAS, **336**, 721.

Krennrich, F., et al. (1999). "Measurement of the multi-TeV gamma-ray flare spectrum of Markarian 421 and Markarian 501," ApJ, **511**, 149

Krennrich, F., et al. (2002). "Discovery of Spectral Variability of Markarian 421 at TeV Energies," ApJ, **575**, 9.

Krennrich, F., Dwek, E., & Imran, A.,(2008). "Constraints on Energy Spectra of Blazars based on Recent EBL Limits from Galaxy Counts," ApJ, **689**, 93.

Kubo, H., et al. (2004). "Status of the CANGAROO-III project," New Astron. Rev., **48**, 323.

Lagache, G., & Puget, J.-L. (2000). "Detection of the extra-Galactic background fluctuations at 170 μm," A&A, **355**, 17

Laurent-Muehleisen, S. A., et al. (1993). "Radio morphology and parent population of X-ray selected BL Lacertae objects," Astronom. J., **106**, 875.

Ledden, J. E., et al. (1981). "The spectral flux distribution of the candidate BL Lacertae object 1218+304 /identically equal to 2A 1219+305/," ApJ, **243**, 47L.

Leinert, C., Bowyer, S., Haikala, L. K., et al. (1998). "The 1997 reference of diffuse night sky brightness," A&AS, **127**, 1

Levenson, L. R., Wright, E. L., & Johnson, B. D. (2007). "IRBE Minus 2MASS: Confirming the CIRB in 40 New Regions at 2.2 and 3.5 μm," ApJ, **666**, 34.

Levenson, L. R., & Wright, E. L., (2008). " Probing the 3.6 μm CIRB with Spitzer in Three DIRBE Dark Spots," ApJ, **683**, 585.

Li, T. P., & Ma, Y. Q.,(1983), "Analysis methods for results in gamma-ray astronomy," ApJ, **272**, 317.

Lin, Y. C., et al. (1996). "EGRET observations of BL Lacertae objects with redshifts below 0.2," ApJS, **120**, 499.

Madau, P., & Pozzetti, L. (2000). "Deep galaxy counts, extragalactic background light and the stellar baryon budget," MNRAS, **312**, L9

Maier, G. (2007). "Systematic errors in spectral energy reconstruction," VERITAS internal note, Analysis and Calibration ELog, **595**.

Malkan, M. A., & Stecker, F. W. (1998). "An Empirically Based Calculation of the Extra-galactic Infrared Background," ApJ, **496**, 13.

Malkan, M. A., & Stecker, F. W. (2001). "An Empirically Based Model for Predicting Infrared Luminosity Functions, Deep Infrared Galaxy Counts, and the Diffuse Infrared Background," ApJ, **555**, 641

Malkov, M., & Drury, O'C. (2001). "Nonlinear theory of diffusive acceleration of particles by shock waves," Reports on Progress in Physics, **64**, 429.

Mannheim, K., & Biermann, P. L.,(1992). "Gamma-ray flaring of 3C 279 – A proton-initiated cascade in the jet?," A&A, **253**, L21.

Mannheim, K.(1993). "Photomeson production in active galactic nuclei," A&A, **221**, 211.

Mapelli, M., Salvaterra, R., & Ferrara, A. (2004). "Extragalactic Background Light: new constraints from the study of the photon-photon absorption on blazar spectra," Dettmar, R., Klein, U., & salucci, P. (eds), Baryons in Dark Matter Halos.

Maraschi, L., Ghisellini, G., & Celotti, A.,(1992). "A jet model for the gamma-ray emitting blazar 3C 279," ApJ, **397**, L5.

Maraschi, L., et al. (1999). "Simultaneous X-Ray and TEV Observations of a Rapid Flare from Markarian 421," ApJ, **526**, 81.

Marscher, A. P., & Gear, W. K., (1985). "Models for high-frequency radio outbursts in extragalactic sources, with application to the early 1983 millimeter-to-infrared flare of 3C 273," ApJ, **298**, 114

Marscher, A. P., Jorstad, S. G., Gomez, J.-L.,Aller, M. F., Terasranta. H., Lister, M. L., & Stirling, A. M. (2002). "Observational evidence for the accretion-disk origin for a radio jet in an active galaxy," Nature, **417**, 625.

Marscher, A. (2006). "Relativistic Jets in Active Galactic Nuclei," in AIP Conf. Proc. **856**, 1.

Martin, C., Hurwitz, M., & Bowyer, S. (1991). "Spectroscopic limits to an extragalactic far-ultraviolet background," ApJ, **379**, 549.

Mastichiadi, A., & Kirk, J. G.,(1997). "Variability in the synchrotron self-Compton model of blazar emission," A&A, **320**, 19.

Mastichiadi, A., & Kirk, J. G.,(2002). "Models of Variability in Blazar Jets," Publications of the Astronomical Society of Australia, **19**, 138.

Matsumoto, T., Matsuura, S., Murakami, H., et al. (2005). "Infrared Telescope in Space Observations of the Near-Infrared Extragalactic Background Light," ApJ, **626**, 31

Mattila, K. (1990). "The Galactic and Extragalactic Background Radiation," ed. S. Bowyer & C. Leinert, IAU Symp. Proceedings, **139**, 257.

Mazin, D. & Raue, M.,(2007). "New limits on the density of the extragalactic background light in the optical to the far infrared from the spectra of all known TeV blazars," A&A, **471**, 439.

Meier, D. L., Koide, S.,& Uchida, Y. (2001). "Magnetohydrodynamic Production of Relativistic Jets," Science, **291**, 84.

Meszaros, R., & Rees, M, (1997). "Optical and Long-Wavelength Afterglow from Gamma-Ray Bursts," ApJ, **476**, 232.

Meszaros, R. (2002). "Theories of gamma-ray bursts," ARA&A, **40**, 137.

Metcalfe, L., Kneib, J.-P., McBreen, B., et al. (2003). "An ISOCAM survey through gravitationally lensing galaxy clusters. I. Source lists and source counts for A370, A2218 and A2390," A&A, **407**, 791.

Mohanty, G. (1995). "The properties of Very High Energy gamma ray sources observed using the air Cherenkov techniques," Ph.D. Thesis, Iowa State University, Iowa.

Moralejo, A., et al. (2009). "Status of Magic-II," in Proc. to 2009 Fermi Symposium, arXiv:0912.3673v1

Mücke, A, & Prothroe, R. J., (2000). "Modeling the April 1997 flare of Mkn 501," AIP Conf. Proc. **515**, 149.

Mücke, A, & Prothroe, R. J., (2001). "A proton synchrotron blazar model for flaring in Markarian 501." Astropart. Phys.,**15**, 121.

Mücke, A, et al. (2003). "BL Lac objects in the synchrotron proton blazar model," Astropart. Phys.,**18**, 593.

Nikishov, A. I. (1961). "Absorption of high-energy photons in the universe," Sov. Phys. JETP, **41**, 549.

Noda, M., et al. (1994). "Near-infrared spectrometer on the Infrared Telescope in Space," ApJ, **428**, 363.

Ong, R.A., et al. (2009a). The Astronomer's Telegram, **2098**, 1.

Ong, R. A. , et al. (2009b), "Highlight Talk: Recent Results from VERITAS," in Proc. to 31^{st} ICRC, Lodz, Poland. http://arxiv.org/abs/0810.0474v1

Padovani, P. (2007). "The blazar sequence: validity and predictions," Astrophys. Space Sci.,**309**, 63.

Papovich, C., Dole, H., Egami, E., et al. (2004). "The 24 Micron Source Counts in Deep Spitzer Space Telescope Surveys," ApJS, **154**, 70

Peacock, J. A. 1999. "Cosmological Physics," Cambridge Univ.Press, Cambridge.

Perkins, J. et al. (2007). "Blazar Discoveries with VERITAS," in Proc. to 31st ICRC, Lodz, Poland, arXiv:0907.4978

Pica, A. J., et al. (1988). "Long-term optical behavior of 144 compact extragalactic objects - 1969-1988," Astronom. J., **96**, 1215.

Pohl, M., Schlickeiser, R., (2000). "On the conversion of blast wave energy into radiation in active galactic nuclei and gamma-ray bursts," A&A, **354**, 395.

Primack, J. R., et al. (2005). "Observational gamma-ray cosmology," AIPC, Proceed. to AIP Conference, **745**, 23.

Puget, J.-L., et al. (1996). "Tentative detection of a cosmic far-infrared background with COBE," A&A, **308**, 5.

Punch, M., et al. (1992), "Detection of TeV photons from the active galaxy Markarian 421," Nature, **358**, 477.

Raue, M., (2007). "New Constraints on the Density of the Extragalactic Background Light and the Discovery of TeV gamma-rays from the BL Lac 1ES 0347-121 and the Extended Source HESS J1023-575," Ph.D. Thesis, University of Hamburg, Germany,

Razzaque, S., Dermer, C., & Finke, J. D., (2009). "The Stellar Contribution to the Extragalactic Background Light and Absorption of High-Energy Gamma Rays," ApJ, **697**, 483.

Reimer, O., (2001). "Unidentified Gamma-Ray Sources," *The Universe in Gamma Rays*, edited by Volker Schönfelder, Springer, New York.

Reimer, O, & Pohl, M., "No evidence yet for hadronic TeV gamma-ray emission from SNR RX J1713.7-3946," A&A, **390**, 43.

Reyes, L., (2007). "Detecting the EBL attenuation of blazars with GLAST," Ph.D. Thesis, University of Maryland, College Park, Maryland.

Reynolds, P. T., et al. (1993). "Survey of candidate gamma-ray sources at TeV energies using a high-resolution Cerenkov imaging system – 1988-1991," ApJ, **404**, 206.

Romero G. E., Benaglia, E.,& Torres, D. F., (1999)"Unidentified 3EG gamma-ray source at low galactic latitudes," A&A, **348**, 868.

Ruderman, M. A., & Sutherland, P. G., (1975). "Theory of pulsars - Polar caps, sparks, and coherent microwave radiation," ApJ, **196**, 51.

Rüger, M., Spanier, F., & Mannheim, K. (2009). "Spectral modelling of 1 ES 1218+30.4," MNRAS, **401**, 973.

Rybicki, G. P. & Lightman, A. P., (1985). "Radiative Processes in Astrophysics," Wiley-VCH, New York.

Salvaterra, R., & Ferrara, A. (2003). "The imprint of the cosmic dark ages on the near-infrared background," MNRAS,**339**, 973.

Sánchez-Conde, M., et al. (2009). "Hints of the existence of axionlike particles from the gamma-ray spectra of cosmological sources," Phys. Rev. D, **79**, 123511.

Sato, R., et al. (2008). "Suzaku Observation of the TeV Blazar 1ES 1218+304: Clues on Particle Acceleration in an Extreme TeV Blazar," ApJ, **680**, L9

Schönfelder, V. (2001). editor, "The Universe in Gamma Rays," Springer,

Schroedter, M.(2005a). "The very high energy gamma-ray spectra of AGN," Ph.D. Thesis, University of Arizona, Arizona,

Schroedter, M.,(2005b). "Upper Limits on the Extragalactic Background Light from the Very High Energy Gamma-Ray Spectra of Blazars," ApJ, **628**, 617.

Shu, H. F.(1991), "The physics of astrophysics", "Volume-I: Radiation", University Science Books, CA

Sikora, M, Begelman, M. C., & Rees, M. J., (1994). "Comptonization of diffuse ambient radiation by a relativistic jet: The source of gamma rays from blazars?," ApJ, **421**, 153.

Spada, M., Ghisellinim G., Lazzati, D., & Celotti, A. (2001). "Internal shocks in the jets of radio-loud quasars," MNRAS, **325**, 1559.

Somerville, R. S. & Primack, J. R. (1999). "Semi-analytic modelling of galaxy formation: the local Universe," MNRAS, **310**, 1087.

Stanev, T., & Franceschini, A., (1998). "Constraints on the Extragalactic Infrared Background from Gamma-Ray Observations of MRK 501," ApJ, **494**, 159.

Stecker, F. W., & de Jager, O. C. (1993). "New Upper Limits on Intergalactic Infrared Radiation from High-Energy Astrophysics," ApJ, **415**, 71.

Stecker, F. W., de Jager , O. C., & Salamon, M. H. (1996). "Predicted Extragalactic TeV Gamma-Ray Sources," ApJ, **473**, 75.

Stecker, F. W., & de Jager, O. C.,(1998), "Absorption of very high energy gamma-rays by intergalactic infared radiation: A new determination," A&A, **334**, 85.

Stecker, F. W., Malkan, M. A., & Scully, S. T. (2006). "Intergalactic Photon Spectra from the Far-IR to the UV Lyman Limit for $0 < z < 6$ and the Optical Depth of the Universe to High-Energy Gamma Rays," ApJ, **648**, 774.

Superina, G., Benbow, W., Boutelier, T., Dubus, G., Giebels, B., (H.E.S.S collaboration) (2007). "H.E.S.S. ICRC 2007 contributions," in Proc. 30th ICRC, Preprint (arxiv:0710.4057, p138).

Takahashi, T., et al. (2000). "Complex Spectral Variability from Intensive Multiwavelength Monitoring of Markarian 421 in 1998," ApJ, **542**, L105.

Tavecchio, F., et al. (2007). " Low-Energy Cutoffs and Hard X-Ray Spectra in High-z Radio-loud Quasars: The Suzaku View of RBS 15," ApJ, **665**, 980.

Teshima, M., et al. (2008). The Astronomer's Telegram, **1500**, 1.

Thompson, R. I., et al. (2007). "Constraints on the Cosmic Near-Infrared Background Excess from NICMOS Deep Field Observations," ApJ, **657**, 669.

Torres, D. F., Domingo-Sanramaria, E., & Romero, G. E.(2004). "High-Energy Gamma Rays from Stellar Associations," ApJ, **601**, 75.

Totani, T. & Kitayama, T., (2000). "Forming Clusters of Galaxies as the Origin of Unidentified GEV Gamma-Ray Sources," ApJ, **545**, 572.

Tramacere, A., et al. (2007). "SWIFT observations of TeV BL Lacertae objects," A&A, **467**, 501.

Toller, G. N. (1983). "The extragalactic background light at 4400 $\AA$," ApJ, **266**, L79.

Urry, C., & Padovani, P., (1995). "Unified Schemes for Radio-Loud Active Galactic Nuclei," PASP, **107**, 803.

Urry, C. M., et al. (2000). "The Hubble Space Telescope Survey of BL Lacertae Objects. II. Host Galaxies," ApJ, **532**, 816.

Villata, M., et al. (2002). "The WEBT BL Lacertae Campaign 2000," A&A, **390**, 407.

Vermeulen, R. C. & Cohen, M. H. (1994). "Superluminal motion statistics and cosmology," ApJ, **430**, 467.

Wagner, R. M., (2006). "Measurement of VHE gamma-ray emission from four blazars using the MAGIC telescope and a comparative blazar study," Ph.D Thesis, University of Mucnich

Wagner, R. M., (2008). "Synoptic studies of 17 blazars detected in very high-energy γ-rays" MNRAS, **385**, 119.

Weekes, T., et al. (1989). "Observation of TeV gamma rays from the Crab nebula using the atmospheric Cerenkov imaging technique," ApJ, **342**, 379.

Weekes, T.(2003), "Very high energy gamma-ray astronomy" IoP series in astronomy and astrophysics, The Institute of Physics Publishing, Bristol, UK.

White, R. L., et al. (2000). "The FIRST Bright Quasar Survey. II. 60 Nights and 1200 Spectra Later," ApJS, **126**, 133.

Wilson, A. S., et al. (1979). "On the identification of the high-latitude X-ray source 2A 1219+305," Royal Astronomical Society, **187**, 109.

Woo, J. & Urry, C. M., (2002). "Active Galactic Nucleus Black Hole Masses and Bolometric Luminosities," ApJ, **579**, 530

Wright, E.,(1998). "Angular Power Spectra of the COBE DIRBE Maps," ApJ, **496**, 1

Wright, E. L., & Reese, E. D. (2000). "Detection of the Cosmic Infrared Background at 2.2 and 3.5 Microns Using DIRBE Observations," ApJ, **545**, 43.

Wright, E. L.(2001). "DIRBE minus 2MASS: Confirming the Cosmic Infrared Background at 2.2 Microns," ApJ, **553**, 538.

Wright, E., & Johnson, B.(2001). "DIRBE Minus 2MASS: the Cosmic Infrared Background at 3.5 Microns," ApJ, submitted (astro-ph/0107205 v2)

Wu, X., et al. (2002). "Supermassive black hole masses of AGNs with elliptical hosts," A&A, **389**, 742

Vassiliev, V. V (2000). " Extragalactic background light absorption signal in the TeV gamma-ray spectra of blazars," Astropart. Phys., **12**, 217.

Vassiliev, V. V., et al. (2003). "VERITAS CFDs," in Proc. to ICRC, **5**, 2851.

Yoshi, Y. (1993). "Detection and selection effects in observations of faint galaxies," ApJ, **403**, 552.